Freie Universität Berlin

Femtosecond spectroscopy of solid hydrogen:

Long lived coherences in a molecular quantum crystal

im Fachbereich Physik
der Freien Universität Berlin
eingereichte Dissertation
von

Falk Königsmann

2012

Erstgutachter: Prof. Dr. Nikolaus Schwentner
Zweitgutachter: Prof. Dr. Ludger Wöste

Disputation: 09. Januar 2012

Abbreviations

2D OKE	Two dimensional optical Kerr effect
BBO	Beta-barium borate
CARS	Coherent anti-Stokes Raman scattering
EQQ	Electric quadrupole-quadrupole
fcc	Face-centered cubic
FFT	Fast Fourier transform
FROG	Frequency resolved optical gating
FTIR	Fourier transform infrared
FWHM	Full width at half maximum
hcp	Hexagonal close-packed
MIS	Matrix isolation spectroscopy
OKE	Optical Kerr effect
PG	Polarization gating
RCS	Rotational coherence spectroscopy
SHG	Second harmonic generation
SRG	Stimulated Raman gain
TO	Transversal optical
TRSRG	Time resolved stimulated Raman gain

Constants (SI units)

c	=	299792458 m/s	speed of light
ϵ_0	=	8.854187×10^{-12} F/m	dielectric permittivity of vacuum
h	=	6.626069×10^{-34} J s	Planck constant
$\hbar$	=	1.054571×10^{-34} J s	reduced Planck constant
k_B	=	1.386650×10^{-23} J/K	Boltzmann constant
m_u	=	1.66057×10^{-27} kg	atomic mass unit
N_A	=	6.022142×10^{23} 1/mol	Avogadro number
R	=	8.314472 J/(mol K)	universal gas constant

Conversion of units

	cm^{-1}	eV	J	MHz	K
1 cm^{-1}	1	1.2398×10^{-4}	1.9864×10^{-23}	2.9979×10^{4}	1.4388
1 eV	8.0655×10^{3}	1	1.6022×10^{-19}	2.4180×10^{-8}	1.1605×10^{4}
1 J	5.0341×10^{22}	6.2415×10^{18}	1	1.5092×10^{27}	7.2429×10^{22}
1 MHz	3.3356×10^{-5}	4.1357×10^{-9}	6.6261×10^{-28}	1	4.7992
1 K	6.9504×10^{-1}	8.6174×10^{-5}	1.3807×10^{-23}	2.0837×10^{-1}	1

Abstract

This thesis, settled within the framework of the SfB 450 'Analysis and control of ultrafast photoinduced reactions', focuses on rotational alignment dynamics in the solid phase. The first direct observation of long lived ultrafast coherences in solid hydrogen is reported and an extended approach to Raman induced coherence spectroscopy, which we call two dimensional optical Kerr effect (2D OKE) spectroscopy, is developed. The growth of pure and doped hydrogen crystals is discussed and investigated in addition by means of Fourier transform infrared spectroscopy in the light of rotational alignment experiments with matrix isolated molecules.

Cryogenic hydrogen is a molecular quantum crystal with outstanding properties. Its weak interactions and large lattice constant allow nearly free rotation of many embedded impurities, and the large zero-point motion of hydrogen causes a high homogeneity. Solid hydrogen, with its very narrow linewidths and long coherence times, appeared to be optimal for coherent experiments in the solid state. The molecular quantum numbers of hydrogen are preserved in the condensed phase and the properties of solid hydrogen are highly dependent on the nuclear spin state of the hydrogen molecules. Hence, we prepared high purity $I = 0$ para-hydrogen with concentrations up to 99.97%. Hydrogen crystals with high optical quality and 3 cm thickness were grown in order to perform polarization sensitive laser spectroscopy.

A two dimensional, spectrally and time resolved Raman technique that is sensitive to induced anisotropies was introduced on gaseous and liquid para-hydrogen samples, and subsequently carried to the solid phase. Thereby, rotational alignment dynamics with periods of about 94 fs, corresponding to the Raman-active $J = 2 \leftarrow 0$ transition of hydrogen, and spectrally well separated Stokes and anti-Stokes shifted sidebands were observed. The transition energies were determined with high accuracies and in excellent agreement with the literature. In the solid, the degeneracy of the $J = 2$ roton state is lifted and the simultaneous detection of three coherent sublevels caused distinct beatings with periods of 8 ps and 17 ps.

The measured dephasing times T_2 vary from about 250 ps in the gas phase (25 K, 900 mbar) to about 8 ps in the denser liquid. The loss of coherence is caused by statistical processes, e.g. by random binary collisions of molecules. The highly ordered solid exhibits roton dephasing times of about 90 ps. However, the $J = 2$ rotons have to be understood as Bloch-waves with a wavevectors $\mathbf{k}$. Thus, defect sites in the lattice, like ortho-hydrogen impurities, act as scattering centers for the roton waves. The scattering into other $\mathbf{k}$-states destroys the roton waves' coherences, and we observed a strong dependence of the dephasing on the ortho-hydrogen concentration.

Additionally, we report the detection of the Raman-active transversal optical phonon mode of hcp para-hydrogen. The phonon shows coherent dynamics with a period of about 900 fs and has a dephasing time of about 20 ps, two times longer than expected. Transition energy and dephasing time of the phonon mode were determined with the highest ever reported accuracy. The simultaneous detection of roton and phonon dynamics at spectrally well separated positions emphasizes the strength of 2D OKE spectroscopy.

The possibilities to grow transparent crystals with high concentrations of isolated dopant molecules were evaluated. Ro-vibrational absorption spectra were recorded to study the clustering behavior of carbon monoxide and methane impurities, which was found to be strongly dopant dependent. Previously unreported, forbidden transitions in the ν_1 stretching-mode of methane were observed and assigned.

Kurzfassung

Diese Arbeit, eingebettet in den SfB 450 "Analyse und Steuerung ultraschneller photoinduzierter Reaktionen", widmet sich der Dynamik von Rotationsausrichtungen im Festkörper. Sie beschreibt die erstmalige direkte Beobachtung langlebiger, ultraschneller Kohärenzen in festem Wasserstoff und entwickelt eine erweiterte Herangehensweise an die Spektroskopie Raman-induzierter Kohärenzen, die wir zweidimensionale optische Kerr Effekt (2D OKE) Spektroskopie nennen. Die Zucht von reinen und dotierten Wasserstoff-Kristallen wird im Lichte von Ausrichtungsexperimenten an Matrix-isolierten Molekülen diskutiert und zusätzlich mit Fourier-Transform-Infrarot-Spektroskopie untersucht.

Kryogener Wasserstoff ist ein molekularer Quanten-Kristall mit herausragenden Eigenschaften. Seine schwachen Wechselwirkungen und große Gitterkonstante ermöglichen die nahezu freie Rotation vieler eingebetteter Fremdkörper, und die große Nullpunktsbewegung führt zu einer hohen Homogenität. Fester Wasserstoff, mit seinen sehr schmalen Linienbreiten und langen Kohärenzzeiten, erwies sich als eine optimale Probe für kohärente Experimente im Festkörper. Die Molekülquantenzahlen von Wasserstoff bleiben auch in der kondensierten Phase erhalten und die Eigenschaften von festen Wasserstoff hängen stark vom Kernspin der Moleküle ab. Daher präparierten wir hochreinen $I = 0$ Para-Wasserstoff mit Konzentrationen bis zu 99,97%. Um Polarisations-aufgelöste Laser-Spektroskopie durchführen zu können, züchteten wir 3 cm dicke Kristalle mit hoher optischer Qualität.

Eine zweidimensionale, spektral- und zeit-aufgelöste Raman Technik zur Untersuchung induzierter Kohärenzen wurde an gasförmigen und flüssigen Para-Wasserstoff eingeführt und anschließend in die feste Phase übertragen. Dabei wurden Ausrichtungsdynamiken mit Periodendauern um 94 fs, entsprechend dem $J = 2 \leftarrow 0$ Raman-Übergang von Wasserstoff, und klar spektral getrennte Stokes- und Anti-Stokes Banden beobachtet. Die Übergangsenergien wurden mit hoher Genauigkeit und exzellenter Übereinstimmung mit der Literatur bestimmt. Im Festkörper ist die Entartung des $J = 2$ Rotonen Zustandes aufgehoben, und die gleichzeitige Detektion von drei kohärenten Unterniveaus verursacht charackteristische Schwebungen mit Periodendauern von 8 ps und 17 ps..

Die gemessenen Dephasierungszeiten T_2 variieren von ca. 250 ps im Gas (25 K, 900 mbar) bis zu ca. 8 ps in der dichteren Flüssigkeit. Der Verlust der Kohärenz wird durch statistische Prozesse verursacht, z.B. durch zufällige Zweikörperstöße. Die Dephasierungszeiten der Rotonen im hoch geordneten Kristall liegen um die 90 ps. Die $J = 2$ Rotonen müssen dabei als Bloch-Wellen mit einem Wellenvektor $\mathbf{k}$ verstanden werden. Daher können Streuprozesse an Gitterstörungen, wie Ortho-Wasserstoff Unreinheiten, zur Streuung in andere $\mathbf{k}$-Zustände und zum Verlust der Kohärenz führen. Das führt zu einer starken Abhängigkeit der Dephasierung von der Ortho-Wasserstoff Konzentration, wie sie auch von uns beobachtet wurde.

Zusätzlich detektierten wir die Raman-aktive, transversal optische Phonon-Mode von hcp Para-Wasserstoff. Sie zeigt kohärente Dynamik mit einer Periodendauer um 900 fs. Die Dephasierungszeit von etwa 20 ps übertrifft die Erwartungen um den Faktor zwei. Sowohl die Energie als auch die Dephasierungszeit konnten mit der höchsten jemals berichteten Genauigkeit bestimmt werden. Die gleichzeitige Messung von Phonon und Rotonen Dynamik an spektral klar getrennten Positionen betont die Stärke von 2D OKE Spektroskopie.

Die Zuchtmöglichkeit transparenter Kristalle mit hohen Konzentrationen eingebetteter Moleküle wurde anhand der ro-vibronischen Absorption von Kohlenmonoxid und Methan Dotierungen untersucht. Dabei zeigte sich, dass die Tendenz zur Clusterbildung stark von der Dotierung abhängt. Des Weiteren konnten bisher nicht beobachtete, verbotene Übergänge der ν_1 Streckschwingung von Methane gemessen und zugeordnet werden.

Contents

1 Introduction

Henry Cavendish recognized the production of a substance that he called 'inflammable air' upon a metal-acid reaction in 1766 [1]. This substance became known under the name *hydrogen*, the Greek word for 'water-former'. Hydrogen atoms are the simplest of all atoms and they form the lightest of all molecules. Thus, the properties of hydrogen are fundamental and have drawn the attention of generations of scientists. In 1899, one of them, James Dewar, was the first to solidify molecular hydrogen [2]. Since then, hydrogen has proved to form one of the most peculiar, and most exciting solids: a molecular *quantum crystal*. This thesis aspires to present a small contribution to the over hundred years of research on solid hydrogen by combining this unique sample with the possibilities of ultrafast time resolved spectroscopy.

The quantum nature of solid hydrogen is a twofold one: Firstly, the light mass and the weak interactions lead to a large zero point motion of the molecules in the lattice. Accordingly, there is a significant overlap of the single-molecule wavefunctions, which gives rise to *quantum diffusion* effects. Secondly, the quantum numbers of the isolated molecule are preserved in the solid phase and play an important role for the properties of cryogenic hydrogen. This leads to many intriguing quantum effects, like a *delocalization* of vibrational, rotational, and orientational excitations. The well defined elementary excitations of solid hydrogen span a broad spectral range and have fascinated spectroscopist since the 1950's [3–8].

Weak interactions and the absence of inhomogeneous broadening lead to very narrow linewidths in solid hydrogen. Therefore, solid hydrogen became an interesting host for the modern *matrix isolation* techniques that were developed by George Pimentel during the 1950's [8–11]. The initial motivation of matrix isolation spectroscopy (MIS) was to study short lived reactive species, which is possible by trapping them within a chemically inert crystal, or 'cage'. Therefore, rare gas and nitrogen solids have been widely applied in the past [12–16]. However, the field has developed far beyond its origins and the 'pottery' of the suitable cage for a desired application becomes more and more important. Next to narrow linewidths, solid hydrogen offers several advantages compared to conventional rare gas solid hosts. It can be prepared in thick, optically transparent samples, which makes the spectroscopy of highly diluted, truly isolated dopants possible. Additionally, the so called cage effect is greatly reduced, which allows to create isolated chemical radicals by photodissociation and opens a pathway to a subsequent solid state chemistry, involving the molecules and excitations of the host [17, 18].

A major objective of this work was to induce and observe the nonadiabatic *rotational alignment* of molecules in a solid host. This is of interest for many reasons, e.g. it might be used to study and control alignment dependent reactions in matrices [19, 20]. The molecular rotation in the condensed phase was first discussed by Linus Pauling in 1930 [21]. Unfortunately, only few combinations of solid state environment and embedded molecule allow rotation in a solid. However, particularly cryogenic *solid para-hydrogen* shows very weak interactions. Therefore, and due to the large lattice constant of hydrogen, a nearly free rotation of hydrogen and many dopant molecules is observed in solid para-hydrogen. This makes rotational alignment in a solid host possible, and brings para-hydrogen matrices into the focus of this work.

The tool of choice for the observation of rotational alignment is femtosecond pump-probe spectroscopy, because rotational dynamics have time constants of femto- to picoseconds. A well established method to do this is the so called *time resolved optical Kerr effect (OKE) spectroscopy*, a Raman technique that is sensitive to induced anisotropies [22–24]. It was extensively used in our workgroup within the doctoral thesis of Nina Owschimikow, who studied rotational alignment dynamics in the gaseous phase [25, 26]. Time resolved OKE spectroscopy has been applied to study Raman induced coherences in several liquids, glasses and solids before [27, 28], but despite its benefits it was never applied to solid hydrogen. Indeed, only few time resolved experiments were ever carried out with solid hydrogen samples at all. Only two experiments with nano- and picoseconds resolution focused on vibrational and rotational decay times in pure solid hydrogen [29, 30], and to our knowledge, there was only one experiment with femtoseconds time resolution. The latter studied the lattice response onto an impulsive electronic excitation of an NO impurity and revealed an over damped, rather liquid like behavior of solid para-hydrogen [31, 32].

We found that a variation of the time resolved OKE technique provided us several benefits, and performed a spectrally and time resolved observation that we call *two dimensional optical Kerr effect (2D OKE) spectroscopy* [33]. It proved to be particularly useful for the simultaneous observation of low and high energy dynamics. Solid para-hydrogen was a perfect sample to establish this novel approach, by virtue of its distinct elementary excitations. Indeed, we successfully observed delocalized rotational dynamics with 94 fs period, lattice vibrations with 900 fs period, and rotational beating patterns, induced by the lifted degeneracy of orientational states in the crystal field, with periods of 8 ps and 17 ps. Thus, the experimental data presented in this thesis are the first direct observation of ultrafast *coherences* in solid hydrogens. Even more, 2D OKE spectroscopy enabled us to determine simultaneously the corresponding wide range of transition frequencies to a very high precision.

Of particular interest was the damping behavior of our signals, which had exponential envelops with decay times of several tens to hundreds of picoseconds. Thus, the observed *coherent wavepacket dynamics* proved to be very long lived, as expected from the narrow linewidths of excitations in solid para-hydrogen. The *decoherence* or *dephasing* of coherent wavepackets is in general induced due to statistical processes, which destroy the well defined phase relation between the quantum mechanical eigenstates that form the wavepacket. Thus, the slow decoherence in solid para-hydrogen stem from the weak interactions and the high order of the solid. Since a well preserved coherence is a necessity for quantum computing, solid para-hydrogen and OKE spectroscopy are also considered for the realization of a molecular quantum computer [34].

Chapter 2 gives a brief introduction into cryogenic solid hydrogens. The vast research that was carried out on the solid phase of hydrogen fills several books [11, 35–38]. We will therefore restrict ourselves to very basic concepts and some of the most important properties of solid hydrogen that are relevant for our expriments.

Chapter 3 is a description of our sample preparation. It consists of two main parts, which describe the conversion between the two species of hydrogen, ortho- and para-hydrogen, and the subsequent growth of a macroscopic crystal in an enclosed cell, respectively. Both were new techniques to our laboratory and are presented in detail.

Chapter 4 explains the basic concepts for the time resolved 2D OKE spectroscopy as it was performed by us. It starts with motivating overviews of the molecular alignment in intense laser field and the nonlinear optical processes that played a role in our experiments. More space is given to the theory of time resolved 2D OKE spectroscopy, with the aim to present analytic equations for our experimental observations.

Chapter 5 introduces the 2D OKE setup. In particular the properties of the applied laser pulses, and the effects of the polarization sensitive detection are discussed. They become of importance in many aspects for the measured 2D OKE spectra. In a second section, we present a set of test experiments with gaseous nitrogen, as it was used by Nina Owschimikow. The comparison with Chapter 4 yields an excellent agreement, and is meant as test of our setup.

Chapter 6 introduces 2D OKE spectroscopy on isotropic hydrogen samples, i.e. gaseous and liquid para-hydrogen. The strength of 2D OKE spectroscopy lies in the spectral separation of Stokes and anti-Stokes bands, however the resolution is limited by the width of the probe laser. A test of this approach therefore required relatively large transition energies. The rotational alignment dynamics of para-hydrogen provided such transitions, and we observed distinct spectral effects. This laid the basis for the understanding of the complex spectra that were obtained with hydrogen crystals.

Chapter 7 is the main part of this thesis. It carries 2D OKE spectroscopy into the solid phase. There, it is able to play out its full strength in the simultaneous observation of low energy phonons and high energy rotational excitations. Next to the direct observation and quantitative analysis of the specific solid state dynamics, we report distinct directional effects that are inherent to an anisotropic sample. Additionally, we discuss the stimulated amplification of Raman sidebands and intriguing higher order effects, which became observable due to 2D OKE spectroscopy.

Chapter 8 gives the results of supplementary infrared absorption spectroscopy that we carried out on pure and doped para- and normal-hydrogen crystals. Absorption spectroscopy proved to be a valuable tool to determine the properties and stability of our samples. The spectroscopy of doped crystals gives insight into the applicable growth parameters of doped samples, which is needed to grow samples with isolated, rotating dopant molecules. It is therefore the basis for future rotational alignment experiments with doped para-hydrogen crystals.

2 Cryogenic solid hydrogens

"The molecular hydrogens (H_2, D_2, HD, etc.) form the simplest of all molecular solids. The combination of the light mass, small moment of inertia, weak interactions, and the quasi-metastable ortho-para species result in a fascinating low-temperature behavior that can be understood to a large extent from considerations of first principles."

I. F. Silvera [35]

This chapter briefly introduces the physics of the most fundamental and most exciting molecular solids, the cryogenic solid hydrogens. Hereby we can refer to several comprehensive reviews that give an overview about the topic. There is the excellent review paper of I. F. Silvera from 1980 onto pure solid molecular hydrogens [35], and the book by van Kranendonk from 1983 [36], which links a detailed theoretical description with experimental findings. Convenient summaries onto pure cryogenic hydrogens are also given in the books 'Hydrogen Properties for Fusion Energy' by P. Clark Souers from 1986 [37], and 'Physics of Cryocrystals' by V. G. Manzhelii from 1997 [38]. An overview onto matrix isolation spectroscopy in solid hydrogens was given most recently in the book 'Physics and Chemistry at Low Temperatures' by M. E. Fajardo from 2011 [11].

2.1 Isolated hydrogen molecules

There are three stable hydrogen isotopes, hydrogen ${}^1_1\mathrm{H}$ (99.99 % of the hydrogen on earth), deuterium ${}^2_1\mathrm{D}$, and tritium ${}^3_1\mathrm{T}$. Under normal conditions on earth, atomic hydrogen is instable. Instead, it forms the simplest of all diatomic molecules, H_2, HD, D_2, etc.. Their electronic ground state is a highly symmetric ${}^1\Sigma^+$. Homonuclear molecules have an even higher symmetry: ${}^1\Sigma^+_g$. They have an even parity considering the change of the electron coordinate signs with respect to the inversion center of the molecule. Their nuclear wavefunctions have to obey similar symmetry considerations regarding the change of the nuclear coordinate signs. For H_2, both nuclei are fermions ($I_H = 1/2$) and therefore subject to the Pauli exclusion principle. The total nuclear wavefunction of H_2,

$$\Psi_{nuc} = \Psi_{spin}\Psi_{rot}\Psi_{vib}, \tag{2.1}$$

has to be antisymmetric. The vibrational wavefunction Ψ_{vib} is always symmetric, but the rotational and the nuclear spin wavefunction, $\Psi_{rot}(J)$ and $\Psi_{spin}(I_{tot})$, can be symmetric (even J, $I_{tot} = 1$) and antisymmetric (odd J, $I_{tot} = 0$). Thus, H_2 comes in two species: ortho-hydrogen, with odd rotational quantum number J and a total nuclear spin $I_{tot} = 1$, and para-hydrogen, with even J and $I_{tot} = 0$.

Figure 2.1 gives an impression of the rotational energy levels of an isolated H_2 molecule in its electronic ground state. Due to the light mass the moment of inertia of hydrogen is small. Consequently, following Eq. 4.7, the rotational splittings are very large. At low temperatures, the sole populated levels are the $J = 0$ and $J = 1$ rotational ground states of para- and ortho-hydrogen. Their angular distributions, described by the spherical harmonics Y_{00} and Y_{1m}, give rise to important differences between the two species, particularly regarding their long-range interactions. Both are nonpolar and have therefore no electric dipole

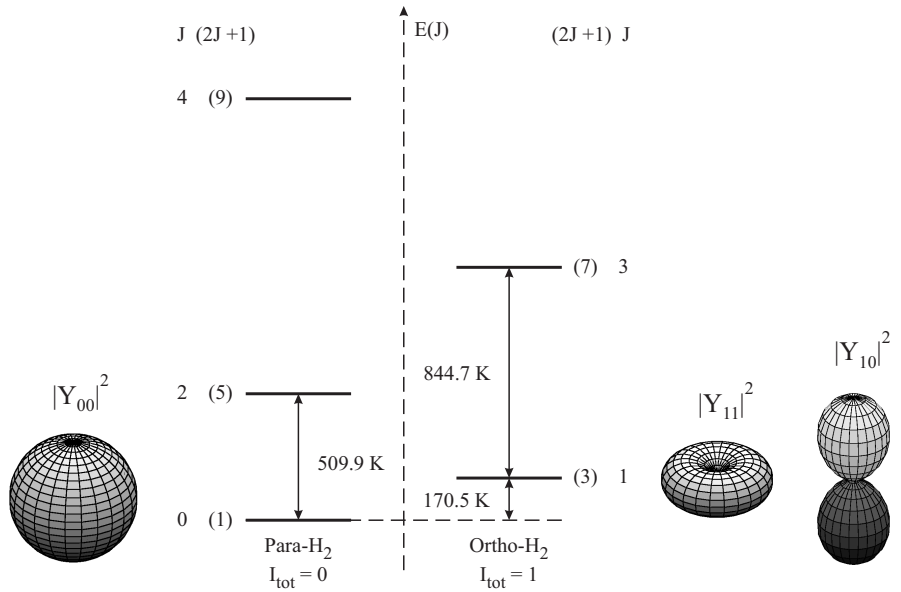

Figure 2.1: *Rotational energy levels and degeneracies for free hydrogen molecules [35]. The angular distributions of the lowest rotational levels for ortho- (Y_{1m}) and para-hydrogen (Y_{00}) are sketched on the right, and left hand side, respectively.*

moment. Indeed, the $J = 0$ molecule is highly symmetric and has therefore no electric multipole moments at all. Ortho-hydrogen instead exhibits electric multipole moments, and its lowest order moment is an electric quadrupole moment. Thus, ortho-hydrogen molecules can interact via electric quadrupole-quadrupole (EQQ) forces, whereas the sole long-range interaction of para-hydrogen molecules are van der Waals forces.

We carried out two types of spectroscopy in our experiments: a coherent Raman spectroscopy that we call two dimensional optical Kerr effect (2D OKE) spectroscopy, and Fourier transform infrared (FTIR) spectroscopy. Therefore, we present some basic molecular constants that become important in the following in Table 4.1. Hydrogen exhibits Raman allowed transitions, which have to follow the selection rules $\Delta J = 0, \pm 2$ for the rotational quantum number, and $\Delta v = 0, \pm 1$ for the vibrational quantum number. Homonuclear hydrogen is infrared inactive, due to its high symmetry. Thus, there are no infrared allowed rotational or vibrational transitions for the isolated molecule. In the solid, however, induced electric multipole moments lead to weak absorption of infrared light. Hence, infrared absorption spectroscopy becomes a valuable tool for the characterization of our solid hydrogen samples.

2.2 Solid hydrogens

Hydrogens forms unique crystals with many fascinating properties. They are considered to be true molecular quantum crystals, which are dominated by quantum effects. Some of the features of solid hydrogens that played important roles in our experiments are introduced below. Hereby we will focus onto a certain species of solid hydrogens in the following, hcp solid para-hydrogen. It was the main topic of our experimental work, since it exhibits extraordinary properties. However, we will see that the properties of hydrogen crystals depent strongly on the ratio of the $J = 0$ and the $J = 1$ species in the solid.

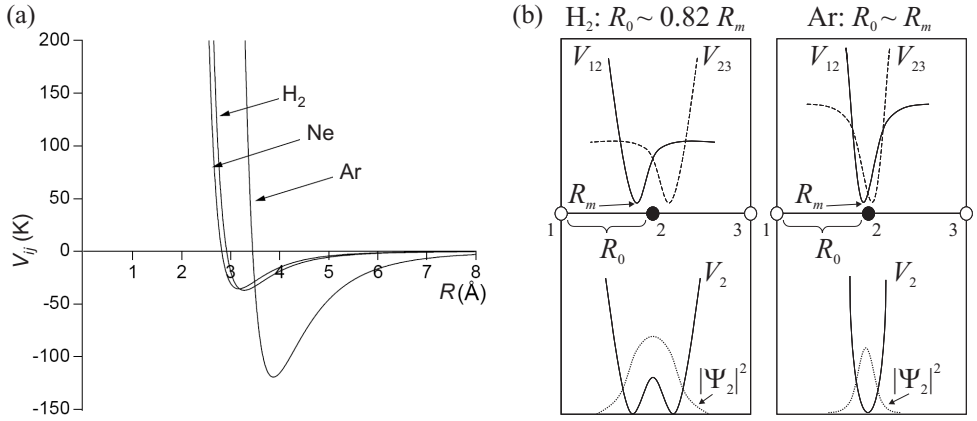

Figure 2.2: *(a) Lennard-Jones pair potentials of H_2, Ne, and Ar [10]. (b) The upper panels show one dimensional sketches of the overlapping Lennard-Jones pair potentials for H_2 and Ar in their lattices, with center molecules 2 and nearest neighbor molecules 1 and 3. The lower panels show the resulting potentials for the molecules 2, and dashed lines give impressions of the corresponding density distributions.*

2.2.1 Quantum crystal

The lattice constant $R_0 = 3.78$ Å of low pressure hcp solid para-hydrogen is large compared to the internuclear separation $R_e = 0.74$ Å. Thus, they really form molecular crystals. Even more, J and M may be treated as good quantum numbers in the solid, due to the weak interaction forces. An almost free rotation of the hydrogen molecules in the solid is therefore possible, and many of the exciting quantum effects in solid hydrogens stem from this quantization. In general, the intermolecular pair interaction between molecules consists of repulsive and attractive terms and has isotropic and anisotropic parts. However, as long as we stick to the $J = 0$ ground state of para-hydrogen, the intermolecular interaction is isotropic. A phenomenological approximation is given by the Lennard-Jones potential,

$$V_{ij} = \epsilon \left[\left(\frac{R_m}{R} \right)^{12} - 2 \left(\frac{R_m}{R} \right)^{6} \right]. \tag{2.2}$$

The parameter ϵ is the depth of the potential well, R is the intermolecular separation, and R_m the separation at which the potential reaches its minimum. The short-range repulsive R^{-12} part describes the exchange interaction due to the overlap of the electronic orbitals. The long-range attractive R^{-6} part instead has its origin in the dispersion force that stems from induced dipoles.

A comparison of the Lennard-Jones potentials of hydrogen, neon, and argon is given in Figure 2.2 (a) and Table 2.1. Although the attractive interaction has the same origin for the three species, the Lennard-Jones potential of argon is more than three times deeper. Indeed, hydrogen, neon, and argon form weakly bound van der Waals crystals at low temperatures. However, whereas argon may be described as an almost classical crystal, neon and particularly hydrogen are considered to be true quantum crystals. The quantum nature stems from the weak intermolecular interaction and the light mass. This is exemplified in Figure 2.2 (b). Due to its deep potential well and large mass argon has a very small zero point motion and is well localized in the minimum of the intermolecular potential. Accordingly, argon has a well localized lattice position. The mean intermolecular separation of hydrogen, however, is much larger than the separation at which the intermolecular

	para-H_2	Ne	Ar
triple point in K	13.80	24.56	83.81
boiling point at 1 bar in K	20.28	27.07	87.29
Lennard-Jones parameter ϵ in K	37	35.6	119.3
Lennard-Jones parameter R_m in Å	3.28	3.08	3.87
lattice structure	hcp	hcp/fcc	hcp/fcc
lattice constant R_0 in Å	3.78	3.16	3.76
polarizability α in Å^3	0.819[b]	0.40	1.64

Table 2.1: *Properties of para-hydrogen molecules, neon atoms, and argon atoms as given in Ref. [10].*

[a]from Ref. [39]

potential reaches its minimum. Obviously, this is caused by the shallow potential and the light mass of hydrogen. Thus, hydrogen is not well localized in the lattice. Instead, it even exhibits a significant overlap of the molecular wavefunctions. Therefore quantum effects, like the quantum diffusion of molecules in hydrogen crystals, become possible. E.g., ortho-hydrogen impurities in a para-hydrogen crystal may exchange their position with neighboring molecules and travel through the crystal at a much higher rate than possible due to thermal diffusion. Furthermore, the large zero point motion allows hydrogen molecules to move to the most favorable position. Molecules in a hydrogen crystal have therefore always the same surroundings and inhomogeneous broadening plays almost no role. Similarly, hydrogen crystals are able to heal defects in their lattice structure due to the high mobility of the molecules.

2.2.2 Crystal structure and properties

The phase diagram of solid hydrogen is complex and not yet fully understood. It shows distinct dependences onto the ortho-hydrogen concentration at low pressures, and promises fascinating physics at high pressures, like supersolidity and the creation of metastable metallic hydrogen. We will restrict ourselfs to the description of the low pressure phases, since all our experiments were carried out well below 1 bar. Later on, the lattice structure will become important for the observable excitations of solid hydrogen.

Hydrogen crystals that are grown from the melt in equilibrium with their vapor pressure are always of hexagonal close packet (hcp) structure, independent from their ortho-para ratio. Depicted in Figure 2.7 (a), it provides an inherent anisotropy along the c-axis with respect to the a-b-directions, which are situated in the vertical plane. Even for $J = 1$ ortho-hydrogen, the hcp structure exhibits no further orientational ordering, and is therefore regarded as disordered. The electric quadrupole moment of the $J = 1$ species, however, may give rise to a long-range orientational ordering effect at low temperatures. Thus, ortho-hydrogen undergoes a phase transition into an ordered face-centered cubic (fcc) structure with a $Pa3$ symmetry space group structure below 3 K. A phase diagram as given by Silvera for ortho-hydrogen is shown in Figure 2.3 (a) [35]. The transition does not happen instantaneous at a certain temperature. It rather exhibits a certain hysteresis behavior, depicted by a heavy line in Fig. 2.3 (a), and contains intermediate phases. The phase transition is driven by the anisotropic EQQ interaction, and occurs in ortho-para mixtures with ortho-hydrogen concentrations down to 56%, as illustrated in Figure 2.3 (b). Grown below 4.2 K, pure para-hydrogen exhibits fcc structures, too [40]. However, these

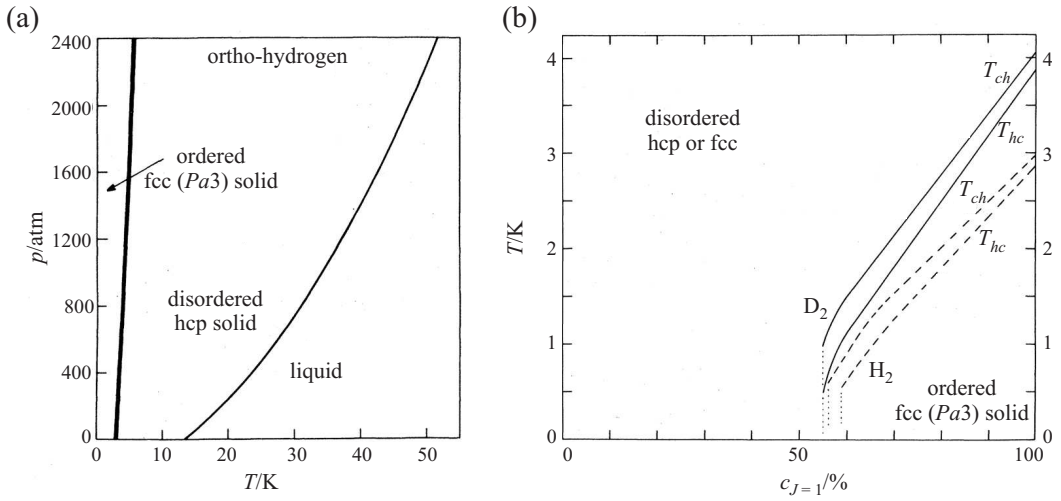

Figure 2.3: *(a) Phase diagram for pure ortho-hydrogen. The heavy line indicates a hysteresis between the ordered $Pa3$ and the disordered hcp phase. (b) Simplified phase diagrams for zero pressure solid H_2 (dashed lines) and D_2 (solid lines). T_{hc} refers to the hcp-fcc transition temperature and T_{ch} to the fcc-hcp transition temperature. No ordering into the $Pa3$ structure is observed below $c_{J=1} \approx 56\%$ [35].*

structures are irreversible lost upon increasing the temperature through 7 K, because there are no permanent electric multipoles in para-hydrogen that might drive the crystal through a phase transition.

Next to the microscopic structure of the crystal, the ortho-para ratio also determines the macroscopic properties of solid hydrogen. Figure 2.4 gives the heat capacity c_p of hydrogen for several ortho-hydrogen concentrations. There is strong dependence of c_p on the temperature. However, the dependence of the heat capacity onto c_{ortho} is even bigger. Indeed, the heat capacity of normal-hydrogen is more than an order of magnitude higher as for para-hydrogen around 4 K [38]. This will become important for the stability of our samples upon radiation with intense laser pulses. Particularly pairs and clusters of $J = 1$ impurities play a significant role for the heat capacity of solid para-hydrogen. The EQQ interaction leads to a splitting of the threefold-degenerated $J = 1$ state, which amounts to several Kelvin for nearest neighbor pairs. Thus, clusters of ortho-hydrogen exhibit many low lying energy levels that correspond to orientational transitions. These additional degrees of freedom may store energy and subsequently increase the heat capacity.

Two other properties of solid hydrogen will become important for the growth of our hydrogen crystals: the molar volume and the thermal conductivity. The dependence of the molar volume onto the temperature is shown for para-hydrogen ($c_{J=1} = 0\%$), normal-hydrogen ($c_{J=1} \approx 75\%$), and ortho-deuterium ($c_{J=1} = 0\%$) in Figure 2.5. Obviously, ortho-deuterium's heavier mass leads to a reduced zero-point motion and therefore to a denser crystal. However, the qualitative behavior of the $J = 0$ solids is similar. Their molar volume follows a simple phenomenolgical equation,

$$V(T) = V(0) + AT^b, \tag{2.3}$$

where the power of the temperature is over four [37]. Thus, the shrinkage of the $J = 0$ solids becomes very small at low temperatures. Solid normal-hydrogen instead behaves very different. One observes a strong shrinkage of the crystal even at low temperatures. Furthermore, the EQQ interaction amounts to about 10 J/mol and pulls the molecules closer together, which makes the crystal denser than solid para-hydrogen.

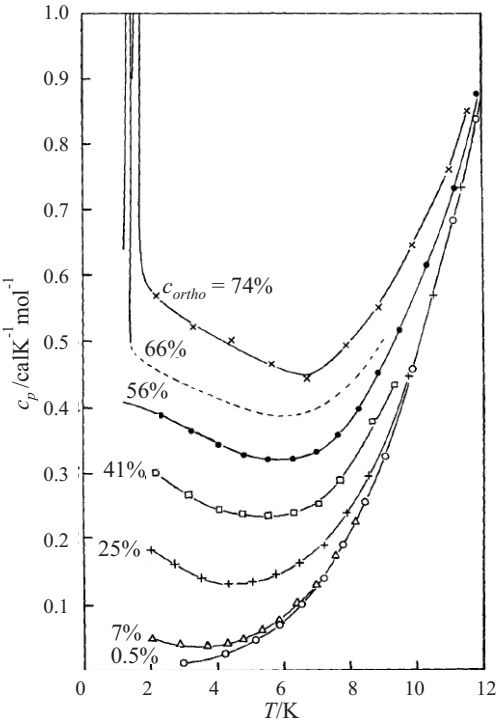

Figure 2.4: *Temperature dependence of the hydrogen heat capacity c_p for various ortho-hydrogen concentrations c_{ortho} after Hill et al. [41].*

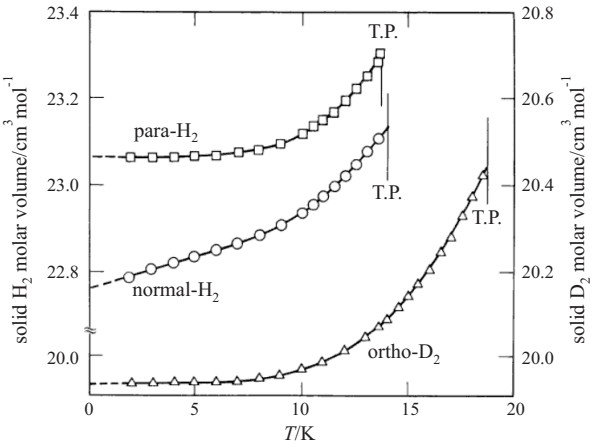

Figure 2.5: *Temperature dependence for the molar volume of para-hydrogen, normal-hydrogen, and ortho-deuterium [37].*

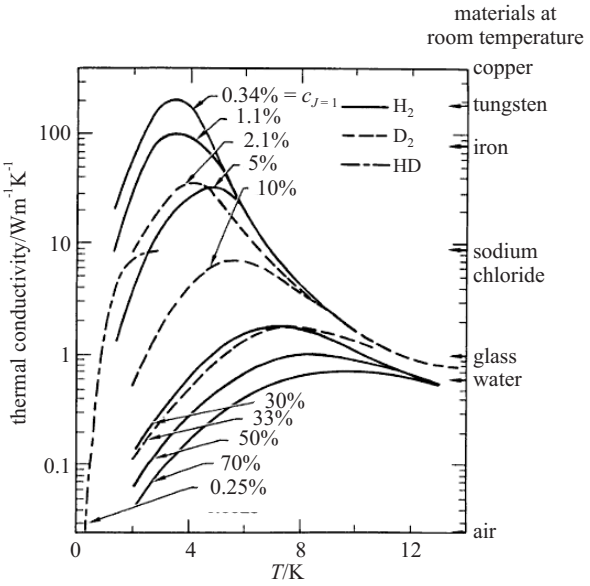

Figure 2.6: *Thermal conductivity of H_2, D_2, and HD at saturated vapor pressure for several $J = 1$ concentrations $c_{J=1}$ [37]. The thermal conductivity of familiar materials at room temperature is given for comparison an the right side.*

Most dramatic are the consequences of the ortho-para ratio onto the thermal conductivity of solid hydrogen [37, 42, 43]. This is depicted for various concentrations $c_{J=1}$ of the $J = 1$ species in Figure 2.6. For high concentrations of ortho-hydrogen, the thermal conductivity of solid hydrogen is very low, comparable to water at room temperature and lower. However, the thermal conductivity increases with decreasing $c_{J=1}$, and eventually increases to the same order of magnitude as for room temperature copper. The origin of the high dependence on $c_{J=1}$ are inelastic phonon scattering on isolated $J = 1$ impurities, and one-phonon absorption and creation processes by pairs of $J = 1$ impurities [38]. Plotted with a logarithmic scale, one recognizes a strong temperature dependence, too. The thermal conductivity is maximal at about 4 K for low ortho-hydrogen concentrations.

2.2.3 Elementary excitations

As a solid, hydrogen exhibits collective vibrational excitations, phonons, which are delocalized in the lattice. Furthermore, the vibrational and rotational excitations of a single molecule are preserved in the solid state. However, the molecular excitations may interact with neighboring molecules via multipole interactions, and there is a probability that an excitation hops from one lattice position to another. To describe the excitation in the crystal, one has to take the probability amplitude of this hopping motion into account. The excitation therefore becomes delocalized, and has to be described as a traveling wave with a wavevector $\mathbf{k}$. Such delocalized vibrational and rotational excitations are subject to a dispersion relation and thus form broad energy bands [44].

We carried out a novel kind of time resolved Raman spectroscopy on our solid hydrogen samples. Hence, an understanding of the possible Raman-active transitions was crucial for the interpretation of our data. Let's begin with the hcp phase of pure solid para-hydrogen. Figure 2.7 (b) gives an overview of the Raman-active, delocalized excitations. They are restricted to the center of the Brillouin-zone ($\mathbf{k} = 0$), due to the optical excitation. The $v = 1 \leftarrow 0$, $\Delta J = 0$ transition of para-hydrogen ($Q_1(0)$) is called a vibron, to account for its delocalization in a para-hydrogen lattice. Its transition energy of about 4153 cm^{-1}

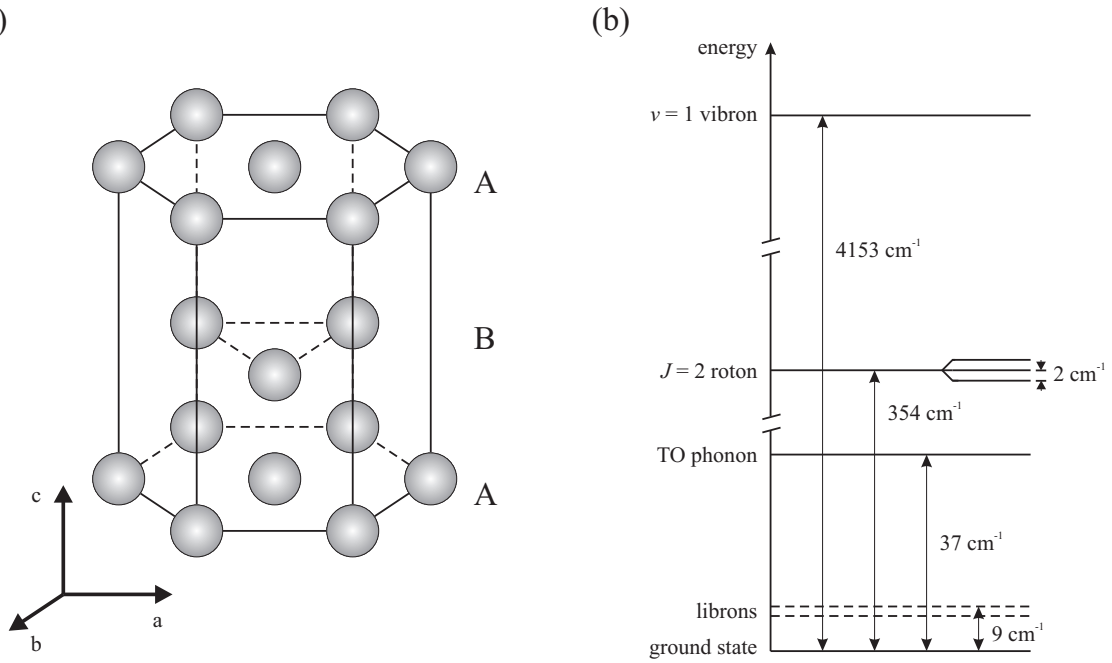

Figure 2.7: *(a) hcp lattice structure of solid hydrogen with the ABABABA stacking sequence. (b) Delocalized, Raman-active, $\boldsymbol{k} = 0$ excitations in hcp solid para-hydrogen (solid lines). Dashed lines represent the Raman-active, $\boldsymbol{k} = 0$ librons that are only present in the ordered fcc phase of solid ortho-hydrogen.*

is slightly shifted from the gas phase value of 4162 cm^{-1} (see Table 4.1. It will become interesting for our time resolved experiments that the vibron transition energy corresponds to a period of 8 fs. The next Raman-active excitation are $J = 2 \leftarrow 0$, $\Delta v = 0$ rotational transitions ($S_0(0)$), called rotons. The $J = 2$ state has five degenerated M-substates in the gas phase. However, the degeneration is lifted in the solid. One observes three Raman-active rotational levels in solid para-hydrogen, centered at 354 cm^{-1} and split by 2 cm^{-1} due to the interaction with the crystal field. The transition frequency of 354 cm^{-1} corresponds to a period of 94 fs. Also the splitting of 2 cm^{-1} between neighboring levels, and 4 cm^{-1} for the two outer levels are important for our experiments, and correspond to 17 ps and 8 ps, respectively. Last but not least, solid hcp para-hydrogen exhibits also Raman-active phonon modes. Figure 2.8 shows the phonon dispersion relations for zero pressure para-hydrogen as obtained by Nielsen from inelastic coherent neutron scattering [45]. A twofold degenerated, transversal optical (TO) phonon mode in the a-b-plane of the hcp lattice is the sole Raman-active phonon excitation of hydrogen [46]. Its transition frequency of about 37 cm^{-1} corresponds to a period of approximately 900 fs, one order of magnitude slower than the rotational period.

The spectra of solid hydrogens depend strongly on the lattice structure. E.g. the disordered hcp solid hydrogen does not show any infrared active phonon modes, but the ordered fcc phase does [47]. Similarly, the fcc phase of para-hydrogen exhibits only two Raman-active rotational levels, instead of three. We can therefore determine the structure of our samples by spectroscopic means. Furthermore, the concentration of the $J = 1$ species plays an important role for the elementary excitations in solid hydrogen. The $J = 1$ has different energy levels, e.g. 4146 cm^{-1} instead of 4153 cm^{-1} for the $v = 1$ excitation. Thus, isolated ortho-hydrogen impurities in a para-hydrogen crystal act as scattering centers for the wavelike, delocalized excitations of para-hydrogen. Indeed, scattering on

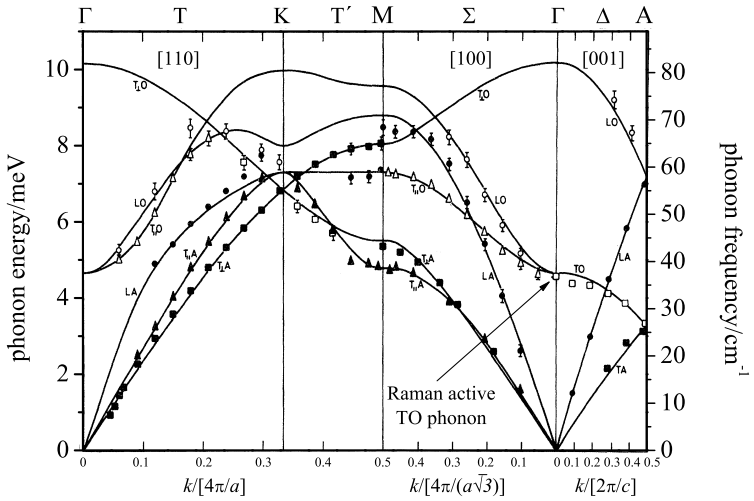

Figure 2.8: *Phonon dispersion relations for zero pressure para-hydrogen at 5.2 K as deduced from inelastic coherent neutron scattering data (dots) by Nielsen [45]. The dispersion curves (full lines) followed from a harmonic model including third-nearest-neighbor interactions. The arrow marks the Raman-active, transversal optical (TO) phonon, observed by Raman spectroscopy [46].*

ortho-hydrogen impurities plays a dominant role in the dephasing of vibrational [29] and rotational coherences in para-hydrogen [48].

Even at low ortho-hydrogen concentrations one also observes a clustering of ortho-hydrogen molecules in the solid, which is caused by their quantum diffusion and the attractive EQQ interaction between $J = 1$ molecules. Such clusters show peculiar orientational excitations. Of particular interest are pairs of ortho-hydrogen impurities and their anisotropic EQQ interaction. The strength of such interactions is determined by the distance, the total angular momentum F, and the orientation of the total angular momentum of the molecules in the lattice M. Therefore, they exhibit a manifold of states $|F, M\rangle$, which leads to a rich spectrum of Raman-active ($\Delta F = 0, \pm 2$) transitions. The highest Raman-transition energy for an isolated pair of nearest neighbor ortho-hydrogen impurities amounts to about 5.5 cm^{-1} [49]. The anisotropic interaction between ortho-hydrogen gives also rise to a long-range orientational ordering and drives crystals with high ortho-hydrogen content into an ordered fcc phase at low temperatures (see Fig. 2.3). In this ordered phase, orientational transitions even become delocalized, too. Such excitation are spin-wavelike and known as librons. They give rise to additional Raman-allowed transitions, depicted as dashed lines in Fig. 2.7 (b).

3 Sample preparation

"I have ... dropped the ortho-para terminology because I have never been able to explain it to my bosses."

P. Clark Souers [37]

This section describes the experimental setup that was used for the preparation of our samples. The first section is a brief description of the ortho- to para-hydrogen conversion, its basic principles and the used techniques. The second section is about the sample growth. It describes the sample gas preparation, the growth of pure and doped hydrogen crystals from the gas phase, and of pure hydrogen crystals from the liquid.

3.1 Ortho-para conversion

As was stated in Chapter 2, one of the key features of hydrogen is that it comes in two species, ortho- and para-hydrogen, which show very different properties. In order to perform experiments with pure para-hydrogen, we had to convert the ortho-hydrogen content of our sample-gas to para-hydrogen. Techniques to do this efficiently are known and well understood [9, 50, 51]. They require to cool the hydrogen sample gas in the presence of a catalyst down to about 15 K. Doing this, we reached a residual ortho-hydrogen concentration after conversion that varied between 0.03 and 0.2 percent.

3.1.1 Basic principles

The key property of hydrogen for the conversion of ortho-hydrogen to para-hydrogen is the large rotational constant of hydrogen (see Table 4.1). Thus, the energy difference between the lowest rotational state of ortho- and para-hydrogen is very large, about 170 K (see Fig. 2.1). In the thermodynamic equilibrium, the ortho-hydrogen concentration $\rho_{I=1}$ can be easily obtained from the Boltzmann distribution as the sum over the concentrations of all uneven J-states. It is given by

$$\rho_{I=1} = \frac{2I+1}{Z} \sum_{J=1,3,\ldots} (2J+1) \exp(-\frac{E_J}{k_B T}), \tag{3.1}$$

with the partition function

$$Z = \sum_{J=0,2,\ldots} (2J+1) \exp(-\frac{E_J}{k_B T}) + 3 \sum_{J=1,3,\ldots} (2J+1) \exp(-\frac{E_J}{k_B T}), \tag{3.2}$$

and plotted in Figure 3.1. Normal-hydrogen at room temperature, as it comes in the bottle, has an ortho-hydrogen concentration of 74.9 percent. In the thermodynamic equilibrium at 17.5 K, however, $\rho_{I=1}$ shrinks to only 0.05 percent, which is a sufficiently low ortho-hydrogen concentration for our experiments.

In order to reach the low temperature thermodynamic equilibrium, a transition from ortho- to para-hydrogen has to occur. This requires a simultaneous change of the rotational

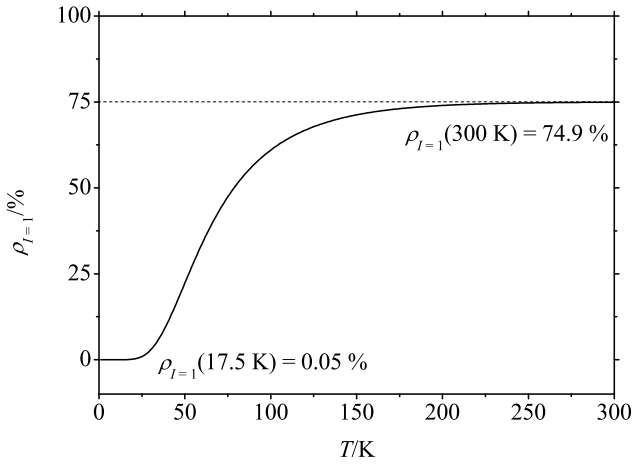

Figure 3.1: *The ortho-hydrogen concentration in the thermodynamic equilibrium as a function of temperature as calculated by Equation 3.1 [52].*

angular momentum by $\Delta J = -1$ and of the nuclear spin state from the triplet to the singlet state. Such transitions are forbidden for isolated molecules, but they can be induced by perturbations that arise from interactions with neighboring molecules. In particular, the nuclear spin transition requires a magnetic field gradient [35]. In the liquid phase, the magnetic field gradient can be provided by the nuclear spin of neighboring $I = 1$ ortho-hydrogen molecules. Unfortunately, the conversion rate due to this process is rather low and decreases with decreasing ortho-hydrogen concentration. The conversion rate depends quadratically on the ortho-hydrogen concentration, since $I = 0$ para-hydrogen molecules cannot induce ortho-para-transitions. Hence, it would take several weeks to reach thermodynamic equilibrium in the liquid [35]. In the solid, the conversion rate is even lower, because of the lowered mobility of the ortho-hydrogen molecules [53]. Fortunately, a paramagnetic salt that acts as a catalyst can drastically increase the conversion rate. In contact with the surface, and thus with the magnetic field gradient, of such a catalyst, like APACHI (a paramagnetic nickel salt supported on particulate silica gel) or iron(III) hydroxide ($Fe(OH)_3$), conversion happens with time constants of seconds to minutes.

3.1.2 Ortho-para conversion system

We used an ortho-para hydrogen converter similar to the one described by Tam and Fajardo [50]. Its main part was a copper tube bobbin, as it is depicted in Figure 3.2, that was partly filled with iron(III) hydroxide (hydrated, catalyst grade, 30-50 mesh, SIGMA-ALDRICH Inc.) as a catalyst. The copper bobbin was vacuum isolated and attached to the cold tip of a closed cycle cryostat (CRYOGEN R 210 Refrigerator, LEYBOLD-HERAEUS GmbH) expander unit (Figure 3.3). The refrigerating capacity of this setup was approximately 2 W at 20 K, and it reached a temperature of 11.5 K, measured at the bottom of the copper bobbin with a Si-diode (DT-670B1-CU, Lake Shore Cryotronics, Inc.). Room temperature, high purity (6.0, Linde) hydrogen gas was led through a needle valve into the cold copper bobbin, and liquefied there. The heatload of the room temperature gas rapidly increased the temperature of the copper bobbin to up to 20 K in the first moments. However, after a short time the copper bobbin was filled with liquid hydrogen. The hydrogen evaporated at the warm outlet of the bobbin, where no catalyst was placed, into the 10 l hydrogen

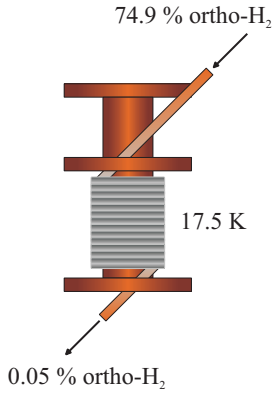

Figure 3.2: *Normal-hydrogen was led through a copper bobbin, filled with iron(III) hydroxide as a catalyst. Attached to a closed cycle cryostat, the bobbin was cooled down to below 17.5 K.*

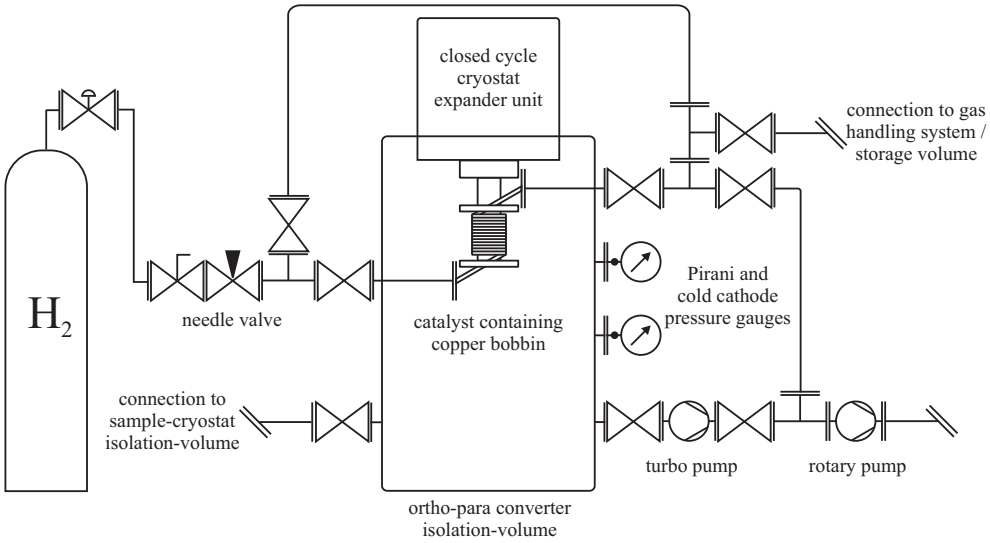

Figure 3.3: *Schematic drawing of the ortho-para conversion system.*

storage-volume that was part of the gas handling system shown in Figure 3.4. Thus, an equilibrium hydrogen flow at temperatures of about 15 K could be reached, which led to a rapid, catalyst induced conversion to para-hydrogen. The pressure of 3 bar before the needle valve ensured a relatively constant gas flow rate of about 100 mmol/h, which was just enough to warm up the bobbin to 15 K, and the storage volume was filled to 900 mbar in 25 min. The converted para-hydrogen was stable in absence of a catalyst, because the conversion due to the interaction with the walls was a rather slow process. Hence, it could be stored and, if intended, also be mixed with other gases. However, the converted para-hydrogen gas was usually used to grow a crystal within two hours to prevent a back-conversion.

3.2 Crystal growth

Hydrogen crystals can be grown in many different ways, resulting in crystals that differ in macroscopic dimensions, transparency, crystallite size, crystal structure, and dopability. In order to prepare samples to perform 2D OKE spectroscopy, a polarization sensitive

laser-spectroscopy that is discussed in detail in the following Chapters, we aimed for the growth of large and transparent crystals with regular shape and high possible dopant concentrations. Centimeter large, transparent, hcp single-crystals with known orientation can be grown with a growth rate of up to 4 cm/h by carefully freezing the liquid, starting the solidification e.g. from a cold sample tube bottom [54]. This works even better if the liquid is pressurized to 3 MPa [55]. However, this techniques have the clear disadvantage that, besides neon and other hydrogens, only few impurities can be solved in liquid hydrogen. Since most impurities freeze out, the crystal growth from the liquid cannot be used for the matrix isolation of dopants. Very high dopant concentrations can be achieved by vapor deposition on a cold substrate in a vacuum. Hydrogen's high vapor pressure demands here very low temperatures of about 2 K [56, 57]. With the rapid vapor deposition technique that was discussed by Fajardo and Tam [58], transparent para-hydrogen matrices of several millimeters thickness and dopant concentrations at and above 1000 ppm can be grown with growth-rates of up to 0.3 mm/h. Such crystals exhibit regions of fcc and hcp stacking, and can be annealed to 4.5 K to become purely hcp. The crystals are transparent and for many applications of very comfortable thickness, but they are too thin and their shape is too unregular to use them as samples for an OKE experiment. The technique that was applied by us was to grow hydrogen crystals from the gas in an enclosed cell at and above 7 K. The enclosed cell technique allows to grow transparent para-hydrogen crystals of more than 10 cm length and with impurity concentrations of up to 200 ppm within about an hour [8, 9, 59]. Such crystals are purely hcp, with a c-axis that is typically perpendicular to the copper surface. This way we grew pure and doped, normal- and para-hydrogen crystals at a variety of temperatures and with different impurities and impurity concentrations.

3.2.1 Gas handling system

Doped crystals were grown from mixtures of hydrogen gas and a dopant gas, as they were prepared using the gas handling system shown in Figure 3.4. It was made of stainless steel, using Viton®-sealings wherever possible. The chemical inertness of Viton®allows experiments with corrosive dopant gases, like halogens. All connections on the main gas mixing volume were ConFlat flanges, the connections to the rotary pump (Leybold Trivac D 8B) were Quick Flange and the connections to the sample cell, the converter system and the dopant gas bottles were carried out in 6 mm Swagelok®. Using a Leybold TURBOVAC 151 (C) turbomolecular pump we reached 4x10^{-7} mbar. The leakage of below 2×10^{-5} mbar l/min, mainly caused by the usage of Viton®-sealings, led to additional 0.25 ppm impurities after two hours of waiting. Such impurities could cluster with our dopants, and therefore cause severe problems. However, attempting to dope crystals with 10 ppm and above, we considered this leakage to be tolerable.

To prepare a mixture of para-hydrogen gas and a dopant gas, e.g. CH_4 (3.5, Linde minican®), CO (3.7, Linde minican®), or N_2 (5.0, Linde), we used two independent gas storage volumes, a small dopant gas storage-volume (0.1 l) and the hundred times larger main volume (10 l) that acted as the para-hydrogen storage-volume during the conversion process. The volumes were filled independently, in order to avoid the sublimation of the dopant gas on the cold parts of the ortho-para conversion system. Both volumes were connected after the conversion process for about thirty minutes to achieve a mixing of the gases due to thermal diffusion. The concentration of the dopant gas was easily regulated by the ratios of the two volumes and the pressures of the gases before mixing. Thus, a para-hydrogen crystal doped with 100 ppm CH_4 was grown from a mixture of 900 mbar para-hydrogen, measured with a MKS Instruments Baratron®-manometer (type 221A, range 1000 mbar) connected to the hydrogen storage-volume, and 9 mbar CH_4, measured

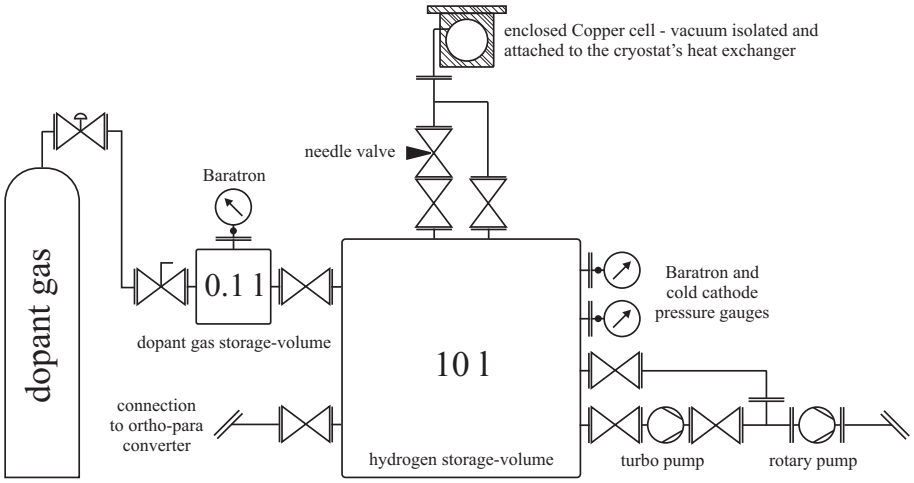

Figure 3.4: *Schematic drawing of the gas handling system.*

with a MKS Instruments Baratron®-manometer (type 121, range 100 mbar) connected to the dopant gas storage-volume.

3.2.2 Crystal growth from the gas

We grew pure and doped normal- and para-hydrogen crystals in enclosed copper cells that were similar to the cells used by Momose and Shida [9]. The cells were bored into a solid copper blocks and thermally attached to the heat exchanger of a liquid helium cryostat (CryoVac GmbH & Co. KG, He-Konti IT-Cryostat), as it is shown in Figure 3.5. The inner diameter of our cells was two centimeter, and they were one and three centimeters long, respectively. Front and back of the cells were closed with CaF_2-windows of 2 mm thickness that were attached with Teflon®-flanges and vacuum sealed with self-made indium gaskets. The sample gas was introduced into the cells through stainless steel tubes with 2 mm diameter, which were connected to the gas handling system.

During the crystal growth we observed the cell-temperature with two calibrated Si-diode (DT-670-CU, Lake Shore Cryotronics, Inc.), one attached to the bottom of the cell and one attached to the heat exchanger of the cryostat. The cooling power of the Konti-IT cryostat was manually controlled by a needle valve that connected the cryostat's liquid helium tank with it's heat exchanger and regulated the helium flow. This way we kept the temperature at a desired value, which ranged between 7 and 13 K during the growth process. The initial sample gas flow into the cell was preset with a needle valve, as it can be seen in Figure 3.4, which determined the speed of the crystal growth. However, we did not use this valve to regulate the gas flow during the growth process. Usually, we prepared 900 mbar sample gas in the 10 l storage volume and used 650 mbar of the sample gas to grow a 3 cm long crystal. Hence, the pressure in the storage volume and therefore the gas flow into the cell decreased during the growth process. This reduced the heatload that was introduced into the cell, and we had to reduce the cooling power of the cryostat to keep the temperature of the cell stable. We decided to regulate the cell's temperature rather than the gas flow to keep the heatload to crystal surface ratio as constant as possible, in order to improve the quality of the crystals. Hereby one has to keep in mind that the surface of the crystal shrank during the growth process, due to the cylindrical geometry of the sample cell.

To monitor the growth progress we took pictures with the camera setup that is shown in Figure 3.6. Figure 3.7 displays the growth history of a para-hydrogen crystal at 10 K.

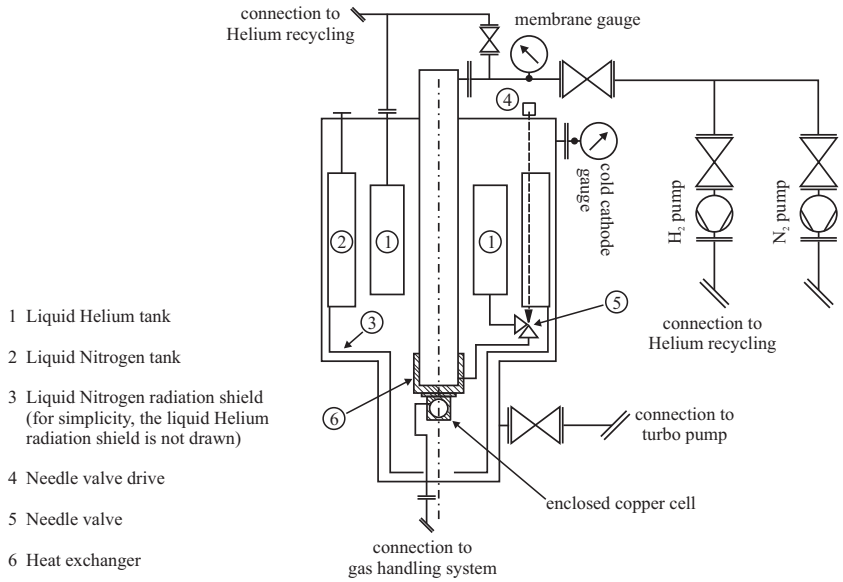

Figure 3.5: *Schematic drawing of the liquid Helium cryostat setup. It was used in three different operational modes to reach different temperature ranges. (I.) A small flow of helium from the liquid helium tank into the heat exchanger, which was at the same time evacuated with a rotary pump, was used to reach temperatures above 4.2 K. (II.) A temperature between 4.2 K down to 2 K was reached by flooding the heat exchanger and simultaneously pumping to the corresponding vapor pressure above the liquid helium level. (III.) Long time stable 4.2 K were achieved by fully connecting liquid helium tank and heat exchanger, effectively turning the cryostat into a liquid helium bath. The liquid helium in the liquid helium tank was observed with a cryomagnetics LM-500 liquid cryogen level monitor. It was enough to last for twenty hours and could be refilled during experiments without damaging the sample.*

As one can see, the gas started to solidify onto the copper surface and the crystal grew towards the center of the cylindrical copper cell. The growth stopped when the gas inlet was completely blocked by solid hydrogen, which left a small void in the center of the crystal. A similar growth process at 13 K is shown in Figure 3.11 (c, e, g, i). On the first glance the crystals differed only in the size of the enclosed void.

The optical quality of the crystals depended strongly on the growth temperature. Crystals grown at 13 K were perfectly transparent, appearing to be completely homogeneous except of the small void in their middle, whereas growth at 7 K led to optically intransparent, milky-white looking crystals with a big void in their middle. The latter is contradictory to the findings of Oka, Momose and Shida [8, 9]. They reported the growth of transparent crystals at this temperature, perhaps due to a higher gas flow in their experiments. Either kind of crystals were infrared transparent and suitable for FTIR spectroscopy, as it is discussed in Chapter 8, but only transparent crystals were suitable for 2D OKE spectroscopy. Unfortunately, dopants tend to cluster strongly in crystals grown at higher temperatures, as we will show in Chapter 8.

A crucial point of the crystal growth was the subsequent lowering of the sample temperature to 5 K or lower. There were several advantages of this. Firstly, it enabled us to bring the cryostat into a more temperature-stable working mode, especially when we flooded the heat exchanger with liquid helium and effectively used the cryostat as a liquid helium bath cryostat. Secondly, low temperatures prevented dopant clustering. And thirdly, the thermal conductivity of para-hydrogen reaches it maximum at about 4 K, depending on the ortho-hydrogen concentration (see Fig. 2.6). This can prevent crystal destruction by

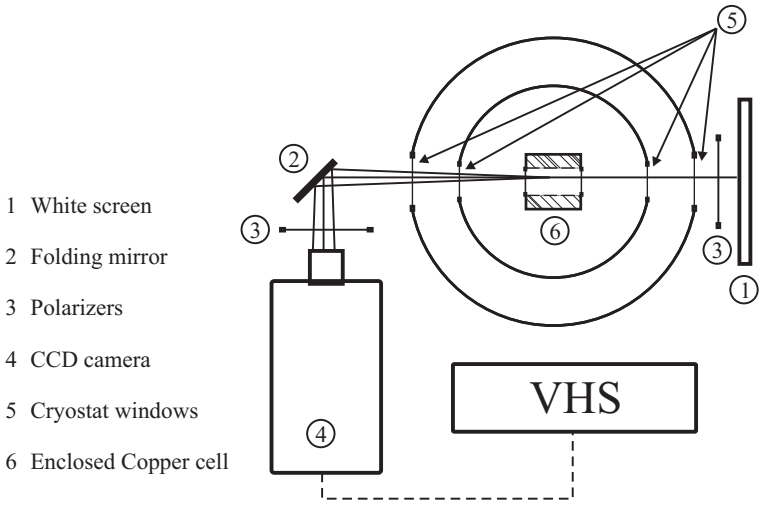

Figure 3.6: *Schematic drawing of the camera setup. It included two polarizers, one in front and one behind the sample cell. This allowed to monitor birefringence, as it can be induced through strain or crystal structure.*

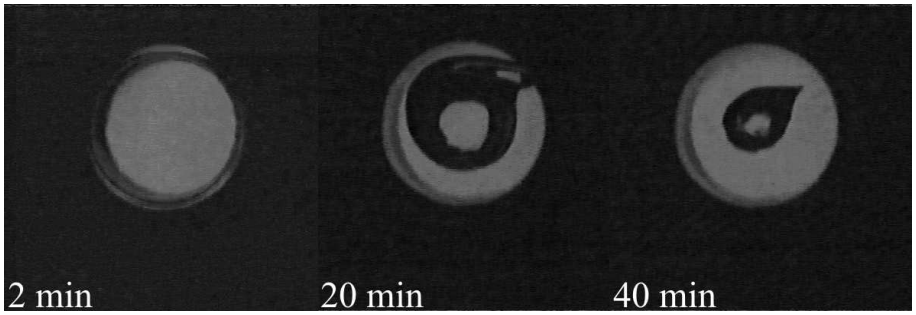

Figure 3.7: *Para-hydrogen crystal growth from the gas at 10 K. The crystal started to grow from the copper surface of the cell (2 min) and slowly became thicker (20 min). A tube starting from the gas inlet stayed free, due to the heatload of the incoming gasflow. The growth was finished when the gas inlet was blocked, resulting in a transparent crystal with a void in its middle (40 min).*

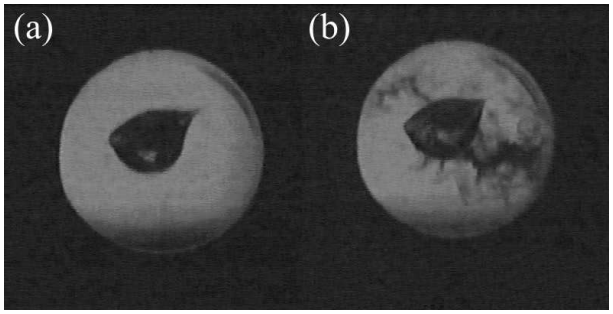

Figure 3.8: *(a) Para-hydrogen crystal grown from the gas at 10 K. (b) Typical cracks, as they can appear due to a too hasty cooling.*

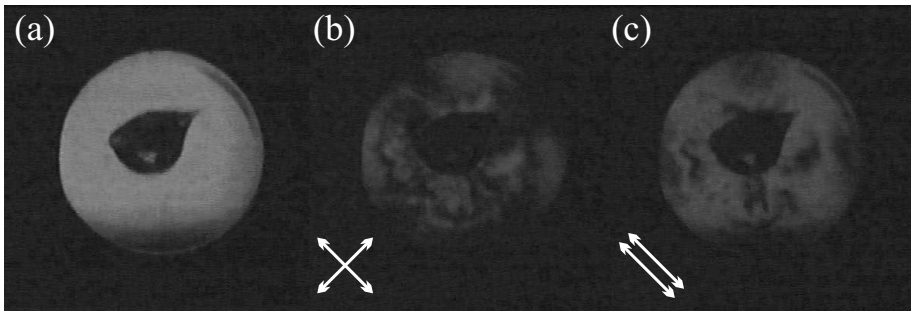

Figure 3.9: *(a) Para-hydrogen crystal grown at 10 K. Seen through two crossed polarizers (b) and two parallel polarizers (c), with the polarizer being oriented 45° to the table. See Figure 3.10 for comparison.*

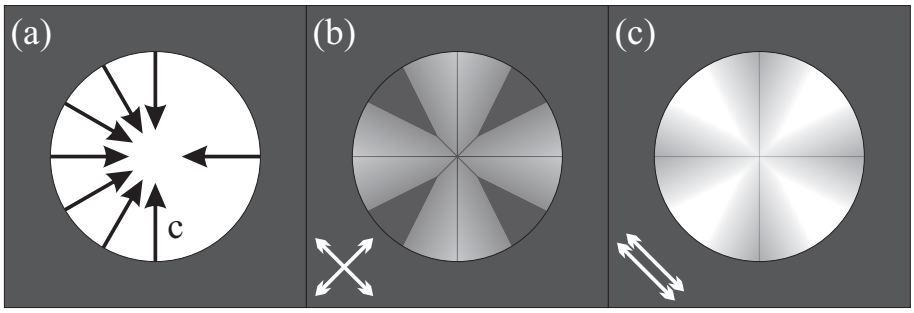

Figure 3.10: *The radial orientation of the hcp lattice c-axis, sketched in (a), and its effect on the light intensity if seen through two crossed polarizers (b), and two parallel polarizers (c), with the polarizer being oriented 45° to the table. There is no effect, if the light polarization is parallel or perpendicular to the c-axis, and maximal effect, if the light polarization is oriented 45° to the c-axis.*

local heating, e.g. due to high laser power in a focus region. Unfortunately, the molar volume of zero-pressure solid para-hydrogen is strongly temperature dependent, particularly at higher temperatures (see Fig. 2.5). Hence, crystals grown at higher temperatures had to be cooled very slowly to prevents cracks due to stress, as they are shown in Figure 3.8 and Figure 3.11 (m).

It is probable that during the growth in an enclosed cell a thin layer of liquid is formed on the surface of the crystal, which is also believed by Oka [8]. This gives the molecules time to fit into the existing lattice structure that grows from the walls to the center of the cell along the thermal gradient. This would be an explanation for the good quality and the radial orientation of the hcp lattice c-axis of the crystals, as it was reported by Momose and Shida [9]. Our crystals did, to a certain extend, also show the expected radial pointing of the c-axis. We demonstrate this for a crystal grown at 10 K that we watched through a polarizer-analyzer pair in Figure 3.9. The crossed polarizer-analyzer configuration allows to observe birefringence effects, e.g. due to the anisotropy along the c-axis. Birefringence leads to the induction of an elliptic component into linearly polarized light, which may be observed because it passes a perpendicular analyzer. The strength of the elliptic component depends on the relative orientation between the polarizer and the optical axis of the birefringent material. For a relative orientation of 45° both components of the initially linearly polarized light, the one parallel to the optical axis and the one perpendicular to the optical axis, are of the same strength. Hence, due to the differing speed of the light for both components, the induced ellipticity is maximal. Figure 3.10 shows that the birefringence effect is maximal, if the light polarization is oriented 45° to

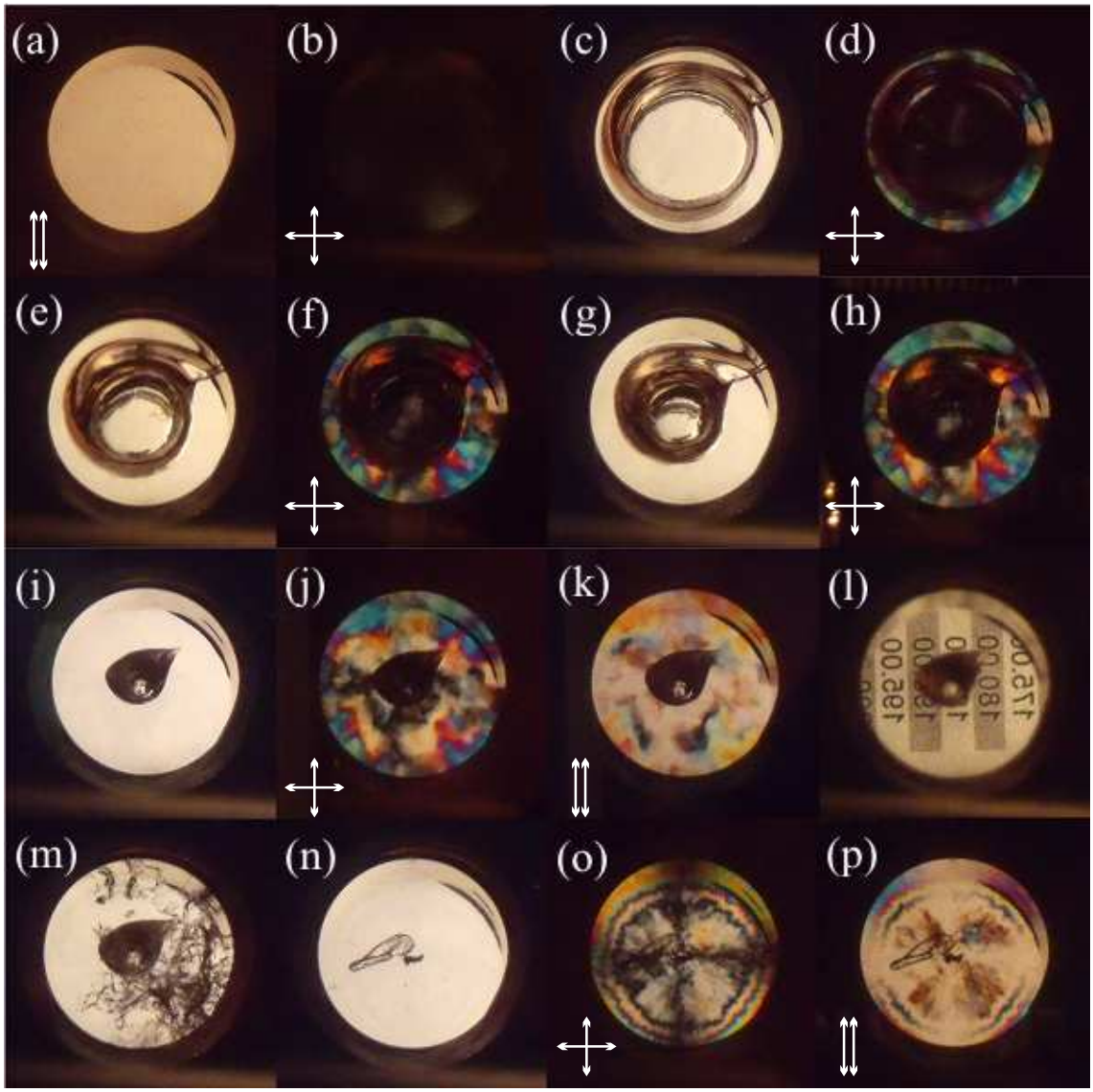

Figure 3.11: *Several pictures of the cell, before (a, b), during (c-h), and after (i-m) the growth of a para-hydrogen crystal at 13 K from the gas. Polarization effects were observed through two crossed polarizers (b, d, f, h, j), and two parallel parallel polarizers for comparison (a, k). Letters are not distorted if viewed through the crystal (l). The crystal cracked after too hasty cooling (m). Grown from the liquid in a rapid freezing manner, surprisingly transparent crystals were obtained (n-p). They showed distinct polarization effects between crossed (o), and parallel (p) polarizers, which are similar to the ones of a crystal grown from the gas at 9 K.*

the c-axis, and that there is no birefringence effect, if the light polarization is parallel or perpendicular to the c-axis. Indeed, the crystal shown in Fig. 3.9 revealed a four-leaved cloverleaf-like radial structure, even if it is hard to notice on the first glance. More obvious in Fig. 3.9 are some very distinct features that appear around the center in the crystal, but are not visible close to the copper surface. We believe that these structures rather arose from unstable temperature and gas flow conditions during growth, than from stress or strain due to shrinkage during cooling. Also visible are small spots in the sub-millimeter range, probably caused by small crystallites of varying orientation or amorphous structures grown on the windows. Important for the optical Kerr effect experiment are the large, homogeneous, outer regions, e.g. close to the gas inlet in the upper right of the crystal. They provide optimal conditions for polarization sensitive experiments.

A comparison of Fig. 3.9 to a crystal grown at 13 K, shown in Figure 3.11 (j, k), reveals striking differences. The higher growth temperature led to the growth of macroscopic, several cubic millimeter to cubic centimeter thick single crystals, seen as regions of equal birefringence. The growth of such big crystallites prevented the crystal to form out the supposed radial symmetry. Additionally, Figure 3.11 (d, f, h, j) demonstrates that the birefringence pattern does not change during the growth. Hence, no further stress was introduced due to the growth process. This is also demonstrated in Figure 3.11 (l), which proves the absence of any lens effects that may arise from density modulations.

3.2.3 Crystal growth from the liquid

Transparent para-hydrogen crystals of sufficient optical quality to perform OKE experiments were also grown from the liquid. This was done in a rapid freezing manner, by rapid cooling of 16 K liquid para-hydrogen to 4 K. The growth of such a crystal has not yet been reported before and is depicted in Figure 3.12. Within less than a minute, a transparent, 3 cm long crystal was grown without cracks. This is also demonstrated in Figure 3.11 (n-p). Particularly the lack of cracks was surprising, given the dramatic shrinkage of the molar volume of more than ten percent from the liquid to the solid [37], and more than one percent from 13.8 K to 4 K [8]. The crack-free growth was probably possible due to the high thermal conductivity of para-hydrogen at 4 K [42, 43]. Hence, the liquid did immediately freeze to almost 4 K on the surface of the crystal, without forming a strong density gradient in the crystal. Indeed, smaller cooling powers and slower growth led to cracked, milky crystals. And a subsequent cooling of transparent crystals, which were grown from the liquid at 13 K, resulted in cracks, too. Maybe most striking was that the same technique failed for normal-hydrogen. One reason for this is that the thermal conductivity of hydrogen is strongly dependent on the ortho-hydrogen concentration (see Fig. 2.6). The other reason for the differences between para- and normal-hydrogen is that the shrinkage of para-hydrogen becomes very small below 10 K, which is not the case for normal-hydrogen (see Fig. 2.5). The properties of the crystals grown from the liquid differed significantly from the ones grown from the gas at high temperatures. This was observed again using two polarizers and is shown in Figure 3.12 and in Figure 3.11 (o, p). Crystals grown in a rapid freezing manner showed a much more pronounced radial symmetry and a higher homogeneity than crystals grown from the gas, but consisted of smaller crystallites.

Similar attempts to grow deuterium crystals from the liquid were reported by Frei et al. in 2009 [60]. They succeeded in growing large, transparent crystals slowly from the gas and from the liquid, as samples for an inelastic neutron scattering study. However, their ‘turbo solid’, solid deuterium grown from the liquid within minutes, became opaque and showed an almost ideal powder diffraction pattern. Hence, the possibility to grow transparent hydrogen crystals in a rapid freezing manner seems to be restricted to the light and weakly

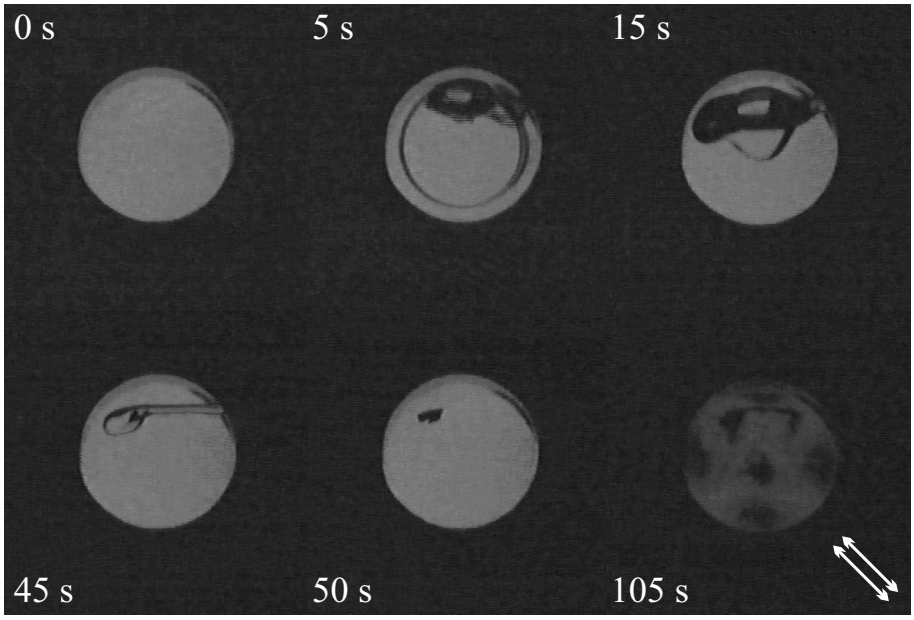

Figure 3.12: *Para-hydrogen crystal growth from the liquid in a rapid freezing manner. The liquid (0 s) para-hydrogen at 16 K was rapidly cooled to 4 K and started immediately to solidify on the copper cell wall (5 s). Upon freezing, the density increased and the occupied volume in the cell shrank. Hence, bubbles appeared on top of the liquid. After a very short time (15 s) most of the cell was filled with solid. The small, remaining void in the upper part of the cell took another 30 s to be filled with gas from the reservoir (45 s). The result was a transparent para-hydrogen crystal (50 s). It showed a lower quality than if it would have been slowly grown at high temperature from the gas. Seen through two polarizers (105 s) it showed the radial structure that was reported by Momose and Shida [9].*

interacting para-hydrogen.

4 Spectroscopic concepts and methods

"Physics would be dull and life most unfulfilling if all physical phenomena around us were linear. Fortunately, we are living in a nonlinear world. While linearization beautifies physics, nonlinearity provides excitement in physics."

Y. R. Shen [61]

This chapter introduces the basic spectroscopic concepts and methods that were applied during this work. The first section is about the nuclear motion of molecules and their nonadiabatic alignment with intense laser fields. It is followed by a brief introduction into nonlinear optics, with a special focus onto the optical Kerr effect and the Raman effect. The last section of this chapter describes the spectroscopic method we applied, time resolved, two dimensional optical Kerr effect (2D OKE) spectroscopy.

4.1 Nuclear motion and alignment of diatomic molecules

We carried out infrared absorption spectroscopy and time resolved Raman spectroscopy experiments that were sensitive to the nuclear motion of the observed samples. E.g. we recorded rotational, vibrational, and ro-vibrational infrared absorption spectra of diatomic molecules, which were isolated in a cryogenic hydrogen matrix. The understanding of the rotational and vibrational degrees of freedom of an isolated diatomic molecule is the basis for the interpretation of these spectra. Additionally, we performed molecular alignment experiments with intense laser pulses that interacted with the rotational degrees of freedom of the molecules. The basic concepts concerning the nuclear degrees of freedom and the rotational alignment of diatomic molecules are presented in this section and a supplementary collection of fundamental molecular constants of molecules that we've investigated in our experiments is given in Table 4.1.

4.1.1 Rotation and vibration of diatomic molecules

This section gives a brief overview of the framework describing the rotation and vibration of a free, diatomic molecule. The eigenstates of a molecule consisting of i particles (electrons and nuclei) follow from the time independent Schrödinger equation [62]

$$\hat{H}_{mol}\Psi_{mol} = E\Psi_{mol}, \text{ with } \hat{H}_{mol} = \sum_i (-\frac{\hbar^2}{2m_i}\Delta_i + V_i). \tag{4.1}$$

The potential V_i in which a charged particle is moving depends on the interaction with all other charged particles. In the Born-Oppenheimer approximation, the nuclear velocity may be regarded as slow compared to the electronic motion. The molecular wavefunction Ψ_{mol} may be broken into its electronic and nuclear components,

$$\Psi_{mol}(\mathbf{r}, \mathbf{R}) = \psi_{el}(\mathbf{r}, \mathbf{R})\psi_{nuc}(\mathbf{R}), \tag{4.2}$$

where $\mathbf{r}$ represents a set of electronic, and $\mathbf{R}$ a set of nuclear coordinates. The time independent electronic Schrödinger equation, $\hat{H}_{el}(\mathbf{r}, \mathbf{R})\psi_{el}(\mathbf{r}, \mathbf{R}) = E_{el}\psi_{el}(\mathbf{r}, \mathbf{R})$, in which

the electronic Hamiltonian depends on the position of the nuclei $\mathbf{R}$, is solved first. It provides the potential, often approximated as a Morse potential, in which the nuclear motion takes place. The motion of the nuclei is introduced in a second step and includes the vibrational and rotational internal degrees of freedom.

A further separation of the nuclear wavefunction $\psi_{nuc}(\mathbf{R})$ into a vibrational and a rotational part is possible. For a diatomic molecule, written in spherical polar coordinates of a center-of-mass frame, this leads to [62]

$$\psi_{nuc}(R,\theta,\phi) = \frac{1}{R}\psi_{vib}(R)\psi_{rot}(\theta,\phi). \tag{4.3}$$

Thus, the total wavefunction may be written as

$$\Psi_{mol} = \frac{1}{R}\psi_{el}\psi_{vib}\psi_{rot}, \tag{4.4}$$

with a total energy of

$$E_{mol} = E_{el} + E_{vib} + E_{rot}. \tag{4.5}$$

In a rigid rotor approximation, the rotation of a diatomic molecule can be considered as the rotation of two point masses m_1 and m_2 that are connected by a massless rod with length R and rotate around their center-of-mass with angular velocity ω. From this so-called dumbbell model, the rotational energy follows classically to be [63]

$$E_{rot} = \frac{1}{2}\Theta\omega^2 = \frac{L^2}{2\Theta} = \frac{L^2}{2\mu R^2}, \tag{4.6}$$

where Θ is the moment of inertia of the system, L the classical angular momentum and μ the reduced mass. In quantum mechanics, the classical angular momentum $\mathbf{L}$ corresponds to the angular momentum operator $\hat{\mathbf{J}}$ and L^2 to $\hat{\mathbf{J}}^2$. The eigenvalue of $\hat{\mathbf{J}}^2$ is $\sqrt{\hbar^2 J(J+1)}$, with the angular momentum quantum number J. Hence, the rotational energy in the rigid rotator approximation is given by [63]

$$E_{rot} = \frac{\hbar^2 J(J+1)}{2\Theta} = \frac{\hbar^2 J(J+1)}{2\mu R^2} = BJ(J+1), \tag{4.7}$$

where B is the rotational constant. The eigenfunctions of $\hat{\mathbf{J}}^2$ are the spherical harmonics [64]

$$Y_{JM}(\theta,\phi) = \sqrt{\frac{2J+1}{4\pi}\frac{(J-M)!}{(J+M)!}}P_J^M(\cos\theta)e^{iM\phi}, \tag{4.8}$$

with the associated Legendre polynomials $P_J^M(\cos\theta)$. Normalized, they form a complete set of orthogonal basis functions for the rotational wavefunction ψ_{rot}. The spherical harmonics are also eigenfunctions to the projection of $\hat{\mathbf{J}}$ onto a z axis, $\hat{J}_z$, with the eigenvalue $\hbar M$ ($M = -J, -J+1, ..., J-1, J$). Hence, the rotation of a diatomic rigid rotator is determined by two quantum numbers, J and M.

However, a diatomic molecule is not a perfect rigid rotor. There is no rod of fixed length, rather a spring between the nuclei. This gives rise to a vibrational motion of the nuclei, and we have to introduce a vibrational quantum number v to describe the vibrational state of the molecule. The simplest approach to describe the vibration of a diatomic molecule is to assume that the molecule behaves as a harmonic oscillator. The motion of the two nuclei may than be reduced to the motion of a single mass point around the potential

	H_2	$^{12}C^{16}O$	$^{14}N_2$	$^{12}CH_4$
R_e in Å	0.7416[a]	1.1281[a]	1.094[a]	-
B_0 in cm^{-1}	59.335[c]	1.9225[c]	1.9896[c]	5.2410[c]
B_e in cm^{-1}	60.800[a]	1.9313[a]	2.010[a]	-
α_e in cm^{-1}	2.993[a]	0.01748[a]	0.0187[a]	-
D_e in cm^{-1}	0.0464[a]	6.43×10^{-6}[a]	5.8×10^{-6}[a]	-
ω_e in cm^{-1}	4395.2[a]	2170.21[a]	2359.61[a]	-
$\omega_e x_e$ in cm^{-1}	117.99[a]	13.461[a]	14.456[a]	-
ν_1 in cm^{-1}	-	-	-	2916.5[b]
ν_2 in cm^{-1}	-	-	-	1533.3[b]
ν_3 in cm^{-1}	-	-	-	3019.49[b]
ν_4 in cm^{-1}	-	-	-	1306.2[b]
α in $Å^3$	0.819[d]	1.99[d]	1.77[d]	2.593[e]
$\alpha_\parallel - \alpha_\perp$ in $Å^3$	(0.30 ± 0.01)[d]	(0.54 ± 0.02)[d]	(0.69 ± 0.03)[d]	-

Table 4.1: *Molecular constants of hydrogen and various dopants in their electronic ground states. See Eq.s 4.10-4.13 for definition.*

[d]from Ref. [39]
[a]from Ref. [63]
[b]from Ref. [65]
[c]from Ref. [66]
[e]from Ref. [67]

minimum of a harmonic potential [63]. Than the vibrational energy levels are equidistant and depend on the vibrational quantum number and the vibrational frequency ω_e,

$$E_{vib} = \omega_e(v + \frac{1}{2}). \tag{4.9}$$

However, the harmonic oscillator serves only as a first approximation for the vibrational motion. In general, one has to consider an anharmonic potential. For a small anharmonicity of the potential, the energy levels may be given by a power series in v,

$$E_{vib} = \omega_e(v + \frac{1}{2}) - \omega_e x_e(v + \frac{1}{2})^2 + ..., \tag{4.10}$$

with a quadratic anharmonicity constant $\omega_e x_e$ that is small compared to the vibrational frequency ω_e [63]. The anharmonicity gives also rise to a coupling of the rotational and the vibrational motion, because the mean internuclear separation is dependent on the vibrational quantum number v. The rotational constant of a non-rigid rotor is therefore dependent on the vibrational state, which may also be described by a power series in v,

$$B_v = B_e - \alpha_e(v + \frac{1}{2}) + ... \tag{4.11}$$

Additionally, in a non-rigid rotator, the centrifugal force influences the internuclear distance and therefore the moment of inertia. The rotational energy of a diatomic molecule may be written as a power series in J,

$$E_{rot}(v, J) = B_v J(J+1) - D_v J^2(J+1)^2 + ..., \tag{4.12}$$

which is usually canceled after the first two terms [68]. The coefficients of this power series are the rotational constant B_v and the centrifugal distortion constant D_v,

$$D_v = D_e + \beta_e(v + \frac{1}{2}) + ..., \tag{4.13}$$

which depend on the vibrational level. However, D_v is typically several orders of magnitude smaller than B_v (see Table 4.1) and the rigid rotor model is a good approximation for small J.

4.1.2 Nonadiabatic alignment with intense laser fields

Electric fields that interact with matter can induce anisotropies by the so-called Kerr effect, which will be discussed in more detail in Section 4.2. The displacement of electrons by the oscillating field of a pump pulse, which is almost instantaneously and takes place within the attosecond timescale [69], is present in any material. Additionally, permanent and pump induced dipole moments can interact with the field, which drives the dipole moments to reorient towards the direction of the electric field. This mechanism allows to align nonspherical particles with respect to the direction of the field. The reorientation depends on the rotational dynamics of the particles and happens within femto- to picoseconds for diatomic molecules. Thus, an intense, nonresonant laser pulse can be used to align molecules, even nonpolar molecules like nitrogen or hydrogen. If the laser pulse is short compared to the rotational period of the molecules, the molecules are to slow to follow the rapidly changing potential adiabatically. However, they can align nonadiabatically, due to the induced rotational dynamics. The induction of coherent rotational dynamics by the nonadiabatic interaction of molecules with an ac laser field was known and used within time-resolved rotational coherence spectroscopy (RCS) since 1975 [22, 23, 70] and has nowadays become a topic of growing interest as tool for the field free alignment of molecules [71, 72]. It has been studied in very detail previously in our group by Nina Owschimikow for the N_2 gas [25, 26, 73, 74] and we refer to this work for simulations and a broader theoretical approach.

Classically, a laser field interacts with sample molecules via induced dipole moments. The strength of these induced dipoles is determined by the polarizability of the molecule, which can be anisotropic and is in general a tensor of rank 2 [62]. E.g., for diatomic molecules, the polarizability is given by $\alpha_\parallel$, the polarizability parallel to the molecular axis, and $\alpha_\perp$, the polarizability perpendicular to the molecular axis (see Fig. 4.1). Thus, diatomic molecules exhibit an anisotropic polarizability $\Delta\alpha = \alpha_\parallel - \alpha_\perp$. The electric field of a linearly polarized laser pulse will polarize a sample of isotropically distributed molecules, according to their polarizability, primarily along their molecular axis ($\Delta\alpha > 0$). The field induces dipole moments, which drive the molecules to align parallel to the laser field polarization. Hence, the molecules start to rotate towards the light field's polarization direction. Due to their moment of inertia, the molecules will continue to rotate even after the laser pulse has been terminated (field free), eventually aligning the sample.

Quantum mechanically, the state of a diatomic molecule can be described as eigenstate or superposition of eigenstates, which are eigenfunctions of the time-independent Schrödinger equation of the field free molecule (Eq. 4.1). The rotational state Ψ_{rot} of a molecule is therefore given by a superposition of spherical harmonics $Y_{JM} = |J, M\rangle$ (Eq. 4.8),

$$\Psi_{rot} = \sum_{J,M} c_{J,M} \, |J, M\rangle \, , \tag{4.14}$$

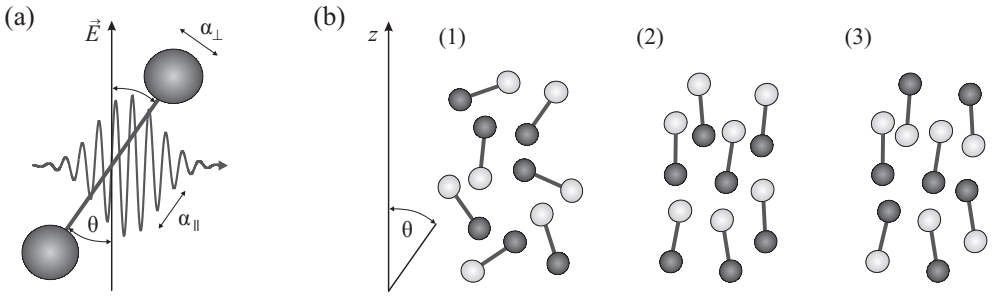

Figure 4.1: *(a) Diatomic molecule with polarizabilities $\alpha_\parallel$ and $\alpha_\perp$ in an aligning laser field $\vec{E}$. (b) Ensembles of asymmetric diatomic molecules in a laboratory frame with axis z: (1) randomly oriented molecules, (2) oriented molecules, (3) aligned molecules. Symmetric diatomic molecules have no discriminable direction and can only be aligned towards a certain axis, not oriented.*

weighted by coefficients $c_{J,M}$. The interaction of a molecule with a laser pulse $\mathbf{E}(t)$, written in the dipole approximation, is described by a perturbed Hamiltonian [75]

$$\hat{H}(t) = \hat{H}_0 + \hat{\mu}\mathbf{E}(t) = \hat{H}_0 + \hat{H}_{ind}(t), \tag{4.15}$$

where $\hat{H}_0 = \hat{H}_{mol}$ (Eq. 4.1) is the field free Hamiltonian of the molecule and $\hat{\mu}$ the dipole moment operator. For a short laser pulse with envelope $E(t)$ that interacts with a diatomic molecule, the induced potential $\hat{H}_{ind}(t)$ can be written as [74]

$$\hat{H}_{ind}(\theta, t) = -\frac{1}{4}\Delta\alpha E^2(t)\cos^2(\theta) - \frac{1}{4}\alpha_\perp E^2(t). \tag{4.16}$$

The wave functions $\Psi_{rot}(t)$ that describe the rotational dynamics follow as solutions of the time-dependent Schrödinger equation, which has to be solved in general numerically [74, 75].

Alignment is caused by a change in the thermal $|J, M\rangle$ distribution by Raman transitions. A nonresonant, linearly polarized laser pulse induces rotational Stokes and anti-Stokes Raman transitions between the rotational eigenstates of the unperturbed molecule, which obey the selection rules $\Delta J = \pm 2$ and $\Delta M = 0$ [74, 75]. If the laser pulse is short compared to the rotational dynamics, it excites a coherent superposition of rotational eigenstates as given in Eq. 4.14. This superposition, also called a rotational wavepacket, has fixed phase relations, which were defined by the laser pulse. Whereas an eigenstate is time independent, this rotational wavepacket will evolve in time according to the transition frequencies between the superimposed rotational states. Due to the differing frequencies associated with the rotational energy levels, the wavepacket will dephase after the excitation at $t = 0$. However, this dephasing is not permanent, because, following Eq. 4.12, all rotational transition energies are approximately multiples of $2B_v$. Given that the coherence between the states is preserved, the wavepacket will eventually rephase after every time interval $T_{rev} = 1/2B_v$, since the so-called revival time T_{rev} is a multiple of 2π for all oscillation periods within the wavepacket. This rephasing is also called a full revival (of the initial wavepacket).

The degree of alignment for a molecule in a given quantum state can be quantified by the expectation value of $\cos^2\theta$, $\langle\cos^2\theta\rangle$, where θ is the polar angle between the molecular axis and an external axis, e.g. the laser field polarization [71]. To compare to experiments, usually the average of the expectation value of $\cos^2\theta$ over all rotational states, $\langle\langle\cos^2\theta\rangle\rangle$, is used, because a thermal sample is not prepared in a single rotational state. An ensemble

of diatomic molecules with isotropic distribution of the molecular axis has an averaged expectation value of $\cos^2\theta$ of $\langle\langle\cos^2\theta\rangle\rangle = 1/3$. However, after excitation with a laser pulse alignment ($1/3 < \langle\langle\cos^2\theta\rangle\rangle < 1$) and anti-alignment ($0 < \langle\langle\cos^2\theta\rangle\rangle < 1/3$) of the sample occurs, due to the evolution of the induced wavepackets. At $t = 0$ and multiples of the revival period $T_{rev} = 1/2B_v$ the angular distribution of the wavepacket is isotropic ($\langle\cos^2\theta\rangle = 1/3$) (neglecting the small contribution of the M-state population mentioned below), but it has to become anisotropic directly beforehand and afterwards of a full revival, as exemplified in Ref. [74].

As a second effect, the selection rules for Raman excitation with a linearly polarized laser pulse, $\Delta J = \pm 2$ and $\Delta M = 0$, lead to a nonthermal population in the M-part of the rotational states $|J, M\rangle$. Transitions into higher rotational states increase the J quantum number, but not the M quantum number. Thus, the highest M-states are not populated. This leads to a time independent, but population dependent alignment, which does not require a coherent coupling of the rotational states. The total alignment can be written as the sum of the coherent alignment $\langle\langle\cos^2\theta\rangle\rangle_c$ and this population part $\langle\langle\cos^2\theta\rangle\rangle_p$ [76],

$$\langle\langle\cos^2\theta\rangle\rangle \equiv \langle\langle\cos^2\theta\rangle\rangle_{tot} = \langle\langle\cos^2\theta\rangle\rangle_c + \langle\langle\cos^2\theta\rangle\rangle_p . \tag{4.17}$$

4.2 Nonlinear optics

The main focus of our experiments was a certain kind of coherent Raman spectroscopy that we call time resolved, two dimensional optical Kerr effect spectroscopy. The basic principles of this technique, light propagation in matter, the optical Kerr effect, and nonlinear Raman scattering, are laid down in this section.

4.2.1 Light propagation in matter

The electric field $\mathbf{E}(\mathbf{k}, \omega)$ of a light wave that propagates in matter interacts with the bound electrons and displaces them in their binding potential. In the harmonic approximation of the potential, which holds for low field strengths, it forces them to oscillate with the light wave's frequency. Thus, it creates oscillating electric dipoles, and therefore a polarization $\mathbf{P}(\mathbf{r}, t)$, which travels through the medium with the same phase velocity as the light wave itself. Composed of Hertzian dipoles, this polarization wave becomes the source of an electric field, phase shifted and of the same frequency as the inducing light wave, that adds to the original field and forms a new light wave of the same frequency. At high field strengths, the harmonic approximation is no longer valid and the displacement of the electrons, and therefore the polarization, is no longer proportional to the field strength of the light wave. In this case overtones of the light wave's frequency can occur and we are entering the regime of nonlinear optics.

Quantitatively, the propagation of light in matter is governed by the Maxwell's equations [61, 77], in which the total current $\mathbf{J}(\mathbf{r}, t)$ and the total charge density $\rho(\mathbf{r}, t)$ act as source terms for the electric field $\mathbf{E}(\mathbf{r}, t)$ and the magnetic field $\mathbf{B}(\mathbf{r}, t)$. Assuming that the material is nonmagnetic and there are no free charges, $\mathbf{J}$ and ρ can be written as

$$\mathbf{J} = \frac{\partial \mathbf{P}}{\partial t}, \tag{4.18}$$

and

$$\rho = -\nabla \cdot \mathbf{P}, \tag{4.19}$$

Thus, the electric polarization $\mathbf{P}(\mathbf{r},t)$ appears now as the source term in the Maxwell's equations. From this we can obtain the wave equation as it is used for the propagation of light in matter,

$$\nabla \times \nabla \times \mathbf{E} + \frac{1}{c^2}\frac{\partial^2 \mathbf{E}}{\partial t^2} = -\frac{4\pi}{c^2}\frac{\partial^2 \mathbf{P}}{\partial t^2}. \tag{4.20}$$

Usually, the electric polarization of a dielectric medium is a complicated nonlinear function of the electric field. To a good approximation, it can be given by a Taylor series in $\mathbf{E}(\mathbf{r},t)$ [78],

$$\mathbf{P}(\mathbf{r},t) = \epsilon_0(\chi^{(1)}(t)\mathbf{E}(\mathbf{r},t) + \chi^{(2)}(t)\mathbf{E}(\mathbf{r},t)\mathbf{E}(\mathbf{r},t) + \chi^{(3)}(t)\mathbf{E}(\mathbf{r},t)\mathbf{E}(\mathbf{r},t)\mathbf{E}(\mathbf{r},t) + ...), \tag{4.21}$$

where $\chi^{(1)}(t)$ is the linear electric susceptibility, $\chi^{(2)}(t)$ the second-order electric susceptibility, and $\chi^{(3)}(t)$ the third-order electric susceptibility of the medium. The susceptibilities are related to the microscopic structure of the medium and need a full quantum-mechanical calculation to be properly evaluated. They are in general complex tensors. Hence, in anisotropic media, the polarization and the electric field have not to be parallel.

Material cannot respond instantaneously to an applied field and the susceptibility tensors are dependent on the time evolution of the electric field. The polarization caused by a monochromatic plane light wave,

$$\mathbf{E}(\mathbf{r},t) = \mathbf{E}(\mathbf{k},\omega) = \mathbf{E}_0 e^{i\mathbf{k}\cdot\mathbf{r}-i\omega t}, \tag{4.22}$$

becomes therefore frequency dependent. If the electric field is a superposition of monochromatic light waves $\mathbf{E}(\mathbf{k}_i,\omega_i)$, the resulting polarization component that oscillates with a frequency ω, interpreted as a polarization wave $\mathbf{P}(\mathbf{k},\omega)$, can be written as [61]

$$\mathbf{P}(\mathbf{k},\omega) = \mathbf{P}^{(1)}(\mathbf{k},\omega) + \mathbf{P}^{(2)}(\mathbf{k},\omega) + \mathbf{P}^{(3)}(\mathbf{k},\omega), \tag{4.23}$$

with

$$\mathbf{P}^{(1)}(\mathbf{k},\omega) = \epsilon_0\chi^{(1)}(\omega)\mathbf{E}(\mathbf{k},\omega), \tag{4.24}$$

$$\mathbf{P}^{(2)}(\mathbf{k},\omega) = \epsilon_0\chi^{(2)}(\omega)\mathbf{E}(\mathbf{k}_i,\omega_i)\mathbf{E}(\mathbf{k}_j,\omega_j), \tag{4.25}$$

$$\mathbf{P}^{(3)}(\mathbf{k},\omega) = \epsilon_0\chi^{(3)}(\omega)\mathbf{E}(\mathbf{k}_k,\omega_k)\mathbf{E}(\mathbf{k}_l,\omega_l)\mathbf{E}(\mathbf{k}_m,\omega_m), \tag{4.26}$$

with $\mathbf{k} = \pm\mathbf{k}_i \pm \mathbf{k}_j = \pm\mathbf{k}_k \pm \mathbf{k}_l \pm \mathbf{k}_m$ and $\omega = \pm\omega_i \pm \omega_j = \pm\omega_k \pm \omega_l \pm \omega_m$. The delayed material response also causes a phase shift between the incident light wave and the induced polarization wave. It leads to a change of the velocity of light in matter, described by its index of refraction $n(\omega)$.

In condensed matter, $\chi^{(1)}$ is of the order of unity, whereas $\chi^{(2)} \approx 10^{-10}$ cm/V and $\chi^{(3)} \approx 10^{-17}$ cm^2/V^2. Hence, the linear term in Eq. 4.21 is strongly dominating at low field strengths. At higher field strengths, as in an intense laser field, the higher order terms are of growing importance and nonlinear effects occur. One of the simplest nonlinear effects, the second harmonic generation (SHG), was first observed by Franken et al. in 1961 [79], and played a role in several stages of our experiments. Considering only the real part of $\chi^{(2)}$, the second order polarization that is induced by an incident monochromatic laser light wave of frequency ω and wavevector $\mathbf{k}(\omega)$ can be written as

$$\mathbf{P}^{(2)}(2\mathbf{k}(\omega),2\omega) = \epsilon_0\chi^{(2)}(2\omega)\mathbf{E}_0 e^{i\mathbf{k}\cdot\mathbf{r}-i\omega t}\mathbf{E}_0 e^{i\mathbf{k}\cdot\mathbf{r}-i\omega t} = \epsilon_0\chi^{(2)}(2\omega)\mathbf{E}_0\mathbf{E}_0 e^{i2\mathbf{k}\cdot\mathbf{r}-i2\omega t}. \tag{4.27}$$

Thus, the incident light wave $\mathbf{E}(\mathbf{k}(\omega),\omega)$ creates a polarization wave that oscillates with 2ω. The orientation and intensity of this polarization wave is strongly dependent on the

symmetry of the medium, which is reflected in the the second-order electric susceptibility $\chi^{(2)}$. E.g. $\chi^{(2)}$ vanishes completely in a crystal with a center of inversion, as do all even order nonlinear processes. The induced polarization travels through the medium together with it's source field and acts itself as source for a new a light wave $\mathbf{E}(\mathbf{k}(2\omega), 2\omega)$. To achieve high intensities, it is necessary to fulfill the phase matching condition $\Delta\mathbf{k} = \mathbf{k}(2\omega) - 2\mathbf{k}(\omega) = 0$, which follows from momentum conservation. It is required at least within the coherence length of the light and is usually achieved using birefringent crystals (quartz, BBO, KDP). Under this condition the driving polarization $\mathbf{P}(2\mathbf{k}(\omega), 2\omega)$ is always in phase with $\mathbf{E}(\mathbf{k}(2\omega), 2\omega)$, and constructive interference is assured.

Similar nonlinear optical effects are wave-mixing processes like the second order sum- and difference frequency generation (SFG, DFG), the second order parametric amplification and the third order four-wave mixing processes. Other nonlinear effects change the index of refraction of a material, like the second order elektrooptic Pockels-effect, the third order elektrooptic Kerr-effect, and the second order magnetooptic Faraday-effect, which are caused by constant external fields. Such changes of the refractive index can also be induced by intense laser fields, leading to the third order optical Kerr-effect and the related self focusing-effect. Of great importance are also the nonlinear absorption and induced scattering processes, namely the two-photon absorption and the stimulated Raman-scattering, which can be interpreted as third order effects. The optical Kerr-effect and the stimulated Raman-scattering are central in our experiments and will be discussed in more detail in the following.

4.2.2 The optical Kerr effect

In 1845 Michael Faraday observed that even isotropic matter can become birefringent by virtue of magnetic fields [78]. The Faraday-effect was therefore the first experimental evidence that light and electromagnetism are related. However, John Kerr observed that liquid and solid dielectrics may also become birefringent in strong external electric fields in 1875 [80]. The so called Kerr-effect can be described using the same formalism as for the second harmonic generation. In general, the polarization $\mathbf{P}(\omega)$ that is induced by a light wave $\mathbf{E}(\omega)$, e.g. a weak probe laser beam, into a medium within a constant electric field $\mathbf{E}(\Omega \approx 0)$ is given by [77]

$$\mathbf{P}(\omega) = \epsilon_0(\chi^{(1)}(\omega)\mathbf{E}(\omega) + \chi^{(2)}(\omega)\mathbf{E}(0)\mathbf{E}(\omega) + \chi^{(3)}(\omega)\mathbf{E}(0)\mathbf{E}(0)\mathbf{E}(\omega) + ...). \tag{4.28}$$

The second order term is known since 1893 as linear electrooptic effect or Pockels-effect [78]. It has an application in the Pockels-cell that is used as a fast optical switch in our femtosecond laser system. As was already stated, such second order processes vanish in materials with inversion symmetry, like in the hcp lattice of a hydrogen crystal. The third order term, however, the electrooptic Kerr-effect or DC Kerr-effect, is always present. It is quadratic in the external field and therefore also called quadratic electrooptic effect, even though it can be regarded as a third order process. The constant field in Eq. 4.28 may also be substituted by an optical field $\mathbf{E}(\Omega)$, e.g. an intense pump laser beam, which leads to the so called optical or AC Kerr-effect. For a medium with inversion symmetry, the component of the total polarization that oscillates with the frequency ω is then given by

$$\mathbf{P}(\omega) = \epsilon_0(\chi^{(1)}(\omega) + \chi^{(3)}(\omega)\mathbf{E}(\Omega)\mathbf{E}(\Omega))\mathbf{E}(\omega) = \epsilon_0\chi_{eff}\mathbf{E}(\omega). \tag{4.29}$$

The effective susceptibility $\chi_{eff} = \chi_{lin} + \chi_{nl}$ comprises of a linear first order term $\chi_{lin} = \chi^{(1)}$ and a nonlinear third order term $\chi_{nl} = \chi^{(3)}(\omega)\mathbf{E}(\Omega)\mathbf{E}(\Omega) \propto |E(\Omega)|^2$. This can be understood as change of the index of refraction n of the medium upon radiation with

the intense pump light. The index of refraction n_i for an optical axis i of an anisotropic medium may be related to the corresponding susceptibility component by

$$n_i^2 = 1 + \chi_{ii}. \tag{4.30}$$

The dependence of the effective susceptibility on $|E(\Omega)|^2 = I$ leads therefore to an intensity dependent index of refraction

$$n(I) = n_0 + n_2 I, \tag{4.31}$$

where n_0 is the weak-field index of refraction and n_2 the second order nonlinear refractive index. The change of the refractive index that is induced by the pump light intensity is of course dependent on the symmetry of the medium and the polarization vector of the light. E.g. linearly polarized pump light enhances the refractive index of an isotropic medium along the axis of its field vector. In such a case, the initially isotropic medium becomes birefringent. Hence, one can observe the induced anisotropie by its effect on the polarization of a weak probe laser beam.

4.2.3 Nonlinear Raman scattering

Light of a frequency ω that is non-resonant with an electronic transition can be scattered by matter. And even though this scattering is mainly elastic, so called Rayleigh scattering, the scattered light may contain new frequencies due to inelastic scattering, too. This spontaneous Raman effect is known since 1928, when it was reported for the first time by Chandrasekhara Venkata Raman [81]. Raman scattering consist of a transition from an initial state $|i\rangle$ to a virtual level, drawn as a dashed line (and associated with an excited state $|e\rangle$) in Figure 4.2, and a subsequent transition from this virtual level to a final state $|f\rangle$ with $\omega_f = \omega_i + \omega_{if}$. The final level can be lower or higher than the initial state, leading Stokes lines with $\omega_S = \omega - |\omega_{if}| < \omega$ (Fig. 4.2 a) or Anti-Stokes (Fig. 4.2 b) lines with $\omega_A = \omega + |\omega_{if}| > \omega$, respectively. As we will see in the following section, such Raman transitions are the basic process behind the optical Kerr effect spectroscopy experiments that are presented in this thesis.

Usually, Raman processes couple rotational, vibrational, ro-vibrational or phonon excitations. For the Stokes- and Anti-Stokes-Raman processes sketched in Figure 4.2 (a, b), the dipole matrix elements $\langle i|\,\mathbf{d}\,|e\rangle$ and $\langle e|\,\mathbf{d}\,|f\rangle$ must be nonzero. From this we can determine the selections rules that apply for diatomic molecules like carbon monoxide or hydrogen. Since the electric dipole operator $\mathbf{d}$ couples states of different parity, a Raman transition couples states of the same parity [77]. Additionally, the selection rule $\Delta J = \pm 2$ for pure rotational transitions, and $\Delta J = 0, \pm 2$ for ro-vibrational transitions have to be fulfilled [82]. The whole manifold of possible excited states $|e\rangle$ has to be considered to calculate the Raman transition probability. Because the incident light is usually not in resonance with any single exited state $|e\rangle$, spontaneous Raman scattering is a rather weak process. Even after propagating through 1 cm of condensed matter, the probability for spontaneous Stokes-Raman scattering for an incident photon is only about $1{:}10^6$ [77]. The relative strengths of the Stokes- and Anti-Stokes-lines are governed by the Boltzmann distribution of the initial states. Only if the virtual level depicted in Figure 4.2 is close to an excited state $|e\rangle$, in the case of Resonance Raman (RR) scattering, the spontaneous transition probability is strongly enhanced.

As a stimulated process, Raman scattering can occur with much higher efficiency. This was observed for the first time in 1962 by Woodbury and Ng and reported more fully by Woodbury and Eckardt in the same year [83]. A Raman transition of a pump laser with frequency ω can be stimulated by a photon whose frequency is shifted by ω_{if}, if the

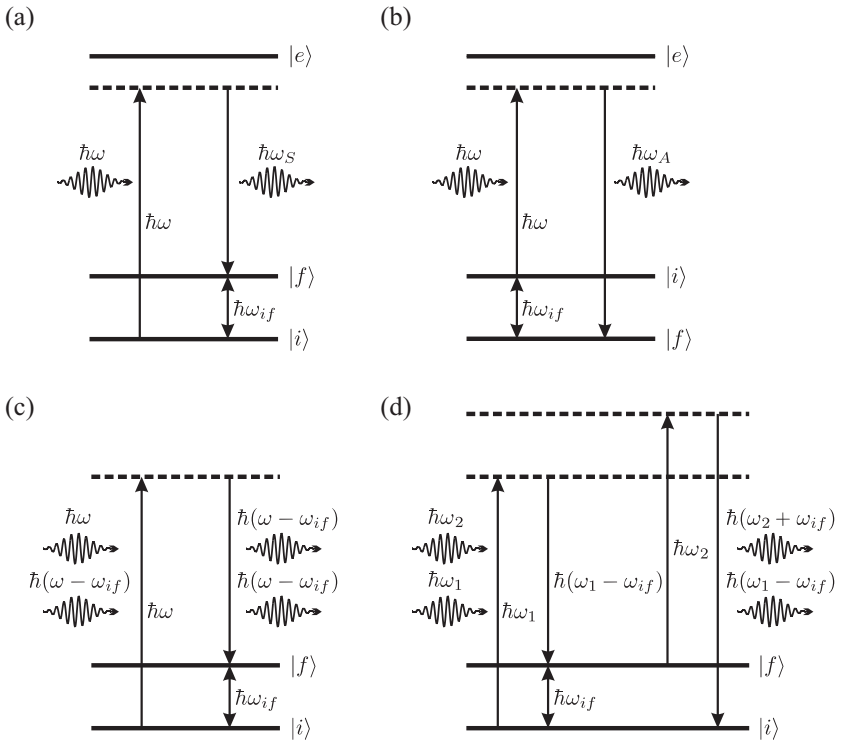

Figure 4.2: *(a) Stokes Raman scattering, (b) Anti-Stokes Raman scattering, (c) stimulated Raman process, (d) CARS process.*

energy shift is equivalent to the shift from the initial $|i\rangle$ to the final state $|f\rangle$ of the Raman process. Such a stimulated transition, in this case a Stokes transition, is sketched in Figure 4.2 (c). Hence, given that an intense laser passes a Raman-active material with length z, the spontaneously scattered Raman intensity at $z = 0$ may amplify the Raman scattering probability at $z > 0$. For a steady state situation and a small Stokes intensity $I(\omega - \omega_{if})$ this stimulated Raman scattering (SRS) leads to an exponential dependence of the Raman intensity on the pump laser intensity $I(\omega)$ and the interaction length z [84]. In presence of a counteracting linear optical absorption α the scattered intensity is given by

$$I(z, \omega - \omega_{if}) = I(0, \omega - \omega_{if}) e^{g_S I(\omega) z - \alpha z}, \tag{4.32}$$

where g_S is the gain factor. $I(0, \omega - \omega_{if})$ is only that fraction of the initially ($z = 0$) spontaneously scattered light, which propagates in the same direction as the incoming pump beam [78].

In the case of this SRS, the stimulating photon has its origin in the spontaneous Raman scattering of the pump beam. However, the stimulated photon may also be provided by a detuned probe laser field $\mathbf{E}(\omega - \omega_{if})$. In this case, the probe beam does gain intensity by stimulated Raman scattering, which is the basic principle of stimulated Raman gain (SRG) spectroscopy. Simultaneously to the gain of the probe beam, the pump beam is depleted of intensity. The effect is used in stimulated Raman loss (SRL) spectroscopy. A theoretical description of these processes is based on the framework of nonlinear polarizability theory as it was introduced above. All the coherent Raman processes, SRS, SRG, SRL, and also CARS (coherent anti-Stokes Raman scattering, sketched in Figure 4.2 d), have their origin in the third order susceptibility $\chi^{(3)}$ and can be regarded as four-wave mixing processes [85]. Thus, the induced stimulated Raman and CARS polarizations, assuming that the incident light beams are plane waves propagating along the z-axis, may be written as third

order polarizations,

$$\mathbf{P}^{(3)}_{SRG}(z,\omega-\omega_{if}) = \epsilon_0((\chi^{(3)}_{SRG}\mathbf{E}(\omega))\mathbf{E}^*(\omega))\mathbf{E}(\omega-\omega_{if})e^{i\mathbf{k}(\omega-\omega_{if})z}, \tag{4.33}$$

$$\mathbf{P}^{(3)}_{SRL}(z,\omega) = \epsilon_0((\chi^{(3)}_{SRL}\mathbf{E}(\omega))\mathbf{E}(\omega-\omega_{if}))\mathbf{E}^*(\omega-\omega_{if})e^{i\mathbf{k}(\omega)z}, \tag{4.34}$$

and

$$\mathbf{P}^{(3)}_{CARS}(z,\omega_2+\omega_{if}) = \epsilon_0((\chi^{(3)}_{CARS}\mathbf{E}(\omega_2))\mathbf{E}(\omega_2))\mathbf{E}^*(\omega_1)e^{i(2\mathbf{k}(\omega_2)-\mathbf{k}(\omega_1))z}. \tag{4.35}$$

As was shown above, these polarizations act as source terms for the wave equation Eq. 4.20. This allows to determine the intensity changes of the pump/probe beam in SRL/SRG and the anti-Stokes intensity created by CARS [85, 86]. The intensity change for SRG is given by

$$\Delta I_{SRG}(z,\omega-\omega_{ij}) = \frac{z(\omega-\omega_{if})}{n_\omega n_{\omega-\omega_{if}}c^2\epsilon_0} Im(\chi^{(3)}_{SRG})I(\omega)I(0,\omega-\omega_{if}), \tag{4.36}$$

and analogous for SRL by

$$\Delta I_{SRL}(z,\omega) = \frac{z\omega}{n_\omega n_{\omega-\omega_{if}}c^2\epsilon_0} Im(\chi^{(3)}_{SRL})I(\omega-\omega_{if})I(0,\omega). \tag{4.37}$$

The intensity of the created anti-Stokes wave at $\omega_2+\omega_{if}$ in a CARS process follows as

$$I_{CARS}(z,\omega_2+\omega_{if}) = \frac{(\omega_2+\omega_{if})^2}{n^2_{\omega_2}n_{\omega_1}n_{\omega_2+\omega_{if}}c^4\epsilon_0^2}\left|\chi^{(3)}_{CARS}\right|^2 I^2(\omega_2)I(\omega_1)z^2[sinc(\Delta kz/2)]^2, \tag{4.38}$$

with the phase matching constraint for CARS $\Delta\mathbf{k} = 2\mathbf{k}(\omega_2)-\mathbf{k}(\omega_1)-\mathbf{k}(\omega_2+\omega_{if})$. It is interesting to note that the CARS intensity is proportional to the squared number density of the particles N^2, because $\chi^{(3)} \propto N$ is valid [87], while the other two processes are linear in N. The particle density dependence of intensities becomes important for the discussion of the origin of observed signals and plays a role for the improvement of signal to noise ratios of experiments.

4.3 Time resolved spectroscopy

Time resolved spectroscopy with femtosecond light sources opens the possibility to directly observe and control molecular dynamics that happen in these ultrashort time scales. Ultrafast spectroscopy was the key aspect of our experimental work on solid hydrogen. Focusing on rotational dynamics, we applied an extended kind of rotational coherence spectroscopy (RCS), which we termed two dimensional optical Kerr effect (2D OKE) spectroscopy. The principles of this technique, starting from the time resolved (one dimensional) optical Kerr effect (OKE) spectroscopy, as it was applied in our workgroup by Nina Owschimikow to study the rotational alignment of gaseous N_2 [25, 26], are laid down in the following.

4.3.1 Optical Kerr effect spectroscopy

The time evolutions of induced anisotropies are widely studied by a time resolved, nonlinear pump-probe polarization spectroscopy that probes the Raman induced transient birefringence of a sample medium. This technique, called time resolved Raman induced Kerr effect spectroscopy (RIKE, RIKES, tr-RIKES), or optical Kerr effect (OKE) spectroscopy was implemented for the first time by Heritage et al. in 1975, who observed a coherent transient birefringence in CS_2 vapor [22]. Applied in the gas phase, where it is often termed Raman

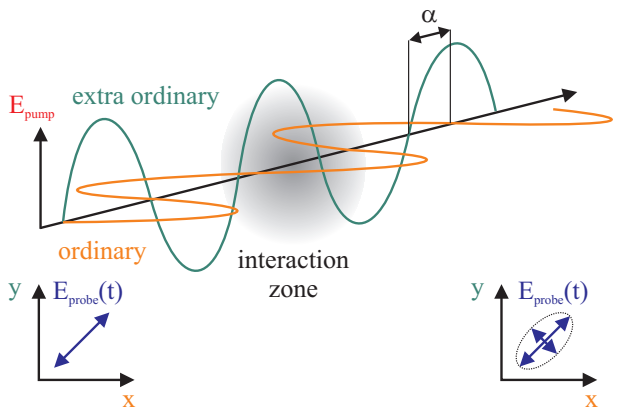

Figure 4.3: *Influence of a birefringent media (interaction zone) on a linearly polarized light wave. Different indices of refraction for the ordinary and the extraordinary beam cause a phase shift α, which induces elliptic components into the initially linearly polarized light.*

induced polarization spectroscopy (RIPS), it can be used to observe rotational dynamics [22–24]. However, OKE spectroscopy was also carried into the condensed phase, studying vibrational and rotational dynamics in liquids, solvents, and glasses [27, 28, 88]. There is no principle difference between RIKE, RIPS and OKE, and they become interchangeably for a broadband, femtosecond pulse excitation. Hence, we will use the term OKE spectroscopy in the following. This pump-probe technique is well understood and offers many benefits. It has a noninvasive detection scheme, a robust setup, and especially the so-called optically heterodyne detected signal, as in the optically heterodyne detected optical Kerr effect (OHD-OKE), offers a good signal to noise ratio.

The general approach of OKE spectroscopy is depicted in Figure 4.3. Birefringence, as induced into an isotropic sample by the electric field of an intense, linearly polarized pump pulse, can be detected by its influence on the polarization of a probe pulse. The linearly polarized probe light wave can be described as combination of two linearly polarized light waves with the same amplitude and phase, ordinary and extra ordinary beam. If ordinary and extra ordinary axis differ in their indices of refraction, a phase shift α between the ordinary and the extra ordinary light wave occurs. This phase shift is identical to the induction of an elliptic component into the probe light, which can be analyzed and eventually detected with the help of a polarizer.

A typical OKE setup is shown in Figure 4.4. It applies an intense, nonresonant, linearly polarized, femtosecond pump pulse with intensity I_{pump}. The pump pulse coherently excites Raman-active modes (vibrational, rotational, translational) that lie in the bandwidth of the pump pulse, which we shall consider to be spectrally broad (and therefore short) compared to the transition energies, via stimulated Raman scattering [28]. These modes have a well defined time origin and phase, and form a coherent wavepacket that evolves in time corresponding to the involved transition frequencies $\Delta\omega$. The temporal evolution of the wavepacket is probed by a second light field E_{probe} after a time delay Δt. The process may be understood as an optical Kerr effect with a time dependent effective third order susceptibility $\chi^{(3)}_{eff}(\Delta t)$. Hence, pump and probe field interact in a four wave mixing process, and the created nonlinear (third order) polarization radiates a field that is proportional to I_{pump} and E_{probe}. The fraction of this field that passes the analyzer A becomes the detected signal field E_s [27],

$$E_s(\Delta t) \propto P^{(3)}(\Delta t) = i\epsilon_0 \chi^{(3)}_{eff}(\Delta t) I_{pump} E_{probe}. \tag{4.39}$$

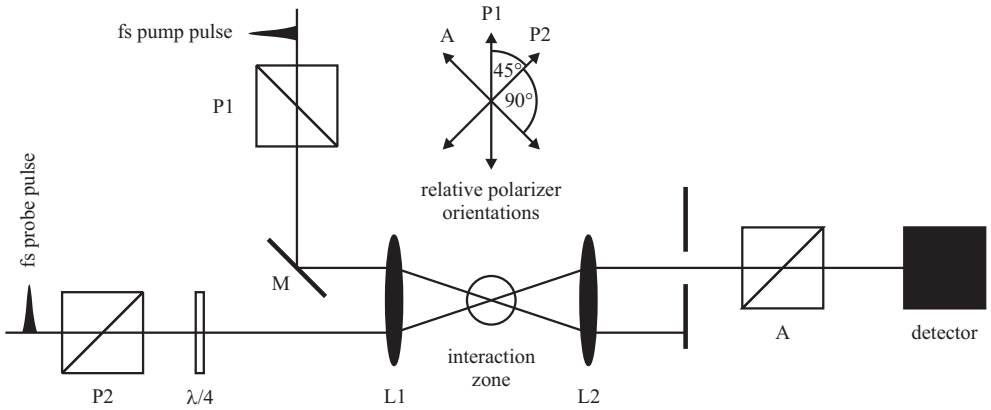

Figure 4.4: *A typical experimental setup for performing a time resolved optical homodyne detected OKE experiment. Pump and probe pulse are linearly polarized (polarizers P1 and P2) and have a controlled time delay. They are focused into the sample (here: under a small angle for subsequent beam separation) by the lens L1. After P1, the sample response onto the pump beam induces an ellipticity into the probe beam. This ellipticity is detected behind the analyzer A. A quarter-wave plate $\lambda/4$ is used to compensate for strain induced birefringence.*

E_s may interfere with any fraction of the probe beam that passes the analyzer, in the following referred to as the optical local oscillator E_{lo}. Thus, the detected signal amplitude I follows from the coherent superposition of all signal fields E_s and the local oscillator field E_{lo} [27],

$$I = (E_s + E_{lo})(E_s + E_{lo})^* = I_{hom} + Re[E_s^* E_{lo} + E_s E_{lo}^*] + I_{lo}. \tag{4.40}$$

In the so called optically homodyned regime, i.e. in absence of a local oscillator, only the signal intensity $I_{hom}(\Delta t) = |E_s(\Delta t)|^2$ is present. This so called homodyned intensity is quadratic in the signal field E_s. However, the deliberate heterodyning of the signal field with a local oscillator field, as it was described by Easley et al. in 1978 [89], is often favorable. The intensity of the local oscillator $I_{lo} = |E_{lo}|^2$ is itself time independent and carries no information. Nevertheless, E_{lo} can be used to amplify the heterodyned signal $I_{het}(\Delta t) = Re[E_s^*(\Delta t)E_{lo} + E_s(\Delta t)E_{lo}^*]$, which is linear in E_s and E_{lo}. Indeed, the dynamics that we observed in our hydrogen samples were often close to the noise level, and became only observable due to the heterodyne detection. Furthermore, the heterodyne detected signal carries the phase information of E_s with respect to E_{lo} that is lost in the homodyned regime. Thus, many of our heterodyned experiments revealed peculiar phase effects.

In the optically homodyned configuration of Fig. 4.4, P2, $\lambda/4$, and A are used to extinguish this local oscillator field. This is accomplished by a perpendicular orientation between P2 and A. Starting from this configuration a controlled manipulation of the probe beam polarization state by the polarizer P2 can be used to generate a defined local oscillator. A small rotation of P2 by an angle $\epsilon \approx \sin\epsilon$ creates an out-of-phase local oscillator

$$E_{lo} = \mp i\epsilon E_{probe} \tag{4.41}$$

that is phase shifted with respect to E_{probe} by $\pi/2$ [27, 28]. A rotation of the analyzer A generates an in-phase local oscillator

$$E_{lo} = \pm\epsilon E_{probe}. \tag{4.42}$$

And a local oscillator that is introduced by the $\lambda/4$ retardation plate is complex (mixed phase),

$$E_{lo} = \mp(\epsilon + i\epsilon)E_{probe}. \tag{4.43}$$

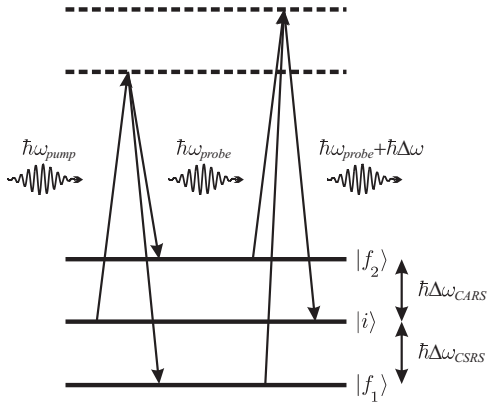

Figure 4.5: *Energy level diagram for OKE spectroscopy [23]. A pump photon excites the system from its initial state $|i\rangle$ into a manifold of final states ($|f_1\rangle$, $|f_2\rangle$) that lie within the bandwidth of the spectrally broad pump pulse. The created coherent superposition of states is probed by Stokes and anti-Stokes scattering processes.*

Insertion of Eq. 4.39 into Eq. 4.40 shows that the heterodyned signal

$$I_{het}(\Delta t) \propto Re[(i\chi^{(3)}_{eff}(\Delta t) I_{pump} E_{probe})^* E_{lo} + i\chi^{(3)}_{eff}(\Delta t) I_{pump} E_{probe}) E^*_{lo}] \tag{4.44}$$

probes $Re\chi^{(3)}_{eff}(\Delta t)$ for an out-of-phase local oscillator. Thus, I_{het} corresponds to the pump induced birefringence, which is the usual approach for optically heterodyned OKE spectroscopy. For an in-phase local oscillator, I_{het} corresponds to $Im\chi^{(3)}_{eff}(\Delta t)$, the sample dichroism. Dichroism plays no role in our experiment, since it is a resonance or near-resonance effect and we are far off any resonance of our sample. A mixed phase local oscillator yields a mixture of dichroism and birefringence.

4.3.2 Energy and momentum conservation

Figure 4.5 shows a schematic diagram that illustrates the excitation mechanism for a femtosecond OKE process. Raman transitions, induced by stimulated Raman scattering of a nonresonant pump pulse, create a coherent superposition of states. This superposition is probed via stimulated Raman scattering of a weak, time-delayed probe pulse in a polarization sensitive way [23]. The comparison of Fig. 4.5 with Fig. 4.2 (d) shows that the process resembles the energy level diagram for coherent Stokes (CSRS) and anti-Stokes (CARS) scattering processes. The energy conservation for the pump step requires [90]

$$\omega_{pump} = \omega'_{pump} + \Delta\omega \tag{4.45}$$

to be fulfilled, where ω_{pump} is the frequency of the incident pump field, ω'_{pump} the frequency of the scattered pump field, and $\Delta\omega$ the transition frequency. If ω'_{pump} lies within the bandwidth of the pump laser, the pump process can be significantly enhanced by stimulated Raman scattering (see Fig. 4.2 (a, b)). The energy conservation for the probe step yields an analogous expression as for the pump step,

$$\omega_{probe} + \Delta\omega = \omega'_{probe}, \tag{4.46}$$

with the frequency of the incident probe field ω_{probe} and the frequency of the scattered probe field ω'_{probe}.

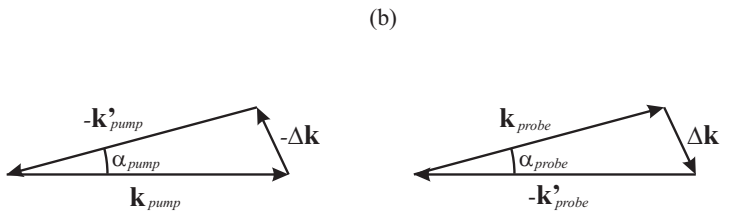

Figure 4.6: *Momentum conservation for OKE spectroscopy [90], following Eq. 4.47 and Eq. 4.48. The pump process (a) imparts a momentum $\Delta\boldsymbol{k}$ into the sample. During the probe process (b), the sample returns this momentum to the radiated field. Stimulated Raman scattering does only occur, if the angle α between the incident field's wavevector $\boldsymbol{k}$ and the radiated field's wavevector $\boldsymbol{k}'$ is smaller than the focusing angle of the laser.*

Simultaneously to the transition energy, the pump pulse imparts a momentum $\Delta\mathbf{k}$ into the sample [90]. Thus, the pump process has to fulfill the momentum conservation

$$\mathbf{k}_{pump} = \mathbf{k}'_{pump} + \Delta\mathbf{k}, \tag{4.47}$$

where $\mathbf{k}_{pump}$ is the incident field's wavevector and $\mathbf{k}'_{pump}$ the scattered field's wavevector. Figure 4.6 (a) is a vector diagram to illustrate Eq. 4.47. In principle, any angle α_{pump} between $\mathbf{k}_{pump}$ and $\mathbf{k}'_{pump}$ is possible. However, stimulated Raman scattering does only occur, if α_{pump} is smaller than the focusing angle of the pump beam, which limits the direction of $\Delta\mathbf{k}$. As for the energy conservation, an analogous momentum conservation is valid for the probe process, as it is depicted in Figure 4.6 (b). Here, the sample gives back the imparted momentum $\Delta\mathbf{k}$ to the radiated signal field,

$$\mathbf{k}_{probe} + \Delta\mathbf{k} = \mathbf{k}'_{probe}. \tag{4.48}$$

The momentum conservation therefore yields

$$\mathbf{k}_{pump} - \mathbf{k}'_{pump} = \mathbf{k}'_{probe} - \mathbf{k}_{probe}. \tag{4.49}$$

If pump and probe beam are collinear and of the same frequency, the momentum conservation for stimulated Raman scattering processes is easily fulfilled. However, we need to separate pump and probe, either spatially or spectrally, for the subsequent detection (see Fig. 4.4 and Fig. 5.2). Under this circumstances, momentum conservation for high energy excitations may be not readily achieved. Instead, the observation of such excitations depends on the beam geometry and the focusing angles.

4.3.2.1 Signal analysis

In a real experiment, the signal will depend on the material response function $R(\chi^{(3)})$, the time delay Δt between pump and probe, the interaction length l, the spectral and temporal laser pulse properties, and the angles between pump polarization, analyzer, and probe polarization. For a standard configuration as depicted in Fig. 4.4, with temporal profiles of pump and probe pulse $E_{pump}(t)$ and $E_{probe}(t)$, respectively, the detected intensity I is given by the sum of three contributions (see Eq. 4.40) [28]:

$$I_{lo}(\Delta t) = \left\langle I_{probe} \sin^2(\epsilon) \right\rangle_t, \tag{4.50}$$

$$I_{hom}(\Delta t) = \left\langle \left| E_{probe}(t-\Delta t) \frac{\omega_{probe} l}{c} \int_{-\infty}^{t} dt' R(t-t') I_{pump}(t') \right|^2 \right\rangle_t, \tag{4.51}$$

$$I_{het}(\Delta t) = 2\left\langle I_{probe}(t-\Delta t)\sin(\epsilon)\frac{\omega_{probe}l}{c}\int_{-\infty}^{t} dt' R(t-t')I_{pump}(t')\right\rangle_t . \tag{4.52}$$

The angle brackets symbolize a statistical average over the laser fields, and a temporal integration to account for the response time of the detector. The dependence onto the temporal profiles, i.e. the pulse durations, of pump and probe beam will become important for the observable signals.

The amplitude of the signal will depend on the number of oscillating dipoles that radiate the signal field. When the dipoles can be treated as noninteracting, e.g. in a gas of low pressure that has a low number density of particles N, the third order electric susceptibility $\chi^{(3)}$ is given by [91]

$$\chi^{(3)}(\omega) \propto N\gamma(\omega_k, \omega_l, \omega_m), \tag{4.53}$$

where γ is the symmetrized response function of a single particle. Following Eq. 4.39, $\chi^{(3)}$ is proportional to the signal field. Hence, the signal field strength E_s is linearly dependent on the particle density. The heterodyne detected intensity scales therefore linear with the sample pressure p, and the homodyne detected intensity I_{hom} scales with the square of the sample pressure p, which is shown in the following chapter for the homodyned alignment signal of gaseous nitrogen.

Let us now consider the rotational alignment of a gaseous sample of molecules, like nitrogen or carbon dioxide, and its detection via time resolved OKE spectroscopy. The degree of alignment $\langle\langle\cos^2\theta\rangle\rangle$ follows directly from the measured intensity [24],

$$I = I_{hom} + I_{het} + I_{lo} \propto \left[\langle\langle\cos^2\theta\rangle\rangle - \frac{1}{3} + C\right]^2, \tag{4.54}$$

where C is a constant proportional to the local oscillator field, $C \propto E_{lo} \propto E_{probe}$ (see Eq. 4.40). The homodyne detected signal I_{hom} is hereby given by

$$I_{hom} \propto \left[\langle\langle\cos^2\theta\rangle\rangle - \frac{1}{3}\right]^2, \tag{4.55}$$

and the heterodyne detected signal I_{het} by [24],

$$I_{het} \propto C\left[\langle\langle\cos^2\theta\rangle\rangle - \frac{1}{3}\right]. \tag{4.56}$$

Keep in mind that an isotropic distribution of θ leads to $\langle\langle\cos^2\theta\rangle\rangle = 1/3$, which, as expected, displays a zero signal intensity. Hence, the OKE signal is a direct measure for the degree of the coherent rotational alignment.

As discussed above, rotational alignment is induced into an isotropic sample by $\Delta J = +2$ Stokes and $\Delta J = -2$ anti-Stokes, $\Delta M = 0$ Raman excitations due to the intense, nonresonant, femtosecond pump pulse. The coherence between the coupled eigenstates $|J, M\rangle$ and $|J \pm 2, M\rangle$ will decay with a coherence dephasing time T_2, due to population relaxation T_1 and pure dephasing τ_{ph}. Thus, the amplitude of the degree of coherent alignment shows a single exponential decay,

$$\langle J \pm 2, M|\cos^2\theta\,|J, M\rangle \propto e^{-t/T_2}. \tag{4.57}$$

Following Eq. 4.55 and Eq. 4.56, this leads to a single exponential decay of the heterodyne detected intensity for a specific transition with a decay time $\tau_{het} = T_2$. It is therefore possible to determine the dephasing times of rotational transitions with OKE spectroscopy. However, we have to emphasize that the general expression $I_{het} \propto e^{-t/T_2}$ is valid for any

kind of Raman mode observed with OKE spectroscopy. Indeed, we will show in Chapter 7 that we measured the dephasing times of Raman-active phonon modes, too. Because the homodyned signal depends on $\left[\left\langle\left\langle\cos^2\theta\right\rangle\right\rangle - 1/3\right]^2$ (see Eq. 4.55), its intensity decays twice as fast than I_{het}, $\tau_{hom} = T_2/2$. It is interesting to note that the population part of the degree of rotational alignment from Eq. 4.17 is not affected by pure dephasing, which opens a door to measure T_2, T_1, and τ_{ph} at the same time.

The commonly used time constant T_2, often simply called dephasing time, is specific for the coupled states under the given environmental conditions. This dephasing also leads to a broadening of observed transition lines, even if other effects, like inhomogeneous or Doppler-broadening, are absent. It is connected with the full width at half maximum (FWHM) $\Delta\nu$ of the corresponding transition, known from e.g. spontaneous Raman scattering experiments, with [87, 92]

$$\Delta\nu = \frac{1}{\pi c T_2}. \tag{4.58}$$

Thus, we are able to compare the directly measured dephasing times from our time resolved experiments to Raman linewidth studies.

However, a more general approach to quantify the dephasing is also possible. For rotational alignment in the gas phase, the radiative relaxation is slow and the dephasing is almost purely collision induced. It is therefore useful to describe the rotational relaxation via a collision cross section σ. Collision cross sections are especially suited to compare theoretical and experimental results, since the latter are often carried out under various temperature and pressure conditions. Let us consider a gaseous mixture of two species, A and B, of which species A is rotationally aligned. In a mean free path model, the probability that a collision between a particle of species A and particles of species B occurs that destroys the rotational coherence can be expressed in terms of collision cross section $\sigma_{AB}(v_{rel})$ [93, 94],

$$\sigma_{AB}(v_{rel}) = \frac{\nu_{AB}}{N_B v_{rel}}. \tag{4.59}$$

Here, N_B is the number density of particles of species B, ν_{AB} the collision rate, and v_{rel} the relative velocity of the colliding particles. In a thermal ensemble we have to average over the relative velocities, which leads to an effective collision cross section σ_{AB} [95]. The average relative velocity $\langle v_{rel}\rangle$ is given by

$$\langle v_{rel}\rangle = \sqrt{8 k_B T/\pi\mu}, \tag{4.60}$$

with the reduced mass μ of the colliding particles, the absolute temperature T and the Boltzmann constant k_B. From the ideal gas law, with a given partial pressure p_B of species B and at a temperature T, follows for the effective collision cross section

$$\sigma_{AB} = \frac{\nu_{AB}\sqrt{\pi\mu k_B T}}{\sqrt{8} p_B}. \tag{4.61}$$

The rotational relaxation cross section for collisions between particles of species A can be obtained in a similar way,

$$\sigma_{AA} = \frac{\nu_{AA}\sqrt{\pi m_A k_B T}}{4 p_A}, \tag{4.62}$$

where m_A is the mass of the particle and p_A the partial pressure of species A. The cross section σ_{AA} follows from the dephasing time T_2 in a pure sample, which equals ν_{AA}^{-1}. If it is known, σ_{AB} can be calculated from the total rotational relaxation collision cross section $\sigma = \sigma_{AA} + \sigma_{AB}$ by measuring the dephasing time T_2 in a mixed sample.

4.3.3 2D optical Kerr effect spectroscopy

Two dimensional OKE spectroscopy, as we call it, is a time resolved OKE spectroscopy that is extended by a spectrally resolved detection of the probe beam. The first experimental and theoretical treatment on such a spectrally dispersed and time resolved detected birefringence was reported by the Ziegler group in 1997 [96, 97]. However, only few applications and further developments have been reported [98–101]. OKE spectroscopy, as it was introduced above, has to be understood as two Raman transitions (see Fig. 4.5). Heritage et al. [22] stated in 1975 already that this has to cause spectral shifts of the probe light, corresponding to the involved Stokes and anti-Stokes transitions. If the probe pulse is short compared to the observed dynamics, then its spectral width exceeds the shifts and they occur only as a broadening. However, a narrow bandwidth probe pulse, which is longer than the dynamics, can resolve these shifts. E.g., a pulse has to be longer than $\Delta t = 1/6B$ to spectrally resolve rotational Raman transitions from the $J = 0$ to the $J = 2$ rotational state with $\Delta\nu = 6B$ (Eq. 4.7). Obviously, one sacrifices the time resolution needed to resolve the dynamics for achieving the spectral resolution. Nevertheless, as was already proposed by Heritage et al., one can still time resolve low frequency beats, as they occur for rotational levels with a lifted degeneracy. Indeed, we observed such beat phenomena in spectrally well separated rotational Stokes and anti-Stokes bands in the case of solid para-hydrogen.

Lets consider a two level system, a lower state $|1\rangle$ and a higher state $|2\rangle$, with an energy difference of $\hbar\omega_{12}$, and a probe field $E_{probe}(\omega)$ with a Gaussian-shape $G(\omega_{probe}-\omega)$ centered at ω_{probe}. Under the rotating wave approximation, the induced third order polarization has to be written as the sum of two components,

$$P^{(3)}(\omega, \Delta t) = P_I^{(3)}(\omega, \Delta t) + P_{II}^{(3)}(\omega, \Delta t), \tag{4.63}$$

which stem from Stokes- and anti-Stokes-Raman transitions. The spectral widths of these components equal the width of the probe pulse field, but they are shifted to $\omega_{probe} - \omega_{12}$, respectively $\omega_{probe} + \omega_{12}$. Hence, we have two signal fields, that oscillate with ω_{12} and decay with the dephasing time $\tau = T_2$ of the corresponding transition. The signal fields can interfere with a local oscillator field $E_{lo}(\omega)$, as shown in Eq. 4.40, at any frequency ω, creating a heterodyned signal $I_{het}(\omega)$. This yields Stokes and anti-Stokes shifted, heterodyne detected signal components [96],

$$I_{het\,I}(\omega, \Delta t) \propto \frac{E_{lo}(\omega)}{\Delta^2} G(\omega_{probe} - \omega_{12} - \omega) \sin(\omega_{12}\Delta t) e^{-\Delta t/\tau}, \tag{4.64}$$

and

$$I_{het\,II}(\omega, \Delta t) \propto \frac{E_{lo}(\omega)}{\Delta(\Delta - \omega_{12})} G(\omega_{probe} + \omega_{12} - \omega) \sin(\omega_{12}\Delta t) e^{-\Delta t/\tau}, \tag{4.65}$$

where Δ is the off-resonance detuning from electronic resonance. Obviously, the spectral distribution of the heterodyne detected signal is strongly dependent on the local oscillator distribution $E_{lo}(\omega)$. The distribution of the local oscillator will therefore play an important role in the experimental data that are presented in the following three chapters. However, the signal fields can also interfere with themselves. If $P_I^{(3)}(\omega, \Delta t)$ and $P_{II}^{(3)}(\omega, \Delta t)$ are well separated, e.g. due to a large rotational constant B as in the case of hydrogen, this leads to two homodyne detected signal contributions, $I_{hom\,I}(\omega, \Delta t)$ and $I_{hom\,II}(\omega, \Delta t)$. They correspond to Stokes- and anti-Stokes-Raman transitions, shifted to $\omega_{probe} - \omega_{12}$ and $\omega_{probe} + \omega_{12}$, respectively, have the spectral width of the probe pulse, and decay twice as fast as the heterodyned signal [101]. Such homodyned signals are discussed for the rotational alignment dynamics of para-hydrogen in Chapter 6 and in Chapter 7.

4.3.4 Frequency resolved Raman induced Kerr effect spectroscopy

For completeness, we have to mention that the term Raman induced Kerr effect is also used for a frequency resolved technique, developed by Heiman et al. in 1976 [102]. This Raman induced Kerr effect spectroscopy may not be confused with time resolved techniques described above, despite they are similar in many ways. However, in this frequency resolved technique a short probe pulse that contains a broad spectrum of frequencies ν_{probe} is used to record Raman spectra of relative high resolution, determined by the linewidth of the pump pulse. The pump pulse ν_{pump} induces a Kerr effect, when $|\nu_{pump} - \nu_{probe}|$ is in resonance with a Raman active mode, which is probed in a spectrally resolved way. The setup is very similar to the one shown in Fig. 4.4, but substitutes the delay stage with a spectrometer and applies a long (ps), narrowband pump pulse.

5 Ultrafast optical Kerr effect spectroscopy

"There are at least three reasons for its (optically heterodyne detected optical Kerr effect spectroscopy) popularity. First, the implementation of the experiment is relatively straightforward, by the standards of ultrafast spectroscopy. Second, the experiment provides data of extremely high signal-to-noise ratio, permitting detailed analysis. Third, as a result of the high signal-to-noise ratio, deconvolution procedures are possible, which yield a time resolution in the experiment which is greatly superior to the temporal pulse width of the laser employed."

N. A. Smith and S. R. Meech [28]

Our experimental approach on time resolved spectroscopy, together with a set of test experiments, is presented in this chapter. The optical setup, including the beam properties and some elementary effects caused by the polarization sensitive detection of spectrally broad light pulses, is described in the first section. The second section summarizes a set of test experiments with gaseous nitrogen samples. The rotational alignment of gaseous nitrogen was extensively studied in our workgroup within the doctoral thesis of Nina Owschimikow [25]. Hence, nitrogen provided an optimal test case to show that the working parameters of our optical Kerr effect setup are well understood.

5.1 Optical Kerr effect setup

Our setup is an extension of a classical optical Kerr effect spectroscopy setup, which offers the possibility to perform, as we call it, two dimensional optical Kerr effect (2D OKE) spectroscopy. Even though many of the key features of this setup were no new invention, it offered us unexpected insight due to the nature of our solid para-hydrogen samples.

5.1.1 Optical Kerr effect setup

The general principle of an optically heterodyne detected OKE setup was already introduced in Section 4.3. Fig. 4.4 shows the standard approach of crossed pump and probe, which allows for a spatial beam separation after the sample. We applied a collinear, two-color pump-probe geometry, as it is shown schematically in Fig. 5.1. The collinear setup provided a larger interaction volume and was significantly easier to align, particularly under the conditions of a spatially large sample cell that did not allow to align the spatial overlap of pump and probe beam focus with an iris. Additionally, the two-color pump-probe scheme increased the signal to noise ratio, since scattered pump light could be suppressed by spectral means. A linearly polarized pump pulse, oriented vertically to the table surface, was used to induce a sample anisotropy, i.e. a birefringence. The time evolution of this anisotropy was probed by a time delayed probe pulse, linearly polarized and turned 45 degrees with respect to the pump pulse, in combination with an analyzer, oriented perpendicular to the probe polarization.

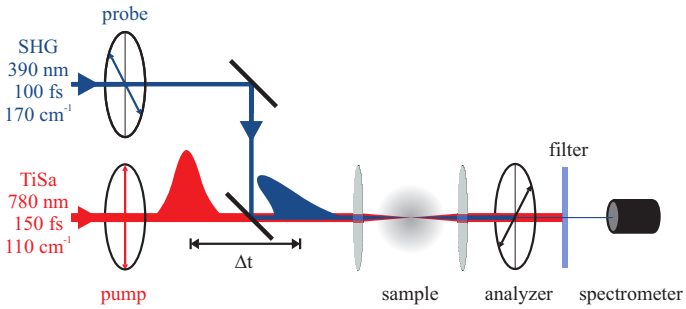

Figure 5.1: *The principle of our two-color, collinear optically homodyned OKE setup. A linearly polarized pump pulse is focused into the sample and induces an anisotropy. Subsequently, the pump beam is blocked by a colored glass filter. The linearly polarized probe pulse is delayed in time and its polarization is turned by 45 degrees with respect to the pump pulse. The sample's anisotropy causes birefringence, and therefore induces an elliptic component in the probe beam polarization (see Fig. 4.3). This component passes the analyzer, which is oriented perpendicular to the initial probe beam polarization, and is subsequently detected in a fiber optic spectrometer.*

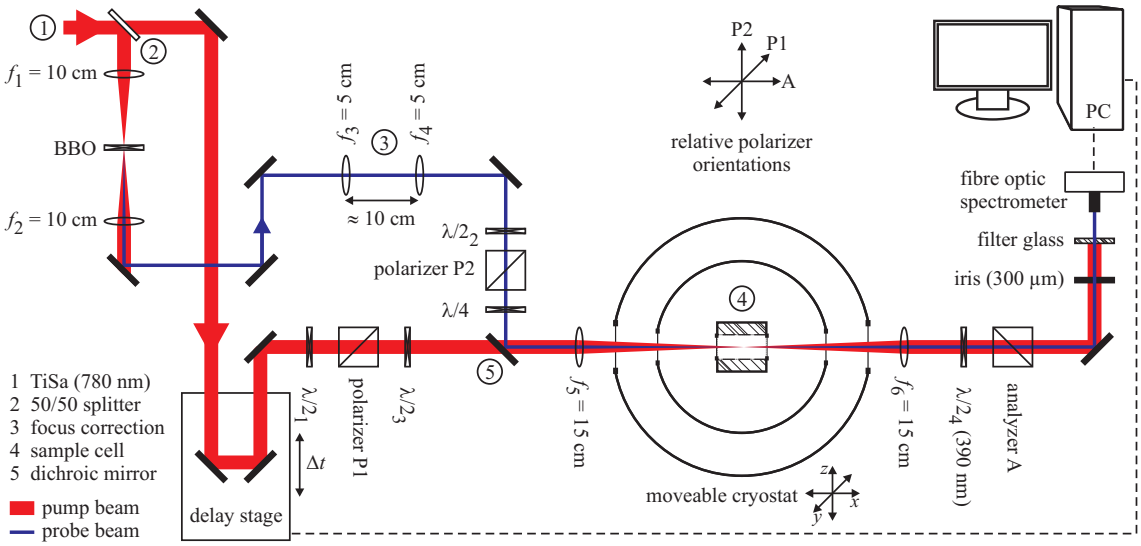

Figure 5.2: *Schematic drawing of the final 2D OKE setup. Collinear pump and probe provided an easy adjustment and good spatial overlap.*

Fig. 5.2 shows the setup as it was used in our experiments. The sample was kept in an enclosed cell attached to the cold tip of a liquid helium cryostat. Delay time and data acquisition were computer controlled, using a LabView routine written by Nina Owschimikow. A commercial Ti:sapphire regenerative amplifier (Clark-MXR CPA 2001) was used as light source. In order to achieve a collinear pump-probe geometry, we probed with the second harmonic of the laser fundamental, generated by frequency doubling in a birefringent crystal (BBO, $d = 0.1$ mm). The nonconverted fundamental, separated from the second harmonic by a dichroic mirror, could therefore be used as pump beam. However, the passage through the BBO caused a spatial distortion of the pump beam polarization. Hence, in the final setup, the splitting into a pump and a probe beam path was performed in front of the frequency doubling by a 50/50 beam splitter (2), as shown in Fig. 5.2. Pump and probe beam were guided by high reflectivity dichroic and UV-coated aluminum mirrors, and all lenses were made of quartz glass.

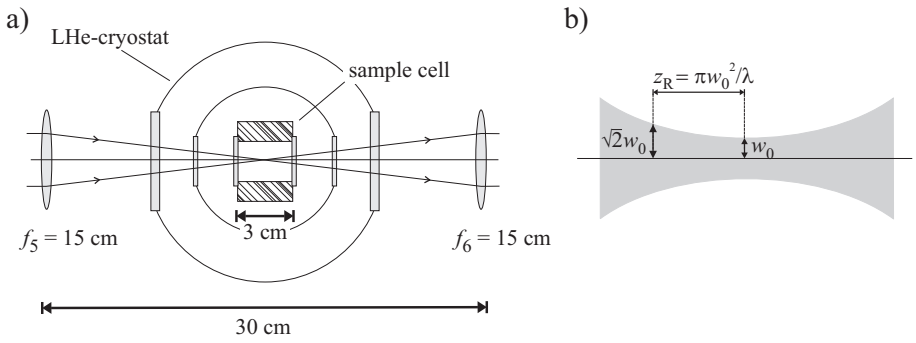

Figure 5.3: *Schematic drawing of cryostat's window-configuration (a) and close-up of the focal region of the pump beam (b). The focal diameter $2w_0$ was measured to be 26(5) μm [103] by the knife-edge method. Assuming a Gaussian beam this leads to a Rayleigh length z_R of 0.7(3) mm.*

The pump beam passed a computer controlled delay stage (Physics Instruments M-505.6PD), which provided a tunable delay of 1 ns (15 cm) with a resolution of 1.67 fs (0.25 μm). The stage had an accuracy of 1 μm per 25 mm. A half-wave plate ($\lambda/2_1$, 800 nm, Thorlabs Inc.) in combination with a Glan-Thomson polarizer (P1, B. Halle Nachfl. GmbH) controlled polarization state and power of the pump beam. The beam was linearly polarized and its plane of polarization set to an angle of 45 degrees with respect to the table surface, its power was tunable between 0.5 mW and 15 mW. An additional half-wave plate ($\lambda/2_3$, 800 nm, Thorlabs Inc.) behind the polarizer P1 was inserted in a number of experiments, to vary the angle of the plane of polarization.

The probe beam passed through a variable telescope (f_3, f_4), which was used to adjust its divergence. This allowed to overlap the focal positions of pump and probe beam in the sample, despite the wavelength dependent index of refraction of the focusing lens (f_5). As for the pump beam, a combination of half-wave plate ($\lambda/2_2$, 390 nm, 4.5 λ, low, B. Halle Nachfl. GmbH) and Glan-Thomson polarizer (P2, B. Halle Nachfl. GmbH) controlled the probe beam's polarization state and power. The beam was linearly polarized with its plane of polarization vertical to the table surface, its power was tunable between 0.04 mW and 0.4 mW. A quarter-wave plate ($\lambda/4$, 390 nm, 2.75 λ, low, B. Halle Nachfl. GmbH) precompensated for elliptical components in the probe light induced by static birefringencies, e.g. due to strain-induced birefringence in the cryostat's windows and the hcp symmetry of the cryogenic hydrogen samples.

Pump and probe beam were merged with a dichroic mirror (5) and focused by a quartz lens ($f_5 = 15$ cm) into the cryostat's sample cell (Fig. 5.3). The later separation of pump and probe beam was achieved by a colored glass filter (BG 18, Schott) directly in front of the detector. The sample cell was cylindrical, 3 cm long and 2 cm in diameter, with 2 mm thick windows attached on front- and backside, the radiation shield had a second pair of 2 mm thick windows, and the cryostat's outer windows had a thickness of 4 mm each. All windows were made from CaF_2. From the pump beam's focal diameter of 26(5) μm [103], we calculated a Rayleigh length of 0.7(3) mm. The Rayleigh length z_R is the distance from the beam waist to the place where the area of the cross section is doubled for a Gaussian beam. Since the optical Kerr effect is second order in I_{pump}, $2z_R$ is a reasonable estimate for the interaction length. As we have discussed in Chapter 3, the solid hydrogen samples exhibited crystallite sizes of cubic millimeters to cubic centimeters. Thus, we could probe monocrystal dynamics of solid hydrogen, which are discussed in Chapter 7. The probe beam was collimated by another quartz lens (f_6) behind the cryostat and analyzed by a

Glan-Thomson polarizer (A, B. Halle Nachfl. GmbH), set horizontally to the table surface. In a set of experiments, an additional half-wave plate ($\lambda/2_4$, 390 nm, 4.5 λ, low, B. Halle Nachfl. GmbH) was inserted in front of the analyzer to avoid the beamshifts that occurred by adjustment of the Glan-Thomson analyzer. Since the homogeneity of the probe beam, which had at this stage a diameter of about 6 mm, suffered from the inhomogeneity of our solid para-hydrogen sample, we used a 300 μm pinhole to cut out only a small area of the beam for detection. This small fraction was recorded by a fiber optic spectrometer (Avantes AVS-SD2000). The spectrometer was calibrated with argon and mercury lamps (Lambda Physics). It provided 2048 pixels, a total wavelength range of 340 nm to 1150 nm, and a resolution of 0.4 nm per pixel.

Typically, the setup was aligned with a 900 mbar N_2 sample kept at 80 K, which provided a very strong signal. A good spatial overlap between pump and probe was relatively easy to accomplish by virtue of the collinear beam paths. In a second step, we blocked the pump beam to adjust the probe beam path. First, we removed the quarter-wave plate ($\lambda/4$) to set the analyzer (A) antiparallel to the probe beam polarization plane. This had to be done prior to the adjustment of the detector, because adjustments of the prism-polarizer could lead to beam shifts. To adjust the fiber optic spectrometer and the pinhole at convenient intensity, we now inserted and detuned the quarter-wave plate. With the detector and the pinhole in place we fine-tuned analyzer and quarter-wave plate to extinguish the probe beam and its static elliptic components. At this point, we opened the pump beam to search for a signal. Usually, the overlap of the focal positions was good enough to find the temporal overlap ($\Delta t = 0$), indicated by the strong electronic response of the sample, without readjustment of the beam paths. The fine-adjustment was carried out at the first half-rotational-revival of nitrogen at $\Delta t = 4.2$ ps. With 12 mW pump power and 0.5 mW probe power we achieved background to signal ratios of 1:1000 and better. The preadjustment had to be carried out in nitrogen gas, since the 2D OKE signal in solid hydrogen suffered from strong scattering and a low signal to noise ratio. The latter was not easy to overcome by increasing the laser powers, due to the low destruction threshold of the hydrogen crystals. Hence, a good preadjustment proved to be crucial for the success of our solid state experiments.

5.1.2 Laser pulse properties

The femtosecond laser light source was a commercial Ti:sapphire regenerative amplifier (Clark-MXR CPA 2001) with 1kHz repetition rate. It was first seeded by an inbuilt erbium-doped fiber oscillator, later by an external fiber oscillator (IMRA femtolite 780). This increased the output power from 900 mW to 1 W and reduced the pulse-to-pulse fluctuations from above 2 percent to 1 percent. The pulse duration remained unchanged and the spectral properties were only slightly affected by this modification. The spectrum, measured with a fibre optic spectrometer (Avantes AVS-SD2000), was Gaussian-shaped with a central wavelength of about 780 nm and a FWHM of 8 nm (internal seed) respectively 7 nm (external seed) (Fig. 5.4 (a)). Measurements with a commercial autocorrelator yielded pulse durations of 156 fs (FWHM) for the externally seeded Ti:sapphire fundamental. The laser system was in use for several experimental setups simultaneously, and less than 10 percent of the output power was used for the OKE setup. About 5 percent were used as pump beam, which retained the spectral properties of the laser fundamental. The other 5 percent were used to generate the second harmonic of the laser fundamental, the probe beam. Its spectrum was also Gaussian-shaped, centered at about 391 nm, with a FWHM of (2.60 $\pm$ 0.01) nm (Fig. 5.5 (d)).

The FWHM of 114 cm^{-1} (pump) and 170 cm^{-1} (probe) transforms into Fourier-limited

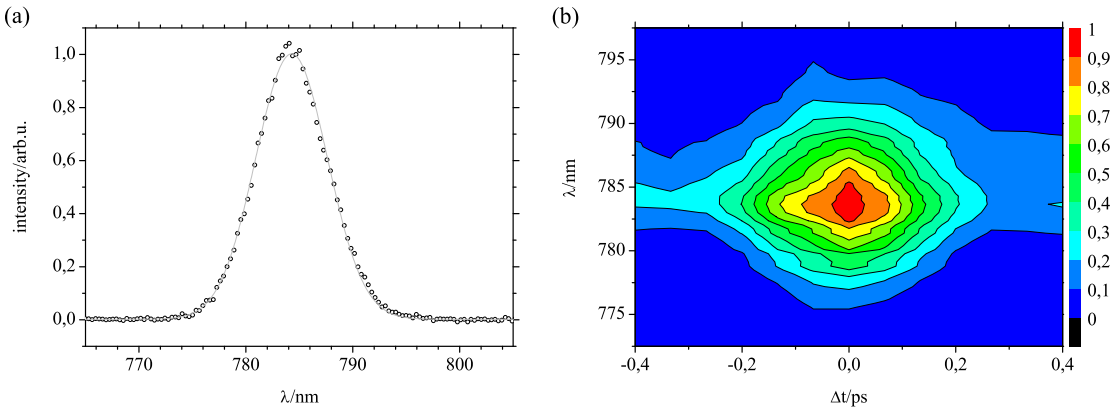

Figure 5.4: *Pump beam characteristics. (a) Spectra of the Ti:sapphire regenerative amplifier seeded by the inbuilt erbium-doped fiber oscillator (dots) measured with a fibre optic spectrometer (Avantes AVS-SD2000). The gray line shows a Gaussian fit centered at 784 nm with 8 nm FWHM. (b) PG FROG surface of the Ti:sapphire fundamental. It exhibits no significant linear chirp.*

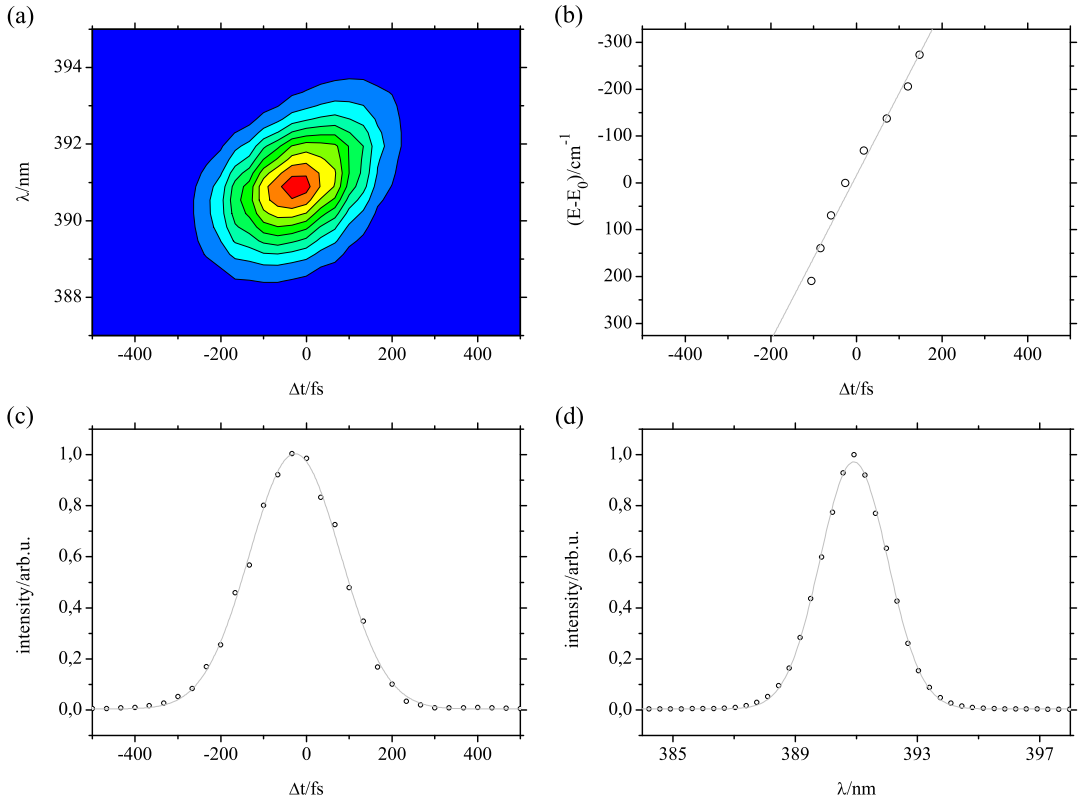

Figure 5.5: *Probe beam characteristics. (a) PG FROG surface measured from the in situ polarization of 900 mbar nitrogen at 80 K. The FROG reveals a significant chirp of the probe pulse, which is predominantly negative and linear with a minor nonlinear contribution (b). A cut through the pulse at 391 nm is shown in (c) (dots), the Gaussian fit (c, gray line) has a FWHM of (251 ± 2) fs. For a pump pulse of 166 fs (FWHM) this corresponds to probe pulse duration of (221 ± 4) fs (FWHM). (d) shows a cut through the FROG surface at $\Delta t = 0$ (dots). The spectral width, taken from a Gaussian fit (d, gray line), is (2.60 ± 0.01) nm.*

pulse durations (FWHM) of 129 fs (pump) and 87 fs (probe), respectively, calculated by [104]

$$\Delta t_{1/2} = \frac{2ln2}{\pi \Delta \nu_{1/2}}. \tag{5.1}$$

However, this represents only a lower limit for the duration of the pulses, which can be broadened by linear and higher order chirps. As a consequence, the measured pulse lengths were slightly longer. The pump pulse duration Δt_{pump} was measured by Nina Owschimikow [25] by means of second harmonic generation (SHG) frequency-resolved optical gating (FROG) [105]. This yielded pulse durations of (166 ± 4) fs (FWHM). Its accumulated linear chirp due to the optical components was small, estimated to be about 20 fs over the FWHM, consistent with the polarization gating (PG) FROG shown in Fig. 5.4 (b). In contrast to this, the PG FROG surface of the second harmonic in Figure 5.5 (a, b) clearly shows that the probe pulse exhibited a significant negative chirp. This was caused by the strong wavelength dependence of the optical components' and the cryostat's windows' dispersion in the UV. Fortunately, since the detection was spectrally resolved, we could eliminate this chirp for the time resolution of our experiment. The chirp-free probe pulse duration Δt_{probe} was determined from a careful simulation of the measured nitrogen revival structure, taking the pump pulse duration of 166 fs and the thermal population of nitrogen into account, which revealed probe pulse durations of about 130 fs (FWHM) [52].

Figure 5.5 (a) shows data from our standard optical Kerr effect setup (Fig. 5.2), which was basically a PG FROG setup. It detected the instantaneous electronic polarization of a gaseous nitrogen sample caused by the pump pulse with the probe pulse. However, the PG FROG was broadened by a signal from the electronic polarization of the cryostat's windows, which was unavoidable due to our collinear setup. Thus, the PG FROG delivered only an upper limit for the probe pulse duration. Assuming Gaussian-shaped pulses, the FWHM Δt_{PG} of a PG FROG is [106]

$$\Delta t_{PG} = \sqrt{\frac{\Delta t_{pump}^2}{2} + \Delta t_{probe}^2}, \tag{5.2}$$

which results from the third order character of a PG FROG, second order in E_{pump} and first order in E_{probe}. The PG FROG in Figure 5.5 was measured with gaseous nitrogen and the PG FROG trace in Figure 5.5 (b) shows a FWHM of (251 ± 2) fs. Similar values were obtained for the electronic overlap in solid hydrogen. With a given pump pulse duration of 166 fs, the upper limit of the chirp-free probe pulse duration follows from Eq. 5.2 to be (221 ± 4) fs (FWHM). This is not in conflict with probe pulse durations of 130 fs, if we accept a significant broadening by the influence of the cryostat's windows. In summary, we found laser pulse durations of $\Delta t_{pump} = 166$ fs and $\Delta t_{probe} = 130$ fs to be consistent with our electronic polarization and nitrogen revival data.

5.1.3 Wavelength dependent birefringence

The use of Glan-Thomson polarizers was a key issue to achieve a high sensitivity, since such polarizing prisms show remarkably high extinction ratios of 10^4:1 to 10^5:1. However, a certain leakage through the analyzer, shown in Figure 5.6, was caused by the spectral bandwidth of the probe pulse. The polarization of the electric field of the spectrally broad probe pulse exhibited a wavelength dependent ellipticity, and the highest extinction ratio was achieved when the polarization optics were optimized for the central wavelength of the probe pulse. I.e. the quarter-wave plate had to be used to compensate the static elliptic components of the central wavelength. The elliptic components of the blue and

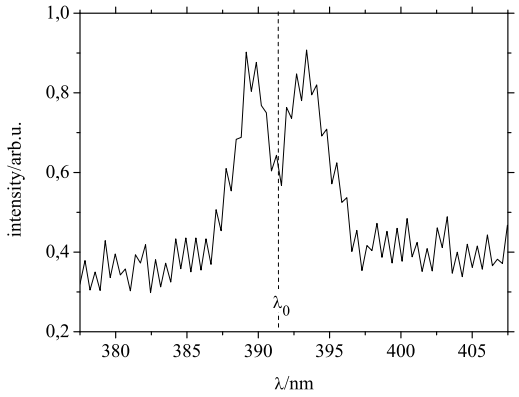

Figure 5.6: *Leakage of the spectrally broad probe pulse through the analyzer caused by wavelength dependent phase shift. The extinction is optimized for the central wavelength λ_0 of the probe pulse. Compare to Fig. 5.7 and Fig. 5.9. An offset of about 0.35 arb.u. is caused by the noise of the detector.*

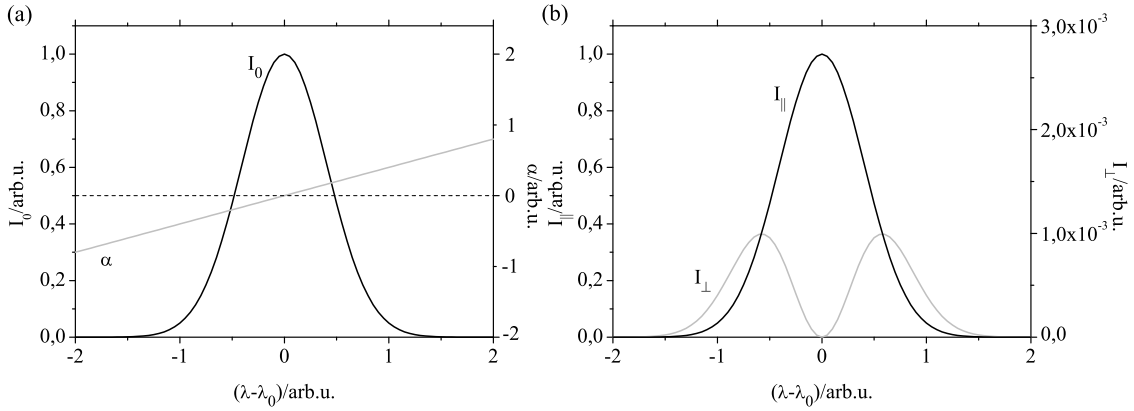

Figure 5.7: *Simulated effect of a spectrally broad pulse onto the polarization sensitive detection [25]. A Gaussian pulse with intensity I_0 and a phase shift approximated to be linear in $\lambda-\lambda_0$ (a) is detected through crossed ($I_\perp$) and parallel polarizers ($I_\parallel$) (b).*

red shifted wings of the Gaussian-shaped probe pulse were less compensated and a small fraction passed the analyzer.

The wavelength dependence is caused by the wavelength dependence of the accumulated phase shift $\alpha(\lambda)$ between extra ordinary and ordinary beam (Fig. 5.1), resulting from the low order quarter-wave plate $\lambda/4$, the strain induced birefringence in windows and lenses, and the birefringence of the sample itself. In a birefringent medium of length l and with indices of refraction n_o and n_{eo}, the accumulated phase shift between extra ordinary and ordinary beam is given by

$$\alpha(\lambda) = 2\pi l(n_{eo} - n_o)/\lambda - \alpha_{\lambda/4}(\lambda_0). \tag{5.3}$$

Here, $\alpha_{\lambda/4}(\lambda_0)$ denotes the phase shift that was introduced by the quarter-wave plate to compensate the ellipticity at the center wavelength of the laser (λ_0). Figure 5.7 shows the effect of such a phase shift, approximated to be linear in λ, onto the detection of a Gaussian pulse with intensity I_0 through crossed and parallel polarizers [25].

The electric field of the probe light, propagating along z and written as an electric field vector with two components that correspond to ordinary beam E_x and extraordinary beam

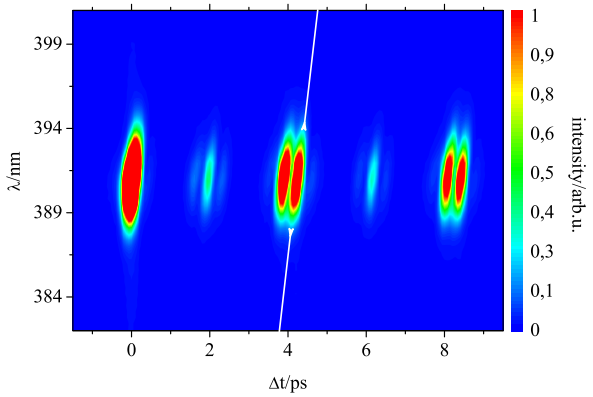

Figure 5.8: *Two dimensional false colour contour plot as recorded with our OKE setup. The sample was 1 atm gaseous nitrogen, kept at 87 K. The chirp of the probe light is clearly visible at $\Delta t = 0$ and in the alignment maxima at $\Delta t > 0$ (see Fig. 5.5). The white line is a guide to the eye.*

E_y, takes the form

$$\mathbf{E}_{probe} = \frac{1}{\sqrt{2}} E_{probe} \begin{pmatrix} \cos(\omega t - kz) \\ \cos(\omega t - kz + \alpha) \end{pmatrix}. \tag{5.4}$$

The local oscillator is given by the part of the beam that passes the analyzer, e.g. the projection onto the analyzer

$$E_{lo} = -E_{probe} \cos(\omega t - kz + \frac{\pi}{2} + \frac{\alpha}{2}) \sin(\frac{\alpha}{2}). \tag{5.5}$$

As intended, the local oscillator vanishes if there is no accumulated phase shift α, but already a small phase shift can induce a local oscillator field. The sign of this field is determined by α, which changes its sign corresponding to Eq. 5.3 from the blue shifted side to the red shifted side of the central wavelength λ_0. The local oscillator is shifted by $(\pi + \alpha)/2$ from the probe field, and we can assume $\alpha << \pi$ to be valid. Thus, it is dominantly an out of phase local oscillator, similar to one induced by a small detuning of the polarizer P2 (Eq. 4.41) that probes $Re\chi^{(3)}_{eff}(\Delta t)$, the sample birefringence. It can therefore mix with the signal field E_s, and leads to heterodyned signal components.

5.2 Test experiments with gaseous nitrogen

The rotational alignment of gaseous nitrogen was extensively studied in the thesis of Nina Owschimikow in the recent years by time resolved optical Kerr effect spectroscopy [25, 26, 73, 74]. Nitrogen is readily available, easy to handle and well understood. It is therefore an optimal sample for proof-of-principle experiments.

5.2.1 Homodyne detection of post-pulse nitrogen alignment

With our setup, we were able to record spectrally and time-resolved data sets. Therefore, two dimensional (wavelength and time delay) contour plots, like the one shown in Fig. 5.8, give a good overview over the spectra. They reveal, e.g., if different wavelengths exhibit different dynamics and also if the probe beam was chirped, as in Fig. 5.8. Hence, many of the spectra that will be shown in the following are such contour plots. They use a color

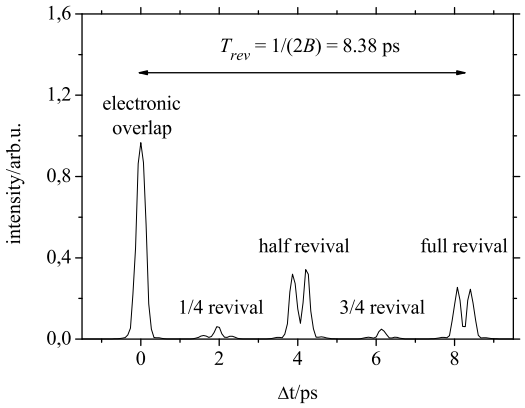

Figure 5.9: *Cut along the x-axis of Figure 5.8 at 391 nm, showing the revival structure of nitrogen.*

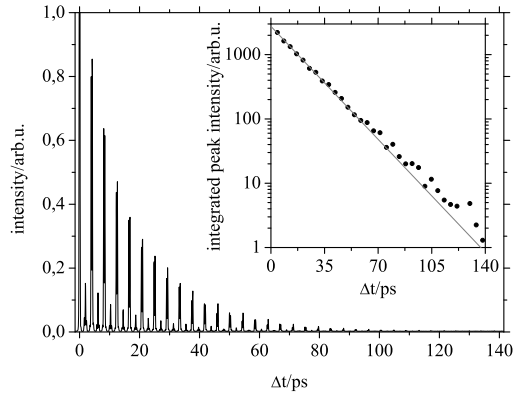

Figure 5.10: *Expanded scan of nitrogen, similar to the one shown in Fig. 5.8 and Fig. 5.9. The integrated revival intensity, traced over three orders of magnitude (see inlet), exhibits a mono-exponentional decay.*

code for the signal intensity, the x-axis for the time delay between pump and probe pulse, and the y-axis for the wavelength. The color code for the intensity is depicted on the right side of Fig. 5.8 and will not be shown in the following. Keep in mind that the central wavelength of the detected probe pulse is about 391 nm, usually positioned in the center of the wavelength scale. However, a quantitative discussion is more easily based on one dimensional spectra, i.e. cuts through a data set or integration over a certain delay or wavelength range. Such a cut through the spectra from Fig. 5.8 at a wavelength of 391 nm is shown in Fig. 5.9.

Fig. 5.8 and Fig. 5.9 show the post-pulse alignment dynamics of gaseous nitrogen in the first few picoseconds after the pump pulse. The spectrum was recorded in absence of a local oscillator, i.e. with crossed polarizer-analyzer geometry, in the so-called optically homodyned detection regime. This means that only the quadratic signal intensity $I_{hom}(t) = E_s(t)^* E_s(t)$ from Eq. 4.40 is present. Thus, a homodyned signal is always positive and does not allow to distinguish between alignment and anti-alignment. Upon a closer look, Fig. 5.9 exhibits a high signal intensity at $\Delta t = 0$. This results from the instantaneous polarization of the electrons, as was already discussed and utilized for the PG FROG in Fig. 5.5). After this electronic overlap, nitrogen shows a rich revival structure (alignment bursts), caused by the coherent rotational motion of the nuclei. There is no significant permanent alignment signal after $\Delta t = 0$, because the population part (Eq.

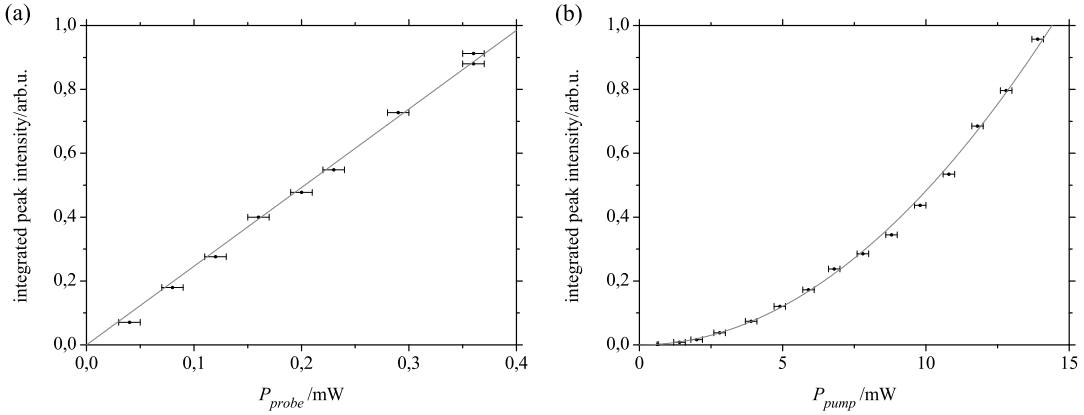

Figure 5.11: *Integrated intensity of the homodyne detected first half revival of 1 atm nitrogen at 87 K. (a) Plotted over the power of the probe beam P_{probe} (dots with error bars) and a linear fit (thin line). (b) Plotted over the power of the pump beam P_{pump} (dots with error bars) and a quadratic fit (thin line).*

4.17) is relatively small [73].

The revival structure decays over time, as it is shown in Fig. 5.10. The decay is caused by the mutual scattering of the nitrogen molecules. Collision between the molecules that occur at statistical distributed times lead to depopulation, depolarization or phase-randomization of the rotation, albeit the latter two play no role in this case [107]. Thus, the coherence is lost and the measured degree of alignment decays. According to Eq. 4.57, the decay is mono-exponentially with $\tau_{hom} = T_2/2$ for a specific transition. Since we observed an overall mono-exponentially behavior, we conclude that there is no significant J-dependence of the N_2-N_2 collision rates. A detailed analysis of this decay, including the cross sections for rotational decoherence for varying environments of nitrogen, is given in Ref. [26].

Figure 5.11 (a) depicts the probe power P_{probe} dependence of the homodyne detected signal intensity. The power was regulated with the half-wave-plate $\lambda/2_2$ and the polarizer P2 in the probe beam path of Fig. 5.2 and measured with a power meter (Coherent Inc., LaserMate-1). The signal is linear in $P_{probe} \propto E^2_{probe}$, as expected from Eq. 4.39 and Eq. 4.40. Analogue to Fig. 5.11 (a), Figure 5.11 (b) shows the pump power (P_{pump}) dependence of the homodyne detected signal. P_{pump} was regulated with the half-wave-plate $\lambda/2_1$ and the polarizer P1 in the pump beam path and also measured with a LaserMate-1 power meter. As expected from Eq. 4.39 and Eq. 4.40, the measured signal intensity depends on $P^2_{pump} \propto E^4_{pump}$.

The result of a variation of the sample's particle density, under otherwise unchanged conditions, is shown in Fig. 5.12. The signal field's strength $E_s(\chi^3)$ (Eq. 4.21) scales linearly with the number density of particles N, since the polarization that is induced in a medium of noninteracting particles is directly proportional to the density of dipoles. Hence, due to the quadratic dependency of the signal intensity on the signal field E_s (Eq. 4.40), the homodyne detected signal intensity depends quadratically on the sample pressure p. Furthermore, the increased pressure leads to a higher collision rate, i.e. to a faster decay of the alignment signal [26].

The signal strength strongly depends on the polarization of the pump beam. Figure 5.13 shows a sinusoidal dependency of the homodyned signal from the relative angle Θ between the probe polarization and the polarization of a linearly polarized pump beam. The signal vanishes for a parallel, and for a perpendicular orientation of the polarizations, because the pump-induced birefringence can only create a signal field, i.e. a probe light

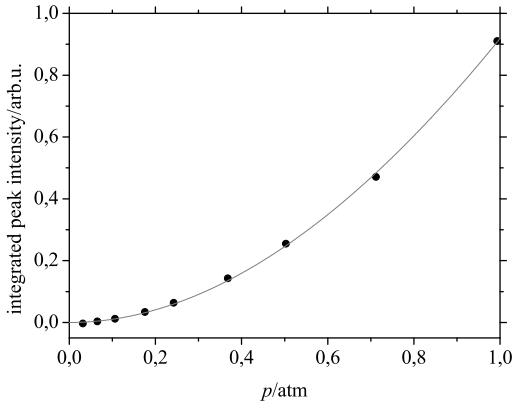

Figure 5.12: *The integrated intensity of the first half revival of nitrogen at 87 K, measured with $P_{pump} = 14.8\ mW$ and $P_{probe} = 0.08\ mW$, plotted over the pressure p of nitrogen in the sample cell (dots) and a quadratic fit (thin line), including a small correction for the varying decay times at different pressures according to Ref. [26].*

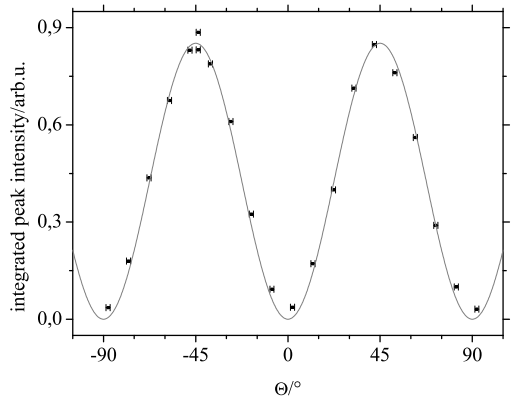

Figure 5.13: *The integrated intensity of the first half revival of 1 atm nitrogen at 87 K plotted over the relative angle Θ of the pump to the probe beam polarization (dots with error bars), fitted to $sin^2\Theta$ (thin line). The angle was controlled by the half-wave plate behind the polarizer P1 in the pump beam path.*

component parallel to the analyzer, if ordinary and extra ordinary probe beam component from Figure 4.3 are present. If both components of the probe field are of equal strength, the signal field becomes maximal ($\Theta = \pm 45°$). For an isotropic sample like gaseous nitrogen, it does not matter for the signal field strength, if the pump polarization is shifted by $+45°$ or $-45°$ from the probe polarization. However, the signal field will change its sign, because ordinary and extraordinary beam are exchanged. This sign becomes visible in a heterodyned detection scheme.

5.2.2 Introducing a local oscillator: heterodyne detection

A small rotation of the probe beam polarizer P2 by an angle ϵ leads to a leakage of the probe beam through the analyzer A. This leakage introduces an out-of-phase local oscillator field E_{lo} (Eq. 4.41) that mixes with the signal field E_s and creates the so-called heterodyne detected signal I_{het} (Eq. 4.44). A heterodyne detected 2D OKE contour plot is exemplified in Figure 5.14 (a). Figure 5.14 (b) (1)/(2) shows the total signal intensity I, detected in a heterodyned configuration with a local oscillator field of opposite/same sign, depending on the rotation of P2 ($\epsilon = +/- 1°$). The subtraction of Fig. 5.14 (b) (1) from Fig. 5.14

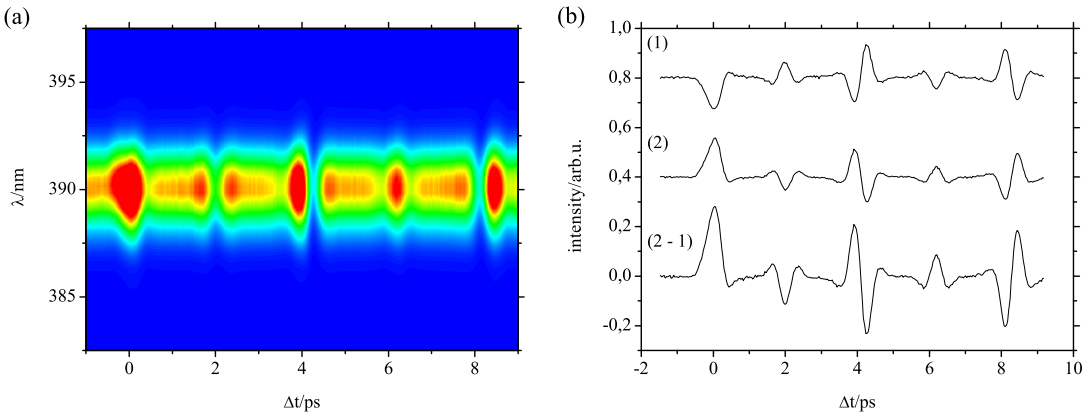

Figure 5.14: *(a) Heterodyne detected contour plot, recorded similar to the homodyne detected contour plot Fig. 5.8, but with a strong positive local oscillator. (b) (1) & (2) Heterodyne detected nitrogen signal traces with homodyned contributions, recorded with a strong (1) negative ($E_{lo} = -i\epsilon E_{probe}$) or (2) positive ($E_{lo} = +i\epsilon E_{probe}$) local oscillator E_{lo}. The pure heterodyned signal (2 -1), background free and without homodyned contribution, follows from the subtraction of (1) from (2).*

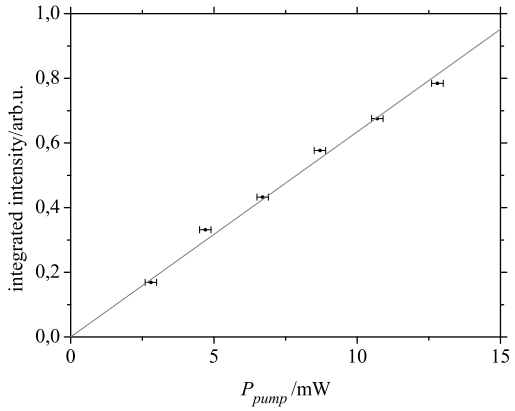

Figure 5.15: *Dependence of the heterodyned signal shown in Fig. 5.14 (b) (2 - 1) on the power of the pump beam P_{pump}.*

(b) (2) eliminates the always positive contributions of the homodyned signal I_{hom} and the pure local oscillator signal I_{lo} from the total signal intensity I. What is left is the pure heterodyned signal I_{het}, shown in Figure 5.14 (b) (2 - 1).

The heterodyned signal is always accompanied by a homodyned part, but it can dominate the time dependent part of the total signal, as it does in Figure 5.14 (b) (1)/(2). For the analysis of a signal, it is important to distinguish between homodyned and heterodyned signal contributions, since they show a significantly different behavior. In contrast to I_{hom}, I_{het} is linear in the signal field and the local oscillator field (Eq. 4.44). Thus, it is linear in p, P_{probe}, and P_{pump}, as is it shown in Fig 5.15. Furthermore, I_{het} exhibits different dynamics (see Figure 5.17) and decays half as fast as the homodyne detected signal ($\tau_{hom} = \tau_{het}/2 = T_2/2$) (see Eq.'s 4.55, 4.56, and 4.57).

The heterodyned detection offers many advantages. A weak signal field E_s can be enhanced by a local oscillator field E_{lo}. This can increase the signal to noise ratio. Additionally, the slower decay enables to follow the signal for a longer time, and the heterodyne detected signal I_{het} carries more information. E.g., it is possible to distinguish between

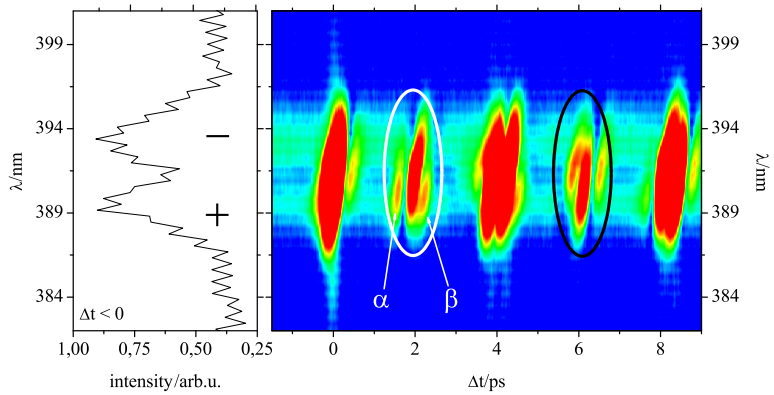

Figure 5.16: *The right panel is a contour plot as in Figure 5.8, but with a logarithmical color scale. It exhibits a small leakage through the analyzer at $\Delta t < 0$, shown in the left panel, that acts as a local oscillator. White and black circles in the contour plot indicate weak alignment bursts within the quarter revivals of nitrogen, which are efficiently heterodyned and show a pseudo wavelength dependence.*

alignment and anti-alignment of nitrogen, as is can be found in positive and negative signals in Figure 5.14 (b) (2 - 1).

To analyze the signal, the properties of the local oscillator E_{lo} have to be known, since the heterodyned intensity depends on the distribution and phase of E_s and E_{lo}. This is exemplified in Figure 5.16. The right panel shows nitrogen alignment dynamics, detected with a weak, but complicated local oscillator field E_{lo}. The left panel of Fig. 5.16 shows that the local oscillator intensity I_{lo} is wavelength dependent. It stems from a leakage through the analyzer due to the spectral broadness of the probe pulse, as described in Fig. 5.7. The local oscillator has a local minimum at 391 nm, the center line of the probe laser, and has maxima at 389 nm and 393 nm. These maxima, red- and blue shifted from the probe laser center line, act as local oscillator fields E_{lo}. E_{lo}(389 nm) and E_{lo}(393 nm) have opposite signs, similar to the local oscillator fields in Fig. 5.14 (b) (1) and (2). Since the local oscillator in Fig. 5.16 is weak, only weak signal fields are predominantly heterodyne detected. They occur, for example, in the weak alignment features α and β shortly before and after the nitrogen quarter revival at 2 ps (see Fig. 5.14 (b) (2 - 1)), marked with a white circle in Fig. 5.16. The heterodyning, i.e. the multiplication, of the positive local oscillator field E_{lo}(389 nm) with the positive signal field leads to a positive contribution, and we observe the two heterodyne detected maxima α and β around 389 nm. The sign change of the local oscillator at 393 nm leads to negative heterodyned contributions for the same alignment bursts superimposed on the homodyned contribution. Hence, the wavelength dependence of the sign of the local oscillator field $E_{lo}(\lambda)$ has created a wavelength dependence of the signal $I(\lambda)$ around 2 ps. The opposite case happens for a negative signal field, like in the weak features within the black circle in Fig. 5.16 around 6 ps. Here, E_s has a negative sign for the weak anti-alignment features shortly before and after the 3/4 revival (see Fig. 5.14 (b) (2 - 1)). In this case, heterodyning with the negative local oscillator around 393 nm leads to positive heterodyned contributions. Due to the changing sign of E_s, the spectral distribution of the dynamics in the black circle in Fig. 5.16 becomes a mirror image of the dynamics in the white circle. However, the wavelength dependence of the detected intensity occurs despite there is no corresponding wavelength dependence of the signal field. Hence, the spectral distribution of these features carries no information about the properties of the sample.

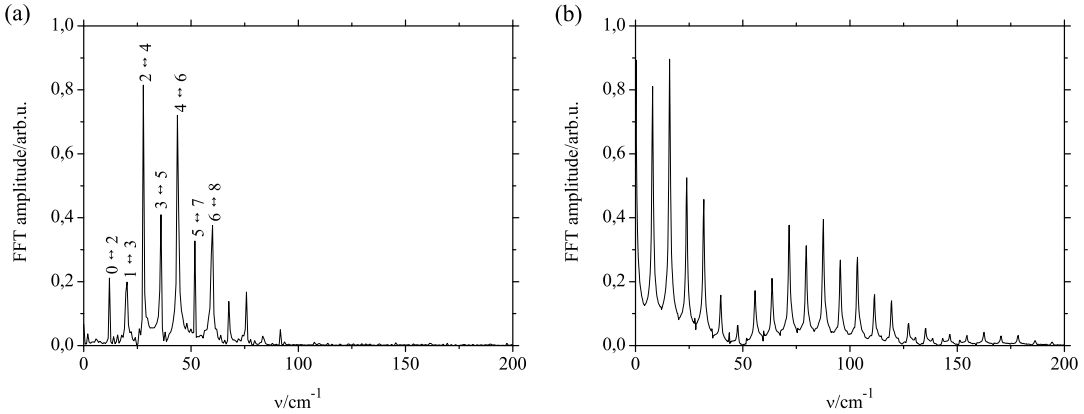

Figure 5.17: *Fast Fourier transform of a (a) heterodyned, and (b) homodyned OKE signal of nitrogen. The marks on the peaks of (a) indicate the corresponding transition $J' \longleftrightarrow J''$.*

5.2.3 Frequency analysis of the time resolved spectra

A convenient method of analyzing the time resolved OKE spectra is a fast Fourier transform (FFT), as shown for nitrogen in Figure 5.17. The FFT of the heterodyned signal, $I_{het} \propto E_s(\nu_1, \nu_2, \nu_3, ...)$ in Fig. 5.17 (a) contains all Raman allowed transition frequencies $\nu(J' \longleftrightarrow J'')$ within the rotational wavepacket. Following the Raman selection rules and Eq. 4.7, it consists of equidistant peaks with $\Delta\nu = 2B \approx 4$ cm^{-1}. The frequency distribution follows directly from the Boltzmann-distribution of the states and the pulse properties [25]. A time resolved heterodyned OKE signal delivers therefore data that are equivalent to the complementary, spectrally resolved rotational Raman spectra. The FFT of the homodyne detected OKE spectrum in Fig. 5.17 (b) is more complex. It contains all possible combinations $\nu_i \pm \nu_j$ of the Raman allowed transition frequencies within the wavepacket, because I_{hom} is proportional to $|E_s(\nu_1, \nu_2, \nu_3, ...)|^2$. The discrimination between heterodyned and homodyned signal becomes therefore the first step in the data analysis that we will carry out for hydrogen samples in the following two chapters.

6 2D OKE spectroscopy of para-hydrogen

"As far as I remember, I have not read or heard of an attempt in this field by any other naturalist. I proceed to offer a few notes of some recent experiments of my own. The investigation is not so complete as I should wish it to be; but it has been carried forward as far as my limited time and means would allow."

J. Kerr [80]

Before we started our 2D OKE experiments with solid para-hydrogen, we carried out a small test series of measurements in the gaseous and liquid phase. This proved to be useful in many aspects. Firstly, it was an additional possibility to test the 2D OKE setup on relatively simple samples. This was of special interest, because the large rotational constant of hydrogen compared to nitrogen, see Table 4.1, gave rise to spectral effects that were absent in nitrogen. Secondly, the direct comparison of gaseous, liquid and solid samples revealed the phase dependence of many effects. Thus, specific solid state contributions, like phonon excitations and crystal field splittings, could be identified. The first and the second section of this chapter summarize our experimental results for gaseous and liquid samples, respectively. In a joint approach, these results are discussed in the third section.

6.1 Gaseous para-hydrogen

Experiments with para-hydrogen in the gas phase were generally carried out at pressures of 900 mbar. The temperature was usually about 25 K, to increase the particle density and accordingly the signal (see Eq. 4.39 and Eq. 4.53). The applied laser powers were not limited by a low destruction threshold, as it was in the solid phase. Hence, we used the full available pump beam power of 15 mW to increase the signal strength. The probe beam power was also maximized, to 0.4 mW, in order to increase the signal to noise ratio. For the same reason, we intended to keep the local oscillator intensity as low as possible. This was necessary, because the observed signals were weaker than the minimal local oscillator strength that we achieved.

6.1.1 Qualitative overview

Figure 6.1 (a) shows a contour plot of a long time measurement with gaseous para-hydrogen. At first glance, there are no dynamics visible within the chosen timescale of 250 ps. Next to the electronic signal at the temporal overlap of pump and probe pulse, there is a dominant constant signal intensity. The constant signal is already present before $\Delta t = 0$, thus represents a probe beam leakage and acts as a local oscillator in a similar way as described for gaseous nitrogen (see Fig. 5.16). It has the typical shape as discussed in Fig. 5.7, with maxima at 390 nm and 393 nm (see Fig. 6.5). However, there is also a periodic response, which is presented in Figure 6.1 (b). It occurs in the outer wings of the local oscillator and is obviously relatively weak.

Figure 6.2 (a) is a 1 ps cut-out of a signal trace at 386 nm from a comparable sample as in Fig. 6.1, carried out with a high temporal resolution (3.3 fs stepwidth). The observed

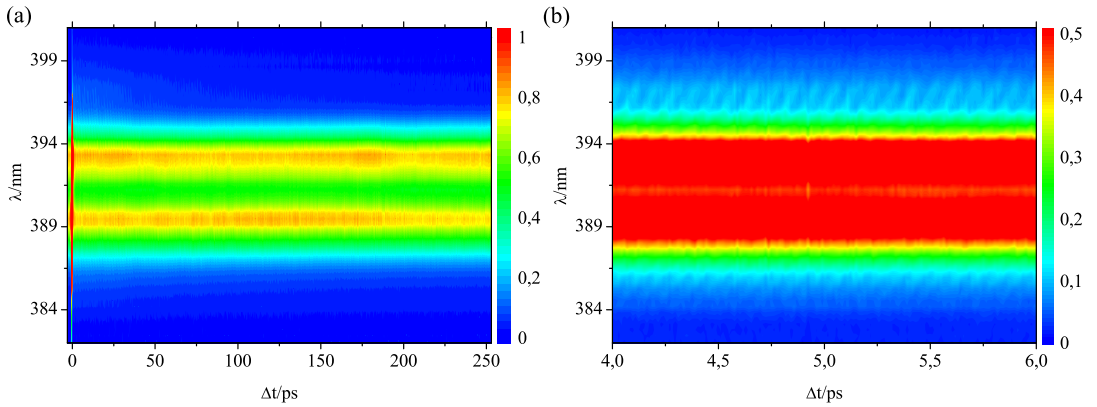

Figure 6.1: *(a) Long time measurement of 900 mbar gaseous para-hydrogen at 25 K. (b) Zoom into (a) with a changed color code for the intensity to increase the contrast at 386 nm and 397 nm. A periodic modulation, albeit with a very weak amplitude, is visible.*

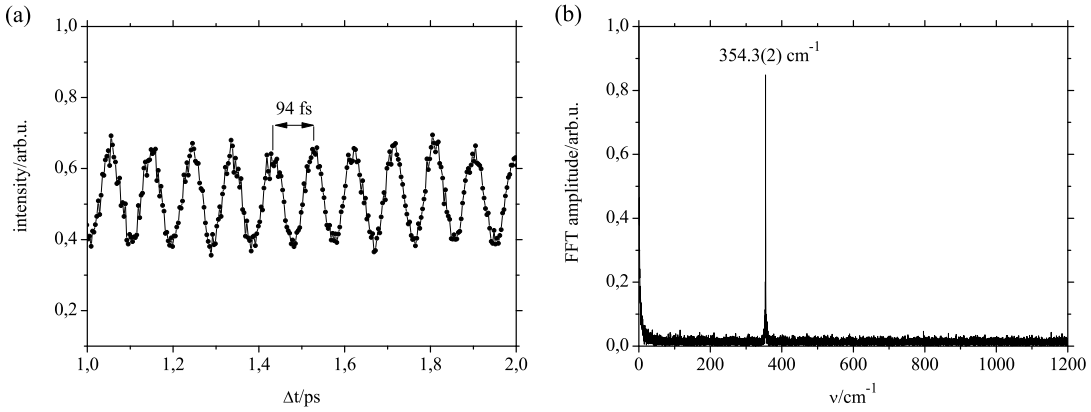

Figure 6.2: *(a) 1 ps cut-out of a signal trace at 386 nm of a high resolution scan, taken under similar conditions as the one in Fig. 6.1 (a). The single sinusoidal oscillation has a period of 94 fs. (b) Fast Fourier transform of a similar signal trace at 386 nm, taken from Fig. 6.1 (a). A single frequency, 354.3(2) cm^{-1}, is found.*

single sinusoidal oscillation has a period of about 94 fs. It is the sole periodic response that we observed in gaseous para-hydrogen. This follows also from fast Fourier transforms of the 2D OKE signal, carried out for signal traces at various wavelengths. Such a fast Fourier transform of a signal trace at 386 nm, taken from Fig. 6.1 (a), Figure 6.2 (b), contains only one, sharp frequency, 354.3(2) cm^{-1}. A second look onto Figure 6.2 (a) reveals that the sinusoidal oscillation is only a fraction of the detected signal. It is a twenty percent modulation of an otherwise unmodulated background. The main part of this background, as mentioned above, is already present before $\Delta t = 0$, and acts as a local oscillator I_{lo}. It is therefore reasonable to consider the detected periodic signal to be strongly heterodyned, similar to the heterodyned nitrogen signal in Fig. 5.14. A cut through the contour plot Fig. 6.1 (a) at a certain wavelength, as shown below in Fig. 6.4, reveals that the observed modulation decays monoexponentially. Additionally, a fraction of the unmodulated background also exhibits a time dependence and decays monoexponentially, too. Thus, it does not stem from the local oscillator intensity alone, which is time independent.

Figure 6.3 contains several traces from a high resolution measurement. As one can see,

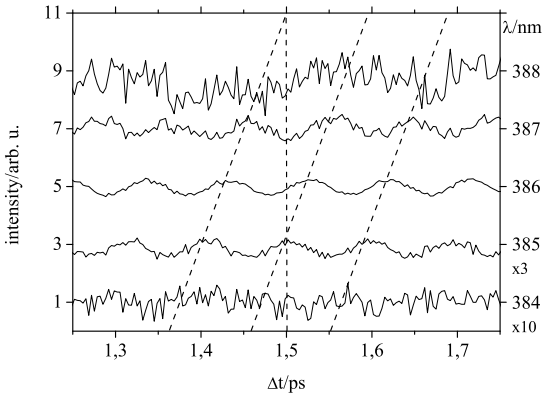

Figure 6.3: *Several traces at wavelengths between 384 nm and 388 nm, taken from the same high resolution scan as in Fig. 6.2 (a). The dashed lines are a guide to the eye. The 94 fs signal modulation exhibits a highly wavelength dependent phase.*

the amplitude of the observed 94 fs single sinusoidal oscillation varies for different wavelengths. Additionally, its phase is wavelength dependent, too. The wavelength dependence of the signal phase is equal to the chirp of the probe beam, which had predominantly a negative linear chirp, albeit with nonlinear contributions (see Fig. 5.5).

6.1.2 Quantitative analysis

As shown above, the detected intensity is an exponentially damped, single sinusoidal oscillation on an unmodulated background intensity that contains an exponentially decaying and a constant contribution. The constant part of this background, although it is itself time independent and carries no information, acts as a local oscillator that interferes with the signal field according to Equation 4.40. Thus, there are three signal contributions, the heterodyned and the homodyned signal intensity, and the local oscillator intensity. As a matter of course, the strength of time resolved spectroscopy lies in the direct observation of the time evolution of induced coherences. However, both, the temporal and the spectral structure of the 2D OKE signal, contain information and will be discussed quantitatively in the following.

6.1.2.1 Analysis of the time resolved signal

A quantitative analysis of the time resolved signal was done by fitting traces of time dependent OKE signals at selected wavelengths to the signal field $E_s(\Delta t)$ and the local oscillator field E_{lo}. To find a suitable fit function, we have to consider the origin of the detected signal. The time dependence of the signal stems from the temporal evolution of coherences, induced into the sample by the pump pulse. The amplitude of the signal field $E_s(\Delta t)$ follows this temporal evolution. In the most simple case of a two level system, the pump pulse creates a wavepacket that oscillates with the transition frequency $\hbar\omega_s = E_2 - E_1$, and decays with the dephasing time T_2 (see Eq. 4.57). Thus, the signal field is modulated by a sinusoidal oscillation, and is exponentially damped, $E_s(\Delta t) = E_s(0)\sin(\omega_s \Delta t + \phi)e^{-\Delta t/T_2}$. In presence of a local oscillator field E_{lo}, the signal intensity $I(\Delta t)$ follows from Equation 4.40. It includes the homodyned, the heterodyned, and the local oscillator intensity. The signal of a two level system is therefore given by

$$I(\Delta t) = E_s^2(0)\sin^2(\omega_s \Delta t + \phi)e^{-2\Delta t/T_2} + 2E_{lo}E_s(0)\sin(\omega_s \Delta t + \phi)e^{-\Delta t/T_2} + E_{lo}^2. \quad (6.1)$$

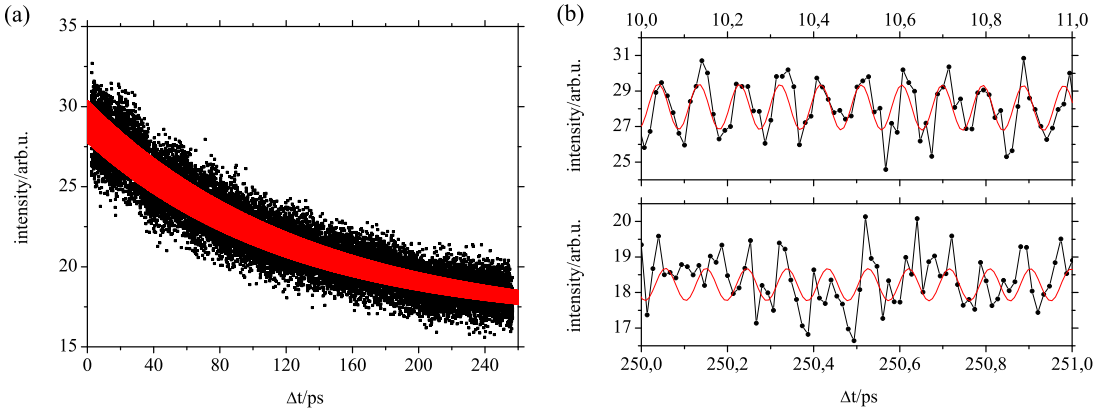

Figure 6.4: *(a) Signal trace at 386 nm of the contour plot shown in Fig. 6.1 (a) and fit following Eq. 6.2 (red line). The heterodyned signal contribution oscillates with a frequency of 354.40(2) cm^{-1}. The decay time of the signal field is $T_2 = 255(3)$ ps. The dampening of the heterodyned signal is $d = 0.03$. (b) Zoom into (a) at 3 ps (upper panel) and 250 ps (lower panel).*

As we will see, we have good reasons to assume that we deal with such a two level system in the case of gaseous para-hydrogen. A heterodyne detected signal should, following Eq. 6.1, contain two frequencies, ω_s and $2\omega_s$. The origin of the $2\omega_s$ contribution is the sin^2 modulation of the homodyned signal term, which gives also rise to an unmodulated signal contribution.

However, we found only one frequency in the fast Fourier transform, $\omega_s/2\pi = 354.3(2)$ cm^{-1}. The reason for this is that Eq. 6.1 is only valid, if the observed dynamics are slow compared to the probe pulse duration. In the present case, we have to consider that the pulse duration of the probe beam, $\Delta t_{probe} = 130$ fs, is long compared to the observed dynamics of 94 fs. Following Eq. 4.51 and 4.52, this directly affect the signal. The heterodyne detected intensity follows from a convolution of the material response onto the pump pulse with the probe pulse, the homodyned intensity from a convolution of the squared material response onto the pump pulse with the probe pulse [27]. For a sinusoidal response, a long probe pulse leads to an averaging of the detected signal. Considering this, a suitable function to describe the OKE signal of a two level system is given by

$$I(\Delta t) = 0.5E_s^2(0)e^{-2\Delta t/T_2} + d2E_{lo}E_s(0)\sin(\omega_s\Delta t + \phi)e^{-\Delta t/T_2} + E_{lo}^2. \qquad (6.2)$$

The described temporal averaging is considered by a damping factor d for the amplitude of the sinusoidal heterodyned signal. The homodyned signal oscillates even twice as fast as the heterodyned signal. Thus, it cannot be resolved with a probe pulse duration of $\Delta t_{probe} = 130$ fs. Instead, its sin^2 modulation is averaged out and yields a constant factor of 0.5.

The result of a fit procedure with Eq. 6.2 is shown in Figure 6.4 (a). The fitted signal trace at 386 nm was taken from Fig. 6.1 (a). We chose the 386 nm trace, because it exhibited a high signal field (see 6.5 (b)) and had the smallest long time fluctuations of the local oscillator. Derived for the signal of a two level system and a long probe pulse duration, Eq. 6.2 describes the measured signal very well. Two close ups in Figure 6.4 (b) exemplify the quality of the fit regarding the heterodyned signal contribution. There is a small phase lag between the fit and the signal trace, which is of the same magnitude as the accuracy of the delay stage. This effect is also clearly visible in the residual of the fit, which exhibits a 94 fs oscillation at smaller delay times that vanishes towards the center

region of the fit. The heterodyned signal is heavily damped, with $d = 0.03$, and therefore close to the noise level. Nevertheless, we could follow the coherent response for several thousand periods and determine the oscillation frequency with high accuracy, 354.40(2) cm^{-1}. The given error is the numerical standard error of the shown fit. It is comparable to the accuracy of the stage, 1 μm per 25 mm, which corresponds to 0.014 cm^{-1}. To compensate for the delay stage inaccuracy, we carried out a fit in which we used a second and third order correction term in Δt. This slightly improved the fit residual, but yielded identical results with identical numerical errors.

The decay time, fitted simultaneously from homodyned and heterodyned signal following Eq. 6.2, is $T_2 = 250(3)$ ps. Fitted separately from the homodyned and the heterodyned signal, similar results for the decay time were obtained, $2\tau_{hom} = T_2 = 255(3)$ ps, respectively $\tau_{het} = T_2 = 234(9)$ ps. The slightly faster and less accurate decay of the heterodyned signal is caused by the poor signal to noise ratio at larger delay times and the mentioned inaccuracy of the delay stage, causing a systematically faster decay of the fit. Thus, of the three presented dephasing times, $2\tau_{hom} = T_2 = 255(3)$ ps is the best value, because it lacks this systematic error. Unfortunately, we observed short time (5-10 ps) instabilities and long time (> 50 ps) drifts in the local oscillator intensity of about five percent. These drifts were clearly visible at traces with lower signal field to local oscillator field ratios, e.g. at 388 nm. Such fluctuations of the local oscillator are not included in Eq. 6.2. For some signal traces, they made a reasonable fit of the heterodyned signal impossible and led to significantly varying decay times of the homodyned signal. However, they also led to a nonexponential behavior of the detected signal, and were therefore clearly discernible. The single exponential decay, and the good agreement between τ_{het} and $2\tau_{hom}$ indicate that the influence of local oscillator drifts is small in the presented data. Nevertheless, the given standard error of the fit, 3 ps, does not account for the instable local oscillator. Other error sources, as temperature variations of the sample, laser instabilities, and possible drifts in the spatial overlap of pump and probe beam, caused by the delay stage, are also not included in the given error. However, we consider these errors to be small compared to the determined dephasing time, since the temperature was constantly monitored, the local oscillator fluctuations of less than five percent indicate that the laser was stable, and the delay stage was carefully adjusted over a four times longer delay than the actually used one.

6.1.2.2 Analysis of the spectral distribution

From the fast Fourier transforms of our gaseous hydrogen data, we know that we observed only one frequency. As we have already discussed (see Fig. 4.5), this frequency must belong to a Raman-active transition. However, the transition frequency of about $\Delta\nu =$ 354.40(2) cm^{-1} is of the same order of magnitude as the bandwidth of the probe pulse. Since the origin of the signal field E_s is Raman scattering of the probe light, it should be well separated from the probe laser line. Hence, Raman scattered from the Gaussian shaped probe laser, two Gaussian peaks of the same spectral width as the probe laser field should appear in the spectrum of $E_s(\nu)$ (see Eq. 4.63). One should be red-shifted by 354.4 cm^{-1}, corresponding to Stokes scattering, and the other blue-shifted by 354.4 cm^{-1}, corresponding to anti-Stokes scattering processes (see Fig. 4.5).

Figure 6.5 reveals the detected intensity distribution of the heterodyned signal contribution $I_{het}(\lambda)$ (solid line) and the local oscillator $I_{lo}(\lambda)$ (dashed line). $I_{het}(\lambda)$ was obtained from fast Fourier transforms, carried out separately for each wavelength, taking the amplitude of the FFT at 354.4 cm^{-1} as a measure for I_{het}. It exhibits a complex spectral structure. The heterodyned signal is zero at the center line of the probe laser at 391 nm,

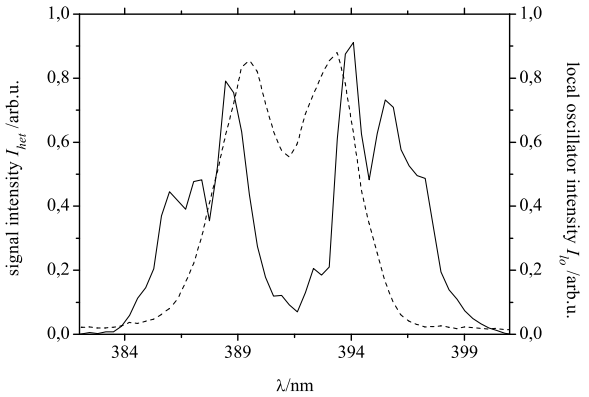

Figure 6.5: *Spectral distribution of the heterodyne detected signal intensity I_{het} of gaseous para-hydrogen from Fig. 6.1, determined from the amplitude of fast Fourier transforms (solid line). The mean 2D OKE signal at $\Delta t < 0$ is taken as a measure for the local oscillator intensity I_{lo} (dashed line).*

and it is maximal in the outer wings of the local oscillator, in agreement with Eq. 4.64 and Eq. 4.65. Following Eq. 4.40, the heterodyne signal stems from the product of local oscillator field E_{lo} and signal field E_s. Thus, the signal field distribution $E_s(\lambda)$ can be determined by

$$E_s(\lambda) = \frac{I_{het}(\lambda)}{2\sqrt{I_{lo}(\lambda)}}. \tag{6.3}$$

$I_{lo}(\lambda)$ was determined from the signal before $\Delta t = 0$, as the mean intensity in the interval -3 ps $< \Delta t < -2$ ps. It has the typical shape that was discussed in Fig. 5.7.

Figure 6.6 compares the homodyne detected intensity $I_{hom}(\lambda)$ and the heterodyned detected field $E_{s\,het}(\lambda)$ with their expected spectral distributions. $I_{hom}(\lambda)$ in Fig. 6.6 (a) was obtained from the subtraction of $I_{lo}(\lambda)$ from the mean intensity in the interval 4 ps $< \Delta t <$ 5 ps of the data shown in Fig. 6.1. $E_{s\,het}(\lambda)$ in Fig. 6.6 (b) follows from I_{het} and I_{lo} depicted in Fig. 6.5 with Eq. 6.3. The expected distributions follow from the spectral width and position of the probe pulse, determined at the electronic overlap, and the Raman-shift of 354.4 cm^{-1}. As predicted, $I_{hom}(\lambda)$ and $E_{s\,het}(\lambda)$ have maxima at 397 nm and 386 nm, which correspond to Stokes and anti-Stokes Raman transitions.

Considering $I_{hom}(\lambda)$, not only the peak positions, but also the linewidth of the peaks fits very well to our assumptions. There are only small deviations from the expected distribution, particularly the negative values of $I_{hom}(\lambda)$. They occur in the region of high local oscillator intensity and are caused by an instable local oscillator, which exhibits fluctuations of about five percent. Indeed, the fluctuations in the center of $I_{hom}(\lambda)$ do not exceed three percent of the local oscillator intensity. For a quantitative analysis, we neglected the region with high local oscillator (388 - 394 nm) and fitted the distribution with two Gaussians, shown as gray line in Fig. 6.7. The difference energy between the two peaks is $2 \times \Delta\nu = 2 \times 354(5)$ cm^{-1}, in agreement with our analysis of the time resolved signal.

The spectral distribution of the heterodyned detected field is more complicated to obtain, because Eq. 6.3 contains a division by the local oscillator field. For a vanishing local oscillator, this becomes a division by zero. Additionally, Eq. 6.3 is only valid if the real out-of-phase local oscillator is known and can interfere with the signal field. Hence, especially for low local oscillator intensity, signal noise and scattering background become severe problems. Nevertheless, the two main peaks of $E_{s\,het}(\lambda)$ can be found at 397 nm and 386

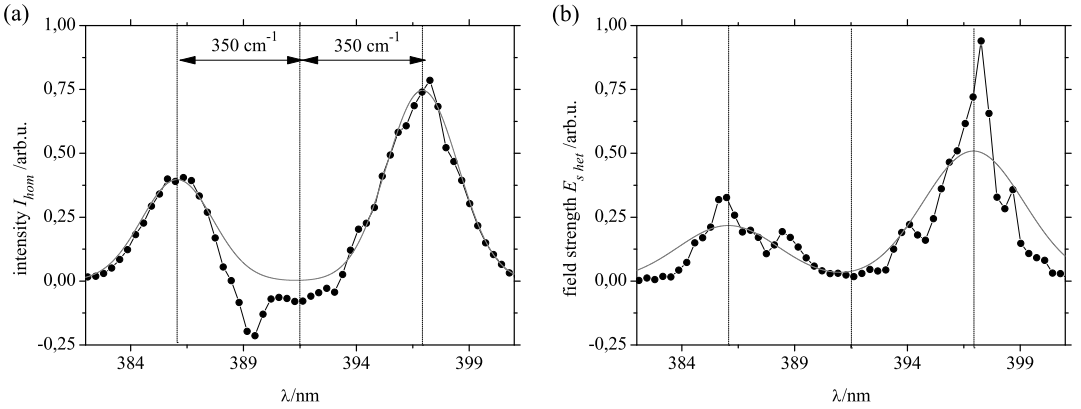

Figure 6.6: *Spectral distributions (connected dots) of (a) the homodyne detected intensity I_{hom} and (b) the heterodyne detected signal field strength $E_{s\,het} = I_{het}/2\sqrt{I_{lo}}$ in Fig. 6.1. The expected distributions (gray lines) are shown by two Gaussian peaks of the same width as the probe pulse intensity (a), respectively field (b). They are red- and blue-shifted by 354.4 cm^{-1} from the central probe laser wavelength, corresponding to Stokes- and anti-Stokes-Raman processes.*

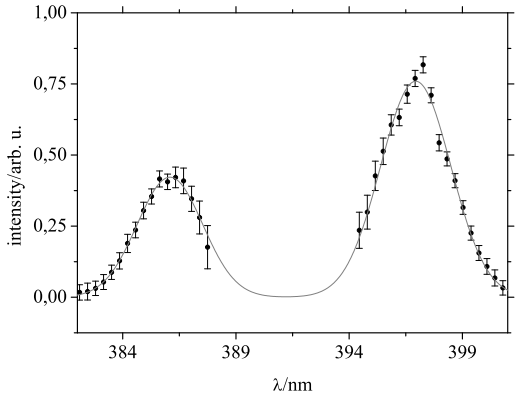

Figure 6.7: *Spectral distribution of the homodyned intensity I_{hom} (dots with error bars) as in Fig. 6.6, but without the center region to overcome the local oscillator fluctuation. The distribution is fitted by two Gaussian peaks (gray line), corresponding to Stokes- and anti-Stokes-Raman sidebands. The difference energy of the bands is $2 \times \Delta\nu = 2 \times 354(5)$ cm^{-1}.*

nm, consistent with our prediction. However, their width is much narrower than expected. Next to the main maxima at 386 nm and 397 nm in Fig. 6.6 (b), there are also minor maxima of $E_{s\,het}(\lambda)$, e.g. at 388.5 nm and 394 nm. Again, these maxima are significantly narrower than the probe laser field. In contrast to this, such maxima are absent in the homodyned intensity. The small shoulder in $I_{hom}(\lambda)$ at 394 nm is rather caused by the discussed local oscillator fluctuations. This discrepancy between the observed heterodyned signal field $E_{s\,het}(\lambda)$ and the expected distribution of the signal field $E_s(\lambda)$ is partially caused by the wavelength dependence of the signal field's phase (see Fig. 6.3), and will be discussed in Section 6.3.0.5.

6.2 Liquid para-hydrogen

Experiments with liquid para-hydrogen were usually carried out at 15 K to 17 K and zero pressure. The laser power was 1 mW to 4 mW for the pump beam, and 0.05 mW for the

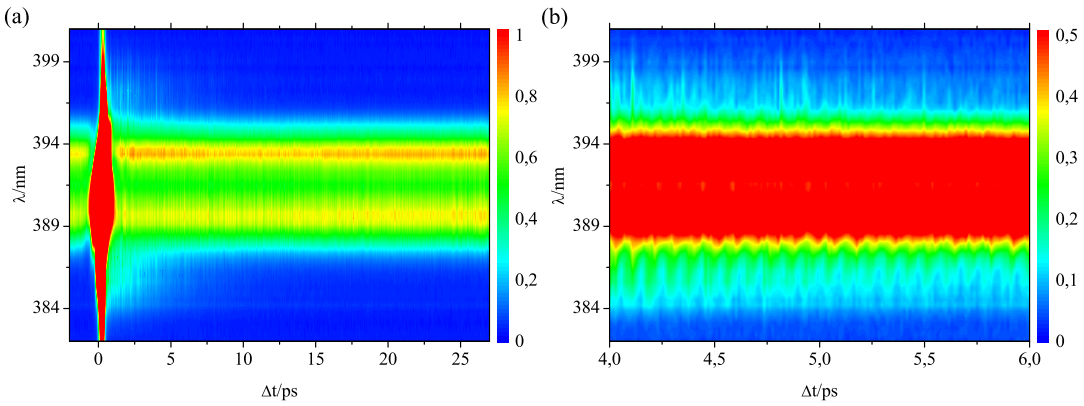

Figure 6.8: *(a) Measurement of a zero pressure liquid para-hydrogen sample kept at 16 K. (b) Zoom into (a) with a changed color code for the intensity to increase the contrast in the region around 386 nm. As in gaseous para-hydrogen, a periodic modulation is visible, albeit with increased amplitude.*

probe beam. Higher pump beam powers P_{pump} could not be applied, because they lead to white light, supercontinuum generation. As for gaseous para-hydrogen, we intended to keep the local oscillator intensity as low as possible. However, this proved to be complicated for higher probe beam powers P_{probe}. Increased probe beam powers yielded indications for the formation of pump laser independent Raman sidebands in the dense liquid. As we have seen in Fig. 5.7, we had to optimize our polarization optics for a certain wavelength in order to minimize the local oscillator. Hence, to extinguish spectrally shifted sidebands was difficult. Therefore, we relied on lower probe powers than in the gas phase.

6.2.1 Qualitative overview

The result of a typical measurement is shown in Figure 6.8. The local oscillator is visible at $\Delta t < 0$ in Fig. 6.8 (a). It has the typical spectral shape and exhibits maxima at about 390 nm and 393 nm. After the electronic overlap at $\Delta t = 0$, there is clear periodic modulation of the signal. This periodic response, shown in Fig. 6.8 (b), is similar to the one found in gaseous para-hydrogen (see Fig. 6.1 (b)). Despite the decreased pump power, the larger density in the condensed phase yielded higher signal intensities than in the gas phase.

Figure 6.9 (a) shows a high resolution 1 ps cut-out of a signal trace at 393 nm. The observed signal is very similar to the one in the gas phase, shown in Fig. 6.2 (a). It is a single sinusoidal, thirty percent modulation with a period of 94 fs, based on a background intensity. Again, the major fraction of the background is already present before $\Delta t = 0$ and acts as a local oscillator that heterodynes with the signal field. The fast Fourier transform of a comparable signal trace, albeit taken from a longer scan with lower resolution, is shown in Figure 6.9 (b). Complementary to the observed single sinusoidal oscillation, it exhibits a sharp, single frequency of 355(4) cm^{-1}. A full signal trace at 386 nm through the contour plot Fig. 6.8 (a) is presented in Figure 6.13 (a). As in the gas phase, the amplitude of the observed modulation decays monoexponentially, albeit at a much faster rate. The same is true for the fraction of the background that does not belong to the local oscillator intensity.

Figure 6.10 (a) is a contour plot of the high resolution measurement that was already shown in Fig. 6.9 (a). It has a rich spectral structure, caused by the spectral and temporal structure of the signal field and the local oscillator field. Figure 6.10 (b) contains several traces through this contour plot at different wavelengths. As one can see, not only the

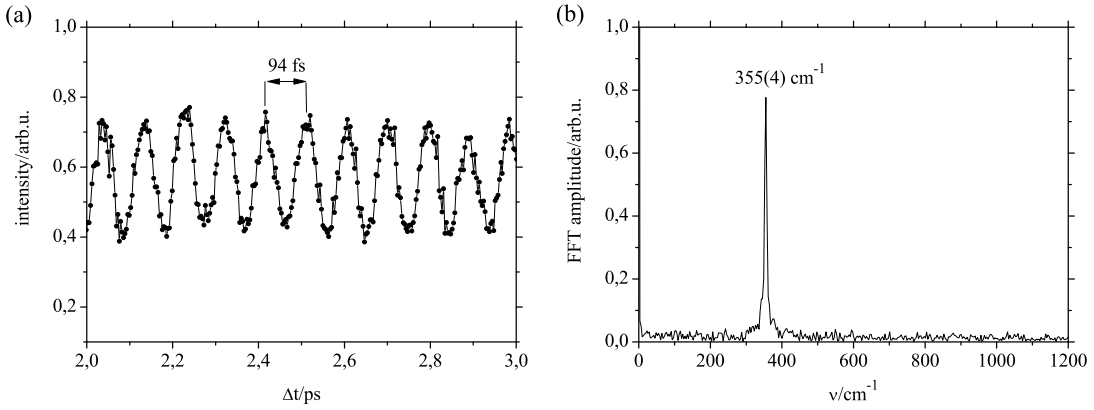

Figure 6.9: *(a) 1 ps cut-out of a signal trace at 393 nm of a high resolution scan. The single sinusoidal oscillation has a period of 94 fs. (b) Fast Fourier transform of a signal trace at 393 nm, taken from a similar data set. It exhibits a single frequency, 355(4) cm^{-1}.*

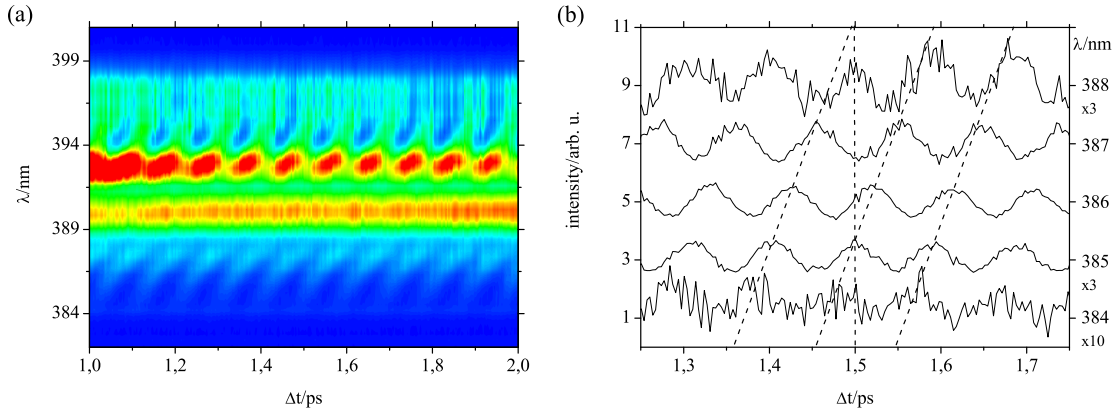

Figure 6.10: *(a) Contour plot of the high resolution scan shown in Fig. 6.9 (a). (b) Several traces through (a) at wavelengths between 384 nm and 388 nm. The 94 fs signal modulation exhibits a highly wavelength dependent phase. The dashed lines are a guide to the eye.*

amplitude of the observed 94 fs single sinusoidal oscillation is wavelength dependent, but also its phase. It is the same effect that was already observed in Fig. 6.3 for gaseous para-hydrogen.

6.2.1.1 Higher order Raman effects

The signals in liquid para-hydrogen were strongly dependent on the properties of the pump and probe pulse. The variation of the signal on the pump power and polarization is surprisingly strong. Figure 6.11 exemplifies the dependence of the detected signal on the pump power. Here, two scans, Figure 6.11 (a) and (b), were carried out with a factor of 1.5 higher pump power in (b) under otherwise identical conditions. As expected, they have same local oscillator structure at $\Delta t < 0$. The intensity of the mainly homodyned detected electronic overlap goes with I^2_{pump}, following Eq. 4.39 and Eq. 4.40, and rises by about a factor of two. However, there are significantly stronger, homodyne detected Stokes- and anti-Stokes shifted signals after the electronic overlap in Fig. 6.11 (b). Compared to Fig. 6.11 (a), they increase by one order of magnitude, which is much higher than the increase of the electronic overlap. Hence, there is a strong nonlinear response onto the pump power

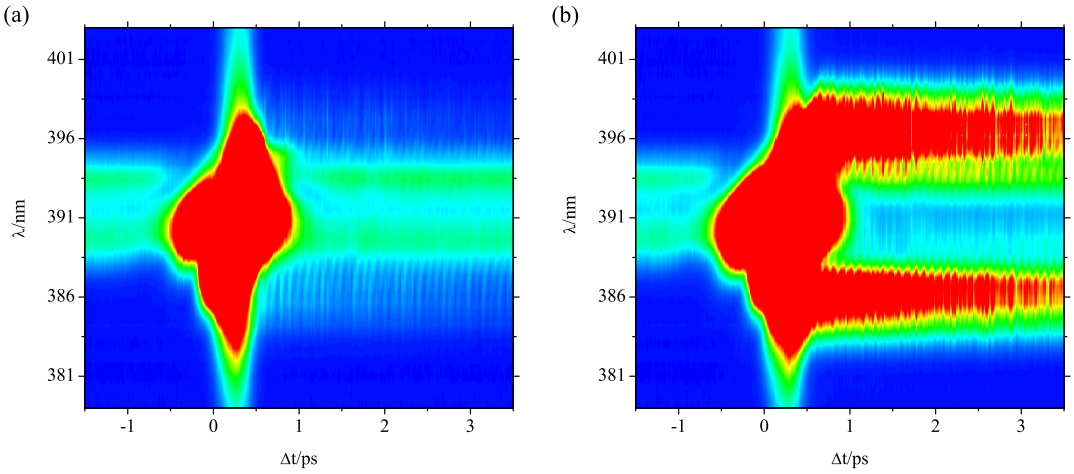

Figure 6.11: *Two measurements in liquid para-hydrogen at 16 K. The pump beam power of the order of 1 mW was increased from (a) to (b) by about fifty percent, under otherwise identical conditions. Both plots exhibit a distinct heterodyned response with a period of about 94 fs in the seam of the local oscillator at 388 nm. However, (b) has by a factor of ten stronger, homodyned detected Raman sidebands at 386 nm and 397 nm.*

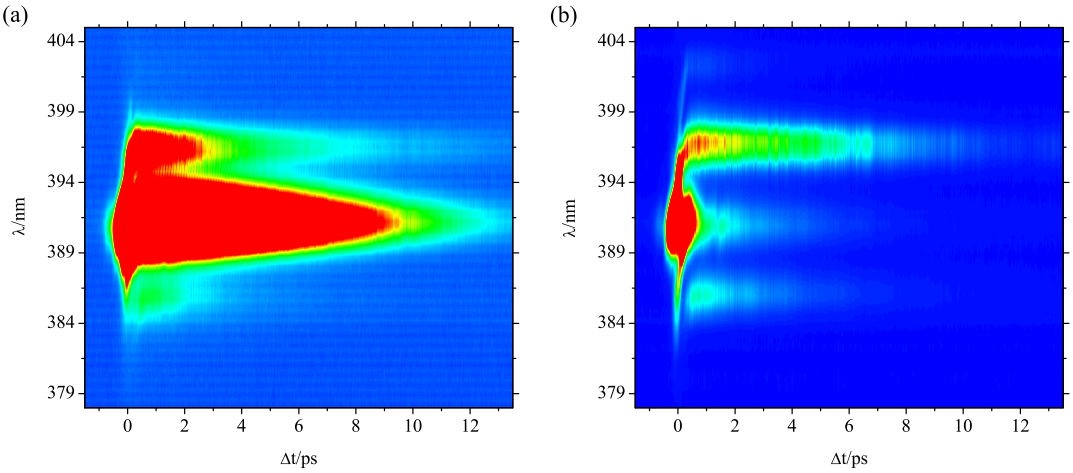

Figure 6.12: *Two measurements in liquid para-hydrogen at 14 K, measured with $P_{pump} = 4$ mW and $P_{probe} = 0.05$ mW. Next to the signal bands at 386 nm and 397 nm, there is a strong response at the center wavelength of the probe pulse at 391 nm in (a). Under otherwise identical conditions, the polarization of the pump beam was turned by 15 degrees between (a) and (b). Not visible here, but shown in Fig. 6.17, is a weak sideband at 402 nm, which is only present in (b).*

for the observed signal. As we will discuss in context with solid para-hydrogen, the origin of this behavior is the exponential amplification of the pump process by stimulated Raman scattering.

The contour plots Fig. 6.12 (a) and Fig. 6.12 (b) were recorded with even higher pump power of 4 mW. Additionally to the signal bands at 386 nm 397 nm, which where already found at lower pump powers, signal bands at 391 nm and 402 nm appear (see Fig. 6.17). As we have seen for gaseous nitrogen, the signal strength depends on the pump power and the pump polarization. However, not only the absolute intensities of the signal bands

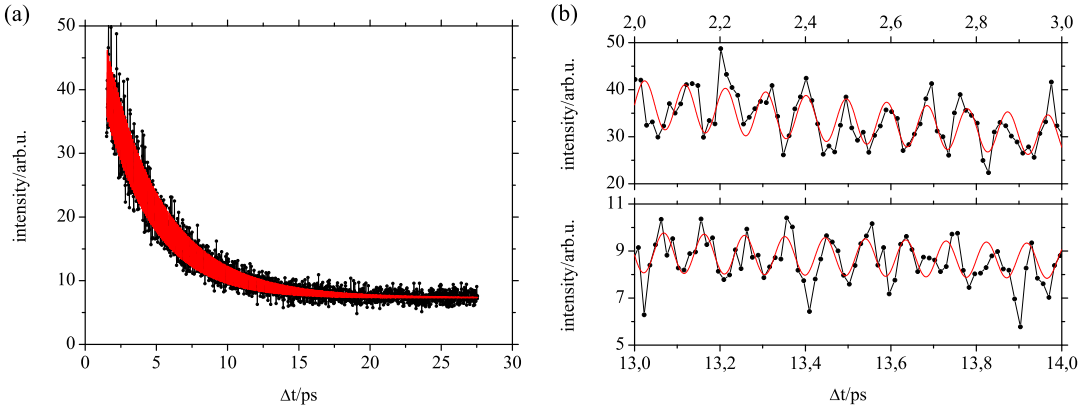

Figure 6.13: *(a) Signal trace from Fig. 6.8 at 386 nm and fit following Eq. 6.2 (red line). The heterodyned signal contribution oscillates with a frequency of 353.4(1) cm^{-1}. The decay time of the signal field is $T_2 = 7.5(1)$ ps. The dampening of the heterodyned signal is $d = 0.13$. (b) Zoom into (a) at 2 ps (upper panel) and 13 ps (lower panel).*

in Fig. 6.12 are pump polarization dependent, but also their relative intensities. In the depicted example, the pump polarization was turned by 15 degrees from Fig. 6.12 (a) to Fig. 6.12 (b). Upon this, the intense response at 391 nm vanished, whereas a weak response at 402 nm appeared (see Figure 6.17).

6.2.2 Quantitative analysis

Our observations in the liquid were in many aspects very similar to the gas phase. We observed a 94 fs modulation that decays exponentially and an unmodulated background. The latter consisted of an exponentially decaying and a constant part. Again, we can identify the three signal contributions as the heterodyne detected, the homodyne detected, and the local oscillator intensity. Hence, we carried out a quantitative analysis that was analogous to the gas phase.

6.2.2.1 Analysis of the time resolved signal

As in the gas phase, the fitting of the time resolved signal for a certain wavelength was carried out by applying Eq. 6.2. For the signal trace from Fig. 6.13 (a) we obtained an oscillation frequency of 353.4(1) cm^{-1} for the heterodyned signal component. Compared to the gas phase, the much faster signal decay led to a larger uncertainty in the oscillation frequency of the heterodyned signal. The decay time of the signal is $T_2 = 7.5(1)$ ps. Decay times, fitted separately from the homodyned and the heterodyned signal, are similar, $2\tau_{hom} = T_2 = 7.6(1)$ ps, respectively $\tau_{het} = T_2 = 7.2(3)$ ps. The given errors are the numerical standard errors of the fits and the same additional error sources apply as for the gas phase fit. The slightly faster decay and larger uncertainty in the decay time of the heterodyne detected intensity is caused by the relatively poor signal to noise ratio for larger delays, as can be seen in Figure 6.13 (b). The same results for T_2 as for the 386 nm trace were found for the complete anti-Stokes sideband (383 nm - 388 nm) and the complete Stokes sideband (395 nm - 400 nm).

The presented data are the best ones from a small series of liquid hydrogen experiments. All yielded comparable results for the modulation frequency and the decay time, even if carried out under different experimental conditions. This is very satisfying, particularly in the light of the observed nonlinear pump power dependence. Figure 6.14 shows that the

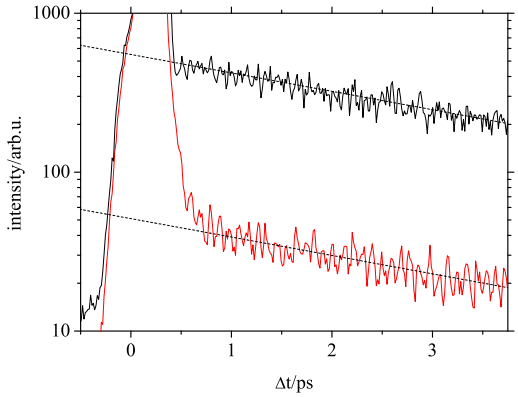

Figure 6.14: *Two signal traces at 386 nm taken from Fig. 6.11 (a) (red line) and Fig. 6.11 (b) (black line). The local oscillator background was subtracted to compare the decay of the two traces in a logarithmic plot. The two dashed lines have the same slope, which corresponds to a decay time* $2\tau_{hom} = 7.5$ *ps. Both traces were recorded at different pump powers and their homodyned signal intensities differ by one order of magnitude, but show the same decay behavior.*

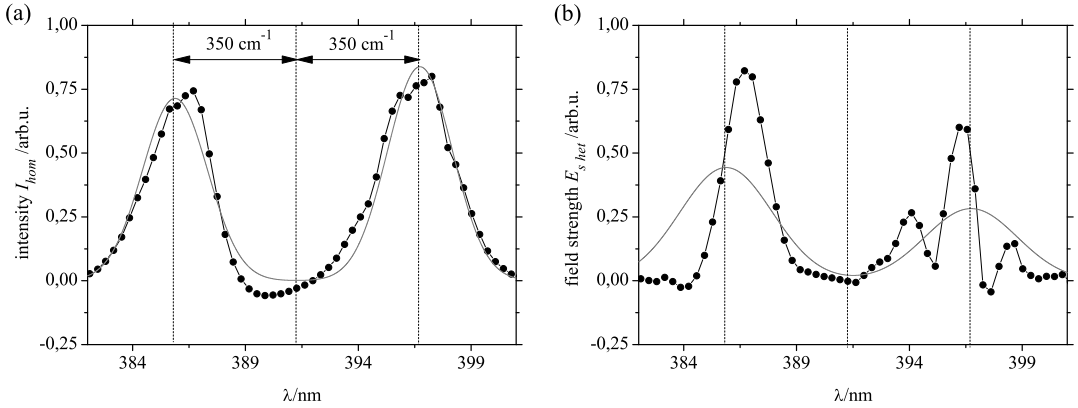

Figure 6.15: *Spectral distribution (connected dots) of (a) the homodyne detected intensity* I_{hom} *and (b) the heterodyne detected signal field strength* $E_{s\,het}$ *from Fig. 6.11 (b). The plots were obtained in the same manner as for the gas phase (see Fig. 6.6). The expected distributions are shown by a gray lines. They consist of two Gaussian peaks, red- and blue-shifted by 353.4* cm^{-1} *from the probe laser. The widths of the peaks resemble the width of the probe laser intensity in (a) and the width of the probe laser field in (b).*

decay times of Fig. 6.11 (a) and Fig. 6.11 (b) are independent of the applied pump power, despite the signal strengths differ by one order of magnitude. Therefore, the nonlinearity onto the pump power did not affect the probing mechanism, at least under the applied conditions. The increase of the signal field, however, did affect the ratio between homodyned and heterodyned signal contribution. From Eq. 4.40 follows that, if the local oscillator is unchanged, lower signal fields yield relatively higher heterodyned signals. Accordingly, the relative signal modulation of the low pump power trace (red line) in Figure 6.14 is strong compared to the high pump power trace (black line).

6.2.2.2 Analysis of the spectral distribution

The time resolved signal yields a transition energy of 353.4(1) cm^{-1}. This is almost identical to the 354.40(2) cm^{-1} in gas phase para-hydrogen. Hence, the spectral distribution of

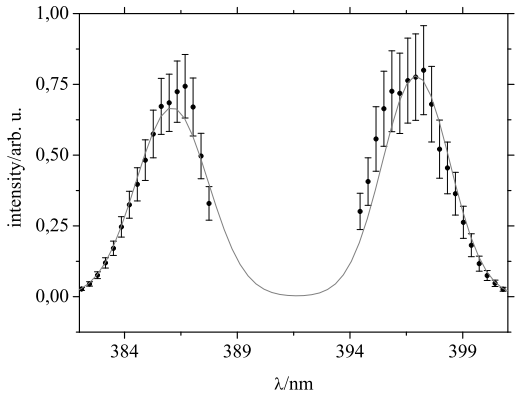

Figure 6.16: *Spectral distribution of the homodyne detected intensity (dots with error bars) as in Fig. 6.15, but without the center region to overcome local oscillator fluctuations. As in Fig. 6.7, $I_{hom}(\lambda)$ is fitted by two Gaussian peaks (gray line). The difference energy between the peaks is $2 \times \Delta\nu = 2 \times 353(3)$ cm^{-1}.*

homodyne detected intensity I_{hom} and heterodyne detected field $E_{s\,het}$ in liquid para-hydrogen should behave very similar to the distributions in the gas phase (see Fig. 6.6). In Figure 6.15 (a) we have obtained $I_{hom}(\lambda)$ from Fig. 6.11 (b). This was done in the same way as for the gas phase in Fig. 6.6 (a). $I_{hom}(\lambda)$ compares well to the expected distribution, which is depicted by a gray line. As in the gas phase, there are two peaks that correspond to Stokes and anti-Stokes Raman transitions at 386 nm and 397 nm, and resemble the width of the probe pulse. However, the signal intensity in the liquid was significantly higher. Therefore, the local oscillator fluctuations, a prominent feature in the gas phase, should play a smaller role. A quantitative analysis was carried out by fitting $I_{hom}(\lambda)$ with two Gaussians, shown as gray line in Fig. 6.16. In agreement with our findings from the time resolved signal, the two peaks have a difference energy of $2 \times \Delta\nu = 2 \times 353(3)$ cm^{-1}. However, there are also deviations from the Gaussian shape, particularly in the regions of high local oscillator intensities.

$E_{s\,het}(\lambda)$ is shown in Figure 6.15 (b). Analogous to the gas phase, it was determined by applying Eq. 6.3. The expected distribution of the signal field is depicted as a gray line in Fig. 6.15 (b). It should consist of two Gaussians of the same width as the probe laser field, each shifted by 353.4 cm^{-1} from the central probe laser wavelength. As in the gas phase, $E_{s\,het}(\lambda)$ consists of several peaks that are much narrower than expected for $E_s(\lambda)$. Since we performed several measurements in liquid para-hydrogen under varying conditions, we carried out the same procedure as in Fig. 6.15 (b) with different data sets. The spectral distributions obtained in this way vary significantly, to an extend that can hardly originate in intensity fluctuations of the local oscillator alone.

The dots in Figure 6.17 represent a cut through the contour plot shown in Figure 6.12 (b) at $\Delta t = 0.5$ ps. It stems from a measurement with high pump beam power, 4 mW. As we will discuss in context with the solid phase, the intensity of the observed response scales exponentially with the pump beam power. As a result, we observed a very high signal intensity. It was two orders of magnitude higher than the local oscillator intensity, and therefore almost entirely homodyned. The presented cut through the data set contains four peaks, of which we assign two, the peak at 397 nm and the peak at 386 nm, to the Stokes and anti-Stokes shifted homodyned intensities. The solid line in Fig. 6.17 describes detected distribution very well and consist of four equidistant Gaussians of the same width as the probe pulse, each shifted by 353.4 cm^{-1}. We can therefore identify the residual peaks, Stokes and anti-Stokes shifted from the intense Stokes peak at 397 nm, as higher

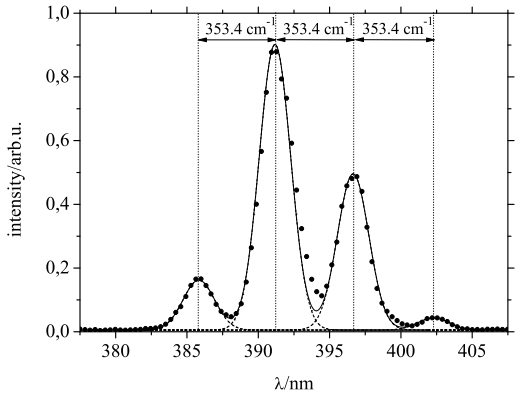

Figure 6.17: *Cut along the wavelength axis of Figure 6.12 (b) at $\Delta t = 0.5$ ps (dots). Four equidistant peaks, at 386 nm, 391 nm, 397 nm, and 402 nm are visible. The solid line is a fit, consisting of four Gaussians (dashed lines). The peaks have the same spectral width as the probe pulse, 2.6 nm.*

order Raman sidebands.

6.3 Discussion

Our experiments with gaseous and liquid para-hydrogen were aimed to built a basis for our solid state spectroscopy, which is described in the following chapter. As we will see, we observed the rotational alignment dynamics appropriate for low temperature para-hydrogen and both samples displayed the same general behavior. They exhibited a single sinusoidal signal modulation with a period of about 94 fs, a monoexponential decay of the signal field, and distinct spectral splittings, which correspond to the observed signal frequency. Therefore, the obtained results are discussed in a common section. A summary of the measured values and comparison to other experiments and theory is given in Table 6.1.

6.3.0.3 Transition frequencies

As for gaseous nitrogen, the observed dynamic in gaseous para-hydrogen corresponds to the energy of a rotational Raman transition. However, the rotational constant of hydrogen of $B_0 = 59.335$ cm^{-1} is much larger than for nitrogen with $B_0 = 1.9225$ cm^{-1} (see Table 4.1). The transition energy for the lowest rotational state of para-hydrogen, $J = 0$, to the next lowest rotational state, $J = 2$, is $\Delta\nu = 354.38$ cm^{-1} [35]. This corresponds to 509.9 K, much higher higher than the temperature of our sample. Thus, at temperatures as low as 25 K, only the ground state is thermally populated. In perfect agreement to this, we observed only one sharp frequency in gaseous para-hydrogen, corresponding to the rotational $S_0(0)$ ($J = 2 \leftarrow 0$, $v = 0$) Raman transition.

Our obtained frequency for 900 mbar gaseous para-hydrogen at 25 K is $\Delta\nu = 354.3(2)$ cm^{-1} from a fast Fourier transform, and $\Delta\nu = 354.40(2)$ cm^{-1} from a time resolved fit, respectively. It follows from a single measurement, since we did not intend to carry out a systematic study on gaseous para-hydrogen. Nevertheless, the result of the time resolved fit is identical to literature values from experiments and theory [35]. This is very satisfying, particularly in the light of high accuracy and the small error margins of the fit result.

In liquid para-hydrogen, we observed the same rotational $S_0(0)$ Raman transition as in the gas phase. The obtained frequency is only slightly lowered by 1 cm^{-1} to 353.4(1) cm^{-1} for the 16 K zero pressure liquid instead of 354.40(2) cm^{-1} for the 900 mbar gas at 25

K. This is identical to results from spontaneous Raman scattering experiments, reported by Bathnagar et al. in 1962 and carried out under comparable conditions at 18 K that yielded a transition energy of 353.3 cm^{-1} [108]. A CARS study by Sliter et al. in 2009 on the $S_0(0)$ transition in liquid para-hydrogen reported a transition energy of 353.0(1) cm^{-1}, which they found to be unchanged in the whole temperature interval from 15 K to 24 K [109]. However, Sliter et al. worked at sample pressures of 2 bar, which explains the small difference in the observed energies.

6.3.0.4 Dephasing times

In the gas, as well as in the liquid, we observed a monoexponential decay that corresponds to the dephasing time T_2 of the coherently coupled rotational states of para-hydrogen, $J = 0$ and $J = 2$. In both samples, the fit results for the dephasing times from the homodyned and from the heterodyned signal contribution were similar, although the latter suffered from the low signal to noise ratio and was more susceptible to systematical errors. Thus, we will rely on the decay time of the homodyne detected signal, $\tau_{hom} = T_2/2$, for comparison with the literature.

The observed dephasing time for 900(10) mbar para-hydrogen at 25(1) K is $T_2 = 255(3)$ ps. Following Eq. 4.62, this corresponds to an effective collision cross section σ of 2.1(1) $Å^2$. As we have seen, our data can be compared to Raman linewidth experiments (see Eq. 4.58). A Raman linewidth study was presented by van den Hout et al. in 1980 [110], who found an effective pH_2-pH_2 collision cross section for the $S_0(0)$ transition of 2.41(1) $Å^2$ at 24.8 K. This is identical to the theoretical results of Coombe and Köhler from the same year, who predict $\sigma(25\ K) = 2.4\ Å^2$ [111]. Given the discussed uncertainties in the presented 2D OKE data, this is in surprisingly good agreement with our results.

The increased particle density in the liquid led to a significantly faster dephasing, compared to the gas phase. From our best fit, we obtained a dephasing time of $T_2 = 7.6(1)$ ps for the zero pressure liquid at 16 K. Identical to our findings, Bathnagar et al. reported a Raman linewidth of 1.4 cm^{-1} at 18 K, which corresponds to a dephasing time $T_2 = 7.6$ ps [108]. Our result is also very close to the dephasing time of $T_2 = 7.5(1.0)$ ps at 15 K and an ortho-hydrogen concentration of 0.14 percent that was reported by the Schoemaker group [30]. They performed a time-resolved stimulated Raman-gain (TRSRG) experiment with picoseconds time resolution, which they carried to the solid phase of hydrogen, too. We will therefore meet them again in Chapter 7.

It is interesting to discuss the origin of the observed dephasing. As was stated above, the decay of rotational alignment in gaseous nitrogen has its origin almost exclusively in population relaxation of the coherently coupled rotational states [107]. In low temperature hydrogen, the situation is dramatically changed. For comparison, we can rely on sound absorption experiments carried out by Jonkman et al. in 1968 [112]. They measured the population relaxation τ of the $J = 2$ rotational excitation of hydrogen due to energetically inelastic collisions in the low density limit at temperatures down to 77 K. In the case of gaseous para-hydrogen, these inelastic collisions are virtually exclusively pH_2-pH_2 ((2,0)-(0,0)) collisions, which transfer rotational into translational energy. Their experimental pressure dependent relaxation time at 77 K was $\tau(77\ K) = 22.0(8)$ ns atm. The relaxation rate is linear in the particle density, due to the binary nature of the inelastic collisions at low pressure. However, 22.0(8) ns atm correspond to an effective collision cross section $\sigma(77\ K) = 3.8(2) \times 10^{-2}\ Å^2$, much smaller than the one observed by us. The experiment is in good agreement with theoretical results for the rotational relaxation due to binary inelastic collisions by Köhler and Schaefer from 1982, who yielded $\sigma(80\ K) = 3.678 \times 10^{-2}$ $Å^2$ [113]. Lee et al. presented similar data, when they reported their calculations on

rotational quenching rates in para-hydrogen in 2008 [114]. For 25 K, the theory predicts effective cross sections for inelastic pH_2-pH_2 ((2,0)-(0,0)) collisions of about 4.5×10^{-2} Å^2. This would be in stark contrast to our observation, if our observed dephasing time T_2 would be purely caused by energetically inelastic binary collisions.

However, Raman linewidth studies are sensitive to T_2, which contains depopulation and all dephasing processes. Next to inelastic collisions, energetically elastic collisions lead to a dephasing, and therefore to a line-broadening in Raman-scattering experiments [93]. The elastic collisions cause mainly reorientation of the radiating molecules. Hence, they change the population of the M-part of the rotational states $|J, M\rangle$. Generally much smaller is a secondary elastic effect, the pure dephasing τ_{ph}. It can occur due to shifts of the rotational phase during a collision. Raman linewidth experiments on the rotational transitions of hydrogen were carried out by Keijser et al. at room temperature in 1974 [94], and by van den Hout et al. at 24.8 K and 77.8 K in 1980 [110]. The linewidth broadening that was observed Keijser et al. was linear in the particle density and therefore caused by binary collisions. This is in agreement with the sound absorption experiments of Jonkman et al. for the population relaxation. A theoretical treatment of the line broadening cross section was given by Coombe and Köhler in 1980 [111]. It is in good agreement with the experiments, and shows that the effects that lead to line broadening are strongly temperature dependent. At low temperatures, the collision time is increased and translational elastic collisions, governed by the long range, quadrupole-quadrupole interaction, become more important. This is particularly true for collisions of identical particles with the same set of energy levels. In this case, translational elastic resonance collisions occur, such that the internal states of the colliding particles exchange energy.

For the liquid, with Eq. 4.59, Eq. 4.60, and the density of the liquid at 16(1) K, given by Younglove [115], the measured 7.6(1) ps correspond to an effective collision cross section of 2.1(4) Å^2. The relatively large error margins are caused by the temperature dependence of the particle density and the uncertainty in the temperature measurement. Thus, we obtained identical cross sections for the 25 K gas and the 16 K liquid. However, one should question if it is appropriate to utilize a mean free path model for the high density liquid. Indeed, the dephasing mechanisms are different and do even lead to a contradictory behavior. At low temperatures, the dephasing of the $S_0(0)$ transition in pure para-hydrogen gas is dominated by translational elastic resonance collisions [111]. Hence, the admixture of energetically nonresonant ortho-hydrogen reduces the effective total collision cross section, and therefore the dephasing time in normal-hydrogen is increased (see Table 6.1). The opposite happens in the liquid, where the dephasing time decreases with the ortho-hydrogen content. It is reduced to 6(1) ps for five percent ortho-hydrogen content and to 3.0 ps for normal-hydrogen with 74.9 percent ortho-hydrogen according to the literature [30, 108].

6.3.0.5 Spectral composition

The spectral distribution of the detected intensity was analyzed according to Eq. 4.40 and Eq. 4.63. Thus, we obtained three signal contributions, a time independent local oscillator intensity, a homodyne detected signal intensity, and a heterodyne detected signal intensity.

Since we intended to minimize the local oscillator intensity, the extinction was optimized for the central wavelength of the Gaussian shaped probe pulse, as proposed in Fig. 5.7. This worked well in gaseous and liquid para-hydrogen. At least at low probe laser powers, both samples exhibited the same local oscillator distribution as nitrogen. However, we found indications for the creation of pump laser independent Raman sidebands in the liquid phase at higher probe laser powers (> 0.1 mW). Such sidebands, caused by stimulated amplification of spontaneously scattered probe light, would contribute to the local oscillator

intensity. Hence, we worked at low probe laser powers of about 0.05 mW.

In the gas phase, the expected distribution of the homodyne detected intensity followed Eq. 4.63 very well. We found two Gaussian shaped peaks of the same width as the probe laser. The difference energy between the peaks, which correspond to Stokes and anti-Stokes Raman transitions, is $2 \times \Delta\nu = 2 \times 354(5)$ cm^{-1}. Thus, the spectral distribution contains the same information on the transition frequency as the time resolved signal, albeit at a lower resolution. A similar analysis for the liquid phase yields a similar result, $2 \times \Delta\nu = 2 \times 353(3)$ cm^{-1}. We even observed higher order Raman transitions in the liquid, so to say Raman sidebands of the Raman sidebands. They followed the very same assumptions as the discussed Stokes and anti-Stokes sidebands of the probe laser. Hence, they were shifted by the observed transition frequency from their mother line, were Gaussian shaped, and shared the linewidth of the probe laser.

However, we found also deviations from the Gaussian shape of the homodyned signal bands. This is particularly interesting in the liquid phase, where the high signal field strengths should render the possible local oscillator fluctuations less important. Indeed, the deviations from the Gaussian shape in our small series of liquid phase measurements did even exceed the deviations observed in the gas phase. It is likely that the conditions that lead to stimulated Raman transitions cause the observed deviations from the Gaussian shape. However, it also possible that phase effects, as discussed for the polarization sensitive detection of a spectrally broad pulse in Section 5.1.3, play a role in our observation, too. In order to reduce the local oscillator intensity, we optimized the probe beam extinction for the center wavelength of the probe beam. Accordingly, the transmittivity of the analyzer A (see Fig. 5.2) for pump induced elliptic components was maximal at the center wavelength. This should lead to a shift of the observed sideband towards center line. In the gas and in the liquid, such a shift is not clearly discernable, however, a clear shift was observed by us in the case of solid para-hydrogen in Fig. 7.22 (a). Indeed, the phase effect should be more pronounced in the solid case, because of the inherent anisotropy of the sample. Nevertheless, we expect the wavelength dependent phase effects to be small.

The spectral distribution of the heterodyned signal follows Eq. 4.64 and Eq. 4.65, and proved to be most complex. Eq. 4.63 predicts that the signal field's distribution consists of two Gaussians, Stokes and anti-Stokes shifted by the observed transition frequency from the probe laser center line and of the same width as the probe laser field. This prediction was well satisfied by the square root of the homodyned signal. However, the heterodyned signal field exhibited several maxima within the predicted distribution, which were much narrower than the probe laser field. The general behavior was identical for both samples, but the exact distribution varied for different measurements. We attribute this to the temporal properties of the fields. This is not unlikely, since Fig. 6.3 and Fig. 6.10 demonstrate that the signal carries a significant chirp.

Obviously, the signal field was only effectively heterodyned by the local oscillator field under certain conditions. E.g., heterodyning is only possible, if both fields overlap temporally on the detector after the spectral separation. Due to the chirp of the probe beam, the local oscillator field E_{lo} and the signal field E_s in a common frequency interval around ν are temporally shifted. E_{lo} is proportional to the probe field $E_{probe}(\nu)$, but E_s stems from Raman shifting of the probe field $E_{probe}(\nu \pm \Delta\nu)$. For $\Delta\nu \approx 350$ cm^{-1}, $E_{probe}(\nu)$ and $E_{probe}(\nu \pm \Delta\nu)$ are shifted by about 200 fs due to the chirp of the probe beam (see Fig. 5.5). This exceeds the chirp-free pulse duration of the probe beam of about 130 fs, and one might assume that there is no temporal overlap of the fields on the detector. However, the spectral separation into small frequency intervals by the fibre optic spectrometer causes a temporal broadening of the initially short pulse, which leads to a temporal overlap of

$E_s(\nu)$ and $E_{lo}(\nu)$.

Still, heterodyning depends on the relative phase of the two light fields, too. A phase shift ϕ between the fields $E_{lo} = E_{lo}(0)e^{i2\pi\nu t}$ and $E_s = E_s(0)e^{i(2\pi\nu t+\phi)}$ would therefore modulates the heterodyne detected intensity,

$$I_{het} = Re[E_s^* E_{lo} + E_s E_{lo}^*] = 2E_{lo}(0)E_s(0)\cos\phi. \tag{6.4}$$

Thus, the signal vanishes for a phase shift of $\pi/4$. We attribute the partially nonlinear chirp of the probe beam to a wavelength dependent phase shift $\phi(\nu)$ between E_s and E_{lo}. This explains the complex structure of the heterodyned signal field, including the apparent spectral narrowing.

A final remark concerns the spectral distributions. One might assume that we should have been able to detect the Raman active vibrational $Q_1(0)$ transition as well. The gas phase transition energy of 4162.06 cm^{-1} is very large, and the Stokes response would be shifted to about 468 nm. However, there are two main reasons that prohibited us to observe $Q_1(0)$ transition. Firstly, the transition dynamics are to fast to be nonadiabatically excited with our pump pulse. And secondly, stimulated Raman transitions are not possible, since the excitation energy exceeds the bandwidth of our laser pulses by more than one order of magnitude. Thus, the absence of the $Q_1(0)$ transition was not unexpected.

6.3.0.6 Signal time resolution

We had introduced a dampening coefficient d in Eq. 6.2 in order to describe the ratio between the heterodyned and the homodyned signal contribution. This became necessary in the first place due to the probe pulse duration (FWHM) of 130 fs. The probe pulse was several times longer than the period of the expected $\sin^2(2\pi\Delta\nu)$ modulation of I_{hom}. Indeed, we were unable to identify a $2\Delta\nu$ frequency component in the FFT. Instead, we observed only an unmodulated monoexponential signal decay, as it follows from an averaging of the $\sin^2$ modulation to 0.5. The heterodyned signal oscillates two times slower and was identified via FFT in both samples. Even so, we expected it to be damped due to the probe pulse duration. Additionally, a scattering background or a phase shift between E_s and E_{lo} would decrease the ratio between I_{het} and I_{hom} even more. Such effects would also be included in d. However, we consider them to be small in the presented data, since we found no indication for a scattering background, not even in the solid phase, and used to work in the maximum of I_{het}.

The heterodyned signal was heavily damped in the presented gas phase fit with $d = 0.03$, and much less damped in the shown liquid phase fit with $d = 0.13$. A simulation of the damping parameter, as depicted in Fig. 6.18, for a period of $T = 94$ fs and a probe pulse duration of 130 fs yielded a damping parameter of $d = 0.03$. This is consistent with the observed values in the gas phase, but not with $d = 0.13$ from the liquid. A probe pulse duration as short as 100 fs is needed to reach $d = 0.13$. Although a 100 fs FWHM would be significantly shorter than the probe pulse duration of 130 fs found from the analysis of nitrogen alignment structures, the Fourier limit of the probe pulse spectral width is with 87 fs even shorter. Hence, we have most probably overestimated the probe pulse duration.

6.3.0.7 Summary

Our attempt to apply 2D OKE spectroscopy on para-hydrogen samples proved to be very successful. A summary of our results, together with a comparison to the literature is given in Table 6.1. Consistent with our experimental conditions, we exclusively observed the purely rotational $S_0(0)$ transition of hydrogen. Hereby, particularly the analysis of the

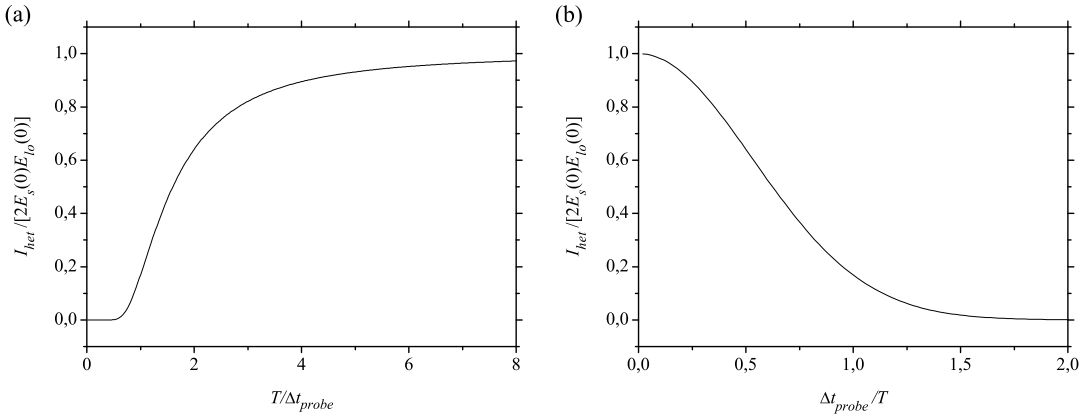

Figure 6.18: *Simulated ratio between the intensity I_{het}, detected with a Gaussian shaped probe pulse with duration Δt_{probe} (FWHM), and its expected value for an indefinitely short probe pulse with the same area. The plotted ratio equals the damping parameter d, if the damping of the heterodyned signal originates exclusive in pulse duration effects.*

time dependent dynamics worked very well. E.g., our findings for the transition energy are in perfect agreement to the literature. In gaseous hydrogen, where we could follow the coherent dynamics for several thousand periods, the accuracy of the result was only limited by the accuracy of the delay stage. Considering the measured decay times, we are in good agreement with the literature, too. However, the test experiments showed that we had to treat the local oscillator very carefully.

As anticipated, the high rotational constant of hydrogen led to distinct spectral effects in the 2D OKE signal. It exhibited a clear sideband structure that we could attribute to Stokes and anti-Stokes Raman transitions. The Raman shifts of these sidebands did agree well to the transition frequency, as predicted by Eq. 4.63. Nevertheless, the spectral structure of these sidebands proved to be very complex. Most surprising to us were two higher order effects that we observed in the liquid phase. Firstly, we found the intensity of the rotational response to grow stronger with the pump beam power than expected. And secondly, we observed higher order Raman sidebands at high pump intensities. Both effects will be discusses in more detail in context with the solid phase.

T/K	p/bar	Method	Reference	ν/cm^{-1}	T_2/ps	σ/Å^2
			gaseous pH_2			
25	0.9	2D OKE	this work	354.40(2)[a]	255(3)[a]	2.1(1)[a]
		Experiment	Ref. [35]	354.38		
		Theory	Ref. [35]	354.39		
25		Theory	Ref. [111]			2.4
24.8		Raman	Ref. [110]			2.41(1)
77.8		Raman	Ref. [110]			0.74(3)
293		Raman	Ref. [110]			0.49(1)
			liquid pH_2			
17	zero	2D OKE	this work	353.4(1)[a]	7.6(1)[a]	2.1(4)[b]
18	zero	Raman	Ref. [108]	353.3	7.6	
15	zero	TRSRG	Ref. [30]		7.5(1.0)	
15-24 H_2	2	CARS	Ref. [109]	353.0(1)		
			gaseous nH_2			
24.8		Raman	Ref. [110]			1.51(2)
			liquid nH_2			
18	zero	Raman	Ref. [108]		3.0	

Table 6.1: *Experimental observations and theoretical values for the frequency and effective collision cross section of the rotational $S_0(0)$ Raman transition in gaseous and liquid para-hydrogen.*

[a] Standard error for a single measurement.
[b] The liquid phase collision cross section is given for comparison. See text for discussion.

7 Ultrafast dynamics in solid hydrogen

"If there is anything you do not understand about solid hydrogen, say that it is a quantum crystal effect."

M. Fushitani [116]

In this chapter we discuss the time resolved 2D OKE spectroscopy of solid hydrogen samples. This has to be done in detail, because of the complexity of the solid state. The main aspect thereby is our work on pure solid para-hydrogen, which is especially suitable to show the usefulness of 2D OKE spectroscopy. For comparison, the second section will summarize our results for normal-hydrogen matrices. As we will see, there are distinct differences between the two types of samples, which originate in the ortho-hydrogen content of normal-hydrogen.

7.1 Solid para-hydrogen

The para-hydrogen crystals had to be of high optical quality, especially very transparent, to perform an OKE experiment as described in Chapter 5 and Chapter 6. During the measurements, they were kept at a stable temperature between 4 K and 11 K. The power of the pump beam had to be relatively low, about 1 mW, corresponding to 1-2 TW/cm^2, in order to stay well below the destruction limit of the crystal. Experiments with slightly higher pump powers of up to 2.5 mW led to a slow deterioration of the crystal in the laser spot and pump powers of 2.5 to 3 mW led to an instantaneous destruction of the crystal. The probe power was usually significantly lower, about 0.02-0.1 mW. These were convenient conditions that kept the probe beam power below the pump beam power. Higher probe beam powers suffered from a significant drawback: they led to the creation of pump independent rotational Raman sidebands. These sidebands could not be easily extinguished and therefore led to an decreased signal to noise ratio.

The result of a typical OKE experiment with a pure para-hydrogen crystal, with a length of 3 cm and kept at a temperature of 4 K, is shown in Figure 7.1. The local oscillator, visible at $\Delta t < 0$, has a less pronounced double maximum structure than in the gaseous or in the liquid phase. This is caused by the lower optical quality and the higher scattering of the solid sample. After the electronic overlap signal at $\Delta t = 0$, solid para-hydrogen shows rich dynamics. These dynamics have, in contrast to the measurements with gaseous nitrogen that were discussed in Chapter 5, a distinct wavelength dependence. Whereas the 2D OKE signal of nitrogen was restricted to the bandwidth of the probe laser, as one can see from Fig. 5.5 (d) and Fig. 5.8, solid para-hydrogen shows two clearly separated sidebands, similar to the signals in gaseous and liquid para-hydrogen that were presented in the preceding Chapter 6 (see Fig. 6.7 and Fig. 6.16). The spectral distribution of the signal intensity in solid para-hydrogen is shown in Fig. 7.2. As in gaseous and liquid para-hydrogen, the sidebands are Gaussian-shaped, and resemble the spectral width of the probe laser. They stem from rotational alignment dynamics and belong to the same $J = 2 \leftarrow 0$ Stokes, and $J = 0 \leftarrow 2$ anti-Stokes transitions of para-hydrogen that were discussed in Chapter 6. However, the central line, which we will call birefringence signal

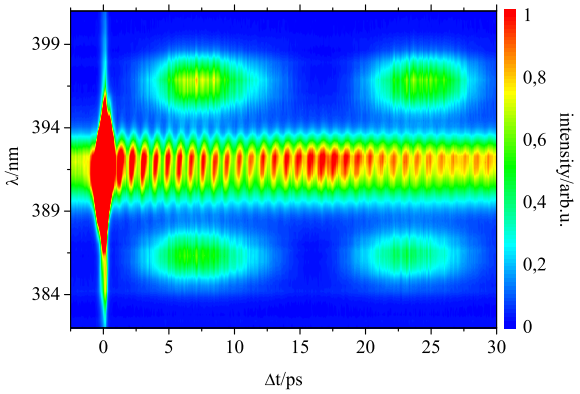

Figure 7.1: *Two dimensional contour plot recorded with our OKE setup. The sample was a 3 cm thick, transparent para-hydrogen crystal, kept at 4 K. Clearly visible is the strong birefringence signal at $\Delta t = 0$ that is centered at 391 nm. It is followed by an 900 fs oscillation in the birefringence region. The oscillating birefringence signal is accompanied by Stokes- and anti-Stokes Raman sidebands, red- and blue-shifted from the probe laser maximum.*

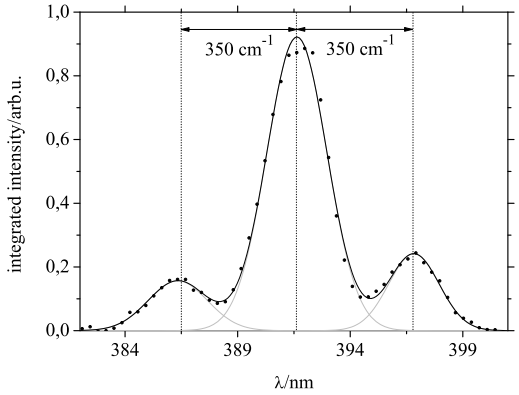

Figure 7.2: *Projection of the integrated intensity from 5 to 10 ps shown in Fig. 7.1 onto the wavelength axis (dots). The fit (black line) consists of three Gaussian peaks (gray lines) of similar width, two of them rotational Raman sidebands, each shifted by about 350 cm^{-1} from the laser line.*

in the following, and the rotational Raman sidebands show very different dynamics. As we will see below, the dynamics in the birefringence region stem from a collective solid state vibration, a twofold degenerated, Raman-active, transversal optical (TO) phonon mode. Hence, it is convenient to discuss them first separately. Later on, we will see that the 2D OKE signal is rather complex, and that it is necessary to correlate phonon dynamics and rotational alignment dynamics in order to get a deeper understanding of the observed spectra.

7.1.1 Phonon dynamics

The dynamics in the birefringence region of the 2D OKE spectra of pure solid para-hydrogen, i.e. the wavelength region that is approximately equal to the bandwidth of the probe pulse, depends strongly on the experimental conditions. It is sensitive to the applied pulse powers, the relative orientations of light polarization and crystal axis, the

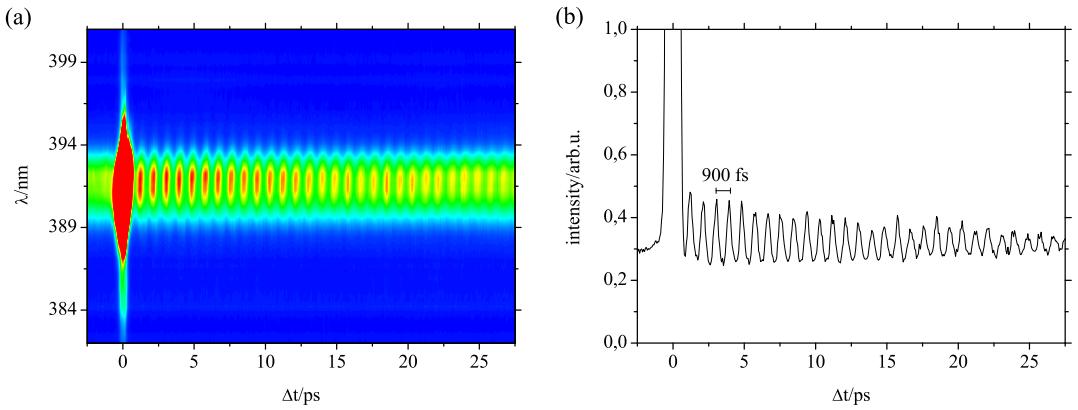

Figure 7.3: *(a) Contour plot as shown in Fig. 7.1. The measurement was carried out with a relatively low pump power of 1.2 mW and shows little to no roton Raman sidebands, but a strongly modulated birefringence region. (b) Trace of the contour plot from (a) in the birefringence region, cut at 391 nm. The signal saturates due to the electronic polarization of the sample at $\Delta t = 0$. The intense electronic response is followed by a damped, sinusoidal oscillation with a period of 900 fs.*

local oscillator distribution, and the properties of the sample crystal. In the simplest case, which we shall discuss first, it is dominated by a single sinusoidal oscillation, as it is shown in Figure 7.3 (b). Figure 7.3 (a) demonstrates that the experimental conditions can be optimized to make this oscillation the sole coherent response of the sample. This was usually achieved for relative low pump beam powers of about 1 mW, and depended on the polarization of the pump beam relative to the c-axis of the hcp lattice, too. The period of the oscillation is about 900 fs, which is a factor of ten larger than the rotational period of 94 fs discussed in the previous chapter. Obviously, this oscillation is absent in gaseous and liquid samples of para-hydrogen. It is a particular solid state response, which stems from a collective vibration in the hexagonal phase of solid para-hydrogen.

Let's take a closer look onto the birefringence trace shown in Figure 7.3 (b). As one can see, there is already a relatively high intensity at $\Delta t < 0$. This is caused by a leakage of probe intensity through the analyzer A2, as we have shown it in Figure 5.6. However, in contrast to a gaseous sample, a significant part of this offset intensity depends on the optical quality of the crystal. It can be caused by scattering due to small cracks, as well as by a spatially inhomogeneous distribution of the crystal orientation over the beam diameter, as shown in Fig. 3.11. The signal intensity is saturated at $\Delta t = 0$ due to the electronic polarization of the sample at the temporal overlap of pump and probe. This electronic polarization is similar to the one discussed in Fig. 5.5. It is Gaussian shaped in time and has a duration of about 250 fs (FWHM). After this electronic overlap, the signal falls back to its offset intensity, and shows a damped, sinusoidal modulation with a period of about 900 fs. The signal modulation is of similar amplitude as the offset. This indicates that the offset intensity acted, at least partially, as a local oscillator, which efficiently heterodyned the signal. The effect of this heterodyned detection is strikingly exemplified in Figure 7.4 by a variation of the local oscillator.

For a further confirmation of the heterodyne detection, we carried out a pump power series. Figure 7.5 shows that the detected amplitude of the birefringence signal I_s is linearly dependent on the power of the pump beam P_{pump}. This validates our expectation, since it is typical for a heterodyne detected intensity, following Eq. 4.44. This finding will become important for the quantitative analysis of the birefringence signal.

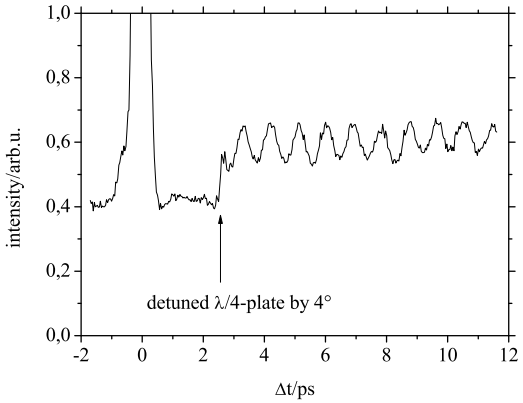

Figure 7.4: *The trace at 391 nm shows a birefringence signal of a para-hydrogen crystal measured at 4 K. The signal falls back to its offset intensity after the electronic signal at $\Delta t = 0$, and shows no significant modulation. However, a slight detuning of the probe beams quarter wave plate (see Fig. 5.2) at $\Delta t = 3$ ps induced a change in the local oscillator's phase and amplitude, heterodyning the detection. This led to a strong heterodyne signal.*

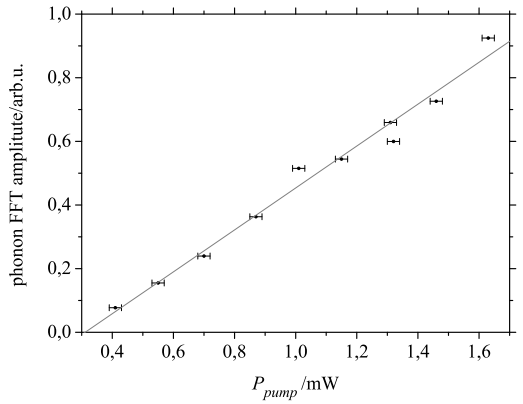

Figure 7.5: *Dependence of the detected 900 fs birefringence signal, measured in a para-hydrogen crystal at 4 K and without strong sidebands, on the power of the pump beam. The amplitude of the signal was taken from a fast Fourier transform of the time resolved signal. The offset intensity of 0.3 mW is most probable caused by a small, depolarized leakage through the polarizer P1 (see Fig. 5.2).*

7.1.1.1 Phase and wavelength effects

As we have already seen for nitrogen, the detected signal is determined by the signal field as well as by the local oscillator field. In a para-hydrogen crystal, we were limited in pump power, which had to be lower than the destruction limit, and the inhomogeneous optical properties of the crystal made it harder to compensate the local oscillator. Hence, compared to the signal field, the local oscillator was usually relatively strong. Indeed, the local oscillator intensity was often the dominating part of the detected intensity in the birefringence region, and we strongly heterodyned our phonon birefringence signal. This played to our advantage for two reasons. Firstly, the local oscillator enhanced the signal amplitude. And secondly, the heterodyned signal carries more information, since it contains the relative phase between local oscillator and signal field.

Figure 7.6 shows how a spectrally broad local oscillator, similar to the one shown in Fig. 5.6, affects the heterodyned signal. The setup was optimized for the central wavelength of the probe beam, causing a minimum in the spectral distribution shown in the inlet of Fig.

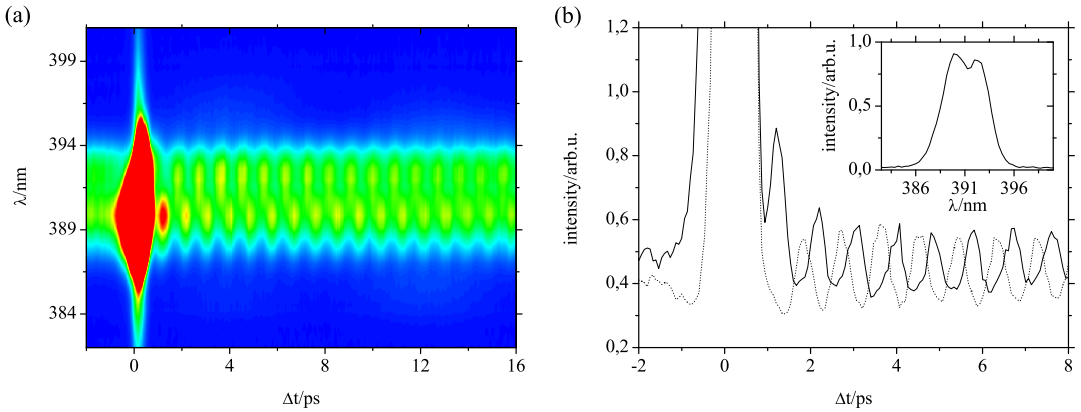

Figure 7.6: *(a) Contour plot measured under identical conditions as Fig. 7.3, but with a strongly wavelength dependent local oscillator. (b) Traces of (a) at 390 nm (solid line), and 392 nm (dotted line). They are phase shifted by π with respect to each other. The inlet shows the wavelength dependence of the detected intensity at $\Delta t < 0$. It has the typical shape that was already depicted in Fig. 5.6. This indicates a phase shift of the local oscillator by π from the blue- to the red-shifted side of the probe laser maximum, as discussed in Section 5.1.3.*

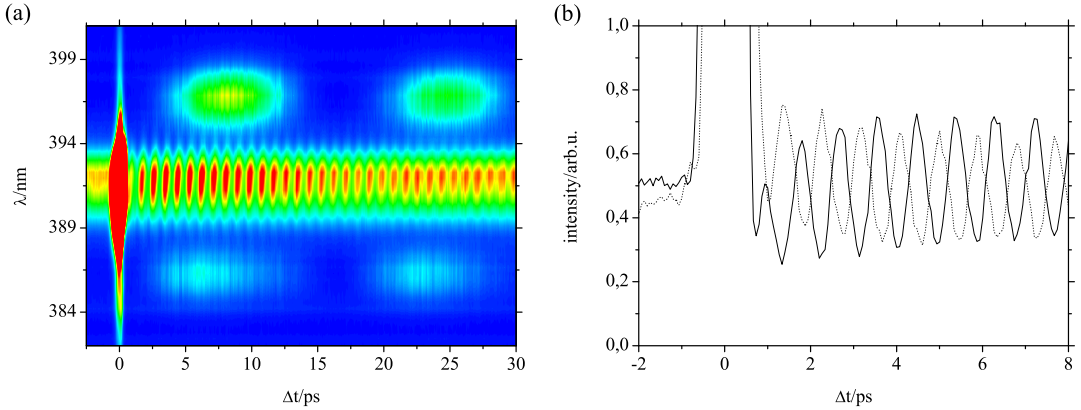

Figure 7.7: *(a) Contour plot measured under identical conditions as Fig. 7.1, but with* 90° *shifted pump polarization. (b) Birefringence traces from Fig. 7.7 (a) (solid line) and Fig. 7.1 (dotted line). The traces were detected with a relative angle Θ of the pump to the probe beam polarization of* 45° *and* −45°*, respectively. They show a strong, heterodyne detected birefringence signal, with a phase shift between the two traces of π. The phase jumps at $\Theta = 0°$, where the signal vanishes.*

7.6 (b) at 391 nm. As predicted by Eq. 5.3 and Eq. 5.5, the local oscillator field $E_{lo}(\lambda)$ has the same strength at 390 nm and 392 nm, but opposite signs. Hence, the heterodyne detected intensity has different signs for both wavelengths, too. The signal field $E_s(\lambda)$ at 390 nm and 392 nm, shifted equally from the central wavelength, has the same strength and phase. Thus, the intensity traces in Fig. 7.6 (b), measured at 390 nm and 392 nm, exhibit a phase shift of π, which stems from the phase of the local oscillator field.

A similar effect, a phase jump of π between two heterodyned birefringence signals, is shown in Figure 7.7 (b). It shows two cuts at 391 nm, but from different scans. The complete signals, one shown in Fig. 7.1 and the other in Fig. 7.7 (a), are very similar and were measured under almost identical conditions. The only difference was a shift in

the pump polarization, which was turned by 90°. Since both traces share the same local oscillator field, the phase jump must have its origin in the signal field. A turn of the pump field from 45° to −45°, with respect to the polarization of the probe beam, simply exchanges ordinary and extraordinary axis for the probe beam. This is identical to a phase shift of π in the signal field. However, the question arises, how the pump field orientation can cause such a phase jump in the signal field under the conditions of an oriented sample with fixed crystal axis. If the pump pulse would create a polarization solely along a single axis of the hcp-lattice, there would be no exchange of ordinary and extraordinary beam. Hence, there would be no possibility for E_{pump} to cause such a shift. Thus, the observed excitation must exhibit an orientational degeneracy.

7.1.1.2 Quantitative analysis

The analysis of the birefringence signal was carried out by fitting the time dependent OKE signal to the signal field $E_s(\Delta t)$. Similar to the rotational alignment dynamics in gaseous and liquid para-hydrogen, we observed a single sinusoidal oscillation, as caused by the wavepacket evolution of a two level system. However, since the birefringence dynamics are much slower than the laser pulse durations, we do not have to take a damping parameter d into account and can directly apply Eq. 6.1. Unfortunately, the local oscillator E_{lo}, which plays a significant role for the detected signal $I(\Delta t)$, proved to be more unstable in the solid phase of para-hydrogen. To account for the fluctuations of the local oscillator, e.g. due to mechanical drifts of the polarization optics, it was approximated by a fourth order polynomial.

The red line in Figure 7.8 demonstrates the result of a fit for a strongly modulated birefringence trace at 392 nm, measured in pure para-hydrogen at 4.2 K. The sinusoidal oscillation with $\nu_s = 36.71(1)$ cm^{-1} decays within $T_2 = 19.9(4)$ ps. The given errors are the numerical standard errors of the shown fit, which were smaller than the scattering of the results from other fits. A series of twenty measurements under identical conditions lead to decay time of $T_2 = 19(1)$, and a frequency of 36.75(3) cm^{-1}. All these measurements were strongly heterodyned, with $E_s \leq 5E_{lo}$. Thus, they had an almost vanishing homodyne detected intensity compared to the heterodyne detected intensity, never exceeding $I_{hom} = 0.1I_{het}$ and usually much smaller (see Eq. 4.40). This is important, because the homodyne detected signal decays twice as fast. This might have led to systematical errors, if there were scattering or in-phase local oscillator contributions to the signal, which were not included into the fit procedure. However, we consider these possible errors to be negligible, due to the weakness of the homodyne detected signal.

The phase ϕ included in Eq. 6.1 is of special interest. We defined $\Delta t = 0$ in our data as the temporal overlap of the pump and the probe pulse. This was achieved by determining the maximum intensity of the electronic signal. However, the temporal overlap varied for different wavelengths because of the chirp of the probe beam. Figure 5.5 (b) shows a variation of about 200 fs over the bandwidth of the laser. Taking this into account, we found that the phase of the signal is zero in all fitted data.

An alternative way to determine the dephasing time T_2 of the observed mode is the analysis of the spectral width of the Fourier transform of the time resolved OKE signal. A fast Fourier transform of the time resolved spectra shown in Figure 7.8 is given in Figure 7.9 (a). Two peaks, at 36.7(3) cm^{-1} and at 73.7(3) cm^{-1}, are visible. The strong peak at $\nu_s = 36.7(3)$ cm^{-1} is caused by the heterodyne detected birefringence signal, and the weaker peak at $2\nu_s = 73.7(3)$ cm^{-1} by the homodyne detected signal contribution. The spectral resolution of 0.3 cm^{-1} of the FFT, determined by the length and the point density of the time resolved spectrum, is unfortunately relatively low. This, and the small linewidth

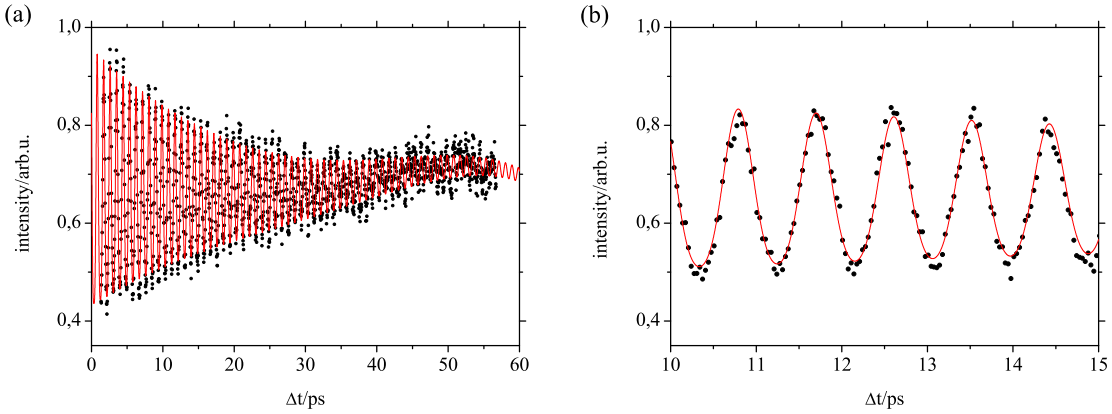

Figure 7.8: *(a) Birefringence signal of a zero pressure para-hydrogen crystal measured at 4.2 K (black dots). The fit with Eq. 6.1 (red line) exhibits a signal field amplitude modulation with a frequency of 36.71(1) cm^{-1}. The fitting procedure includes the homodyned, the heterodyned, and the local oscillator signal intensity. Since the offset intensity of $E_{lo}^2 \approx 7$ arb.u. varies by about ten percent, we applied a fourth order polynomial approximation for the local oscillator field. The signal field amplitude decays exponentially within $T_2 = 19.9(4)$ ps. (b) Zoom into (a).*

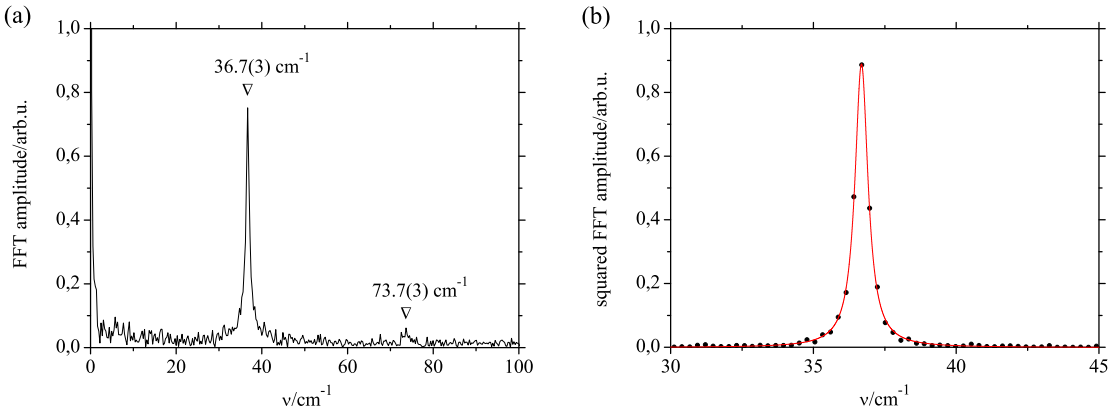

Figure 7.9: *(a) Fast Fourier transform of the time resolved birefringence signal shown in Fig. 7.8. It shows a frequency component at 36.7(3) cm^{-1}, which stems from the heterodyne detected birefringence signal. The weak frequency component at 73.7(3) cm^{-1} is caused by the homodyne detected contribution of the signal. (b) Lorentzian fit (red line) of the squared, heterodyne detected FFT amplitude (black dots). The FWHM is $\Delta\nu = 0.55(5)$ cm^{-1}.*

of the observed mode, makes the FFT less suitable to determine ν_s. Figure 7.9 (b) shows a Lorentzian fit of the squared FFT amplitude of the heterodyne detected signal. It has a full width at half maximum (FWHM) $\Delta\nu$ of 0.55(5) cm^{-1}. This linewidth should correspond to the linewidth (FWHM) of Raman scattering experiments, since the heterodyned signal decays with T_2. With Eq. 4.58 follows a dephasing time $T_2 = 19(2)$ ps, fully consistent with the time resolved result. We have, however, to consider systematic errors, due to the inability of the FFT to compensate for fluctuations of the local oscillator.

7.1.2 Rotational alignment dynamics

Next to the birefringence dynamics in the region around 391 nm, the contour plot in Figure 7.1 reveals two distinct sidebands around 386 nm and 397 nm. We already know

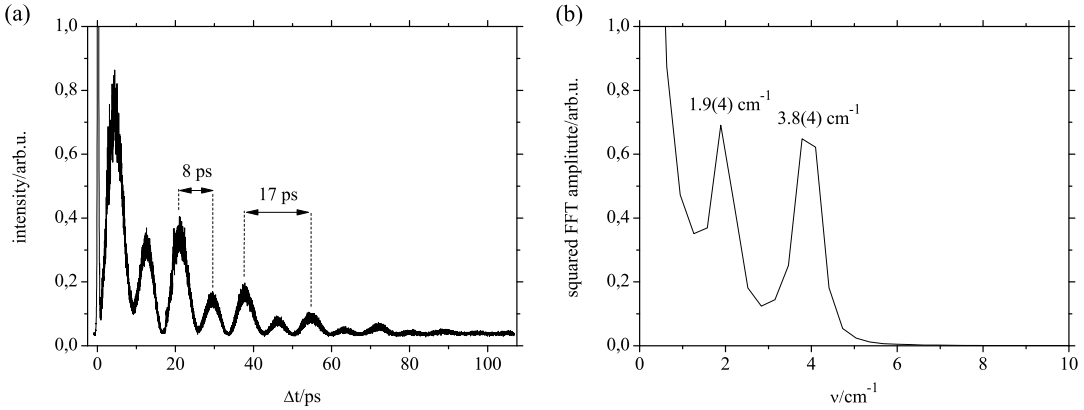

Figure 7.10: *(a) Signal trace at 386 nm of a contour plot similar to Fig. 7.1, recorded at 4 K with $P_{pump} = 1.30$ mW and $P_{probe} = 0.07$ mW. The dominant structure is an exponentially damped* $\sin^2$ *modulation, which is composed of two characteristic beat periods, 8 ps and 17 ps. (b) The low energy edge of a fast Fourier transform of (a) shows two beating frequencies, 1.9(4) cm^{-1} and 3.8(4) cm^{-1}.*

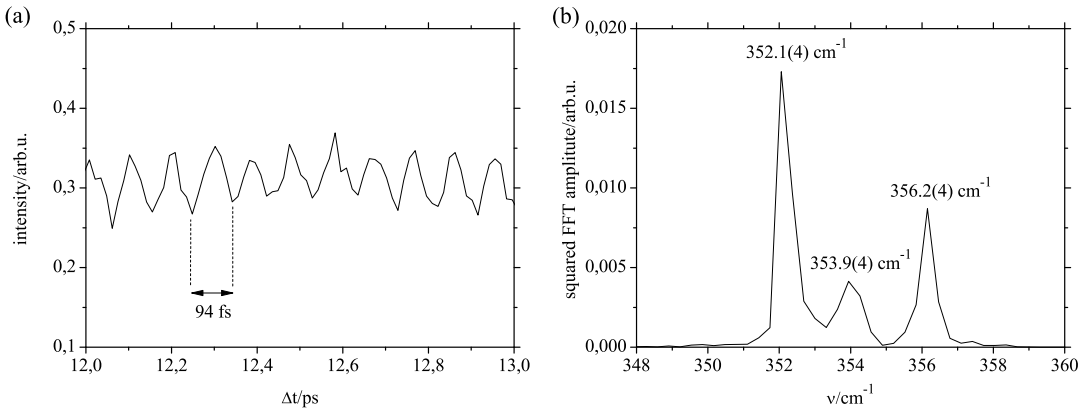

Figure 7.11: *(a) 1000 fs cut-out of the signal trace shown in Fig. 7.10 (a). The sinusoidal oscillation has a period of about 94 fs. (b) High energy region of the fast Fourier transform shown in Fig. 7.10 (b). Three frequency components are found, 352.1(4) cm^{-1}, 353.9(4) cm^{-1}, and 356.2(4) cm^{-1}.*

this behavior from the gaseous and the liquid phase, where we found similar sidebands. There, we attributed them to Stokes and anti-Stokes rotational Raman transitions, and it stands to reason that we observed the same in the solid. However, a cut along one of these sidebands, as can be seen in Figure 7.10 (a), demonstrates that the dynamics in the solid are more complex. At delay times $\Delta t < 0$, barely visible in Fig. 7.10 (a), we find a constant intensity that may act as local oscillator, I_{lo}. The intensity rises around $\Delta t = 0$, due to the electronic polarization of the sample at the temporal overlap of pump and probe pulse. At longer delays, we observe exponentially damped, high and low frequency oscillations.

Lets have a closer look onto a short cut-out of the signal trace, Figure 7.11 (a). One recognizes a sinusoidal modulation with a period of about 94 fs, superimposed on a slowly modulated background. This period is well known to us from our test experiments in gaseous and liquid para-hydrogen. There it corresponds to the frequency of the Raman-active, purely rotational $S_0(0)$ transition, 354.40(2) cm^{-1} and 353.4(1) cm^{-1}, respectively, and was detected as a heterodyned intensity I_{het}. In a fast Fourier transform of the full signal trace, however, we do not find one, but three high frequency components. As can be

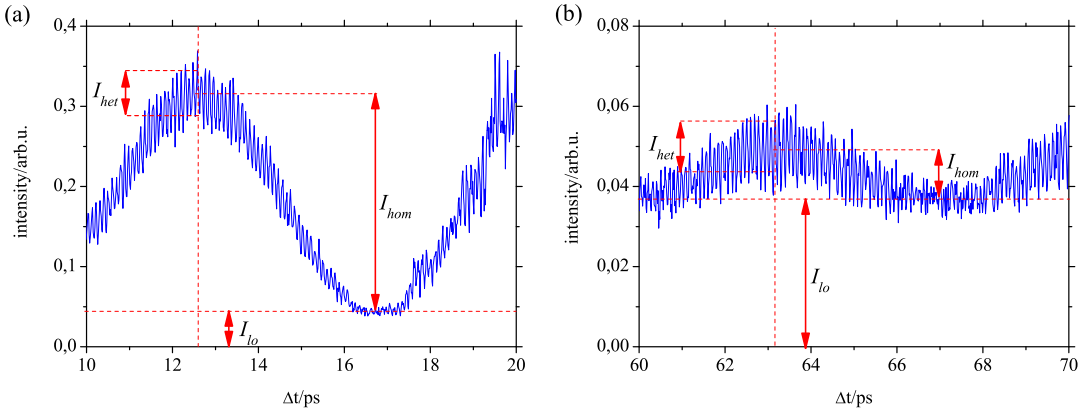

Figure 7.12: *Two 10 ps cut-outs of Fig. 7.10 (a) at (a) shorter and (b) longer pump-probe delays. Both exhibit a high frequency 94 fs oscillation, the heterodyne detected intensity I_{het}, and low frequency 8 ps and 17 ps beatings, the homodyne detected intensity I_{hom}, based on an 0.04 arb.u. local oscillator background I_{lo}. The strength of the three intensity contributions is exemplified for the 12.7 ps beat maximum in (a) and the 63.2 ps beat maximum in (b) by red arrows. Dashed red lines are a guide to the eye.*

seen in Figure 7.11 (b), the three components are centered at about 354 cm^{-1}, and split by about 2 cm^{-1}. Hence, we observed three signal fields, $E_{s\,1}(\omega_1)$, $E_{s\,2}(\omega_2)$, $E_{s\,3}(\omega_3)$.

According to the observed splitting, the full signal trace in Figure 7.10 (a) exhibits a distinct beating pattern. The difference frequencies between the three frequency components, 2 cm^{-1} and 4 cm^{-1}, lead to beatings in the heterodyne detected 94 fs oscillation with periods of about 8 ps and 17 ps. Besides the beating in the 94 fs oscillation, we find the same beat periods as a slowly modulated background (see also Fig. 7.12). Thus, the fast Fourier transform Fig. 7.10 (b) contains low frequency components that correspond to the difference frequencies, too. Even though we did not observe such a slow beating pattern in the gas or the liquid, we did observe a signal component that lacked the 94 fs period modulation: the homodyne detected signal $I_{hom} = |E_s|^2$. In the solid, we observe more than one rotational signal field. Hence, a beat pattern is created by the homodyne detection of two different signal fields that superimpose to a total signal field $E_s = E_{s\,1} + E_{s\,2}$,

$$I_{hom} = |E_{s\,1} + E_{s\,2}|^2 = |E_{s\,1}|^2 + E_{s\,1}E_{s\,2}^* + E_{s\,1}^* E_{s\,2} + |E_{s\,2}|^2 . \tag{7.1}$$

The heterodyning of two signal fields with a sinusoidal amplitude modulation, $E_{s\,1} \propto \sin(\omega_1 t)$ and $E_{s\,2} \propto \sin(\omega_2 t)$, yields homodyned intensity contributions that are modulated with the difference and the sum of the modulation frequencies ω_i, $I_{hom} \propto \sin[(\omega_1 - \omega_2)t]$ and $I_{hom} \propto \sin[(\omega_1 + \omega_2)t]$, respectively. Even though these intensity components originate in the heterodyning of different fields, we refer to them as homodyne detected intensities, because they stem from the (total) signal field and not from heterodyning with a local oscillator field. Obviously, the slowly modulated beating pattern in our spectra reflects the homodyne detected difference frequency. The fast modulated sum frequency component is absent in our spectra due to our limited time resolution.

The dynamics in Figure 7.10 (a) consist of an exponentially damped low frequency beating pattern and exponentially damped high frequency oscillations, which we assign to the homodyne detected intensity I_{hom} and the heterodyne detected intensity I_{het}, respectively. The total intensity I follows as the sum of these two intensities and the local oscillator intensity I_{lo},ity I follows as the sum of these two intensities and the local oscillator intensity I_{lo},

$$I = I_{hom} + I_{het} + I_{lo}. \tag{7.2}$$

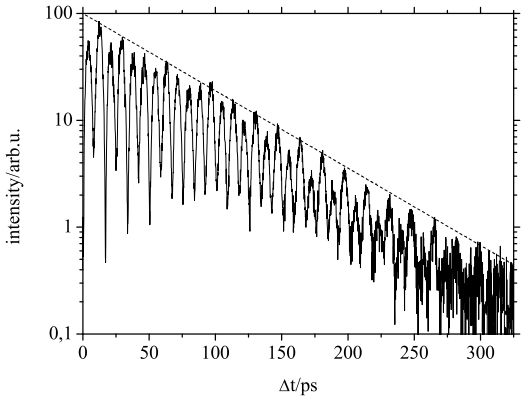

Figure 7.13: *Logarithmically plotted signal trace at 397 nm of a long time and low resolution scan, similar to Fig. 7.10 (a). The trace is far off the center line with a vanishing local oscillator, and therefore predominantly homodyned. We find 2 cm^{-1} and 4 cm^{-1} beatings. The dashed curve represents an exponential damping with $\tau = 60$ ps.*

The exponential damping of the homodyned contribution is exemplified by the logarithmic plot in Fig. 7.13. In a first approximation, a dashed curve that represents an exponential decay with $\tau = 60$ ps is used to quantify the damping of the signal. Figure 7.12 depicts two cut-outs from Fig. 7.10 (a), at shorter (Fig. 7.12 (a)) and at longer (Fig. 7.12 (b)) delays. Red arrows are used to exemplify I_{het}, I_{hom}, and I_{lo} at the 12.7 ps and 63.2 ps beat maximum. Both diagrams exhibit the same, constant local oscillator intensity of about 0.04 arb.u., which is constant in time. At shorter delays, the signal is dominated by the low frequency beat pattern of I_{hom}, and the amplitude of the high frequency 94 fs period modulation of I_{het} amounts only to about ten percent of I_{hom}. However, this changes for longer delays. In Fig. 7.12 (b), 50 ps later, I_{het} equals I_{hom}. Hence, the low frequency beat pattern decays much faster, as expected for a homodyned signal.

7.1.2.1 Geometry dependence

Figure 7.11 (b) shows an exemplary fast Fourier transform of a signal trace at 386 nm, anti-Stokes shifted from the probe laser center line. The three depicted frequencies, 352 cm^{-1}, 354 cm^{-1}, and 356 cm^{-1}, are the sole rotational transition frequencies that we observed in solid para-hydrogen. However, the relative intensities of the three components differed widely for the various orientations of crystal axis and probe beam polarization. Accordingly, the observed beatings differed, too. A comparison of the sidebands in the contour plot Fig. 7.1 and the beat structure in Fig. 7.10 (a) shows this clearly. Whereas we find a fast 8 ps (4 cm^{-1}) beating and a slow 17 ps (2 cm^{-1}) beating in Fig. 7.10 (a), there is only a slow 17 ps beating in Fig. 7.1. The absence of the fast 4 cm^{-1} beating indicates that either the 352 cm^{-1} or the 356 cm^{-1} component is missing in Fig. 7.1.

Furthermore, the sideband structure did not only vary for different measurements, but also for the Stokes and anti-Stokes sideband of a single measurement. While Stokes and anti-Stokes sideband have the same beating structure in Fig. 7.1, they exhibit the very opposite behavior in Fig. 7.14 (a). Here, we observed a 4 cm^{-1} beating in the Stokes sideband, but a 2 cm^{-1} beating in the anti-Stokes sideband. Even more, not only the frequency distribution of Stokes and anti-Stokes sideband differed, but also the phase of the components. Fig. 7.15 displays two signal traces of the same measurement, blue- and red-shifted from the probe laser center line. They share similar amplitudes for the three frequency components, which is demonstrated by the fast Fourier transforms in Fig. 7.15

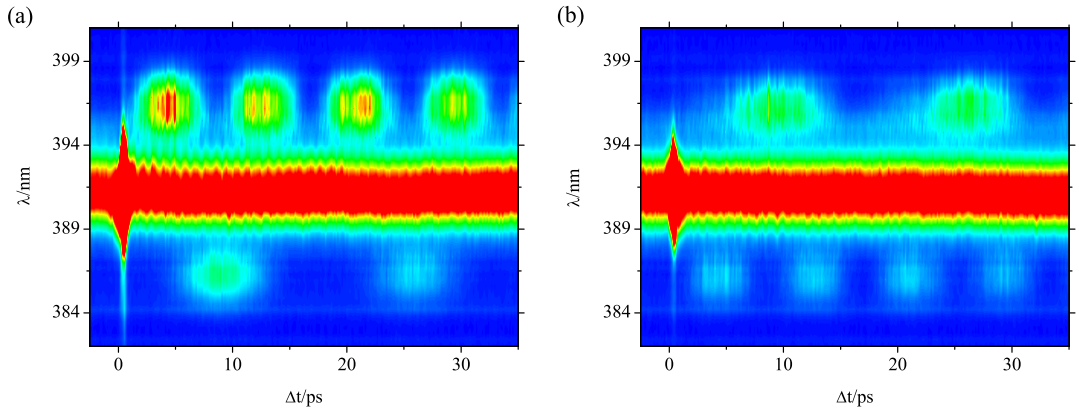

Figure 7.14: *Contour plots of measurements taken with a relative angle between pump polarization and analyzer Θ of (a) 45° and (b) −45°, respectively, but otherwise identical conditions.*

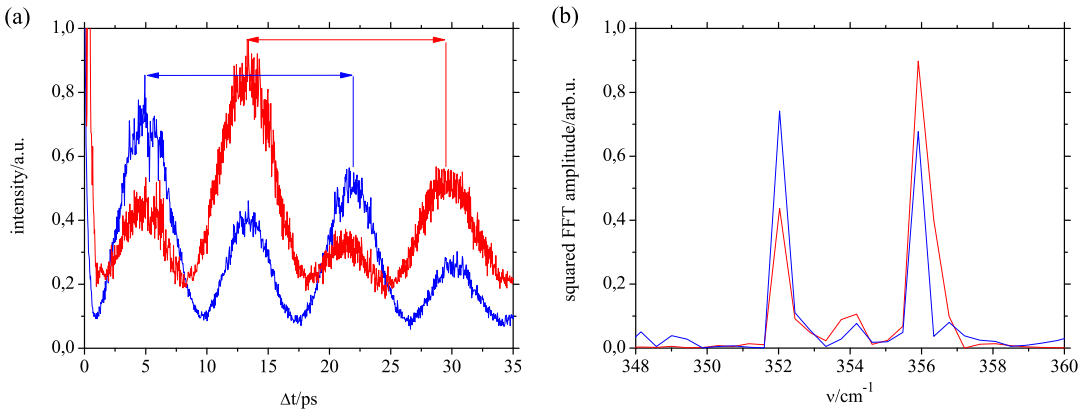

Figure 7.15: *(a) Two signal traces of the same measurement, Stokes (red line) and anti-Stokes (blue line) shifted from the center wavelength of the probe laser. Fast Fourier transforms of the traces, using the same color code, are shown in (b). Both traces have a similar beat pattern, with an almost identical frequency distribution. The full period of the 17 ps (2 cm^{-1}) beating is indicated by blue and red arrows in (a).*

(b). The 352 cm^{-1} and the 356 cm^{-1} components are strong in both traces. Accordingly, both traces exhibit a 4 cm^{-1} (8 ps) beating. Additionally, both FFTs contain the 354 cm^{-1} component, too. Hence, blue and red trace exhibit a 2 cm^{-1} (17 ps) beating as well. The full periods of the 17 ps beats are indicated by blue and red arrows in Fig. 7.15 (a), and we observe the first 17 ps beat maximum at about 4 ps for the blue anti-Stokes, and at about 12 ps for the red Stokes trace. The 17 ps beat maxima reflect the rephasing of all three components. I.e., a rephasing of all three components takes place at $\pi/2$ for the anti-Stokes signal, and at $3\pi/2$ for the Stokes signal. Their beat pattern are shifted by π in Fig. 7.15 (a), which is only possible if the phases of the signal fields were shifted. Lets consider that the phases of the three components would be $\phi_1 = 0$, $\phi_2 = \pi/2$, and $\phi_1 = \pi$ for the anti-Stokes trace, which yields the observed beating pattern. Then a phase shift of the weak 354 cm^{-1} component by π, from $\phi_2 = \pi/2$ to $\phi_2 = 3\pi/2$, would lead to the observed phase shifted Stokes trace.

The sideband intensity did also depend on the geometry of the experiment, i.e. the orientation of the pump field and the analyzer. Fig. 7.14 (a) has strong sidebands and

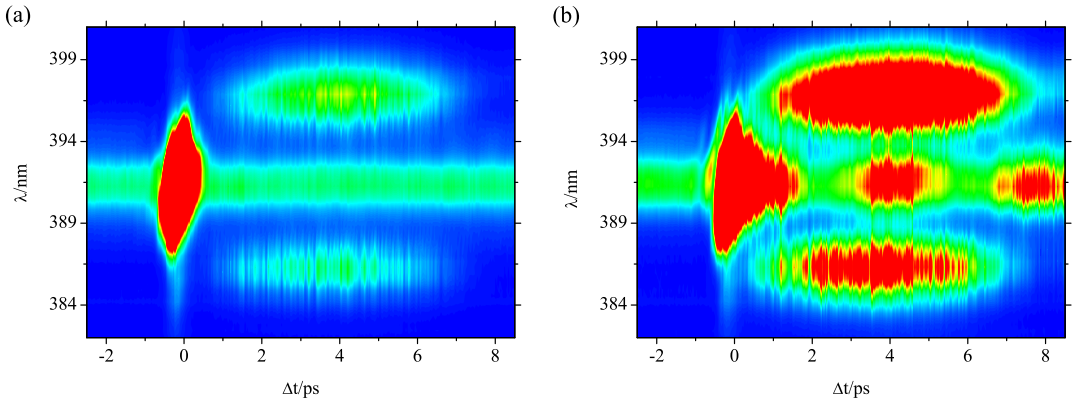

Figure 7.16: *(a) Contour plot measured with a para-hydrogen crystal at 4 K as part of a pump power series with $P_{pump} = 1.10$ mW. It exhibits intense sidebands around 386 nm and 397 nm, and a weak phonon modulation in the birefringence region around 391 nm. (b) Contour plot as shown in (a), but with $P_{pump} = 1.55$ mW. It shows new features within the birefringence region.*

was recorded with a relative angle between pump polarization and analyzer of $\Theta = 45°$. However, the sidebands vanished completely upon turning the pump polarization by 45° to $\Theta = 0°$. This behavior is familiar to us, since the dependence of the amplitude and phase of the OKE signal field onto the pump beam orientation was already demonstrated above for gaseous nitrogen and the TO phonon in solid para-hydrogen (see Fig. 5.13 and Fig. 7.7). An additional effect is presented in Figure 7.14 (b). Recorded with $\Theta = -45°$, Fig. 7.14 (b) reveals that a reorientation of the pump polarization may also exchange the temporal structures of Stokes and anti-Stokes sideband in the presented case. Hence, the amplitude distribution of the contributing frequency components was pump polarization dependent, too.

7.1.2.2 Pump power dependence

For the rotational alignment of nitrogen (see Fig. 5.11), and the phonon dynamics in solid hydrogen (see Fig. 7.5) we found a linear dependence between the signal field and the applied pump beam power P_{pump}, as expected from Eq. 4.39. Accordingly, the homodyned sideband signal should scale with the square of the P_{pump}.

Figure 7.16 gives a first impression on the pump power dependence of the 2D OKE signal of solid para-hydrogen. Figure 7.16 (a) displays a contour plot recorded with $P_{pump} = 1.10$ mW. It exhibits intense Stokes- and anti-Stokes Raman sidebands, and a closer look reveals weak phonon dynamics in the birefringence region. As we have seen above, the sidebands can vary widely in composition and intensity, depending on the geometry, and we present the rare case of very similar sidebands. However, upon increasing the pump laser power to 1.55 mW in Figure 7.16 (b), the intensity of the sidebands increased by a factor of five. This is much more than expected from Eq. 4.39 and resembles our observations for the $S_0(0)$ transition in liquid para-hydrogen (see Fig. 6.11). Furthermore, new features arose in the birefringence region around delays of about 0 ps, 4 ps, and 8 ps.

A closer look onto a sideband is given in Figure 7.17 (b). Taken from a comparable pump power series as the contour plots in Fig. 7.16, we present three Stokes traces, recorded with pump powers of 1.0 mW, 1.5 mW, and 1.9 mW. The maximum peak intensity increased by two orders of magnitude upon increasing the pump power from 1.0 mW to 1.9 mW (see

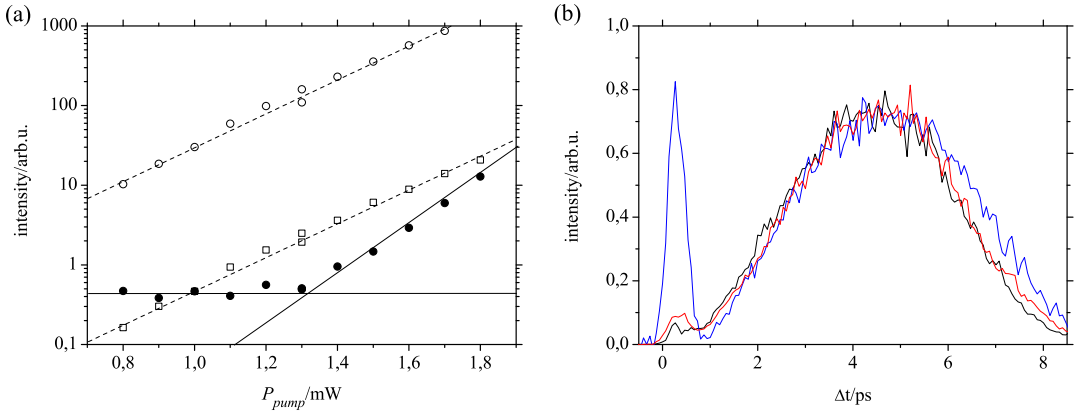

Figure 7.17: *(a) Logarithmically plotted pump power dependence of the integrated Stokes beat intensity (open circles), the Stokes maximum intensity (open squares), and the maximum intensity in the beat region of the center line (black dots). The data were obtained from a similar pump power series as in Fig. 7.16, but without any anti-Stokes response. The two solid lines, and the two parallel, dashed lines are guides to the eye. (b) Three normalized signal traces at 397 nm from the series in (a). The traces were recorded with $P_{pump} = 1.0$ mW (blue line), $P_{pump} = 1.5$ mW (red line), and $P_{pump} = 1.9$ mW (black line).*

Fig. 7.17 (a)), and the traces in Fig. 7.17 (b) had to be rescaled to be comparable in shape. The pump power dependence of the beat structure was highly nonlinear, much higher than the one of the electronic signal at $\Delta t = 0$. Thus, the electronic overlap peaks of the 1.5 mW trace and the 1.9 mW trace become evanescently small due to the rescaling. At first glance, the three beat structures agree well in shape, which makes this pump power series suitable for a more quantitative analysis.

Taking the maximum intensity of the 4 ps beat as a measure for the signal intensity, Figure 7.17 (a) demonstrates a surprisingly strong pump power dependence. Above a certain detection threshold, below which the signal was lost in the noise level, the beat maximum of the Stokes sideband rose exponentially. Within an increase of the pump power by a factor of two, the sideband rose by two orders of magnitude. The same holds true for the integrated intensity of the 4 ps beat, which proves that the structure of the signal was pump power independent within the depicted range. The maximum intensity of the new 4 ps beat in the birefringence region behaved very similar to the Stokes sideband peak. After surpassing a noise level the beat maximum rose exponentially, too. We observed even a higher pump power dependence than for the Raman sidebands. Thus, the center line beat intensity often eventually surpasses the sideband intensity at high pump powers.

A comparable signal as the new response at the center wavelength shown in Fig. 7.16 (b) was already discussed above, in context with the rotational response of liquid para-hydrogen at high pump powers (see Fig. 6.12). In the liquid, we found also signal components at a doubled Stokes shift, at 402 nm. It stands to reason that solid para-hydrogen displays similar higher order transitions. Figure 7.18 (a) is a long time scan with a wider wavelength range that was recorded from a para-hydrogen crystal with exceptional optical quality. Though pumped with only $P_{pump} = 1.26$ mW, one third of the laser power that was used for the liquid sample in Fig. 6.12, Fig. 7.18 (b) displays the expected band at 402 nm, and we even find two additional blue-shifted bands at 381 nm and 376 nm.

The bands were almost equidistant, each shifted by about 350 cm^{-1}. Approximately, this corresponds to the observed transition frequencies. A closer look onto the center line beat pattern in Fig. 7.18 (a) reveals slight wavelength shifts between e.g. the 4 ps beat and the

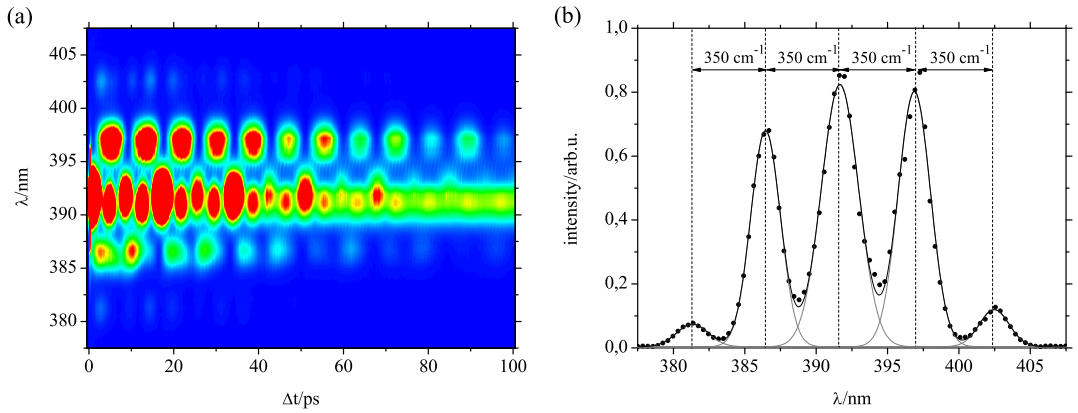

Figure 7.18: *(a) Contour plot measured with a para-hydrogen crystal of high optical quality at 4 K as part of a pump power series with $P_{pump} = 1.26$ mW. (b) Cut through (a) (black dots) at $\Delta t = 3$ ps. It displays five approximately equidistant Gaussian peaks (gray lines) of the same width as the probe laser. A weak sixth peak at 376 nm, blue-shifted by additional 350 cm^{-1} from the peak at 381 nm, is not shown here.*

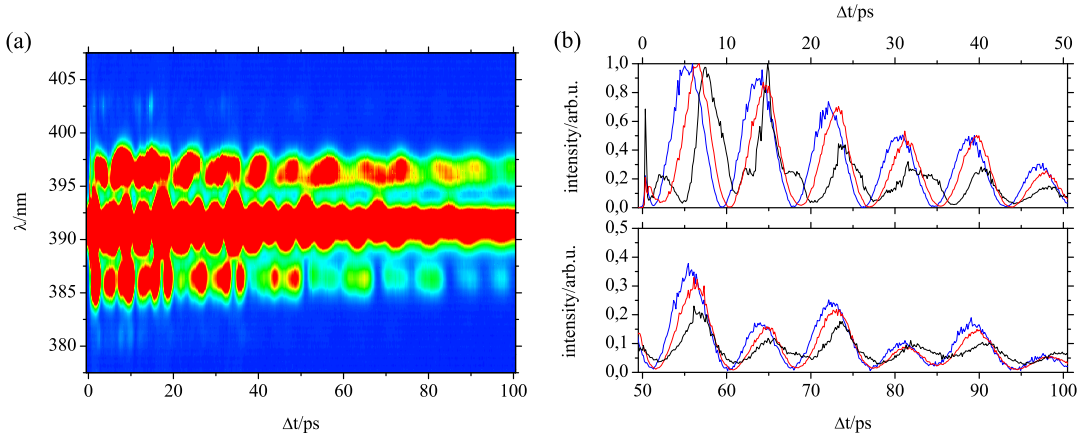

Figure 7.19: *(a) Contour plot of the same series as in Fig. 7.18 (a), but recorded with $P_{pump} = 1.86$ mW. (b) Normalized traces at 398 nm of the same series as in (a) with $P_{pump} = 1.06$ mW (blue line), $P_{pump} = 1.46$ mW (red line), and $P_{pump} = 1.86$ mW (black line). The upper panel shows the first 50 ps of the data set, the lower panel the last 50 ps.*

8 ps beat. This indicates that the center line structures are more complex and stem from higher order processes, as will be discussed in Section 7.1.3.4. The same conclusion follows from the temporal structure of the beat pattern. Whereas the 8 ps period of the Stokes sideband complies with the observed 4 cm^{-1} splitting between the frequency components, the higher order center line had a 4 ps beating. As we will see, a corresponding 8 cm^{-1} splitting would be inconsistent to the rotational states of our sample.

In general, the temporal structure of the beat patterns proved to be pump power dependent, too. Whereas Fig. 7.18 (a) exhibits a regular 8 ps beating pattern in the Stokes sideband, Figure 7.19 (a), which was recorded with a higher pump power, shows much more complex structures. Figure 7.19 (b) displays three normalized traces at 398 nm, far off from the intense beatings in the birefringence region, recorded with different pump powers. In the upper panel, the blue line, recorded with a low pump power, has a simple beat structure. However, an increase of the pump power shifts and steepens the beat pattern

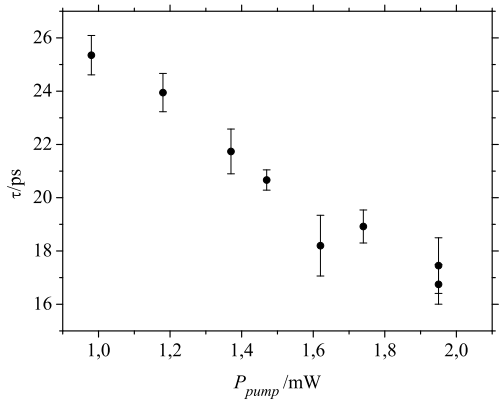

Figure 7.20: *Decay time τ of a homodyne detected signal vs. the power of the pump beam P_{pump}. The decay times were obtained in a rough approach from the maxima of the anti-Stokes shifted beat pattern, composed by the 352 cm^{-1} and the 356 cm^{-1} component. An exemplary measurement of this series is shown in Fig. 7.10.*

(red line), and a further increase even led to the occurrence of new features (black line). Both effects were reproducible, and cannot be traced to structural changes of the crystal due to deterioration.

In the lower panel of Fig. 7.19 (b), we find that the traces with higher P_{pump} are systematically lower at longer delays. Thus, we have to assume that the decay times of the signal were pump power dependent, too. As a first approximation of the pump power dependence of the decay times, we followed the damping of the beat maxima in a similar approach as in Fig. 7.13. Figure 7.20 shows that the obtained decay times in a pump power series decreased with increasing P_{pump}. Unfortunately, one has to apply relatively high pump powers within long time measurements in order to determine the signal decay. This led to a slow, laser induced deterioration of the crystal during the measurements, which might have contributed to the observed decay times. Nevertheless, we observed decay times for the beats that ranged from about 60 ps in the low pump power measurement in Fig. 7.13 to less than 20 ps for the high pump power measurements in Fig. 7.20.

7.1.2.3 Spectral distribution

Figure 7.21 (a) is a contour plot from a measurement with medium pump and low probe beam power. It exhibits a clear phonon modulation in the birefringence region, and two distinct rotational sidebands. Carrying out a fast Fourier transform for each spectral position, i.e. for each frequency shift $\Delta\nu$ from the probe laser center line, we obtained the spectral distribution of the 2D OKE signal frequencies ν, shown in Figure 7.21 (b-d). Three interesting frequency intervals are shown in Fig. 7.21 (b), Fig. 7.21 (c), and Fig. 7.21 (d). The first one contains the local oscillator offset at 0 cm^{-1}, the heterodyned phonon response at 37 cm^{-1}, and the homodyned phonon response at 74 cm^{-1} and 0 cm^{-1}. The phonon signals have no observable spectral splitting into Stokes and anti-Stokes band, because the 37 cm^{-1} transition energy is about five times smaller than the probe beam width of about 170 cm^{-1} (FWHM). Additionally, we find sidebands with the homodyne detected rotational signal contributions at 0 cm^{-1}, 2 cm^{-1}, and 4 cm^{-1}. The splittings in ν are hardly visible in the chosen scale of Fig. 7.21 (b), however equivalent to the ones shown in Fig. 7.10 (b). They are shifted from the probe laser center line, since they stem from rotational transitions that give rise to spectral splittings in $\Delta\nu$, which are two times

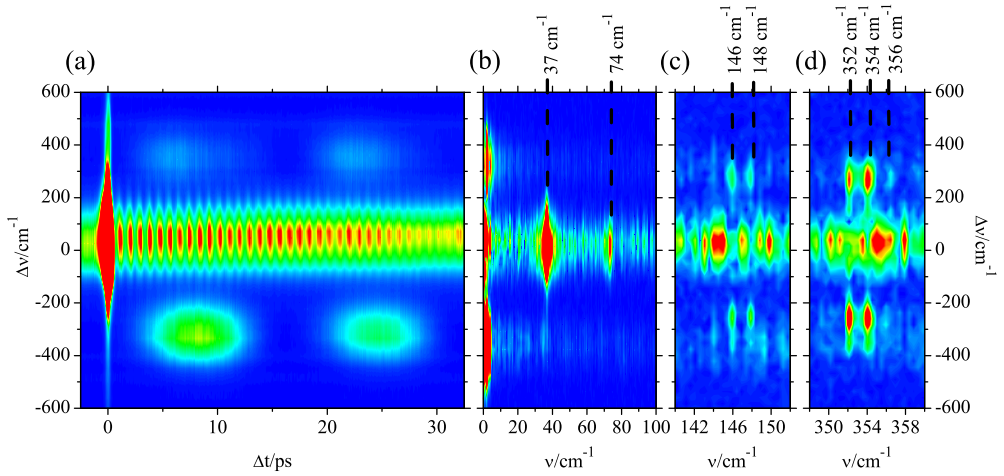

Figure 7.21: *(a) Contour plot of a para-hydrogen crystal, recorded at 4 K with medium pump and low probe beam power, $P_{pump} = 1.20\ mW$ and $P_{probe} = 0.02\ mW$. For convenience the wavelength scale is substituted by an energy scale that represents the spectral shift from the probe laser center line $\Delta\nu$ in wavenumbers. (b, c, d) Frequency distribution ν versus $\Delta\nu$ in the contour plot as obtained by fast Fourier transforms along cuts in $\Delta\nu$, (c) and (d) are plotted with the same, (b) with a different color code. The center line is relatively noisy, due to the high local oscillator intensity. The presented intervals are discussed in the text.*

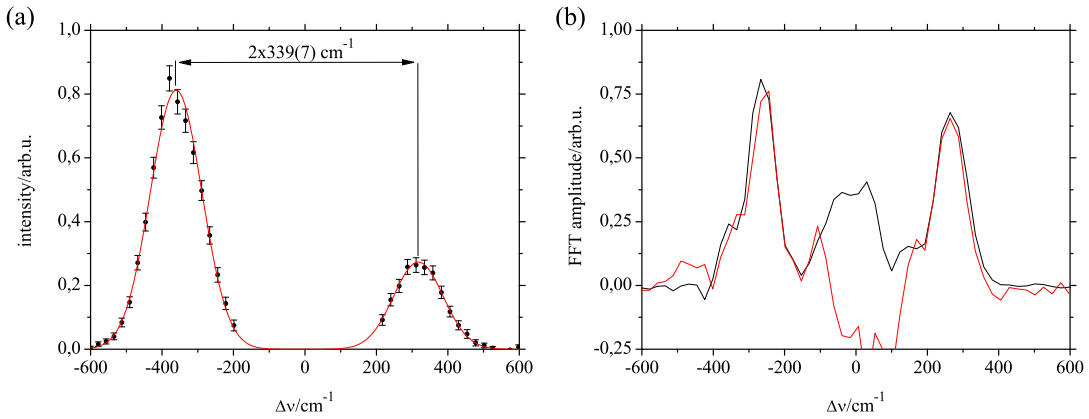

Figure 7.22: *(a) Homodyne detected rotational sidebands (black dots with error bars) of Fig. 7.21 (a), obtained in a similar way as for the gas and the liquid in Fig. 6.6 (a) and Fig. 6.15 (a). The red fitting curve consists of two Gaussian peaks that have the same spectral width as the probe beam. (b) Integrated intensity of the FFT frequency intervals shown in Fig. 7.21 (c) (red line) and Fig. 7.21 (d) (black line), subtracted by an average FFT background and normalized to match each other. The center area suffers from local oscillator noise.*

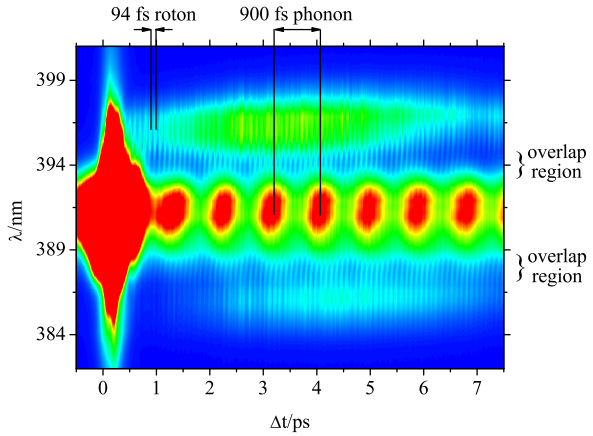

Figure 7.23: *Contour plot of a high resolution measurement with low effective pump beam power. The heterodyned phonon signal and the heterodyned rotational signal are clearly discernible. The corresponding signal fields overlap in the regions around 394 nm and 388 nm.*

bigger than the probe laser FWHM. Figure 7.22 (a) gives an impression of the sideband structure. Both sidebands are shifted by $2 \times 339(7)$ cm^{-1} from each other, a little less than expected from the rotational frequencies of 352 cm^{-1}, 354 cm^{-1}, and 356 cm^{-1} that were obtained from fast Fourier transforms.

Shown in Figure 7.21 (d) are the three heterodyne detected rotational components. They are well observable despite the intense noise of the local oscillator intensity around $\Delta\nu = 0$, because the rotational signal fields are significantly shifted from the probe laser center line. However, their splittings of 2 cm^{-1} and 4 cm^{-1} in the ν-scale are about two orders of magnitude smaller than the FWHM of the probe pulse. Hence, they show no difference in their $\Delta\nu$ spectral distributions. To our surprise, we find an additional FFT component at the same spectral position as the heterodyned rotational signal in Figure 7.21 (c). It contains Stokes and anti-Stokes shifted signal contributions at 146 cm^{-1} and 148 cm^{-1}, which exhibit the same splitting of 2 cm^{-1} as the rotational components. Figure 7.22 (b) shows the heterodyned rotational signal and the signal component around 148 cm^{-1} in more detail. Their spectral distributions are fully identical, at least in the relevant regions of high signal field and low local oscillator noise. However, their distributions may not be equal, since a real transition frequency of 148 cm^{-1} demands a spectral shift that differs from the shift of the rotational components. We can therefore readily conclude that the observed features around 148 cm^{-1} are artifacts. A conclusion that would not have been easily possible from one dimensional OKE data. Indeed, there are to our knowledge no Raman-allowed transitions with energies of 148 cm^{-1}, neither in solid para-hydrogen, nor in impurities like ortho-hydrogen, HD, D_2, H_2O, N_2, or O_2.

7.1.2.4 Heterodyning of signal fields

The signal fields of the phonon excitation in the center line and the rotational transition in the sidebands have the spectral width of the probe field. Thus, the spectral separation of phonon and roton contribution of about 350 cm^{-1} is somewhat bigger than their FWHM of about 240 cm^{-1}. Nevertheless, they exhibit a certain overlap. We should therefore observe a heterodyning of phononic and rotational signal fields in this overlap region. The relative contribution of the created intensity component becomes maximal, if both fields are of similar strength. Hence, the spectral position of the signal varies, depending on the

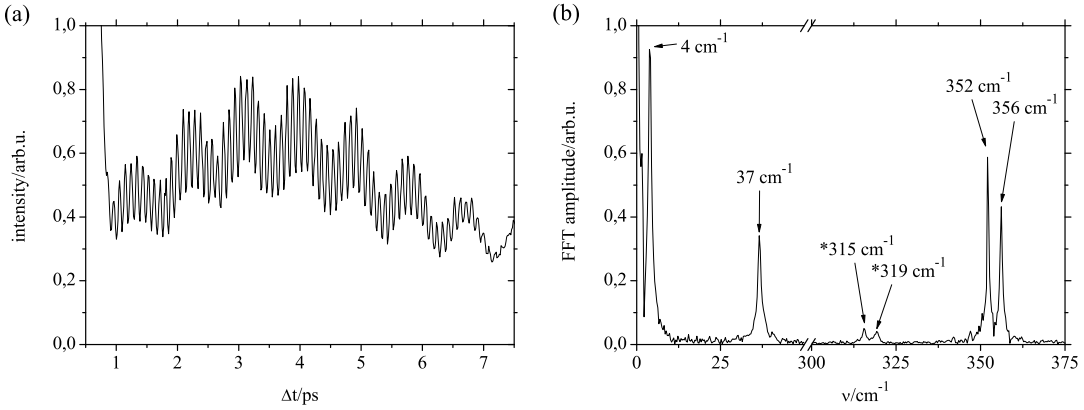

Figure 7.24: *(a) Signal trace at 394 nm, taken from Fig. 7.23. (b) Fast Fourier transform of (a). We find a homodyne detected rotational beat at 4 cm^{-1}. Heterodyned with the local oscillator, we detect a phonon response at 37 cm^{-1}, and two rotational components at 352 cm^{-1} and 356 cm^{-1}. Marked by stars, two additional peaks at 315 cm^{-1} and 319 cm^{-1} stem from heterodyning of phononic and rotational signal fields.*

strengths of the contributing fields.

Figure 7.23 shows a contour plot of a high resolution measurement with intense phonon and roton response. The corresponding signal fields show a good overlap in the regions around 394 nm and around 388 nm. Taken from Fig. 7.23, Figure 7.24 (a) displays a signal trace at 394 nm, i.e. half way between center line and Stokes sideband, with almost equal phononic and rotational signal fields. They were detected together with a local oscillator intensity and a homodyne detected intensity that included a rotational 8 ps beating. The fast Fourier transform Figure 7.24 (b) exhibits all these components. The phonon response, heterodyned with the local oscillator field, at 37 cm^{-1}, and the rotational response, heterodyned with the local oscillator as well, is found at 352 cm^{-1} and 356 cm^{-1}. Homodyne detection of single signal fields yielded difference frequency components at 0 cm^{-1}, and sum frequency components that were to weak to be observed here, but were discussed above (see Fig. 6.18 and Fig. 7.9). The beat pattern between the rotational components led to a difference frequency component at 4 cm^{-1}. There is no 2 cm^{-1} beating, since the 354 cm^{-1} component is absent in the presented data. The mixing of the phononic and the rotational signal fields yields two additional difference frequency components at 315 cm^{-1} and 319 cm^{-1}, shifted by 37 cm^{-1} from the heterodyne detected rotational components. Again, caused by the probe pulse duration, the sum frequency components were to weak to be observed. To sum up, the signal in Fig. 7.24 (a) was composed of three signal fields, modulated with 37 cm^{-1}, 352 cm^{-1}, and 356 cm^{-1}, respectively, and a constant local oscillator field. We observed all combinations of the fields that could be resolved with our probe pulse duration, including the difference frequency components of phonon and rotational response.

Upon increasing the pump beam power, we observed new rotational beatings in the birefringence region. These features grew exponentially with P_{pump}, whereas the phonon scaled linear with it. Figure 7.25 is a contour plot that has a clearly visible phonon response and higher order rotational beatings of comparable amplitude in its birefringence region. As in Fig. 7.18, the beat pattern exhibits slight wavelength shifts. We find these wavelength shifts reflected in the intensity of the phonon response. Figure 7.26 (a) demonstrates this with the help of two cuts through Fig. 7.25, blue- and red-shifted from the probe laser center line by 1 nm. They exhibit the rotational beating and a corresponding intensity

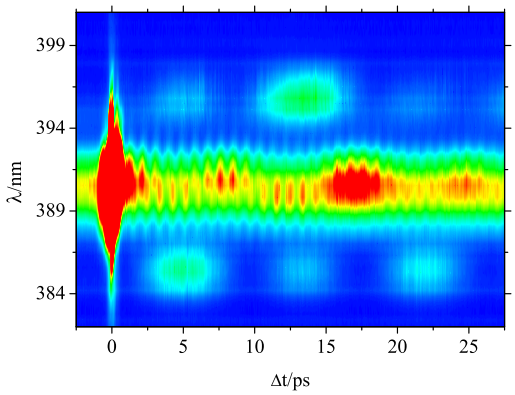

Figure 7.25: *Contour plot recorded with a medium effective pump beam power. The birefringence region exhibits a phonon modulation and a higher order Raman beat as already shown in Fig. 7.18, which has a slight wavelength dependence.*

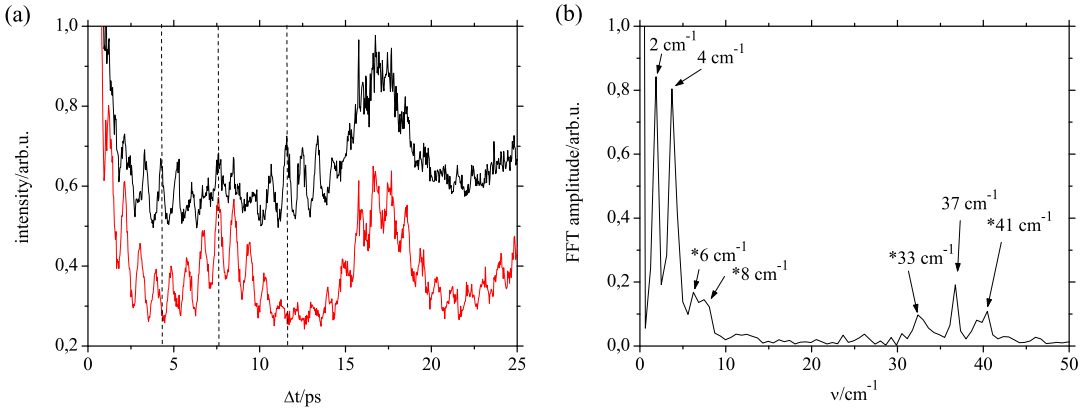

Figure 7.26: *(a) Signal traces from Fig. 7.25 at 390 nm (black line) and 392 nm (red line). Three dashed lines mark extrema of the phonon signal at approximate extrema of the higher order Raman beats. (b) Fast Fourier transform of a signal trace from Fig. 7.25 at 391 nm. New components are marked by a star.*

variation of the phonon modulation amplitude. There are also phase shifts between the signal traces. We have already discussed similar phase shifts for the phonon response, and found them to be caused by phase difference between the phonon signal field and the local oscillator field. In the presented case, however, the phase of the phonon modulation varies with time. We exemplify this for three delays, marked by dashed lines in Fig. 7.26 (a). At 4 ps and 12 ps, both traces are phase shifted by π. At 8 ps, in the maximum of a higher order beat, they are in phase. The comparison with Fig. 7.25 clarifies that at 8 ps the growing intensity of the phonon amplitude, which dominated the 392 nm trace from the beginning, simply exceeds the phonon amplitude that dominated the 390 nm trace at 4 ps. Thus, we observed a phase sensitive amplification of the phonon response by a higher order Raman rotational beat.

Figure 7.26 (b) shows a fast Fourier transform of a cut through Fig. 7.25 at 391 nm. It contains the beat frequencies, 2 cm^{-1} and 4 cm^{-1}, and the phonon frequency, 37 cm^{-1}, from heterodyning of the phonon signal field with the local oscillator field. Due to the amplification of the phonon response by the beat, we find components that are sum and difference frequencies of the 37 cm^{-1} phonon signal and the 2 cm^{-1} and 4 cm^{-1} beating

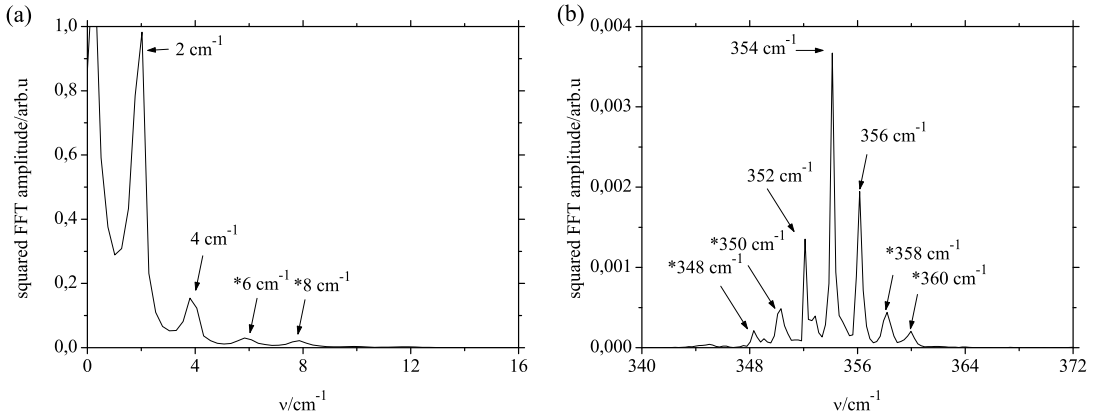

Figure 7.27: *Fast Fourier transforms of a trace at 395 nm from the high pump power measurement in Fig. 7.18. (a) Low frequency region. (b) Rotational frequency region. New components are marked by a star.*

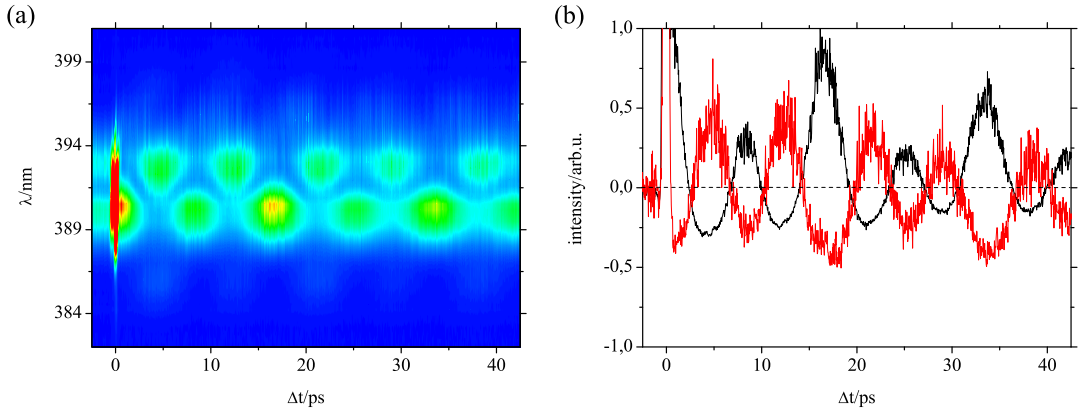

Figure 7.28: *(a) Contour plot of a measurement with a spectrally broad local oscillator, as shown in Fig. 5.6, and an almost vanishing rotational Raman response. The contour plot compares well to Fig. 7.6 (a). (b) Signal traces of (a), taken from the regions of high local oscillator amplitude at 390 nm (black line) and 393 nm (red line). The local oscillator intensity was subtracted to bring both traces to zero (dashed line).*

frequencies, albeit the sum and difference frequencies with the 2 cm^{-1} beating are hard to identify in the presented case. A similar signal amplification by higher order Raman beatings was also observed for the 94 fs rotational response, and even for the rotational beats themselves. The fast Fourier transforms in Figure 7.27 depict peaks at $(2+4=6)$ cm^{-1} and $(4+4=8)$ cm^{-1} and all possible sum and difference frequency combinations of the three rotational frequencies 352 cm^{-1}, 354 cm^{-1}, and 356 cm^{-1} with 2 cm^{-1} and 4 cm^{-1}. Thus, we observe new frequency components at $(352-4=348)$ cm^{-1}, $(352-2=350)$ cm^{-1}, $(356+2=358)$ cm^{-1}, and $(356+4=360)$ cm^{-1}.

The described observations are readily explained if we consider that there were two additional signal fields, which were amplitude-modulated with 2 cm^{-1} and 4 cm^{-1}. Indeed, Figure 7.28 demonstrates a heterodyning of such fields and the local oscillator field. In this peculiar measurements we observed a typical local oscillator, however no phononic and almost no rotational Raman response. The local oscillator had maxima at 390 nm and 393 nm, clearly visible at $\Delta t \leq 0$. As described for Fig. 5.6, the local oscillator fields of the two maxima were phase shifted by π and therefore of opposite sign. A very

similar measurement was presented in Fig. 7.6 for a high phononic signal field with its periodic time of 900 fs. However, in contrast to Fig. 7.6, we observed 8 ps and 17 ps signal modulations in Fig. 7.28 (a). Figure 7.28 (b) depicts two traces through Fig. 7.28 (a) in the regions of high local oscillator amplitude. The signal intensity partly fell below the local oscillator intensity, a clear prove for a heterodyne detected signal. Even more, the depicted signal traces are phase shifted by π, similar to the heterodyned phononic signal in Fig. 7.6. This is the expectation for the heterodyned signal of two signal fields, which are amplitude-modulated with 2 cm^{-1} and 4 cm^{-1}, because the local oscillator field exhibit opposite signs in its two maxima. Obviously, the homodyned signal is independent of the local oscillator distribution and sign. The simultaneous detection of homodyne and heterodyne component can therefore lead to wavelength effects in the higher order signal. Thus, the wavelength dependences in Fig. 7.18, Fig. 7.25, and Fig. 7.28 stem from different spectral distributions of the higher order signal field and the local oscillator field.

7.1.2.5 Quantitative analysis

The quantitative analysis of the time dependent signal follows the same principles as applied for the gaseous and liquid phase with Eq. 6.2. We write the detected intensity $I(\Delta t)$ as the sum of its three components,

$$I(\Delta t) = I_{hom}(\Delta t) + I_{het}(\Delta t) + I_{lo}, \tag{7.3}$$

the homodyned intensity $I_{hom}(\Delta t)$, the heterodyned intensity $I_{het}(\Delta t)$, and the local oscillator intensity I_{lo}. Hereby we consider the local oscillator intensity to be time independent, $I_{lo} = E_{lo}^2$. Since we observed three high frequency components and the corresponding beat pattern, we have to consider three signal fields $E_i(\Delta t)$ for the heterodyned signal. Analog to our approach to the gas and liquid phase signal field, we consider these signal fields to be exponentially damped, single sinusoidal oscillations. Hence, they are determined by their amplitudes E_i, their frequencies ω_i, their phases ϕ_i, and their decay times $\tau_i = T_2$. Now, the heterodyned intensity follows as

$$I_{het}(\Delta t) = d2E_{lo} \sum_{i=1}^{3} E_i \sin(\omega_i \Delta t + \phi_i) e^{-\Delta t/\tau_i}. \tag{7.4}$$

To account for our limited time resolution, we introduce a damping constant d, which we consider to be equal for the three frequencies. The mixing of the three signal fields leads to the homodyned signal,

$$I_{hom}(\Delta t) = 0.5 \sum_{i=1}^{3} \sum_{j=1}^{3} E_i E_j \cos(\omega_{ij} \Delta t + \phi_{ij}) e^{-\Delta t/\tau_i} e^{-\Delta t/\tau_j}, \tag{7.5}$$

with $\omega_{ij} = \omega_i - \omega_j$ and $\phi_{ij} = \phi_i - \phi_j$. As in Eq. 6.2, we neglect the sum frequencies $\omega_i + \omega_j$, because they are to fast to be resolved by our probe pulse and average to zero. The difference frequencies, however, are slow compared to the duration of the probe pulse, so that d becomes unity for the homodyned beat pattern.

An exemplary fit of a Stokes signal trace, recorded at 8.5 K, is shown in Fig. 7.29. The general behavior of the measured signal trace is resembled very well, reinforcing our fit approach. Two cut-outs of the fit in Figure 7.30 (b) prove the very good congruence between fit and measurement, even for the high frequency oscillation. Figure 7.30 (a) shows the residual of the fit. Assuming that noise plays a bigger role at high intensity, the statistical deviations in the regions of the beat maxima are no surprise. Next to this, we

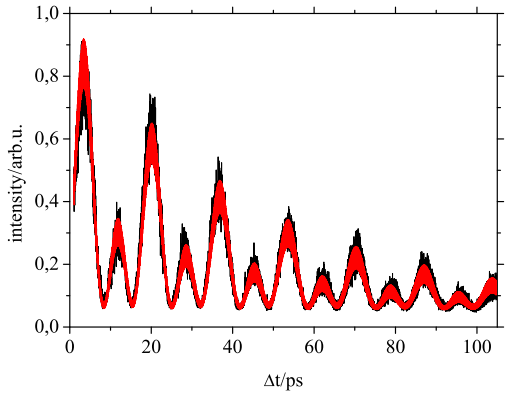

Figure 7.29: *Stokes signal trace at 394 nm (black dots and line) and fit (red line) following Eq.'s 7.3, 7.4, and 7.5. The trace was taken from a measurement with high resolution, high probe beam power, and high local oscillator intensity around 394 nm.*

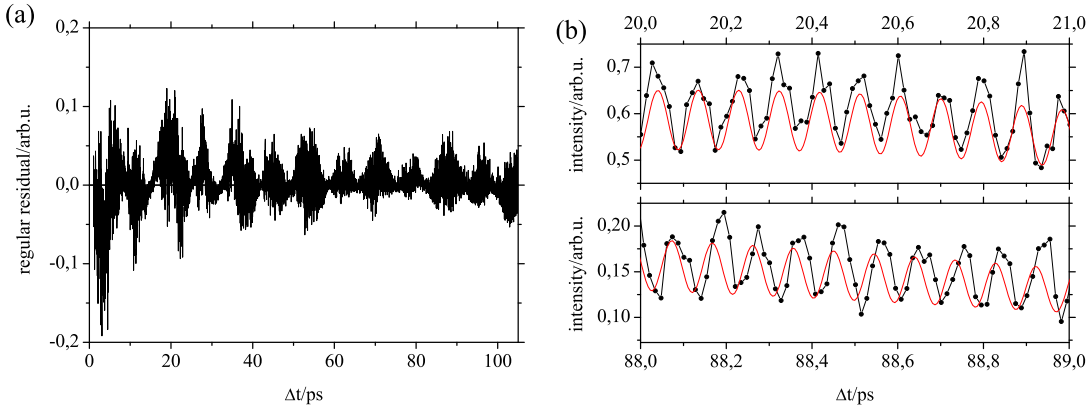

Figure 7.30: *(a) Residual of the fit shown in Fig. 7.29. (b) Two cut-outs of Fig. 7.29 at beat maxima with smaller and larger delays.*

also find systematic deviations. For instance in the beat maxima around 20 ps, shown in the upper panel of Fig. 7.30 (b), where the fit is systematically lower than the signal. This is also reflected in the residual, which we find to be largely positive around 20 ps. On the other hand, we find the 4 ps beat to be overestimated by the fit. Since the local oscillator is smaller than the residual, this mismatch is not caused by a local oscillator fluctuation. It stands to reason that the fit underestimated the decay times, or that the signal did already suffer from higher order effects. Another deviation of the fit is demonstrated in the lower panel of Fig. 7.30 (b). The fit is systematically phase shifted compared to the signal. Accordingly, the residual grows towards larger delays. This phenomena is known to us from test experiments in the gas phase, where we traced it to the inaccuracy of the delay stage.

For many reasons, we have to treat the fit result with caution. Of course, there are statistical error sources like noise and fluctuations of the local oscillator, but more important are systematical and numerical problems. First of all, the pump power dependence of the signal structure is a problem, since it renders our fit approach inappropriate. We must therefore rely on measurements with low pump powers to avoid higher order processes. Secondly, the decay times and frequencies are very similar for the three components. Even more, the splittings between the neighboring frequencies are almost identical. They cannot be distinguished by the homodyned beat pattern, which is only determined by the

difference frequencies. This is particularly troublesome for the fitted decay times, which are dominated by the homodyned contribution and are most sensitive to local oscillator fluctuations, too. Furthermore, the inaccuracy of the delay stage lead to systematical mismatches of the fit and the heterodyne detected signal. However, the major problem is the high number of fit parameters. The fitting function is overparametrized in the homodyne signal. Due to all these reasons, the fitting procedure tended to drive into local minima. Thus, opposite to our gas and liquid phase fits, the starting parameters became very important. For the fit shown in Fig. 7.29, we used the results of our fast Fourier transforms for the frequencies, and the time resolved stimulated Raman gain data of the Schoemaker group [30] for the decay times. Indeed, this approach yielded a satisfying fit, but an unambiguous determination of frequencies and decay times proved to be difficult. Different starting parameters, e.g. a change of the absolute frequencies by 0.1 cm^{-1}, or decay times by 20 ps, led also to converging fits, however with different fit parameters.

The used parameters for the three frequencies in the fit of Fig. 7.29 were $\nu_1 = 352.01(2)$ cm^{-1}, $\nu_2 = 354.01(2)$ cm^{-1}, $\nu_3 = 356.00(2)$ cm^{-1}. Since the numerical standard errors for the given fit variables were misleadingly small, we attribute the inaccuracy of the delay stage as the minimal errors to the presented values. The fit results for the corresponding decay times were $\tau_1 = 101(2)$ ps, $\tau_2 = 80(2)$ ps, and $\tau_3 = 73(2)$ ps. The damping parameter was $d = 0.1$. For comparison, we carried out the same fit with independent parameters for homodyne and heterodyne detected signal. This lead to a very similar fit with, judged from the FFT of the fit residual, comparable frequency mismatch. We obtained identical results from the heterodyned signal for the three frequencies, $\nu_1 = 351.98(4)$ cm^{-1}, $\nu_2 = 353.99(8)$ cm^{-1}, and $\nu_3 = 356.00(4)$ cm^{-1}. The numerical standard errors are bigger than the ones given above, but the results are more trustworthy. They solely depend on the heterodyned signal, which is, in contrast to the homodyned signal, sensitive to the absolute frequencies. From the homodyne signal we determined the energy splittings $\nu_2 - \nu_1 = 2.00(2)$ cm^{-1} and $\nu_3 - \nu_2 = 1.98(2)$ cm^{-1}. The fit results for the decay times, taken from the homodyned signal, were $\tau_1 = 101(4)$ ps, $\tau_2 = 79(3)$ ps, and $\tau_3 = 77(3)$ ps. We neglect the heterodyne detected decay times for the same reasons as in the gas phase. Both fitting procedures yielded the same results from the same starting parameters in the presented case.

Similar fit results for the three frequency components were obtained from a series of fits. However, in view of the discussed problems, the presented standard errors have to be reevaluated. Based on the fit shown in Fig. 7.29, we could follow the high frequency oscillations for about 1100 periods. As in the gas phase, there are small phase shifts between data and fit. These shifts occur in the beginning and in the end of the signal trace, and have always the same direction. Still, the phase shifts never exceed $\pi/2$ within 1100 periods, and we can therefore assume this to be an upper limit for our inaccuracy. This yields $\nu_1 = 351.98(8)$ cm^{-1}, $\nu_2 = 353.99(8)$ cm^{-1}, and $\nu_3 = 356.00(8)$ cm^{-1}. The corresponding beat frequencies are $\nu_2 - \nu_1 = 2.00(8)$ cm^{-1} and $\nu_3 - \nu_2 = 1.98(8)$ cm^{-1}. In the gas phase, where we observed a single sinusoidal oscillation, we attributed similar phase shifts to the inaccuracy of the delay stage. However, the superposition of three frequencies in the solid might be more ambiguous. Therefore, we included a second and third order correction term to compensate the delay stage's inaccuracy. We had already implemented the same approach for the gas phase and yielded an improved fit that exhibited the same parameters as a fit without correction terms. Indeed, the correction terms yielded an improved fit for the solid phase, too. However, the fit results did not differ to a fit without correction terms within 0.02 cm^{-1}.

As was already stated, the decay times were strongly pump power dependent. The fitting of several signal traces, taken from spectra recorded under varying conditions, yielded

therefore a wide range of decay times. Thus, we rely on a measurement with exceptionally slow decay for the quantitative analysis presented here. We assume that pump power effects onto the signal decay time of the presented data are small, because several low pump power measurements yielded similar results. However, the fitted decay times exhibited a high ambiguity, even for a single data trace. The given times for the presented fit, $\tau_1 = 101(4)$ ps, $\tau_2 = 79(3)$ ps, and $\tau_3 = 77(3)$ ps, were obtained for specific starting parameters taken from Ref. [30]. In another fit we chose 90 ps as starting parameter for all three components, and obtained $\tau_1 = 90(2)$ ps, $\tau_2 = 89(2)$ ps, and $\tau_3 = 90(3)$ ps. Unfortunately, there was no qualitative difference between the residuals of both fits. Hence, we have no measure to judge, which fit result is better. In the light of a series of fits, we can only present an average decay time that has a high uncertainty for each component, $\tau_i = 90(20)$ ps.

7.1.3 Discussion

Solid para-hydrogen showed rich dynamics, with a wide range of characteristic periods that correspond to Raman-active transitions in our samples. The nature of these transitions are discussed below, and summaries of our quantitative results for the observed phononic and rotational dynamics are given in Table 7.1 and Table 7.2.

7.1.3.1 Phonon dynamics

As we have shown in Section 7.1.1, the single sinusoidal oscillation observed in the birefringence region of our 2D OKE signal obtained from solid para-hydrogen was heterodyne detected and accordingly analyzed. Due to the absence of a similar 2D OKE response of gaseous or liquid hydrogen samples, we conclude that it is specific solid state response. Thus, it has to originate in the crystal field splitting of a molecular excitation, or in a librational, or phonon excitation. The observed frequency of several ten cm^{-1} and the absence of librational degrees of freedom in spherical para-hydrogen ($J = 0$) indicate that we observed a phonon mode.

A phonon dispersion curve for para-hydrogen was measured in a neutron scattering experiment under similar conditions by Nielsen [45] and is shown in Figure 2.8. From the manifold of possible phonon frequencies in hcp solid hydrogen, we observed only one. This is caused by our excitation mechanism with near infrared light. It restricts the possibly excited phonon modes to the optical phonon branches at the center of the Brillouin zone ($k \approx 0$). Additionally, the pump light is far off-resonant. Hence, only Raman-active phonon modes can be excited. The sole Raman-active, $k \approx 0$ phonon mode of hcp solid hydrogen is marked by an arrow in Fig. 2.8. It is a twofold degenerated, transversal optic (TO) phonon, which is polarized within the hexagonal plane (ab-plane) of the lattice [46].

The impulsive Raman excitation of a phonon mode with our short pump pulse explains the unshifted phase of the observed sinusoidal signal [117]. Furthermore, the twofold degeneracy of the TO phonon is supported by the sensitivity of the 2D OKE signal onto the pump polarization, as discussed in Figure 7.7. We showed that the phase of the signal field is shifted by π, if the pump field polarization is turned by 90°. As was stated above, the orientation of an excitation solely oriented along one fixed axis would not be sensitive onto the pump polarization. Thus, the signal field's phase would be independent from the pump polarization. However, the TO phonon is polarized not along a single axis, but in the ab-plane of the crystal. Therefore, a change in the orientation of the pump field by 90° does affect the orientation of the induced polarization, too. This makes a corresponding exchange of ordinary and extraordinary axis for the probe field possible, which results in the observed signal field phase shift of π.

Our result for the frequency of the Raman-active TO phonon in zero pressure hcp para-hydrogen at 4.2 K, $\nu = 36.75(3)$ cm^{-1}, was obtained from a series of fits to our time resolved 2D OKE spectra. As is summarized in Table 7.1, our finding is in excellent agreement with the 36.79(5) cm^{-1} that were observed by Raman scattering by Silvera et al. [46]. It is also fully consistent with inelastic neutron scattering experiments, carried out by Nielsen [45], which led led to a frequency of 37.3(9) cm^{-1}. However, Silvera et al. had significant problems in determining the linewidth of their Raman peaks. They obtained a Raman linewidth of 1.1 cm^{-1} with error limits of order 0.5 cm^{-1}, which would correspond to a decay time of about 10 ps. Nielsen had even more problems in determining the linewidth of his peaks. From his data he concluded that the phonon linewidth does not exceed 10 percent of its energy, corresponding to a dephasing time $T_2 > 3$ ps for the boundary TO phonon. With 2D OKE spectroscopy we could show that the coherence of the Raman-active TO phonon mode actually lasts significantly longer. In solid para-hydrogen at 4.2 K, using the same series of fits as for the frequency, we observed a lifetime as long as $T_2 = 19(1)$ ps.

It is important to note that the frequency of the TO phonon mode in solid hydrogen is dependent on the sample properties. It is affected by the pressure, the temperature, and the ortho-para ratio of the crystal [118, 119]. Hence, measurements under different conditions should indicate a shift of the TO phonon frequency. Indeed, an exemplary measurement carried out at 7 K shows a decrease to $\nu = 36.55(4)$ cm^{-1}. This is no surprise, since the density of solid para-hydrogen, and therefore the coupling strengths, is temperature dependent. A similar behavior was shown by Silvera et al. for para-deuterium ($J = 1$). They measured an energy decrease for the Raman-active TO phonon from 37.27(5) cm^{-1} at 4.2 K to 35.48(20) cm^{-1} at 14.2 K [46]. Although the shift is small, a systematical study of this behavior with OKE spectroscopy is possible. We also confirmed the dependence on the ortho-para-ratio. Measurements at 6 K on crystals grown from unconverted normal-hydrogen with ortho-hydrogen concentrations of up to 74.9 percent led to a significantly shifted phonon frequency of $\nu = 37.5(1)$ cm^{-1}.

Not only the frequency, but also the lifetime of the TO phonon is dependent on the sample properties. E.g. Silvera et al. demonstrated a significant temperature dependence of the linewidth of their Raman-scattering data [118]. On the other hand it is reasonable to assume that impurities and crystal defects act as scattering centers, which could lead to a dephasing of the phonon wave. Indeed, Schoemaker and co-workers demonstrated that scattering by ortho-hydrogen and other impurities leads to a dephasing of $k \approx 0$ roton waves in solid para-hydrogen [48, 120], and Abram et al. proved the same for $k \approx 0$ vibron waves [29]. Thus, temperature, pressure, ortho-para ratio, and crystal quality might be possible explanations for the discrepancy in the measured lifetime between Silvera et al. and us. However, Silvera et al. reported that their crystals were perfect single crystals, kept under the same conditions as ours [46]. The only difference was a slightly higher temperature of the ortho-para conversion system, 20.4 K instead of 15 K as in our setup, which led to an ortho-concentration of 0.2 percent [38]. As we have seen, the ortho-concentration in our samples ranged from 0.03 to 0.2 percent, very similar to Silvera et al.. Additionally, even though we did no systematical study on the ortho-hydrogen concentration, we found no indication of a drastic change of lifetimes within our experiments. Even in solid normal-hydrogen, with an ortho-content of 74.9 percent, the lifetime decreased only by a factor of two. Hence, we conclude that the Raman-scattering data of Silvera et al. and our 2D OKE data are measured under well comparable conditions. The significant longer lifetime of the TO phonon, measured with a lower uncertainty, demonstrates that the experimental approach, time resolved OKE spectroscopy, is especially suitable for low energy Raman

modes. With this data, a further discussion, revealing the dephasing process, becomes possible and is given in context with our experiments on solid normal-hydrogen in Section 7.2.0.6.

As we have demonstrated, the agreement of the experimental results for the frequency of the Raman-active phonon mode in para-hydrogen is excellent. However, a theoretical simulation of the phonon dispersion relation of solid para-hydrogen has proven to be a hard task. Particular the high energy edge of phonons is still in debate [121, 122]. The agreement of experimental and calculated values of the boundary TO phonon of para-hydrogen is only moderate, too. The results of the present studies are included in Table 7.1. The first attempts on the phonon dispersion relation were carried out by Klein et al., who used a self consistent phonon (SCP) method based on an isotropic Lennard-Jones potential in 1970 [123]. A random phase approximation method was presented by Mertens and Biem in 1971 [124]. Both calculations were especially modified to account for short range correlation effects. The comparison with experimental data for hcp para-hydrogen and hcp ortho-deuterium proves a significantly better agreement with the SCP method applied by Klein et al.. A further inclusion of a translational-rotational coupling was considered by Janssen and Avoird in 1990, who applied a time-dependent Hartree (TDH) formalism based on an ab initio potential [125]. They achieved an excellent agreement with experiment for the rotational excitations, but their results for the phonon energy do not agree better with experimental data than the results of Klein et al.. The latest study on the phonon dispersion relation of para-hydrogen was presented by Saito et al. in 2003 [121]. Unfortunately, they were unable to calculate values for the frequency of the Raman-active TO phonon. However, as all cited calculations, they predict systematically higher phonon energies than the empirical dispersion curve given by Nielsen. Thus, given the excellent agreement of three experimental approaches on the energy of the $k \approx 0$ TO phonon, a further theoretical investigation on the phonon dispersion relation of solid para-hydrogen would be desirable.

7.1.3.2 Rotational alignment dynamics

In the two distinct Raman sidebands, we observed three heterodyne detected frequencies, $\nu_1 = 351.98(8)$ cm^{-1}, $\nu_2 = 353.99(8)$ cm^{-1}, $\nu_3 = 356.00(8)$ cm^{-1}, that are very close to our results for the rotational $S_0(0)$ transition in gaseous and liquid para-hydrogen. Hence, we did successfully observe the rotational alignment dynamics of para-hydrogen in its solid phase. Since we observed only one transition frequency for the $S_0(0)$ excitation of the free molecule, we can conclude that the observed splitting is a solid state effect. The degeneracy of the five orientational M-substates within the lattice is lifted due to the EQQ interaction of the nonspherical $J = 2$ state with the crystal field. Indeed, the rotational excitation interacts with neighboring molecules and may even hop from molecule to molecule. Thus, it becomes delocalized and is described as a Bloch-wave, called roton, that forms broad energy bands [36].

Following van Kranendonk [36], hcp solid para-hydrogen exhibits three $\Delta\mathbf{k} = 0$, $\Delta J = 2$ Raman-active $J = 2$ roton levels, fcc solid para-hydrogen instead only two. The observation of three states is therefore an unambiguous prove that the crystal structure is hcp rather than fcc. Our samples, grown at and above 7 K, displayed a triplet of transition frequencies, even after cooling to 4 K. An analogous behavior was reported by Collins et al. from conventional Raman spectroscopy in 1996 [40]. Grown below 4 K, they found their samples to exhibited both, hcp and fcc structures, of which the latter were irreversible lost after warming to 5.5 K. Hence, our samples had a pure hcp structure for all employed conditions. This approves our expectation and becomes important e.g. for the possible col-

T/K	Method	Reference	ν/cm^{-1}	$\Delta\nu$/cm^{-1}	T_2/ps
		pH_2			
4.2	2D OKE	this work	36.75(3)	0.55	19(1)
5.4	Neutron	Ref. [45]	37.3(9)	< 4	> 3
4.2	Raman	Ref. [46]	36.79(5)	1.1(5)	10
	Theory SCP	Ref. [123]	40.5		
	Theory RPA	Ref. [124]	48.4		
0	Theory TDH	Ref. [125]	45.4		
		o-H_2			
4.2	Raman	Ref. [46]	38.55(5)	1.1(5)	10
	Theory SCP	Ref. [123]	40.8		
		n-H_2			
6	2D OKE	this work	37.5(1)	1.0	11(3)
		o-D_2			
5	Neutron	Ref. [126]	37.0(8)		
4.2	Raman	Ref. [46]	35.83(5)	0.6(5)	18
	Theory SCP	Ref. [123]	38.2		
	Theory RPA	Ref. [124]	45.2		
0	Theory TDH	Ref. [125]	39.0		
		p-D_2			
14.2	Raman	Ref. [46]	35.48(20)		
4.2	Raman	Ref. [46]	37.27(5)	1.3(5)	8
	Theory SCP	Ref. [123]	38.3		

Table 7.1: *Experimental observations and theoretical values for the frequency and lifetime of the Raman-active TO phonon in zero pressure hcp solid hydrogen. Errors are only given for direct experimental results, not for theoretical or deduced values.*

lective excitations, or in the light of inhomogeneous broadening effects for matrix isolation spectroscopy.

Given in order of growing energy, the three Raman-active levels correspond to five orientational substates of the rotational $J = 2$ excitation of para-hydrogen in the hcp lattice, $M = \pm 1$, $M = \pm 2$, and $M = 0$ [36]. Accordingly we assign our results from zero pressure hcp solid para-hydrogen at 8.5 K to the $|M|$-levels, $\nu_{|M|=1} = 351.98(8)$ cm^{-1}, $\nu_{|M|=2} = 353.99(8)$ cm^{-1}, $\nu_{M=0} = 356.00(8)$ cm^{-1}. A comparison of experimental and theoretical results for the $S_0(0)$ transition in cryogenic hcp para-hydrogen is given in Table 7.2. First high resolution Raman spectroscopy data were reported by Bathnagar et al. in 1962 [108]. The most detailed study on the Raman-active roton excitations in hcp para-hydrogen was carried out by Schoemaker and coworkers in the late 1980's [30, 48, 120, 127].

However, they focused their work on the dephasing times T_2 of the roton excitations. The 2D OKE data resemble the experimental data from high resolution Raman scattering very well for the absolute and relative frequencies. The transition frequencies given by Bathnagar et al., still the best experimental data available, are in general somewhat smaller [108]. This might be a temperature and density effect, since Bathnagar et al. performed their Raman scattering at 2 K. To our knowledge, there have been no systematic studies on this topic.

Full agreement to Bathnagar et al. is found about the splittings between the transition levels. From the homodyne detected beat pattern we determined splittings of $\Delta\nu_{12} = \nu_{|M|=2} - \nu_{|M|=1} = 2.00(8)$ cm^{-1} and $\Delta\nu_{02} = \nu_{M=0} - \nu_{|M|=1} = 1.98(8)$ cm^{-1}. This also compares well to time resolved stimulated Raman gain (TRSRG) experiments with picoseconds resolution carried out at 8 K by the Schoemaker group, who obtained $\Delta\nu_{12} = 2.00(1)$ cm^{-1} and $\Delta\nu_{02} = 1.96(2)$ cm^{-1} [30, 48]. Slightly higher are results from high resolution Raman spectroscopy experiments that were carried out at 9 K by the Schoemaker group as well, $\Delta\nu_{12} = 2.104(16)$ cm^{-1} and $\Delta\nu_{02} = 2.055(11)$ cm^{-1} [48, 120]. However, they determined the center of the triplet to be 355 cm^{-1} in the same experiment. Since their results from high resolution Raman spectroscopy are systematically higher as the ones reported by Bathnagar et al., Collins et al., and the ones found via 2D OKE spectroscopy by us, we assume that Schoemaker and his coworkers suffered from a scaling error.

The determination of the dephasing times T_2 of the roton excitations proved to be most difficult. There are several reasons for this, notably the high pump power dependence of the signal in the Raman sidebands, the ambiguity of the homodyned signal onto the substates, the small influence of the decay time on the quality of the fit, and the hard to control local oscillator. Additionally, the dependence onto impurities is high. Following the Schoemaker group, an increase from $c_{ortho} = 0.05\%$ to $c_{ortho} = 0.2\%$ decreases the dephasing times by about 15% [48]. It is interesting to note that this impurity induced dephasing has its origin in the wave-like character of the roton excitation. The $\mathbf{k} \approx 0$ roton-wave propagates in a pure sample, and an impurity acts as a scattering center. Independent of the kind of impurity, it does not share the energy levels of para-hydrogen and may therefore be treated as a defect site for the propagation of the roton-wave. The Raman-active $\mathbf{k} \approx 0$ rotons scatter on these defect sites into rotons with the same energy and different $\mathbf{k}$ vectors. Thus, the coherent state with its definite $\mathbf{k}$ vector decays. Due to the delocalized, Bloch-wave character of the $J = 2$ excitation in the solid, its dephasing exhibits therefore the very opposite dependence onto impurities than in the gas phase (see Section 6.3.0.4).

A rough estimate of $2\tau_{hom} = T_2 \leq 120$ ps for the dephasing times follows from the decay of the homodyne detected beat pattern, as presented in Fig. 7.13. From our fitting attempts we obtained an average decay for all three components of $2\tau_{hom} = 90(20)$ ps. Taking into account the uncertainty of the ortho-hydrogen concentration, we yield $T_2 = 90(30)$ ps for $c_{ortho} = 0.1\%$. Unfortunately, we were not able to separate the decays of the three signal components, neither spectrally, nor via the fitting procedure. Instead, the fit exhibited a high ambiguity onto the decay times of the single components. This is reflected in the large error that we attribute to our result. However, our 2D OKE data do not suffer from a high inaccuracy, but rather from a high ambiguity in the case of the $S_0(0)$ transition in solid para-hydrogen. Using the decay times that were reported by the Schoemaker group from TRSRG spectroscopy as starting parameters, we obtained a satisfying fit with very similar dephasing times as reported by them [30]. In agreement with their earlier high resolution Raman scattering experiments, they reported significant differences between the dephasing times of the different substates [120]. However, the results of their two

approaches differed quantitatively by a factor of almost two. Hereby it is interesting to note that the theoretical expectations of the Schoemaker group were qualitatively different [127]. Following their calculations, the three dephasing times are almost equal, 95 ps, 92 ps, and 89 ps. Indeed, a fit of our data with 90 ps as starting parameter for all components yields a satisfying fit with 90(2) ps, 89(2) ps, and 90(3) ps, very close to the theoretical data. Thus, we are not able to judge between their experiments and their theory. It is possible that the Schoemaker group suffered from a systematic experimental error in their TRSRG experiments that they were not aware of.

As we have seen above, the recorded 2D OKE spectra differed widely in their sideband dynamics. The dynamics, however, depend on the observed splitting of the rotational $S_0(0)$ transition, which is caused by the EQQ interaction of the rotational $J = 2$ excitation with the crystal field. Hence, the origin of the sideband variations is the geometry dependency of the orientational M-substates. Their excitation with the linearly polarized pump pulse depends on the orientation of the crystal, which was neither homogeneous, nor easily controllable (see Fig. 3.11). A wide range of variations is therefore no surprise. Still, the sidebands exhibited very distinct structures in each single spectrum. This indicates that the specific interaction volumes had homogeneous crystal orientations - a finding that coincides with our assumptions in Section 5.1.1. Most interesting is also the phase of the rotational beats. In the birefringence region we found that the phase of the impulsively excited TO phonon at $\Delta t = 0$ is always zero. If this would the case for the rotational signal fields, they would be in phase at $\Delta t = 0$ and we'd had to observe a rotational beat. Indeed, there were examples for this, but in general we observed a rephasing at π. This behavior is caused by the sign of the rotational signal fields. The probing process, like the pump process, depends on the orientation of the M-substates. Thus, the absolute value and the orientation of the third order polarization varies for the substates. Dependent on the polarization vector the signal field has a positive or negative sign, corresponding to a phase jump of π. One might assume that at least Stokes and anti-Stokes sideband of a single spectrum ought to be identical. We found that this is not the case. Obviously, the probabilities for Stokes and anti-Stokes transitions of the probe beam are orientation dependent, too. Nevertheless, we observed distinct correlations between the sidebands. A ninety degree turn of the pump polarization e.g. exchanged the sideband patterns of an exemplary measurement. Hereby we have to keep in mind that we have observed three rotational levels that correspond to five Raman-active orientational states. Thus, the observed dynamics cannot be traced back to their substates without ambiguity.

7.1.3.3 Stimulated Raman gain

In opposition to our expectations from Eq. 4.39, we observed an exponential growth of the rotational Raman sidebands with the power of the pump beam. In fact, we have to conclude that Eq. 4.39 is inappropriate to describe our 2D OKE spectra of para-hydrogen. In classical OKE spectroscopy, the pump pulse is considered to be short compared to the observed transition frequencies ω_s. Hence, it contains a broad spectra of frequencies ω, including $\omega - \omega_s$. All dynamics that happen to be in the bandwidth of the pulses are excited via stimulated Raman scattering processes, as introduced for SRG spectroscopy in Eq. 4.33. This process is linear in $I_{pump}(\omega)$ and in $I_{pump}(\omega - \omega_s)$ (see Eq. 4.36). Consequently, the excited population scales with I^2_{pump}, as the observed homodyned OKE signal for nitrogen. However, ω_s exceeds the bandwidth of 114 cm^{-1} (FWHM) of our pump pulse due to the large rotational constant of hydrogen. The wing of the Gaussian pump pulse that stimulates Raman transitions with the center line of the laser is therefore relatively weak. Still, one may observe a significant intensity gain, depending on the gain

	c_{ortho}/%	T/K	Method	Reference	ν/cm^{-1}	T_2/ps
$\|M\| = 1$	0.1	8.5	2D OKE	this work	351.98(8)	90(30)
		2	Raman	Ref. [108]	351.84	
	< 1	5.5	Raman	Ref. [40]	352	
	0.05(3)	9	Raman	Ref. [120]		171(16)
	0[a]	8	TRSRG	Ref. [30]		102(7)
	0	4.2	Theory	Ref. [127]	354.346	95
			Theory	Ref. [40][b]	352.0	
$\|M\| = 2$	0.1	8.5	2D OKE	this work	353.99(8)	90(30)
		2	Raman	Ref. [108]	353.85	
	< 1	5.5	Raman	Ref. [40]	354	
	0.05(3)	9	Raman	Ref. [120]		125(9)
	0[a]	8	TRSRG	Ref. [30]		81(9)
	0	4.2	Theory	Ref. [127]	356.821	92
			Theory	Ref. [40][b]	354.5	
$M = 0$	0.1	8.5	2D OKE	this work	356.00(8)	90(30)
		2	Raman	Ref. [108]	355.83	
	< 1	5.5	Raman	Ref. [40]	356	
	0.05(3)	9	Raman	Ref. [120]		98(9)
	0[a]	8	TRSRG	Ref. [30]		71(5)
	0	4.2	Theory	Ref. [127]	359.279	89
			Theory	Ref. [40][b]	357.0	

Table 7.2: *Experimental observations and theoretical values for the frequency and lifetime of the $S_0(0)$ transition in zero pressure hcp solid para-hydrogen.*

[a]Extrapolation from a concentration study to $c_{ortho} = 0$ %.
[b]With the theory given by van Kranendonk [36].

factor g_s of the material. By virtue of the high density of the solid and relatively narrow linewidths, the gain factor of the roton transitions in solid para-hydrogen becomes large. Hence, the stimulated scattring of the high pump laser intensity at the center line ω_0 may become very efficient. The scattered intensity at $\omega_0 - \omega_s$ may therefore exceed the incident intensity $I_{pump}(\omega_0 - \omega_s)$ in the wing of the Gaussian pump pulse. In this case, the system runs into a stimulated Raman scattering regime and the Stokes-scattered intensity grows exponentially with the pump beam power, as described by Eq. 4.32. Thus, the energy that is deposited into the sample by the pump process, and therefore the coherently excited population, grows exponentially with the laser intensity, too. Accordingly, the intensity of the observed 2D OKE signal depended exponentially on the pump power.

Albeit bigger than for the pump laser, the bandwidth of the probe laser of 170 cm^{-1} (FWHM) is also smaller than the transition frequency. Hence, the probing process might also drive into a stimulated Raman scattering regime. The connection to the pump intensity is clear: an increased excitation density of the sample leads to an increased Raman gain for the probe laser. Indeed, we observed distinct effects that correspond to an exponential amplification of the Raman scattered probe intensity, notably a steepening of the Raman beats and decreased decay times. We did not observe the latter in the liquid over one order of magnitude in scattered intensity, an indication that the described process plays no role

below a certain threshold. Hence, decay times that were determined from measurements with low Raman gain are a good measure for the dephasing time T_2. However, measurements with high Raman gain, e.g. due to high pump power, may only give an lower limit for T_2.

7.1.3.4 Higher order Raman transitions

Next to the stimulated Raman amplification of our signals, we observed the creation of higher order Raman sidebands at $\omega_0 \pm n\omega_s$ ($n = 0, 1, 2, 3$). Indeed, solid para-hydrogen is known to be a very efficient Raman shifter, since the combination of high density and narrow linewidths lead to high Raman gain factors [128]. Most intense was the second order Raman band in the birefringence region, where the intense probe laser center line stimulated the process. It exhibited a higher pump power dependence, and also different dynamics than the original Raman sidebands at $\omega_0 \pm \omega_s$. Hereby we must keep in mind that we detected only the part of the original Raman response, which passed the analyzer. Even more, we detected only a tiny fraction of the probe laser power, since we worked with a crossed polarizer-analyzer pair. The higher order Raman exhibited always the same structure, as being composed of a 2 cm^{-1} and a 4 cm^{-1} signal field, including homodyned beatings with 6 cm^{-1} and a 8 cm^{-1}. These signal fields heterodyned with the local oscillator field, the phononic signal field, and the rotational signal fields, too. Thus, we found the corresponding sum and difference frequencies in our signals, and also the spectral effects that are caused by the phase distribution of fields. The higher order Raman was driven by the intensity of the original Raman response. The homodyned intensity in the beats of the original Raman response in the sample, i.e. before the analyzer, acted as source intensity, which was most efficiently seeded by the high intensity center line of the probe laser. Again, we want to emphasize that only a fraction of this original Raman response passed the analyzer, and that the analyzer induced phase jumps of π between the signal fields of the orientational substates. Hence, the dynamics of the detected rotational Raman response did not necessarily equal the ones of the original Raman response in the sample. However, the two additional signal fields of 2 cm^{-1} and a 4 cm^{-1} carried no additional information about the excited transitions, since both were only the result of higher order effects.

7.2 Solid normal-hydrogen

To complement our para-hydrogen data, we carried out a series of measurements with hydrogen crystals, grown from room-temperature normal-hydrogen gas. With an ortho-para ratio of about 3:1 (see Fig. 3.1), we expected normal-hydrogen crystals to behave rather like solid ortho-hydrogen.

7.2.0.5 Solid normal-hydrogen

The growth of the samples was very similar to para-hydrogen crystals, resulting in transparent crystals of 3 cm thickness. The crystals were grown at 11 K and kept at 6 K, to ensure that the lattice is purely hcp. Grown from room temperature hydrogen as it comes in the bottle, the crystals had an ortho-hydrogen concentration of up to 74.9 percent. This ortho-hydrogen concentration decreases over time with a conversion rate of 1.90(5) percent/h, due to conversion processes caused by the low temperature and the inherent magnetic moments of $J = 1$, $I = 1$ ortho-hydrogen [35]. In contrast to solid para-hydrogen, some of the measurement carried out with solid normal-hydrogen applied relatively high

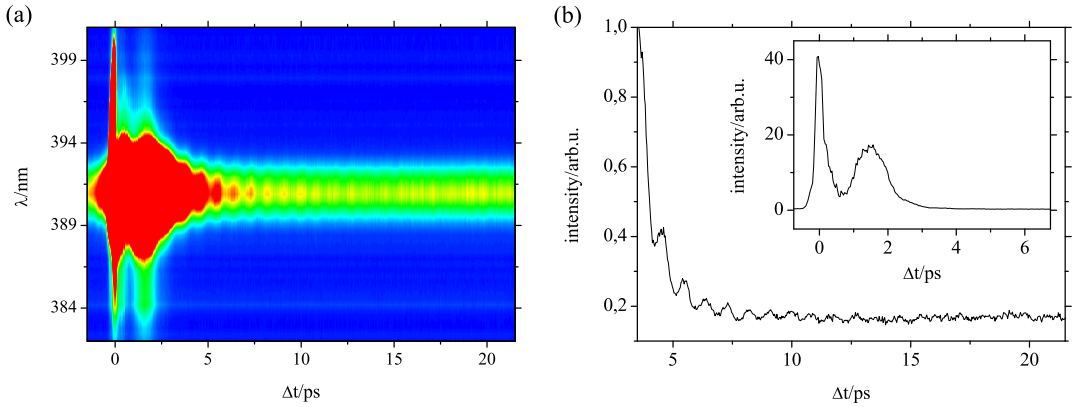

Figure 7.31: *(a) Contour plot measured from a zero pressure normal-hydrogen crystal at 6 K. (b) Birefringence trace from Fig. 7.31 (a), showing a weak phonon modulation after 4 ps. The inlet demonstrates the behavior in the first few picoseconds. After the sharp electronic overlap (FWHM ≈ 250 fs) an intense signal builds up that rapidly decays after 2 ps.*

pump beam powers. Even pump beam powers of up to 15 mW did not lead to an immediate deterioration of the crystal. This indicates that the destruction threshold for solid normal-hydrogen is up to one order of magnitude higher than for solid para-hydrogen.

Figure 7.31 (a) shows a typical contour plot, measured with solid normal-hydrogen. It consists solely of a birefringence response, without any significant Raman sidebands. The lack of Raman sidebands, including roton Raman sidebands, was typical for all measurements done with normal-hydrogen. The birefringence trace in Figure 7.31 (b) contains a single sinusoidal oscillation with a period of about 900 fs, similar to the birefringence trace measured from solid para-hydrogen in Fig. 7.3 (b). However, the birefringence traces measured from para- and normal-hydrogen behave different in the first two picoseconds. A comparison of Fig. 7.3 (b) and the inlet in Fig. 7.31 (b) shows that both exhibit a sharp (250 fs FWHM) electronic overlap signal at $\Delta t = 0$. For normal-hydrogen, this is followed by broad feature (0.5 - 1 ps FWHM), which can even exceed the intensity of the electronic overlap. The shape and height of this feature varied for different experimental conditions, but it was always present for normal-hydrogen. Since solid para-hydrogen lacked this kind of signal, we consider it to be a specific normal-hydrogen effect.

7.2.0.6 Phonon dynamics

The observed single sinusoidal oscillation was excited and observed in the same way as in para-hydrogen. Both samples exhibit a similar oscillation period and decay time of the same order of magnitude. Obviously, the 900 fs oscillation in solid normal-hydrogen stems from the same Raman-active TO phonon mode as the one already discussed for solid para-hydrogen. Therefore, we carried out an analogue analysis, applying Eq. 6.1 as a fit function. From a series of ten measurements, we derived the frequency and dephasing time of the TO phonon of a zero pressure normal hydrogen crystal at 6 K to be $\nu = 37.5(1)$ cm^{-1} and $T_2 = 11(3)$ ps.

Compared with zero pressure solid para-hydrogen at 4 K, the frequency is significantly higher (see Table 7.1). This is no temperature effect, since the volume expansion due to a higher temperature would lead to lower phonon energies. The difference in the phonon frequencies is rather caused by a change of the intermolecular potential due to the anisotropic EQQ interaction between ortho-hydrogen molecules [118]. The changed potential also

causes a significant decrease of the molar volume (see Fig. 2.5), from 23.16 cm^3/mol for para-hydrogen to 22.97 cm^3/mol for normal-hydrogen at 4.2 K [35]. Taking the potential and the volume effect into account, the frequency dependence on the ortho-hydrogen concentration C_1 and the volume V at a constant temperature T_0 follows from [118]

$$\nu(C_1, V, T_0) = \nu_0 - \alpha_{TO} C_1 - \gamma \nu_0 \Delta V / V_0. \tag{7.6}$$

The parameter $\alpha_{TO} = 0.75(12)$ cm^{-1} and the Grüneisen parameter $\gamma = 2.05$ are given by Silvera et al. [118]. The first describes the ortho-para dependence of the pair potential, and the latter the described volume effect. For $T_0 = 4.2$ K and zero pressure, with the given molar volume for para- and normal-hydrogen and $\nu_0(C_1 = 0, V_0, T_0) = 36.75$ cm^{-1}, the TO phonon frequency would increase to 37.9 cm^{-1} for an ortho-hydrogen concentration of $C_1 = 0.75$. This value is higher than the 37.5(1) cm^{-1} observed by us. However, as we have seen for para-hydrogen, a simultaneous temperature increase to 6 K slightly decreases the frequency. Given this and the uncertainty in the parameters of Eq. 7.6, our result is reasonably consistent with an estimated value of 37.9 cm^{-1} for normal-hydrogen at 4.2 K.

As we have seen, the decay times measured by Silvera et al. have large uncertainties and do not fit to the new results presented by us. It is nevertheless interesting to note, that they observed the same lifetimes for both species, para- and ortho-hydrogen [46]. In normal-hydrogen, we observed a dephasing time for the TO phonon of 11(3) ps, which is a factor of two smaller than in para-hydrogen (see Table 7.1). How can we explain such a change? The decay of a coherent phonon wave can happen via two distinct channels: (a) inelastic scattering into other modes (T_1), and (b) elastic $\mathbf{k}$ scattering at defect sites (τ_{ph}), which leads to a randomization of the wavevector. Additionally, (a) might become more efficient at a defect site, depending on the density of states. Thus, a large inhomogeneity or concentration of impurities, which act as defect sites, can lead to a significantly shortened lifetime, and therefore to a strong dependence on the ortho-para ratio. This was observed for delocalized, high energy, rotational and vibrational waves in hydrogen crystals, which exhibit a very strong correlation between lifetime and ortho-para ratio [29, 48, 120].

Following Eq. 7.6 the different pair potentials for ortho- and para-hydrogen shifts the TO phonon frequency by $\alpha_(TO) = 0.75(12)$ cm^{-1}, three times more than the observed lifetime broadening in para-hydrogen. Hence, random clusters of ortho- or para-hydrogen molecules could act as such defect sites. Given this, it is surprising that the TO phonon in normal-hydrogen, a very inhomogeneous mixture of 74.9 percent ortho- and 25.1 percent para-hydrogen, shows shortened lifetime by only a factor of two. We conclude that process (b), inelastic scattering at ortho-hydrogen defect sites, plays no significant role in the dephasing of the TO phonon in solid para-hydrogen. Thus, the decoherence of the low energy phonon is dominated by direct population loss due to inelastic scattering (T_1), which happens faster than any pure decoherence due to elastic scattering (τ_{ph}). This is plausible, because the relaxation due to multiphonon processes also becomes more probable for low energy excitation. The higher energy roton (≈ 350 cm^{-1}) and $v = 1$ vibron (≈ 4150 cm^{-1}) excitations are significantly longer lived, ≈ 100 ps, respectively ≈ 5 μs [120, 129], hence τ_{ph} becomes the dominant term if impurities are present.

However, we assume that the factor of two difference between the TO phonon lifetimes in para- and normal-hydrogen is also not dominated by inelastic scattering. There is an additional effect that must be considered. The mixture of ortho- and para-hydrogen might also lead to inhomogeneous broadening. How can we understand this? Well, let's suppose that the normal-hydrogen crystal consists of large, homogeneous areas of ortho- or para-hydrogen. This is a simplified approach, because ortho-hydrogen tends to cluster only at low temperatures [35], but it provides a good visualization. With a phonon energy splitting

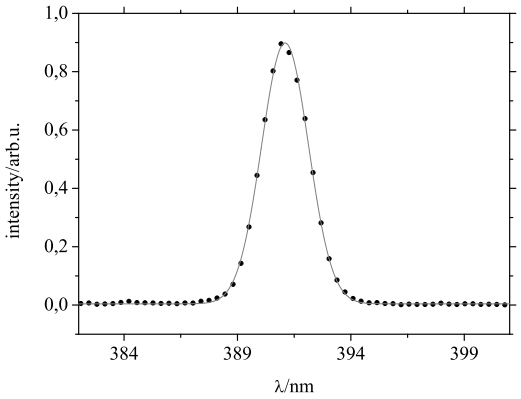

Figure 7.32: *Cut at $\Delta t = 2.5$ ps through the initial birefringence response from the first picoseconds of the contour plot Fig. 7.31 (a). The measured signal (dots) is perfectly Gaussian (line) and has the same center wavelength (391 nm) and width as the probe beam (see Fig. 5.5 (d)).*

of 0.75(12) cm^{-1}, the phonons in pure ortho- and para-hydrogen crystals develop opposite phases after about 22 ps. Therefore, the para-hydrogen content of about 25 percent could lead to a nonexponential decay of the measured signal. Since this happens within the same time scale as the depopulation, inhomogeneous broadening could significantly affect our signal. In the simple picture applied, the further propagation would lead to a rephasing after 44 ps, which was never observed by us. However, random positions of para-hydrogen molecules in the lattice lead to a Gaussian distribution of frequencies. Whereas such a distribution shows no rephasing, it shows an additional nonexponential decay leading to a non-Lorentzian linewidth. Unfortunately, we cannot prove this effect within our accuracy. But it is most likely, that it contributed to our data. We therefore assume that there is no significant difference in the T_1 times between para- and normal-hydrogen.

7.2.0.7 Orientational interactions

In contrast to solid para-hydrogen, normal-hydrogen exhibited a strong birefringence response within the first few picoseconds (see Fig. 7.31 (b)). In fact, the signal is orders of magnitude higher than the local oscillator intensity. Hence, we are in the homodyne detection regime (Eq. 4.40). The feature rises for about 1.5 ps, and decays rapidly afterwards. However, it does not exhibit any significant modulation. The latter could be caused by two contradictory sources. On the one hand, the time resolution of the homodyne detection, determined by the 130 fs probe pulse, could lead an averaged out signal, and on the other hand, the rapid decay within 3 ps could be faster than inherently overdamped dynamics.

As described above, the interaction with the probe beam is based on a Raman-transition. Hence, high energy excitations of several hundred wavenumbers, which exceed the bandwidth of the laser pulse, lead to signal fields that are spectrally separated from the probe field. The complete 2D OKE signal in Fig. 7.31 (a) reveals no indication that the intense signal within the first picoseconds is spectrally shifted. Figure 7.32, a cut through the described feature along the wavelength axis of Fig. 7.31 (a) demonstrates that its main intensity forms an unshifted and perfectly Gaussian peak, exactly resembling the width and spectral position of the probe pulse. Thus, we exclude high energy excitations to be the origin. Hence, the observed decay within 3 ps happens faster than the underlying dynamics, which must therefore correspond to low energy (< 6 cm^{-1}) excitations.

As we have seen, the observed initial birefringence response of normal-hydrogen cannot

stem from high energy excitations. Thus, it is not caused by a molecular vibration or rotation. There are also no optical phonon modes with energies below 6 cm^{-1} (see Fig. 2.8), and the sole Raman-active phonon in hcp solid hydrogen was already identified above. Libron modes, a prominent feature of the ordered state of $J = 1$ hydrogens [38, 44], are of low energy. They stem from long range orientational ordering of the $J = 1$ molecules. In the ordered $Pa3$ fcc phase of ortho-hydrogen, Raman-active libron modes can be found in an energy range from 6 to 12 cm^{-1} [130]. However, librons are absent in the disordered hcp phase, in which our samples are prepared. Hence, the observed excitations are no collective phonon or libron modes.

We assign the observed signal to orientational transitions caused by the EQQ interaction in pairs and clusters of $J = 1$ molecules. The spectroscopy of isolated pairs of ortho-hydrogen molecules in solid para-hydrogen reveals well separated transitions with energies below 6 cm^{-1} [49]. However, normal-hydrogen offers a multitude of possible surroundings and clusters, which cause a strong inhomogeneous broadening. Observed in the time domain, such a broad, random superposition of frequencies dephases rapidly and does not exhibit any recurrences. Hence, orientational excitations of pairs and clusters might indeed lead to the observed initial birefringence response in solid normal-hydrogen.

7.2.0.8 Rotational alignment dynamics

In contrast to pure para-hydrogen, which exhibited an intense, long living rotational Raman response (see Fig. 7.2), nothing comparable was observed in solid normal-hydrogen (see Fig. 7.31 (a)). Neither time resolved dynamics, nor distinct spectral shifts corresponding to the expected rotational Raman transition of para- ($J = 2 \leftarrow 0$), or ortho-hydrogen ($J = 3 \leftarrow 1$) were present. Fig. 7.31 (a) contains only tiny signals that stretch as wings of the intense initial birefringence response into the rotational anti-Stokes region in the first picoseconds. As we did see, the intensity of the Raman sidebands in para-hydrogen grows exponentially with P_{pump}. Due to the high destruction threshold of solid normal-hydrogen, we were able to carry out some of our measurements with significantly higher pump beam power than applied for para-hydrogen. Thus, it seems even more surprising that we have not observed any significant roton Raman sidebands in normal-hydrogen.

However, the high energy of the $S_0(1)$ transition in ortho-hydrogen corresponds to a period below 60 fs. Since our laser pulse durations are significantly longer, neither an efficient pump ($\Delta t_{pump} = 166$ fs), nor an efficient probe ($\Delta t_{probe} = 130$ fs) step is possible. Hence, only para-hydrogen might have contributed to our 2D OKE data. This already reduces the possible rotational alignment signal significantly, since normal-hydrogen has only a para-hydrogen concentration of 25%. This high ortho-hydrogen content also reduces the lifetime and therefore increases the linewidth of the $S_0(0)$ transition in cryogenic normal-hydrogen. The Schoemaker group studied the linewidth of the $J = 2$ rotons in para-hydrogen up to an ortho-hydrogen concentration of five percent, and reported a linear depence on c_{ortho} [48]. A linear extrapolation yields dephasing times of about 1 ps for the $S_0(0)$ transition of para-hydrogen in normal-hydrogen. Indeed, a linear extrapolation from 5% to 75% might be justified to a certain extend, since the origin of the dephasing is an energy mismatch between neighboring molecules, which prohibits the hopping of the rotational excitation. This means that the decay time of the homodyne signal would decrease to about 0.5 ps. Thus, the tiny intensities that we observed in the rotational anti-Stokes region might be caused by rapidly decaying rotational transitions.

8 Infrared absorption experiments

"In a nutshell, the IR spectrum of a free rotor in a cryogenic matrix can be understood as a low-temperature gas-phase rovibrational spectrum, with additional splittings and line broadening due to the dopant-host interactions."

M. E. Fajardo [11]

We determined the properties of our samples by their infrared absorption. This means, firstly, by the fundamental vibrational absorption of solid hydrogen itself, and, secondly, by the absorption of dopant species. By this, we learned how to control the growth and stability of pure and doped hydrogen matrices. The applied setup is described in the first section of this chapter. The second and third section deal with the analysis of the fundamental vibrational band of hydrogen and describe our findings from the spectroscopy of dopant species in solid hydrogen, respectively. The last section gives an outlook onto the promises and problems of time resolved 2D OKE spectroscopy on matrix isolated species in hydrogen crystals in the light of the absorption spectroscopy we have carried out.

8.1 FTIR spectroscopy setup

We carried out infrared absorption spectroscopy on our solid hydrogen samples with a Fourier transform infrared (FTIR) spectrometer BRUKER IFS 55 EQUINOX®. It had an ultimate resolution of 0.5 cm^{-1}, an accuracy of 0.01 cm^{-1}, and a spectral range from 600 to 12,000 cm^{-1}, using a MCT detector. In general, the spectra were taken from 1,000 to 5,500 cm^{-1}, accumulating 32 scans with a resolution of 1 cm^{-1}. We used it in an external mode, the setup is shown in Figure 8.1. In order to increase the signal to noise ratio, we used gold coated parabolic mirrors and silver coated plane mirrors with high reflectivity in the infrared. A good IR transmissibility of the cryostat's and the cell's windows was achieved by using CaF_2, which shows a good transmission in the infrared range down to 1,280 cm^{-1}, .

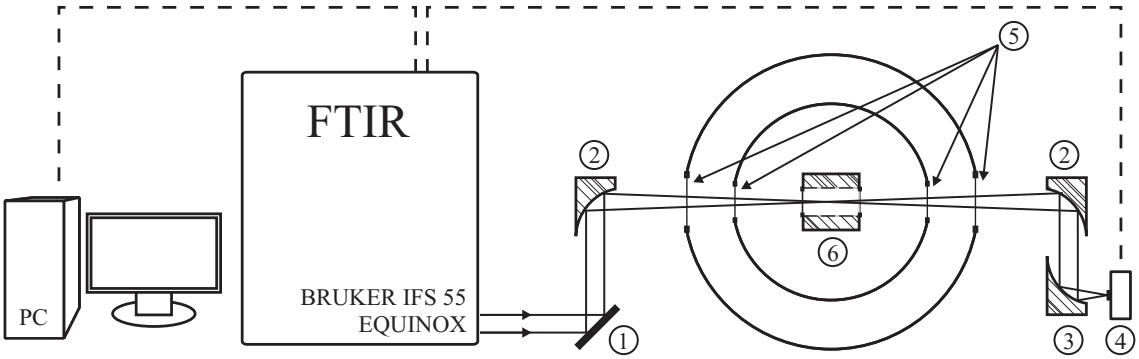

1 Folding mirror, 2 Parabolic mirror (f = 30 cm), 3 Parabolic mirror (f = 5 cm), 4 MCT detector, 5 Cryostat CaF_2 window, 6 Enclosed cell with CaF_2 windows

Figure 8.1: *Schematic drawing of the FTIR spectroscopy setup.*

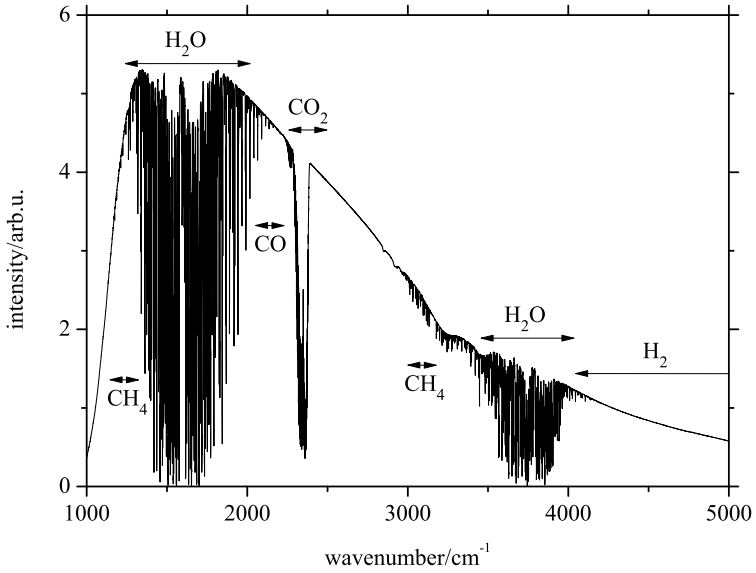

Figure 8.2: *Intensity profile of the used globar broadband radiation source, detected with the setup shown in Figure 8.1. Clearly visible are strong H_2O and CO_2 absorption bands.*

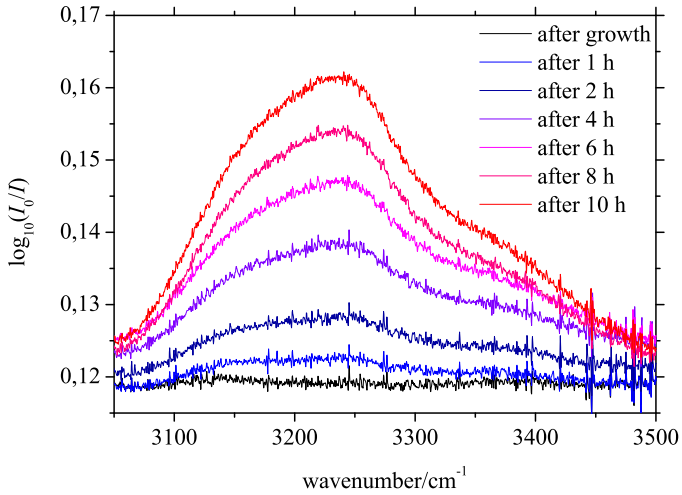

Figure 8.3: *The broad ν_{OH} absorption band of water ice as it grows over time on the liquid nitrogen radiation shield's windows due to a small leakage into the sample cryostat's isolation volume. It was observed simultaneously with a para-hydrogen crystal that was kept at 4.4 K.*

Because we did not purge the setup with dry and CO_2 free air, all our spectra are disturbed by the strong H_2O and CO_2 absorption bands, located around 1,600 and 3,800 cm^{-1} [131], and 2,350 cm^{-1} [132], respectively, which can be seen in Figure 8.2. But, as one can see, these bands do not interfere with the absorption of solid hydrogen between 4,000 and 5,500 cm^{-1} [3] or the absorption of our test dopants, which lie around 1,310 cm^{-1} and 3,020 cm^{-1} for CH_4 [10], and around 2,140 cm^{-1} for CO [133].

All spectra were recorded using a scan of the empty cell before crystal growth as reference. However, the optical quality of crystals and the position of the infrared light beam in the crystal varied. Thus, scattering led to a varying offset in the spectra. Scattering could also be caused by amorphous solids (e.g. water ice) that condensed on the cell's and the liquid nitrogen radiation shield's windows. Hence, a leakage, or degassing into the sample

cryostat's isolation volume had to be avoided. In Figure 8.3 the growth of a water ice film is shown. In this case, the strong infrared absorption of the ν_{OH} band of water ice, located between 2,800 and 3,800 cm^{-1} [134], would have not been a problem for our purposes. But it led in addition to scattering and caused a slightly increasing offset in a broad wavelength range, visible in the wings of Fig. 8.3.

8.2 Solid hydrogen spectroscopy

The properties of hydrogen crystals depend strongly on the ortho-hydrogen concentration. Hence, it was very important to control the efficiency of our ortho-para conversion setup. The infrared spectra of solid hydrogen reflect the relative ortho-hydrogen concentration. Therefore they offer an easy possibility to determine the ortho-para ratio spectroscopically. A general introduction into the absorption spectroscopy of solid hydrogen is given in the first part of this section. The second part describes how we used this to determine our ortho-para conversion efficiency.

8.2.1 The infrared absorption spectra of solid hydrogen

As a homonuclear, diatomic molecule, isolated hydrogen is Raman active, but infrared inactive. Almost immediately after the discovery of the Raman effect in 1928, the Raman spectrum of liquid normal hydrogen was observed by McLennan and McLeod [135] in 1929. They found a vibrational Raman transition, $v = 1 \leftarrow 0$, at 4,149 cm^{-1} and two rotational transitions, $J = 2 \leftarrow 0$ and $J = 3 \leftarrow 1$, at 354 cm^{-1} and 588 cm^{-1}, respectively. However, analogous rotational and vibrational infrared absorption transitions can be induced by intermolecular forces, too. In the gas phase, hydrogen may become infrared active by virtue of electric dipole moments that are induced by multipolar interactions, and isotropic and anisotropic overlap interactions among the molecules [136]. This was first observed by Welsh et al. in 1949, who studied the infrared absorption of gases at high densities [137]. In mixtures of gaseous hydrogen with foreign gases they observed absorptions proportional to the partial pressure of the foreign gas around 4,155 cm^{-1}, the vibrational frequency of the hydrogen molecule. First absorption spectra of liquid and solid hydrogen were reported in 1955 by Hare et al. [3, 138] in the same spectral region. They exhibited a multitude of lines, strongly dependent on the ortho-hydrogen concentration [138]. Similar absorption spectra, recorded in our laboratory and in excellent agreement with Hare et al., are shown in Figure 8.4. Over the years the development of high resolution and high sensitivity Fourier transform and tunable difference Laser frequency spectrometers, coupled with long multipass cells, opened gates to a high level of understanding of the solid hydrogen absorption. Spectroscopic information ranging from 40 cm^{-1} [139] to 19,150 cm^{-1} [140], over wide ranges measured with resolutions of 0.1 to 0.01 cm^{-1} [6], and partly with resolutions up to 0.0005 cm^{-1} and an accuracy of 0.0020 cm^{-1} [141] are nowadays available, observing transitions with integrated absorption coefficients as small as $2.2(3) \times 10^{-23}$ $cm^3 s^{-1}$ [142]. This supplied the basis for an extensive, and still ongoing detailed theoretical description of solid hydrogen transitions [44, 143–146].

First we have to introduce the standard notation convention of vibration-rotation transitions that will be used in the following. E.g., we will denote certain transition as $Q_1(0)$ or $S_0(1)$ transitions. Capital letters Q, S, U, and so on represent a change of the rotational state by $\Delta J = 0$, 2, 4, and so on. Their subscripts 0, 1, 2, and so on show the vibrational quantum number v in the upper state. The subscript R is used for phonon sideband transitions with simultaneous molecular and lattice excitations. The number in parentheses

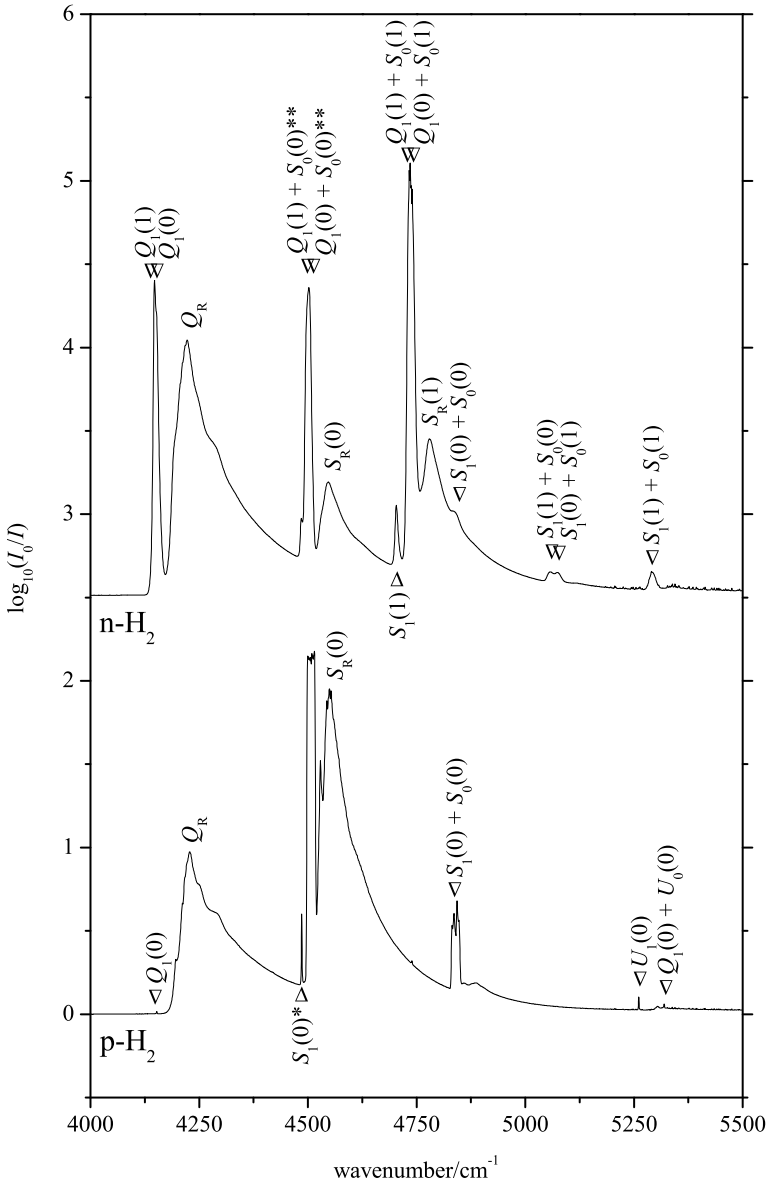

Figure 8.4: *IR absorption spectra of 1 cm thick hydrogen crystals grown at 7.5 K and recorded with a 1 cm^{-1} resolution in the region of the fundamental vibrational excitation. The upper trace belongs to normal, the lower trace to para-hydrogen. Transitions that are discussed in more detail are marked with asterisks.*

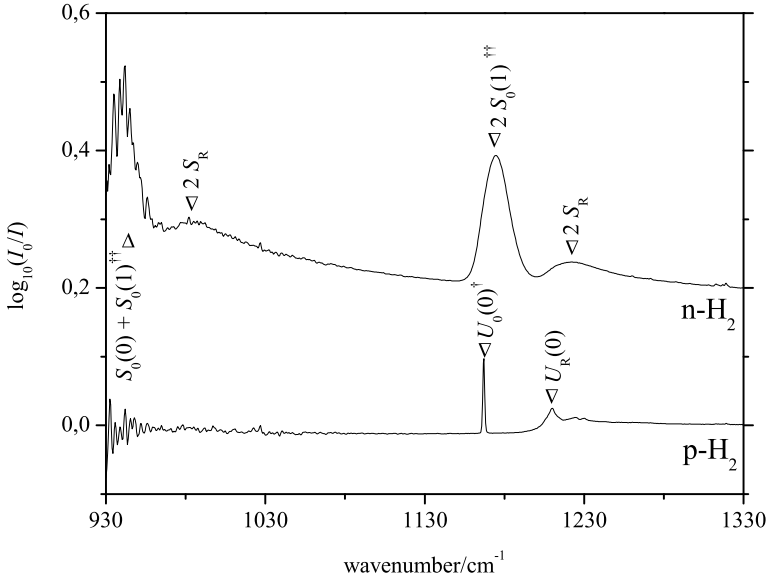

Figure 8.5: *Pure rotational transitions recorded simultaneously with the spectra from Figure 8.4. Transitions that are discussed in more detail are marked with daggers. The noise in the red wing is caused by the absorption of the CaF_2 windows.*

represents the rotational quantum number in the lower state. Thus (0) denotes para-, and (1) ortho-hydrogen in the ground state. Hence, the $Q_1(0)$ transition is a pure vibrational transition ($v = 1 \leftarrow 0$) in a para-hydrogen molecule that does not change the rotational state ($\Delta J = 0$) and the $S_0(1)$ transition is a pure rotational transition ($\Delta J = +2$) in an ortho-hydrogen molecule that does not change the vibrational state ($\Delta v = 0$).

8.2.1.1 Low resolution spectroscopy

The infrared absorption spectra of solid hydrogen that were recorded by us have a relatively low resolution of about 1 cm^{-1}. Nevertheless, they provided us valuable information about our samples and a more detailed discussion of the spectra shall be given in the following. Figure 8.5 and Figure 8.4 show the parts of the solid hydrogen absorption spectrum that we recorded and could use to determine our sample's ortho-para composition. Figure 8.5 shows some pure rotational transition and Figure 8.4 shows vibrational and ro-vibrational transitions with $\Delta v = 1$. Sharp transition lines are formed by pure vibrational ($Q_v(J)$), pure rotational (like $U_0(0)$), and rovibrational (like $S_1(0)$) single transitions of one hydrogen molecule. However, also strong multiple transitions (like $Q_1(1) + S_0(0)$ and $2S_0(1)$), simultaneous excitations of more than one molecule, occur and form relatively sharp lines. Next to these transitions, the major amount of the integrated absorption intensity is located in broad phonon-sidebands (like $S_R(0)$), which are combination transitions involving the internal degrees of freedom of the molecules and the collective degrees of freedom of the lattice. The origin of all these transitions are dipole moments, induced by multipolar intermolecular interactions. The strongest of these interactions is the electric quadrupole-quadrupole (EQQ) interaction. It is responsible for transitions with $\Delta J = 0$ and $\Delta J = 2$, i.e. Q and S transitions [147, 148].

The relative strength of the phonon-branches is no surprise, given the strong dependence of the EQQ interaction on the intermolecular separation (R^{-5}). The integrated intensity of the phonon branches depends on the mean square displacements of the molecules from their equilibrium positions. Thus, the phonon branch transition $S_R(0) = S_1(0) + \nu_L$

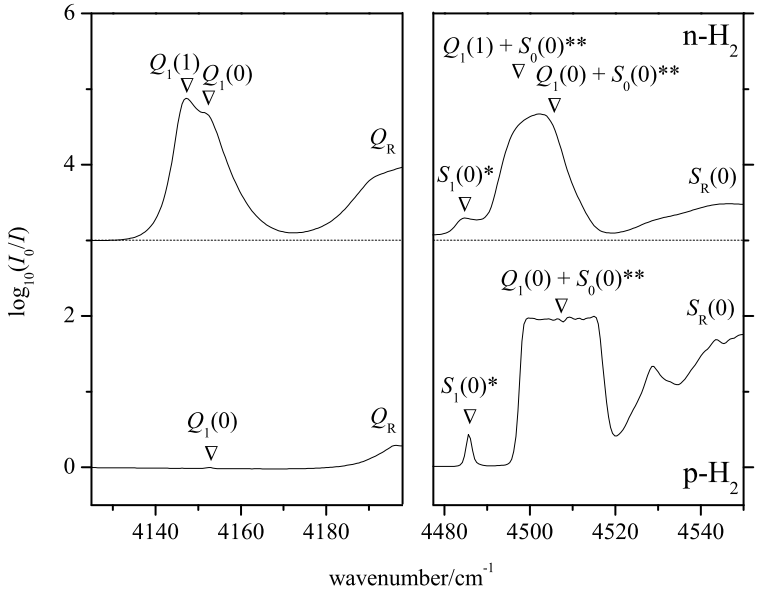

Figure 8.6: *Details of the absorption spectra shown in Figure 8.4. The linewidth of the $S_1(0)$ transition is limited by our resolution. The $Q_1(0) + S_0(0)$ transition in the para-hydrogen trace has a flat top, and the comparison with the literature shows that its lineshape is indeed not Gaussian, but almost rectangular with a linewidth of about 20 cm^{-1}.*

exhibits a high intensity although the corresponding single transition $S_1(0)$ is relatively weak. In Raman spectra of solid hydrogen, which are determined by the polarizability of the molecules that is largely independent from the intermolecular separation, the phonon branches play a less significant role [148].

For a deeper understanding of the presented spectra, we should discuss the strengths of the transitions that consist of a vibrational excitation $v = 1 \leftarrow 0$ and a rotational excitation $J = 2 \leftarrow 0$ in more detail. The excitations can take place as a single transition in one hydrogen molecule, leading to the $S_1(0)$ transition, marked by an asterisk in Figure 8.4, or as a double transition in two hydrogen molecules, one rotationally and one vibrationally excited. For the latter case, it does not matter if the vibrational excitation does take place in an ortho- or a para-hydrogen molecule, which leads to two possible transitions, $Q_1(1) + S_0(0)$ and $Q_1(0) + S_0(0)$, marked by double asterisks in Fig. 8.4. These three transition, shown in more detail in Figure 8.6, are separated from each other because of the rotation-vibration interaction. Obviously, compared with the single transition, the double transitions have a relatively high intensity. This can be explained due to the so-called cancellation effect. In an hcp lattice any hydrogen molecule is almost, but not quite, a center of inversion. Considered hydrogen would form a fcc lattice, any hydrogen molecule would be a center of inversion. This would mean that the dipoles induced by it in two diametrically opposite neighbor molecules, for which it would be the center, would be the same, but opposite in direction, and therefore would cancel themselves. The single transition would thus be absent in a fcc lattice, while a weak transition remains in hcp. What would happen, if the rotational transition would be located in one of the neighboring molecules? Because their is no phase relation between the rotation of the neighboring molecules the dipole moments induced in the central molecule would not cancel and it could undergo a pure vibrational transition. Hence, double transitions can have a significant intensity in fcc and hcp. They depend on the interaction strength, but not directly on the lattice symmetry.

Let us now look at the linewidths of the transitions. The pure rotational $U_0(0)$ single transition, marked with a dagger in Figure 8.5, and the pure rotational $2S_0(1)$ and $S_0(1) + S_0(0)$ double transitions, marked with two daggers in Figure 8.5, have very different linewidths. The single transition is remarkably sharp and has a FWHM of 0.06 cm^{-1} [141]. The double transitions, however, are very broad, about 40 cm cm^{-1} [149]. The reason for this is the EQQ interaction, which opens a path to intermolecular energy transfer. This allows excitations to hop from one molecule to another. The therefore delocalized excitations must be described as travelling Bloch waves that are subject to **k**-dispersion relations, similar to the phonon dispersion relations shown in Fig. 2.8, and form broad exciton bands. E.g., the rotational $S_0(0)$ ($J = 2$) and $S_0(1)$ ($J = 3$) excitations are called rotons and form energy bands with widths of about 20 cm^{-1} [147]. However, the momentum conservation for an optical excitation leads to a $\mathbf{k} = 0$ selection rule. Hence, single transitions, like the $U_0(0)$ transition, are limited to the $\mathbf{k} = 0$ states of the energy band, and therefore sharp. The same applies for the Raman-active single transitions that we observed in our time resolved experiments, which were sharp, too. The double transitions, on the other hand, may consist of wavevectors **k** and $-\mathbf{k}$. In the case of the $2S_0(1)$ and $S_0(1) + S_0(0)$ double transitions, the excitations can run through the entire width of the two roton bands, both about 20 cm^{-1} each and combined about 40 cm^{-1}. Thus, the linewidths of these double transitions become very broad, about 40 cm^{-1}, because the $J = 2$ and $J = 3$ rotational excitations may span over the whole **k**-space.

We may illustrate this a little further for the $J = 2$, $v = 1$ ro-vibrational transitions in pure para-hydrogen that are shown in the lower trace of the right panel of Figure 8.6. Due to the absence of ortho-hydrogen, no transitions that involve ortho-hydrogen molecules, like the $Q_1(1)$ transition and the $Q_1(1) + S_0(0)$ transition, are possible. Hence, the double transition $Q_1(1) + S_0(0)$ cannot contribute to the broad absorption feature around 4.510 cm^{-1} in the para-hydrogen trace of Fig. 8.6. The linewidth of the remaining $Q_1(0) + S_0(0)$ double transition is about 22 cm^{-1} [150], by virtue of the bandwidth of the $J = 2$ roton. The $S_1(0)$ transition, the simoultaneous rotational and vibrational excitation of a single molecule, is with about 0.1 cm^{-1} much sharper, even though we cannot resolve this with our limited resolution [151]. For the $S_1(0)$ excitation, the energy conservation localizes the rotational excitation on the vibrationally excited molecule. However, the $S_1(0)$ excitation can in principle also hop and forms a band with a width of about 1 cm^{-1}. The linewidth of only 0.1 cm^{-1} is caused by the optical excitation mechanism, which limits the excitation to the $\mathbf{k} = 0$ states of the $S_1(0)$ energy band.

8.2.1.2 Comparison to state-of-the-art experiments

As was already mentioned, in addition to the EQQ induced Q and S zero-phonon and phonon-branch transitions we identified weak lines belonging to higher order $U_v(J)$ transition with $\Delta J = 4$ in Figure 8.5. Higher electric multipoles (2^4, 2^6, 2^8) lead to weaker multipole interactions, which do induce subsequently weaker transition (U, W, Y) by the 2^l multipole induction mechanism. Higher order transitions, as they were theoretically treated by Ma, Tipping and Poll [146, 152], have already been observed experimentally up to $\Delta J = 8$ ($Y_0(0)$) [153]. However, their weak transition probabilities make it very hard to actually detect them. To give an example, the $Y_0(0)$ transition is located at about 4,044 cm^{-1} and therefore within our spectral range, but its integrated absorption intensity $\tilde{\alpha}$, defined as

$$\tilde{\alpha} = \frac{c}{Nl} \int log_e \frac{I_0(\bar{\nu})}{I(\bar{\nu})} \frac{d\bar{\nu}}{\bar{\nu}}, \tag{8.1}$$

in which N is the number of molecules per cm^3, l the sample length, and c the speed of light, is only about $\tilde{\alpha} = 2.5(3) \times 10^{-22}$ cm^3s^{-1} [153]. Hence, it is very small compared to about 3.3×10^{-15} cm^3s^{-1} [154] to 4.5×10^{-16} cm^3s^{-1} [7] for the observed $S_1(0)$ transition, or 5.5×10^{-17} cm^3s^{-1} to 7.5×10^{-17} cm^3s^{-1} [7] for the observed $U_1(0)$ transition. This makes it impossible to see the $Y_0(0)$ transition in our spectra.

Not resolved in our spectra are also fine splittings, as they occur due to the anisotropic EQQ interaction with the crystal field. As was already stated above, the delocalized rotational excitations have to be described by their wavevector $\mathbf{k}$, their orientation M, and their parity p. In single transitions, only the $\mathbf{k} = 0$ states of an energy band can be infrared or Raman excited. Their degeneracy in M and p may be lifted by the anisotropic EQQ interaction in an hcp lattice, which gives rise to a crystal field splitting of the transition lines. In the case of the $S_0(0)$ transition, for symmetry reasons, only one of these transitions ($M = \pm 2$, $p = -1$) is infrared active [36] and was experimentally observed [139]. However, three are Raman active ($M = 0, \pm 1, \pm 2$, $p = 1$), split by 2 cm^{-1} from each other, and have been observed by us in the time domain (see Chapter 7.1). In the case of $U_0(0)$ and $W_0(0)$ transitions in an hcp lattice, both exhibit infrared active triplets. Indeed, the splitting of the $U_0(0)$ transition was successfully observed in the group of Oka [8, 141]. However, the crystal field splitting of the $U_0(0)$ transitions, estimated to be +0.0109, +0.0236, and -0.0133 cm^{-1} for the three states [141], is very small, smaller than the observed linewidth of 0.06 cm^{-1}. Given this, it is no surprise that we did not resolved such splittings in our spectra. Next to crystal field splittings, which are still a topic of ongoing research [145], other fine structures of solid para-hydrogen absorption spectra were also identified. Fine splittings in para- and ortho-hydrogen transitions can also be caused by interactions with impurities. Such nearest and next nearest neighbor interaction with ortho-hydrogen impurities in para-hydrogen were addressed by several studies [4, 8, 141, 155].

A final remark has to be done about the linewidths of the described single transitions in para-hydrogen that can be remarkably sharp, much sharper than our spectral resolution of about 1 cm^{-1}. An overview of the linewidths of single transitions, pure rotational and ro-vibrational in the fundamental vibrational band, was given by Okumura et al. [151]. In matrix isolation spectroscopy, the most important line broadening mechanisms are inhomogeneous and lifetime broadening, whereas Doppler broadening can be neglected. Inhomogeneous broadening results from interaction with impurities that are randomly distributed in the crystal, as it was described above, but also from macroscopic nonuniformity and stress. Lifetime broadening results from population relaxation and phase coherence relaxation. With a FWHM of 0.006 cm^{-1}, the $W_0(0)$ transition has the smallest observed linewidth, as reported by the Oka group. They could isolate the fine splittings arising from nearest and next nearest neighbor ortho-hydrogen impurity interaction, but found a dependency of the linewidth from the ortho-hydrogen concentration. Therefore, they attributed the linebroadening, at least partially, to inhomogeneous broadening caused by the EQQ interaction with ortho-hydrogen impurities [8]. In contrast to this the linewidth of the $S_0(0)$ transition is, in agreement with our time resolved experiments, relatively broad, 0.1 cm^{-1} [156]. This broadening is explained by the dephasing of the Bloch state, and the resulting violation of the exciton momentum selection rule [30, 127]. For the $W_0(0)$ excitation, which exhibits a much weaker interaction and thus a much lower hopping frequency, this strong dephasing does not apply.

8.2.2 Ortho-para conversion efficiency

The resulting ortho-hydrogen concentration after conversion was obtained from the infrared activity of the $Q_1(0)$ band of the crystal, which is shown with higher sensitivity

in Figure 8.7. The $Q_1(0)$ band is particularly sensitive to the ortho-para-ratio, which we will discuss in the following. As was already stated, this pure vibrational transition ($\Delta J = 0$) of a para-hydrogen molecule ($v = 1 \leftarrow 0, J = 0 \leftarrow 0$) is forbidden for an isolated molecule. Even for a pure para-hydrogen solid no $Q_1(0)$ lines are present, due to the absence of any electric multipoles. No quadrupolar interaction is possible, in both the initial and the final state, as all molecules are in the $J = 0$ rotational state. However, the presence of an ortho-hydrogen impurity can induce transition dipoles into neighboring para-hydrogen molecules. Thus, the polarization of the surrounding nearest neighbor para-hydrogen molecules by the ortho-hydrogen's quadrupole moment can induce such, otherwise forbidden, pure vibrational transitions [36, 44]. The strength of the $Q_1(0)$ band, however, cannot be explained by a single transition, which would be affected by the cancellation effect. In fact, it owes most of its intensity to a double transition. A pure vibrational transition of a para-hydrogen molecule induced by its ortho-hydrogen neighbor is accompanied by an orientational transition of one of its nearest neighbors. And this orientational transition can only occur in the $J = 1$ ortho-hydrogen molecule itself [150]. As for the $S_0(0)$ rotons, the $Q_1(0)$ excitation of para-hydrogen is delocalized and can hop from one molecule to another. Hence, these vibrons have to be described as Bloch waves and form an exciton band. The density of states of this band is reflected in the asymmetric shape of the $Q_1(0)$ band demonstrated in the inlet of Figure 8.7 [8], which shows a steep blue flank and a broad red wing.

As it is shown in Figure 8.7, the $Q_1(0)$ transitions can be remarkably strong, stronger than the corresponding $Q_1(1)$ transition of the ortho-hydrogen itself. It provides therefore a good measure to determine the ortho-para ratio, especially for low ortho-hydrogen concentrations. We used the $Q_1(0)$ band's integrated absorbance, which is given by Welsh et al. [150] as

$$\int log_{10}(\frac{I_0(\bar{\nu})}{I(\bar{\nu})})d\bar{\nu} = l(a\rho_{I=1}^2 + b\rho_{I=1}\rho_{I=0}) = l(b\rho_{I=1} + (a-b)\rho_{I=1}^2), \tag{8.2}$$

where l is the sample length, $\rho_{I=1}$ the ortho-hydrogen fraction, $\rho_{I=0}$ the para-hydrogen fraction, and a and b are empirical constants. For small ortho-hydrogen fractions, only b, which has a value of about 30 cm^{-2} [50], is relevant. Using this, we determined our residual ortho-hydrogen concentrations to vary between 0.03 and 0.20 percent. For the example given in Figure 8.7, with an integrated absorbance from 4,150 to 4,157 cm^{-1} of 0.117 cm^{-1} and the length l of the cell of 3 cm, the residual ortho-hydrogen concentration was estimated to be 0.13 percent.

8.3 Dopants in solid para-hydrogen

In this section, we sum up our results for methane and carbon monoxide doped hydrogen crystals. To describe the excitations of a molecule in a crystal, one has to use a total Hamiltonian that is the sum of the standard rotation-vibration Hamiltonian $H_{vib-rot}$ of the molecule, and the potential due to the electric field of the surrounding lattice V_{crys},

$$H = H_{vib-rot} + V_{crys}. \tag{8.3}$$

Both, the symmetry of the crystal and the symmetry of the embedded molecule, have to be treated for the crystal field interaction, which is done by the extended group theory that was initially introduced by Devonshire in 1936 [157]. Impurities in a solid are strongly influenced by their surrounding, which has a direct impact on their infrared activity. Infrared absorption spectroscopy could therefore provide significant information about the

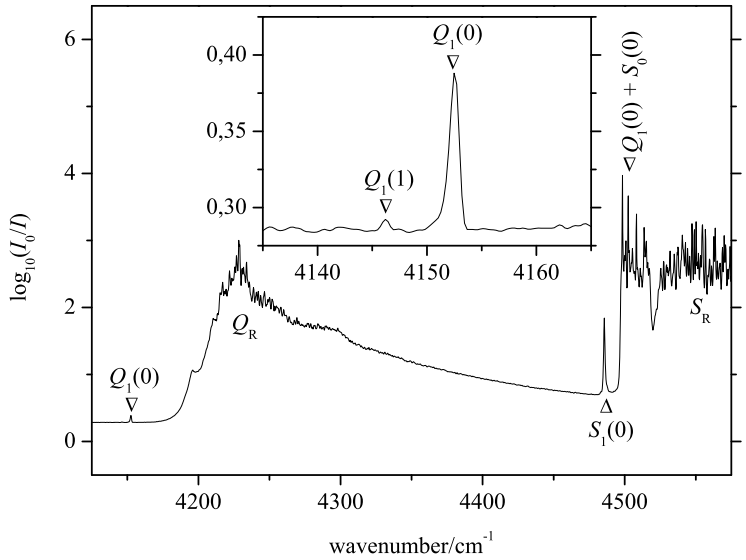

Figure 8.7: *IR absorption spectra of a 3 cm thick para-hydrogen crystal with a residual ortho-hydrogen content of 0.13 percent. The inlet shows the ortho-hydrogen induced $Q_1(0)$ band with increased sensitivity.*

local structures around the dopant. We performed Fourier transform infrared (FTIR) spectroscopy, often called the experimental 'workhorse' of matrix isolation spectroscopy (MIS), to investigated the clustering of impurities depending on growth parameters, the long time sample stability and the degrees of freedom of dopants in solid hydrogen.

8.3.1 Methane

Methane doped hydrogen crystals were extensively studied in recent years [10, 158–163] and showed remarkable features. The van der Waals radius of methane is only about 1.62 Å, much smaller than the intermolecular distance of 3.783 Å of a para-hydrogen crystal [158]. Hence, isolated methane molecules are trapped in single-substitutional sites and do not seriously distort the crystal. Furthermore, it is known from matrix isolation spectroscopy that methane performs a hindered rotation even in rare gas solids [164]. In para-hydrogen, high resolution FTIR spectroscopy revealed extremely sharp linewidths, as small as 0.003 cm^{-1} FWHM, and clearly resolved rovibrational transitions [159]. Even clusters of methane in para-hydrogen exhibit a rich spectral structure with linewidths as narrow as 0.007 cm^{-1}, and, at least for small clusters, show well quantized rovibrational levels [160]. Other studies focused on methane's nuclear spin conversion in solid hydrogen and its dependence on the ortho-hydrogen concentration [161], or dealt with deuterated methane [10]. And not least to mention are the experiments about chemical reactions including methane and methyl radicals, prepared by photolysis of methyl halogens [17]. All this made methane a very convenient probe for the quality of our sample preparation.

The well studied, infrared active, threefold degenerated ν_3 stretching and ν_4 bending modes of methane were in the focus of our experiments. As one can see in Figure 8.8, they consist of rotational bands, assigned to the $P(1)$, $Q(1)$, $R(1)$ and $R(0)$ transitions of methane. The four rotational bands reflect the dipole allowed transitions of the isolated molecule from the $J = 0$ and the $J = 1$ rotational states. These transitions are split into several lines due to the crystal field interaction, which was experimentally shown by Momose et al. [159] with high resolution FTIR spectroscopy. Momose et al. also

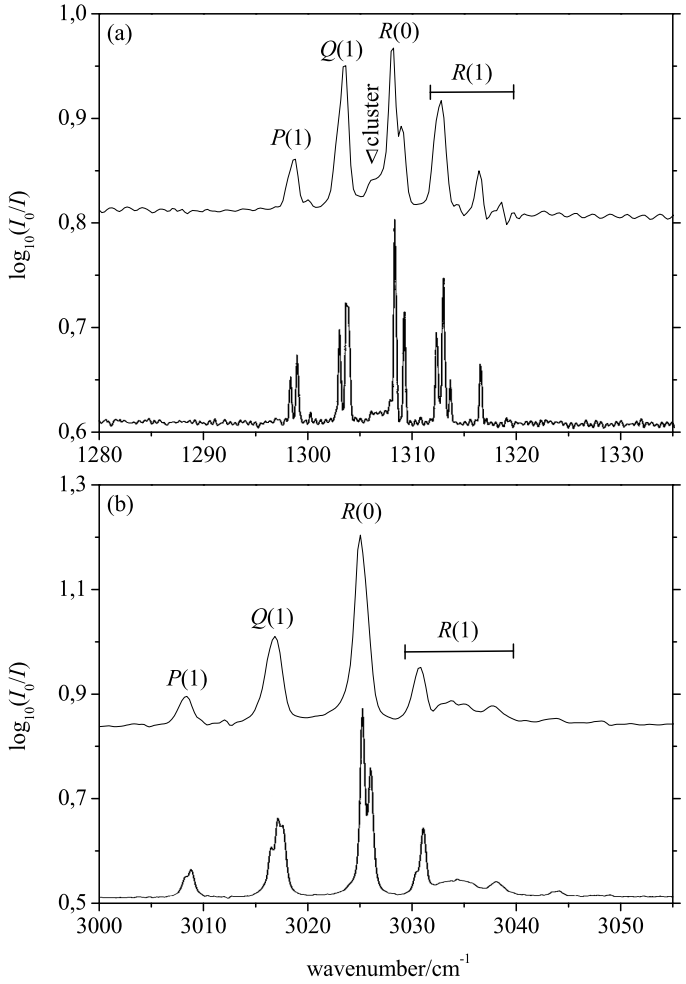

Figure 8.8: *Absorption spectra of 10 ppm methane trapped in a para-hydrogen crystal grown at 8 K, (a) shows the ν_4 bending mode and (b) the ν_3 stretching mode of methane. The upper traces were recorded in our laboratory with a resolution of 1 cm^{-1}. The lower traces are from Momose et al. [159], recorded with a resolution of 0.25 cm^{-1}.*

successfully treated the observed transitions theoretically. From this they concluded that the rotational constant of methane in para-hydrogen is only about ten percent smaller than in the gas phase, proving the expected weak disturbance in a para-hydrogen matrix. We successfully reproduced their spectra, which is shown in Figure 8.8. And, even though our low spectral resolution of 1 cm^{-1} is not enough to fully resolve the crystal field splitting, larger splittings like in the $R(1)$ branch of the ν_4 bending mode are clearly distinguishable.

For us most interesting were the partially broad bands, which are located slightly red-shifted from the $R(0)$ branch, indicated as clusters by an arrow in Figure 8.8. They can be assigned to cluster transitions [160], and depend on the degree of clustering. Hence, they are a good measure for the isolation quality of our samples. Our goal was to grow crystals with a high amount of isolated dopant molecules and an optical quality that was as good as possible. Therefore, we grew various methane doped crystals under different conditions and measured their infrared absorbance. Figure 8.9 shows a selection of FTIR spectra of such crystals. Figure 8.9 (a), already shown in Figure 8.8 (a), exhibits almost no clustering. This is no surprise, because it was a sample with a small amount of impurities (10 ppm methane) grown at a relatively low temperature of 8 K. As was already stated, the optical quality of

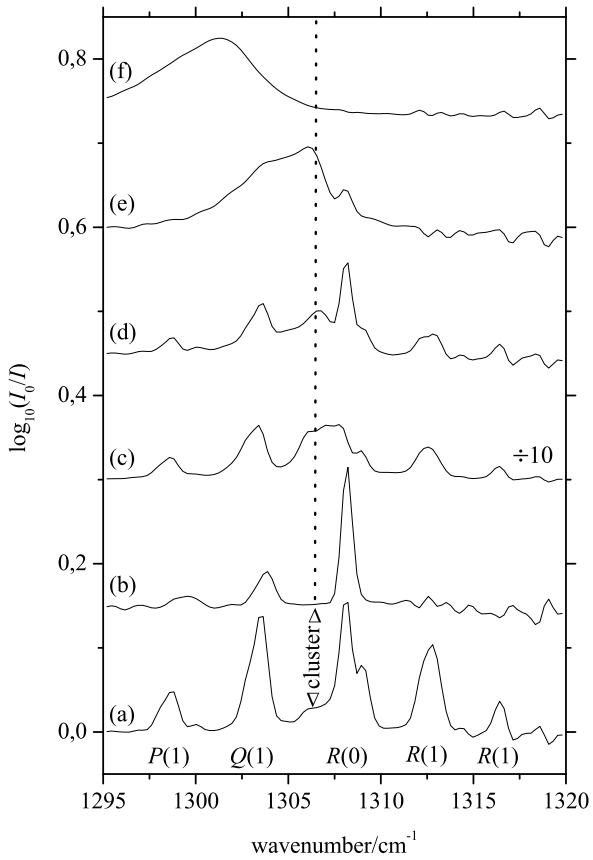

Figure 8.9: *Absorption spectra in the ν_4 bending mode region of CH_4. (a) 10 ppm methane in a para-hydrogen crystal grown at 8 K. (b) 10 ppm methane in a normal-hydrogen crystal grown at 8 K. (c) 100 ppm methane in a para-hydrogen crystal grown at 8 K (intensity divided by ten). (d) 10 ppm methane in a para-hydrogen crystal grown at 9 K. (e) Methane clusters observed after warming up trace (d) to 12 K. (e) Spectrum of methane in liquid para-hydrogen at 14.5 K.*

our para-hydrogen crystals improved for higher growth temperatures. An increase of the growth temperature led to a higher mobility of the molecules and allowed them to position correctly into the given lattice structure. Hence, the optical quality of a para-hydrogen crystal grown at 9 K improved significantly. However, at growth temperatures of 9 K the clustering increased and the methane peaks shrank, as it is demonstrated in Figure 8.9 (d). A one magnitude higher concentration of methane led also to higher clustering, which is depicted in Figure 8.9 (c). Nevertheless, the increase of the peaks that belong to isolated methane molecules in the crystal (note the scaling factor of ten) made it worthwhile to reach for higher dopant concentrations, even though the increase is less than a magnitude.

Here, we have a point to make about the temperature stability of the sample. Figure 8.9 (e) shows what happens when a slightly clustered sample is warmed up to 12 K for only a few minutes. The thermal diffusion of impurities increased drastically, leading to a fully clustered sample. At the same time, the increased mobility of the hydrogen molecules led to the famous self healing effect of hydrogen crystals. Annealing the sample can repair crystal disorder, like random or fcc stacking, and even small cracks. Thus, it may be used to increase the optical quality of solid hydrogen samples. However, we decided to cool our samples down to 5 K and below to avoid clustering due to thermal diffusion.

Figure 8.9 (b) shows the spectra of methane in a normal hydrogen crystal. Although

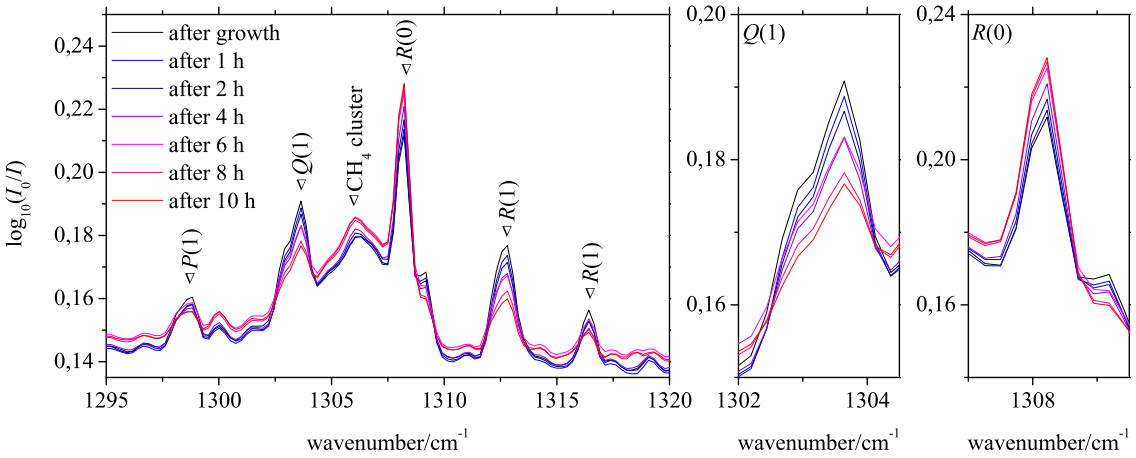

Figure 8.10: *Absorption spectra in the ν_4 bending mode region of CH_4 of a para-hydrogen crystal grown at 9 K, doped with 10 ppm CH_4 and kept at 4.4 K for 10 hours. The nuclear spin conversion is exemplified for the Q(1) transition and the R(0) transition in the two small panels on the right.*

the crystal was grown under the same conditions as the one from Figure 8.9 (a), it shows a different behavior in several aspects. First of all, the rotational structure from Figure 8.9 (a) is partially lost, the $R(1)$ ($J = 2 \leftarrow 1$) branch is even completely absent. We see the reason for this in the anisotropic EQQ interaction with the 74.9 percent $J = 1$ ortho-hydrogen content in normal-hydrogen, which may block the rotation of methane. Secondly, the relative contribution of the $R(0)$ branch is increased. This may be attributed to a conversion of the nuclear spin of methane, which is a known and well studied phenomena [161]. It works similar to the nuclear spin conversion of hydrogen, and is therefore dependent on the $I = 1$ ortho-hydrogen concentration. Methane, which has four equivalent hydrogen atom with $I = 1/2$, comes in three nuclear spin states, $I = 0$, $I = 1$, and $I = 2$. These spin states correspond to different rotational states, similar as discussed for hydrogen in Section 2.1. At low temperatures, the $I = 0$ state couples to $J = 2$, the $I = 1$ state couples to $J = 1$ and $J = 2$, and the $I = 2$ state couples to $J = 0$ and $J = 2$. The nuclear spin conversion of the $I = 0$ state happens very fast, and transitions from the $J = 2$ state have never been observed in solid para-hydrogen [161]. However, an increased ortho-hydrogen concentration enhances also the spin conversion from $I = 1$ to $I = 2$, which increases the relative contribution of the $R(0)$ ($I = 2$, $J = 0$, $\Delta J = 1$) branch. Last but not least, no indication for clustering of methane does occur in Fig. 8.9 (b). The reason for this is probably a reduced mobility of methane in normal-hydrogen, due to the EQQ interaction between methane and ortho-hydrogen molecules.

The Figures 8.10 and 8.11 summarize a series of measurements we have performed to characterize the long time stability of our samples. On the first glance, no significant change in the recorded spectra occurred during 10 hours. Most important was to prevent the growth of methane clusters, which was obviously achieved. Unfortunately, the Figures exhibit an increase of the background. Due to its finer scale this is seen best in Figure 8.10. Figures 8.3, recorded at the same time, shows the most probable reason for this. A thin film of ice grew on the windows and lead to increasing scattering. Fortunately, this could be avoided in later experiments. An interesting feature is pointed out in the side panels of Figures 8.10 and 8.11, showing exclusively the $Q(1)$ and $R(0)$ branches. The nuclear spin conversion of methane, as it was discussed above for a normal-hydrogen matrix, led to a slow increase in the $R(0)$ branch's intensity, whereas the intensity of the $Q(1)$ branch,

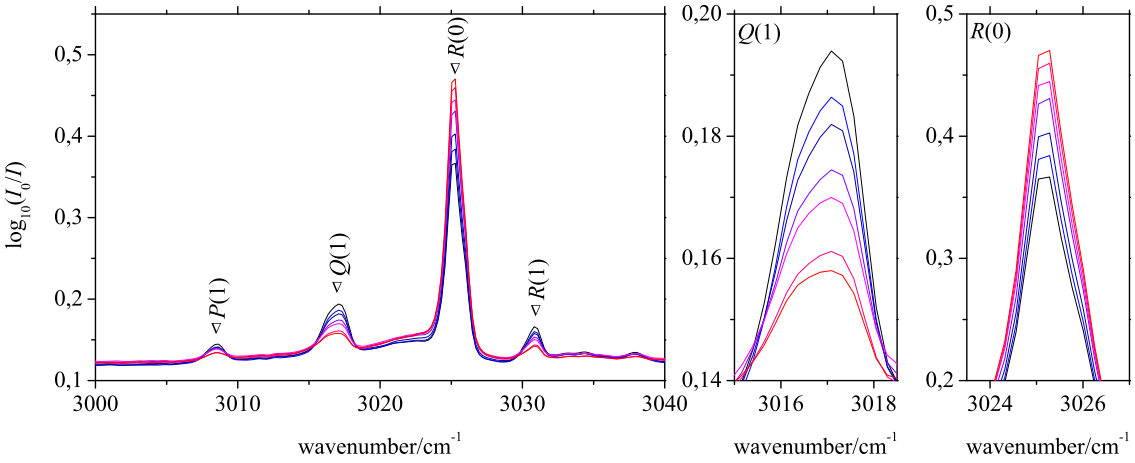

Figure 8.11: *Absorption spectra in the ν_3 stretching mode region of CH_4 of a para-hydrogen crystal grown at 9 K, doped with 10 ppm CH_4 and kept at 4.4 K for 10 hours. The nuclear spin conversion is exemplified for the Q(1) transition and the R(0) transition in the two small panels on the right. The color code is the same as in Figure 8.10.*

together with the $P(1)$ and $R(1)$ branches, shrinks.

The spectra in Figure 8.12 shall complete this section. Figure 8.12 (a) and (b) repeat the gas phase infrared allowed ν_4 bending and ν_3 stretching mode of methane that we have already shown. However, Figure 8.12 (c) presents an additional absorption that we assign to the ν_1 stretching, or breathing, mode of methane (see Table 4.1). The ν_1 mode is infrared inactive in the gas phase, and is indeed significantly weaker than the ν_4 and ν_3 modes that are presented in Fig. 8.12 (a) and (b). Nevertheless, it has a similar spectral composition and we could reproduce it several times in methane doped para-hydrogen solids. To our best knowledge, and surprise, this is the first report on the observation of this forbidden transition.

8.3.2 Carbon monoxide

Carbon monoxide behaves very different from methane as a dopant. It has a dipole moment of $p(R_e) = 0.4079 \times 10^{30}$ Cm [165]. Thus, it interacts stronger with its surrounding and tends to cluster more strongly than methane. Furthermore, being a linear molecule, it also exhibits an anisotropic polarizability of $\alpha_{\parallel} - \alpha_{\perp}(632.8nm) = 0.53(2)$ Å^3 [39], which makes it in principle suitable for ultrafast alignment spectroscopy. Carbon monoxide is relatively small, with an equilibrium internuclear separation of about $R_e = 1.128$ Å [165], and van der Waals radii of about 1.40 Å for oxygen, and 1.65 Å for carbon [166]. It occupies therefore a single substitutional site in solid para-hydrogen, as methane, in which it exhibits an only slightly hindered rotation [167]. This made it a valuable test dopant for our sample growth technique.

In 2007, when we started to grow carbon monoxide doped para-hydrogen crystals, only very few studies about this system were available. Fushitani et al. [168] had observed carbon monoxide as product of a chemical reaction in 2000, however did not analyze the observed spectra. Tam et al. [169] reported on highly structured, carbon monoxide spectra in solid para-hydrogen in the same year, and published a first assignment of the observed transitions in 2001 [170]. However, the first rotationally resolved and completely assigned rovibrational spectrum for carbon monoxide in solid para-hydrogen, which is included in Figure 8.13, was published in 2009 by Fajardo et al. [167]. The spectroscopic properties of

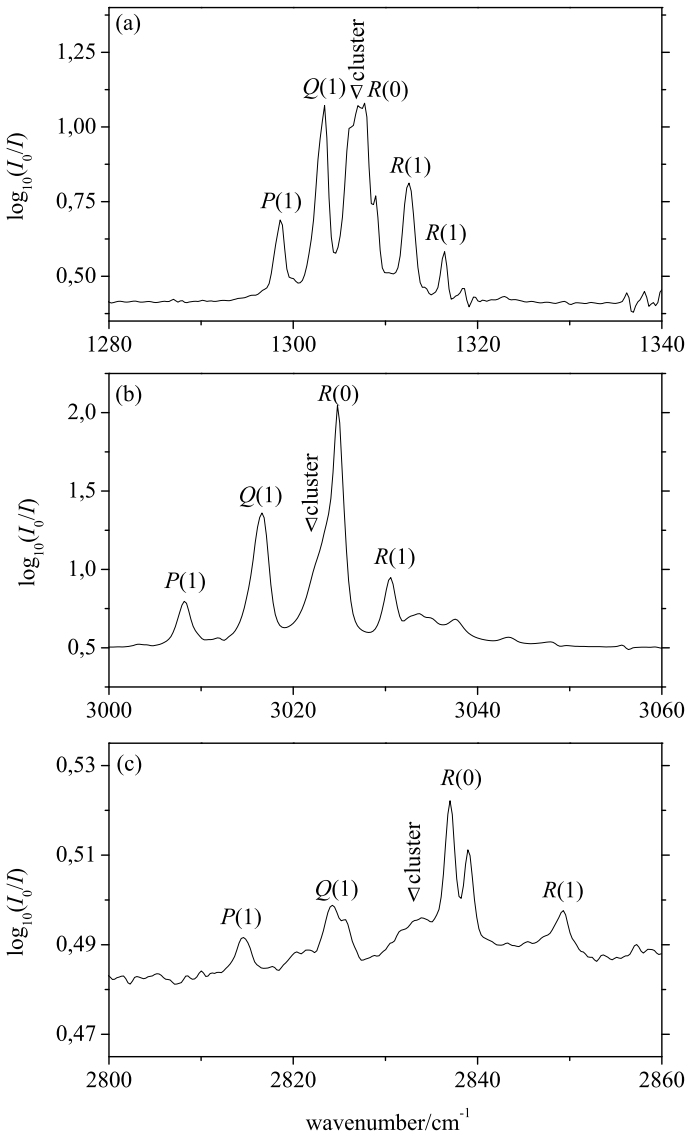

Figure 8.12: *Absorption spectra of 100 ppm methane in a para-hydrogen crystal grown at 8 K. Panel (a) shows the ν_4 bending, panel (b) the ν_3 stretching, and panel (c) the supposed ν_1 stretching mode of methane.*

isolated carbon monoxide are known to very high precision [165] and it was also object of many spectroscopic and theoretical studies, as a pure solid, and in a variety of environments [167]. Many of these studies focused on the rotational degrees of freedom. Whereas in the liquid state carbon monoxide molecules can undergo a nearly free rotation, in solid carbon monoxide only librational degrees of freedom remain [171], and the same holds true for rare gas matrices [166, 172, 173]. Nevertheless, next to solid para-hydrogen, the rotation of carbon monoxide was also observed in zeolithes [174], fullerenes [175], and small para-hydrogen clusters [176].

Figure 8.13 shows that our low resolution spectrum, measured at 7.5 K, reproduces the main features of the high resolution spectrum that was recorded by Fajardo et al. at 2.4 K [167]. The rotational constant of carbon monoxide in hcp para-hydrogen is relatively small, $B_e = 1.577(1)$ cm^{-1}, and amounts to about 80 percent of the gas phase value. Therefore several rotational states are thermally populated, even at 2.4 K. In the high resolution

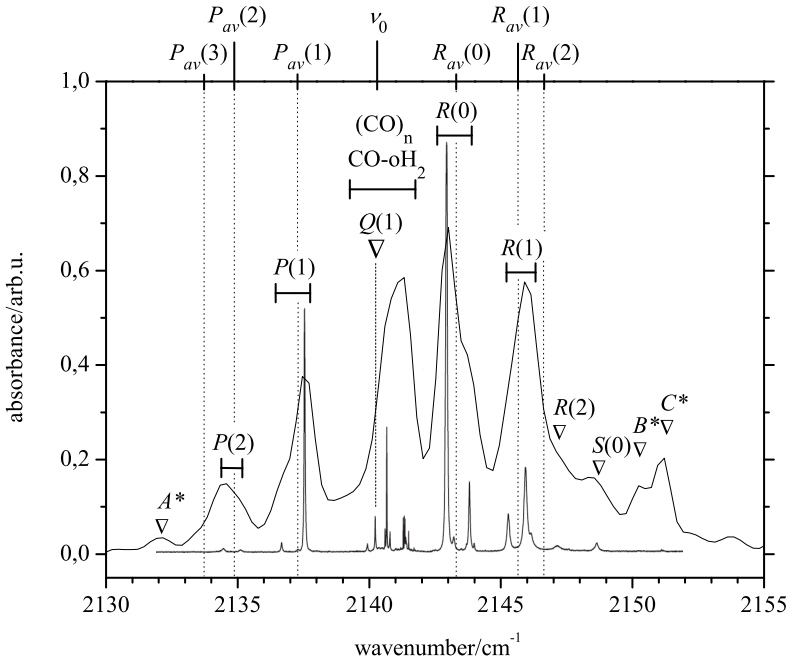

Figure 8.13: *Rotationally resolved infrared absorption spectra of isolated carbon monoxide in solid hcp para-hydrogen. The high resolution spectra with 0.0075 cm^{-1} resolution was recorded by Fajardo et al. [167] from a para-hydrogen film at 2.4 K. The low resolution spectra, recorded with a 1 cm^{-1} resolution at 7.5 K, was recorded in our laboratory. The transitions are labeled as given by Fajardo et al. [167], with the exception of A^*, B^*, and C^*, which have not been reported previously. Average transition energies $X_{av}(\Delta J)$, obtained from Eq. 8.4 and Eq. 8.5, are marked by dotted lines.*

spectrum, the $J = 0, 1$, and 2 levels are sufficiently thermally populated to contribute to the observed signal. Hence, the general structure shows $\Delta J = 1$ R-transitions that originate from different J-states, $R(0)$, $R(1)$, and $R(2)$, which are also resolved in our spectra. The same applies for $\Delta J = -1$ P-transitions. Fajardo et al. used their spectrum to obtain the crystal field parameters, the $v = 1 \leftarrow 0$ vibrational band origin ν_0, the rotational constant B_e, the centrifugal distortion constant D_e, and the vibration-rotation interaction constant α_e for CO in hcp and fcc solid para-hydrogen.

As for hydrogen and methane, the crystal field interaction V_{crys} partially lifts the $(2J+1)$-fold M-degeneracy of the rotational states, causing a fine structure of the transition lines. This is not resolved in our spectra, and only visible in the occurrence of shoulders in the $R(0)$- and $P(1)$-transition peaks. The crystal field interaction causes also a mixing of different J-states, which leads to weakly allowed $\Delta J = 2$ S-transitions and $\Delta J = 0$ Q-transitions. The center of the spectra is given by the $v = 1 \leftarrow 0$ vibrational band origin $\nu_0 = 2140.295(2)$ cm^{-1}. The strong splitting of the Q-branch is caused by overlapping Q-transitions of isolated CO, CO-oH$_2$-complexes, and $(CO)_n$-clusters. Since the latter two block any rotation, they do not contribute to $\Delta J \neq 0$ transitions.

We used carbon monoxide to work out the growth parameters for our samples. Most interesting was of course the clustering of carbon monoxide, which we observed by comparison of the relative intensities of the ro-vibrational transitions of isolated carbon monoxide and the pure vibrational transitions in $(CO)_n$ clusters. Figure 8.14 shows a series of measurements, carried out with differing dopant concentrations. As had to be expected, higher dopant concentrations led to a relative increase of the $(CO)_n$ cluster-peak around 2,141.3(3)

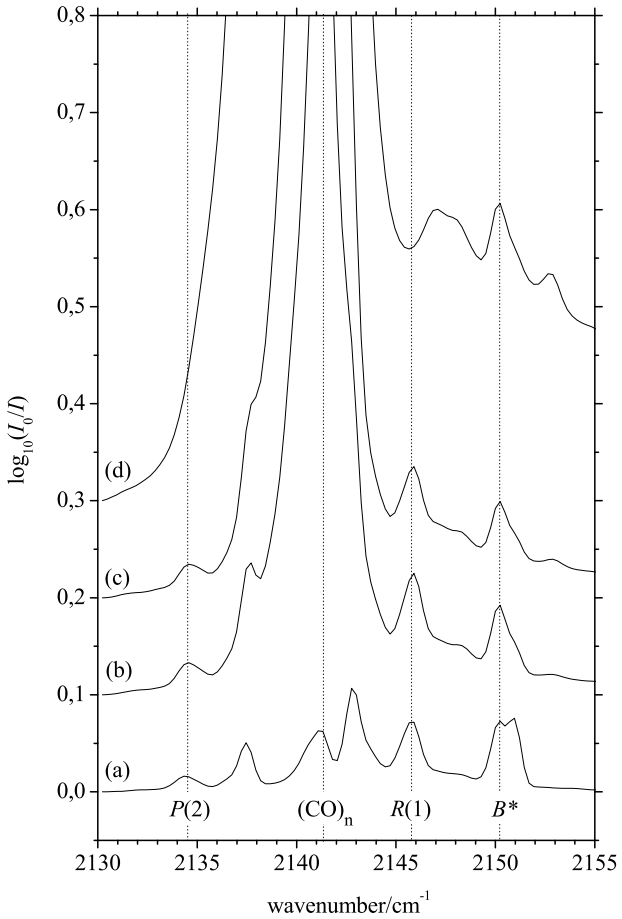

Figure 8.14: *IR absorption spectra of 1 cm thick, carbon monoxide doped para-hydrogen crystals grown at 7.5 K. Crystal (a) was doped with 10 ppm, (b) with 50 ppm, (c) with 100 ppm, and (d) with 1.000 ppm carbon monoxide. Higher dopant concentrations led to an increased clustering, and therefore to a loss of the rotational structure. Trace (d), highly saturated by virtue of the high methane concentration, shows no rotational structure at all.*

cm^{-1}. Lets take trace (b) from Figure 8.14, doped with 50 ppm carbon monoxide, as a reference, since it exhibits significant clustering and free rotation of isolated carbon monoxide at the same time. The decrease of the carbon monoxide concentration in trace (a) by a factor of 5, from 50 to 10 ppm, led only to a decrease of the $P(2)$- and $R(1)$-bands of isolated carbon monoxide by about 25 percent, whereas the cluster peak shrank significantly and did almost vanish. The increase of the concentration in trace (c) by a factor 2, from 50 to 100 ppm, resulted in an increase of the cluster peak by a factor of 2, whereas the amount of isolated carbon monoxide decreased by about 20 percent. Finally, the further increase of the dopant concentration in trace (d), doped with 1000 ppm carbon monoxide, resulted in a completely different spectral structure. The $P(2)$- and $R(1)$-bands of isolated carbon monoxide vanished, new peaks were observed, and the $(CO)_n$ cluster-peak was highly saturated.

Trace (a) of Figure 8.15 is identical to trace (a) of Figure 8.14. Warmed up to 11.5 K the spectral pattern changed significantly in trace (b) and lost the rotational structure. The new structures arising around $(CO)_n$ are probably caused by the formation CO-$(oH_2)_n$ complexes with small n, due to thermal diffusion of ortho-hydrogen impurities. The simultaneous increase of the B^*-transition will be discussed below. The increase of the growth

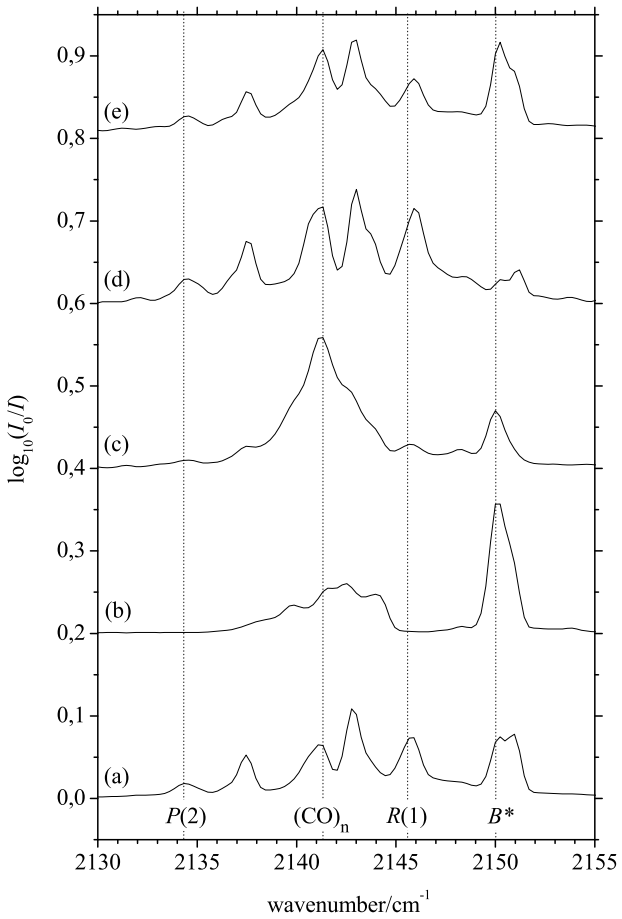

Figure 8.15: *IR absorption spectra of 1 cm thick para-hydrogen crystals, doped with 10 ppm carbon monoxide. Trace (a) belongs to a crystal grown at 7.5 K. Trace (b) was recorded 10 min after the crystal from trace (a) was warmed up to 11.5 K. Trace (c) belongs to a crystal that was grown under similar conditions as in trace (a), but at a higher growth temperature (8.5 K). Trace (d)/(e) was recorded from a crystal grown under similar conditions as in trace (a), but with a lower/higher gas flow into the sample cell.*

temperature in trace (c) has a different effect, which is similar to the growth of crystals at lower temperature, but with higher dopant concentration. The rotational structure is less intense, and an undisturbed and relatively sharp $(CO)_n$ cluster-peak arises. Whereas in the 11.5 K solid in trace (b) carbon monoxide is immobile and only the thermal diffusion of ortho-hydrogen is activated, the crystal surface during growth at 11.5 K is covered with a thin layer of liquid, in which ortho-hydrogen and carbon monoxide are mobile. The increase of the growth temperature increased the thickness and temperature of this layer, and therefore the clustering of carbon monoxide within it. Simultaneously, the crystal's optical quality improved, as was discussed above. This interpretation should also apply to the traces (d)/(e), recorded from crystals that were grown with a lower/higher gas flow into the sample cell, and under otherwise identical conditions as in trace (a). Although the crystals were grown at the same temperature of the copper cell, the temperature at the surface of the crystal was different. The heat load of a higher/lower gas flow onto the crystal surface increased/decreased the temperature of the liquid layer. This lead to a higher/lower degree of mobility and clustering. However, no significant change in the relative height of the Q-branch, comparable to trace (c), is visible. The intensity of the

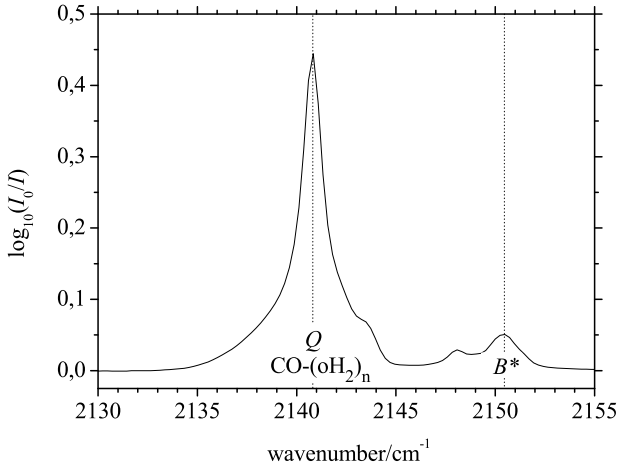

Figure 8.16: *IR absorption spectra of a 1 cm thick normal-hydrogen crystal, doped with 10 ppm carbon monoxide. The crystal was grown at 5 K to avoid any clustering.*

B^*-transition varies significantly and the overall intensity of the rotational structure increases with decreasing B^*-intensity. We therefore assume that the surface temperature was increased to a certain degree, but not the thickness of the liquid layer. This might be caused by the high thermal conductivity of solid para-hydrogen, which is strongly temperature dependent at lower temperatures (see Fig. 2.6). Compared to the CO-CO interaction, the CO-oH_2 interaction is weaker, because ortho-hydrogen has no dipole moment. Nevertheless, it can be more likely to form CO-oH_2 complexes in a thin film of liquid, given the higher concentration of ortho-hydrogen impurities of above 500 ppm and their higher mobility. The formation of such complexes would block the rotation of carbon monoxide and decrease the overall intensity of the rotational structure. The strong dependence of the B^*-transition on the growth parameters, as it is shown in Figure 8.15, might thus help to assign this transition. The additional comparison with normal-hydrogen, which showed an absorption at 2,150.4(3) cm^{-1} (Figure 8.16), indicates that B^* might origin from the simultaneous librational and vibrational excitation of CO and ortho-hydrogen, $Q + \nu_{lib}$. This would also be perfectly consistent with our interpretation of Figure 8.15 (b), which shows a dramatic increase of the B^*-band.

We observed several differences to the spectra presented by Fajardo et al. [167] in addition to the lower resolution of our spectra and the already discussed B^*-transition. Our crystals had the same structure, but were grown and observed at higher temperature, 7.5 K instead of 2.4 K for the one shown in Fig. 8.13. The thermal population is therefore different, which is reflected in the intensity distribution of the absorption lines. Furthermore, we could also observe a red-shifted peak at 2,132.0(3) cm^{-1} (A^*) and two blue shifted peaks, at 2,150.1(3) (B^*) and 2,151.2(3) cm^{-1} (C^*). A^* and C^* in Fig. 8.13 might origin in the thermal population of higher J-states, due to our higher temperature. However, this is in conflict with the present literature. Neglecting the crystal field splitting, average rovibrational transition energies can be obtained using the energy eigenvalues $E_{vib-rot}(v, J)$ of the standard rotation-vibration Hamiltonian $H_{vib-rot}$ (see Eq. 4.10, Eq. 4.12, and Eq. 4.11),

$$E_{vib-rot}(v = 0, J) = B_e J(J+1) - D_e(J(J+1))^2 - \frac{1}{2}\alpha_e(J(J+1)), \tag{8.4}$$

$$E_{vib-rot}(v = 1, J) = \nu_0 + B_e J(J+1) - D_e(J(J+1))^2 - \frac{3}{2}\alpha_e(J(J+1)). \tag{8.5}$$

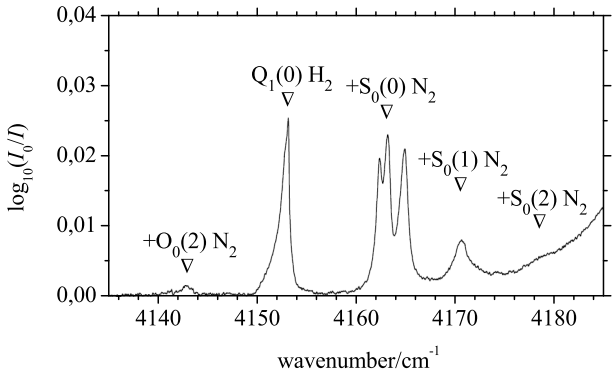

Figure 8.17: *Dopant induced IR absorption of a 3.1 mm thick para-hydrogen crystal at 4.8 K, doped with 1000 ppm nitrogen and approximately 100 ppm ortho-hydrogen impurities, recorded with 0.1 cm^{-1} resolution by Hinde et al. [177].*

With the empirical constants given by Fajardo et al., $\nu_0 = 2140.295(2)$ cm^{-1}, $B_e = 1.577(1)$ cm^{-1}, $D_e = 0.0271(1)$ cm^{-1}, and $\alpha_e = 0.0129(6)$ cm^{-1}, average transition energies for $R_{av}(0-2)$, and $P_{av}(1-3)$ can be obtained, which are included in Figure 8.13. If our A^*-peak origins from thermal population of the $J = 3$-level, it has to converge with the $P(3)$-transition around $P_{av}(3) = 2,133.7(3)$ cm^{-1}, but this is certainly not the case. For C^*, which might also origin from a higher J-level, the discrepancy is even bigger. Since the centrifugal distortion constant D_e found by Fajardo et al. is 4000 times bigger than in the gas phase (see Table 4.1), no R-transition exceeds $R(2)$ at about $R_{av}(2) = 2,146.64(8)$ cm^{-1}, which is far red-shifted from our C^*-peak. In the light of our spectra, a further investigation of carbon monoxide doped hydrogen crystals would therefore be desirable.

8.3.3 Nitrogen

Nitrogen was widely used by us as sample in nonresonant, ultrafast OKE spectroscopy in the gas phase [26, 73]. Its properties, namely the absence of a dipole moment and its comparatively high anisotropic polarizability (see Table 4.1), made it a dopant of choice for OKE spectroscopy in solid para-hydrogen. Unfortunately, gaseous nitrogen is infrared inactive and it was not possible for us to characterize our para-hydrogen matrices, doped with comparatively low nitrogen concentrations, with our low resolution FTIR spectrometer. However, Hinde et al. [177] applied the rapid vapor deposition technique to grow para-hydrogen crystals doped with 1000 ppm nitrogen, ten times more than it is possible in an enclosed cell. They showed that nitrogen undergoes a hindered rotation in a para-hydrogen matrix, which is demonstrated is Figure 8.17.

As ortho-hydrogen impurities, $J = 1$ nitrogen dopants induce $Q_1(0)$ transitions in neighboring para-hydrogen molecules by the EQQ interaction, and the spherical $J = 0$ nitrogen dopants induce $Q_1(0)$ transitions by a similar symmetry breaking isotropic induction mechanism, which is based on short range intermolecular exchange interactions. Both, EQQ and overlap-induced $Q_1(0)$ transitions in para-hydrogen, can be accompanied by pure rotational $\Delta J = 2$ transitions of the nitrogen dopant. The spectrum shown in Fig. 8.17 contains the pure vibrational $Q_1(0)$ (H_2) transition of para-hydrogen, which is accompanied by several cooperative transition of para-hydrogen and nitrogen, like $Q_1(0)$ (H_2) + $S_0(0)$ (N_2). Recorded at 4.8 K, the majority of the nitrogen population is in the ground states, $J = 0$ for ortho-nitrogen and $J = 1$ for para-nitrogen. Only about 15 percent of the ortho-nitrogen species is in the $J = 2$ state, and 1 percent of para-nitrogen in the $J = 3$

state. Therefore the $Q_1(0)$ (H_2) + $S_0(0)$ (N_2) and $Q_1(0)$ (H_2) + $S_0(1)$ (N_2) transitions are the dominating cooperative transitions. Interesting to note is that the orientational degeneracy of the nitrogen $J = 2$ is lifted and the $Q_1(0)$ (H_2) + $S_0(0)$ (N_2) transition is therefore split into a triplet. From the analysis of their data Hinde et al. concluded that nitrogen exhibits a rotational constant of $B_0 = 1.79(4)$ cm^{-1} in solid para-hydrogen, which is only ten percent lower than the gas phase value of $B_0 = 1.99$ cm^{-1} [66].

8.3.4 Outlook to dopant dynamics in solid hydrogen

The behavior of methane and carbon monoxide in solid hydrogen, as was shown in the previous subsections, is similar in many aspects. Both occupy single substitutional sites and perform a hindered rotation in solid para-hydrogen. However, particularly their tendency to form clusters, of major importance for any matrix isolation technique, is different. We were able to grow transparent methane doped hydrogen crystals with concentrations of 100 ppm and a low clustering rate. Unfortunately, methane is not suitable for alignment experiments, because it does not exhibit an anisotropic polarizability $\Delta\alpha$ (see Table 4.1). Carbon monoxide exhibits an anisotropic polarizability, however it clusters very easily by virtue of its electrostatic dipole moment. Thus, we were not able to grow unclustered samples with good optical properties at carbon monoxide concentrations of more than 10 ppm. This is a pity, especially in the light of possible alignment experiments that focus on dopant dynamics in solid hydrogen.

The desired properties of a dopant for alignment experiments are an anisotropic polarizability and the absence of a permanent dipole moment, to reduce the clustering. This is the case for any diatomic, homonuclear molecule. Thus, next to methane and carbon monoxide, we doped hydrogen crystals with nitrogen. Since it lacks a dipole moment, nitrogen is infrared inactive. We were therefore not able to investigate the growth of nitrogen doped crystals by our spectral means. However, we may assume that nitrogen behaves very similar to methane, which should allow us to grow transparent hydrogen crystals with nitrogen concentrations of 100 ppm. Given the particle density of solid para-hydrogen, a nitrogen concentration of 100 ppm corresponds to a nitrogen density of 4.3×10^{-6} mol/cm^3. A particle density that was sufficient for our gas phase alignment studies. Indeed, we successfully carried out homodyne detected alignment experiments with good signal to noise ratio on gaseous nitrogen at 87 K and pressures as low as 30 mbar, which corresponds to a particle density of 4.1×10^{-6} mol/cm^3.

However, we face a severe obstacle for OKE spectroscopy in solid para-hydrogen: the low destruction threshold of the sample of about 1-2 TW/cm^2. This forces us to reduce the power of our pump laser by one order of magnitude compared to the gas phase. Therefore, the homodyne detected nitrogen alignment signal of the gas phase would be reduced by two orders of magnitude, which would render the observation of nitrogen alignment dynamics in solid para-hydrogen impossible. Fortunately, we are able to enhance the alignment signal by introducing a local oscillator field. The optically heterodyne detection scheme has several advantages: it increases the signal to noise ratio, is linearly dependent on particle density and pump laser intensity, and exhibits two times longer lifetimes. Indeed, we recorded heterodyned phonon dynamics in solid hydrogen that exceeded the corresponding homodyned signal contributions by more than one order of magnitude. Still, with signals close to the detection limit the direct observation of rotational alignment dynamics of dopants in solid para-hydrogen stays a challenging task. Additionally, a clear identification of such dynamics may also be obscured by the inherent dynamics of the host. Particularly the discussed higher order Raman transitions of para-hydrogen must be considered, since their 2D OKE signals have the same spectral position and similar dynamics as the alignment

signals of many possible dopant molecules. In a first series of 2D OKE experiments on para-hydrogen crystals, doped with various concentrations of nitrogen, we were therefore unable to identify the observed dynamics without ambiguity.

Due to the only slightly hindered rotation of many dopants in solid para-hydrogen, known from infrared absorption experiments as they were carried out within this work, there is no doubt that rotational alignment of dopants in a solid can be achieved. The direct observation of the alignment dynamics via 2D OKE spectroscopy is however a nontrivial task. Further experiments might therefore focus on an improved test sample. Oxygen is a very interesting candidate, because it exhibits an almost two times higher anisotropic polarizability than nitrogen. It has no permanent dipole moment, which enables high dopant concentrations. Additionally, it can be prepared in a $J = 0$ state, which eliminates all electric multipole moments, and it even has a lower polarizability than nitrogen, which reduces the long range van der Waals interactions that lead to clustering. Last but not least, alignment dependent oxygen-hydrogen reactions, involving the $J = 2$ rotational excitations of both molecules, open an exciting field of solid state chemistry. Further improvements of the 2D OKE setup can also be considered. E.g. increased/decreased laser pulse durations decrease/increase the nonadiabatic excitation of high energy modes. Furthermore, the excitation of Raman-active modes depends with ω^4 on the frequency of the light pulses. An improved setup might therefore apply pump and probe laser pulses in the visible or ultraviolet region to surpass the low destruction threshold of solid para-hydrogen.

9 Summary

This thesis presents an experimental study that focuses on ultrafast dynamics in solid hydrogen. It is the first report on the direct observation of coherent rotons and phonons in this fundamental system. Therefore, we applied an extended approach to the time resolved spectroscopy of Raman induced coherences, which we call two dimensional optical Kerr effect (2D OKE) spectroscopy. Further important aspects of this thesis are the preparation of para-hydrogen, the growth of transparent para- and normal-hydrogen crystals, and the possibilities to dope these crystals with small molecules.

2D OKE spectroscopy

A spectrally resolved extension of the well established time resolved optical Kerr effect (OKE) spectroscopy was introduced on gaseous and liquid para-hydrogen, and subsequently carried to the solid phase. It is sensitive to Raman active coherences, and provides the possibility to observe the dynamics of different Raman modes at different spectral positions. Test experiments on rotational alignment dynamics of isotropic gaseous and liquid para-hydrogen samples yield very high accuracies and excellent quantitative agreement with the literature. We observed the coherent alignment dynamics of para-hydrogen gas for thousands of periods and the accuracy of the determined rotational transition frequency was only limited by the mechanical accuracy of our delay stage. The two dimensional optical Kerr effect spectra provide important information, since they allow to distinguish the origin of all signal components by their spectral distribution. The spectral separation makes it possible to analyze data quantitatively and reveals dynamics that would have be obscured using traditional OKE spectroscopy. Indeed, we simultaneously observed very different Raman-active roton and phonon modes. Additionally, 2D OKE spectroscopy allowed us to identify and exclude artifacts in our experiments on the basis of their spectral distribution. We enhanced our signals by heterodyning them with a local oscillator field, and found that a careful determination of the local oscillator is crucial for the understanding of the 2D OKE spectra. The spectra of isotropic samples revealed a distinct dependence on the orientation of the laser pulse polarizations. For solid para-hydrogen, which has an hcp lattice structure, we also observed a strong influence of the crystal orientation, as expected for an anisotropic sample. Most interesting is the observation of stimulated and higher order Raman transitions in dense hydrogen samples. These effects are highly dependent on the applied laser powers and have to be properly identified, since they lead to signal variations that affect the decay times and frequencies in 2D OKE spectra.

Solid state dynamics

We applied femtosecond spectroscopy on solid para- and normal-hydrogen with great success. The 2D OKE spectra carry the information on all long lived, $\mathbf{k} \approx 0$, Raman-active excitations that lie within the resolution limit of the laser pulses. We quantitatively observed collective vibrations of a twofold degenerated transversal optical phonon mode with periods of about 900 fs and simultaneously rotational alignment dynamics of a delocalized $J = 2$ roton excitation with periods of about 94 fs in solid para-hydrogen. The observed

transition energies of $\nu_{TO\,phonon} = 36.75(3)$ cm^{-1} for the phonon and $\nu_{|M|=1} = 351.98(8)$ cm^{-1}, $\nu_{|M|=2} = 353.99(8)$ cm^{-1}, and $\nu_{M=0} = 356.00(8)$ cm^{-1} for the threefold split roton are in excellent agreement with the literature. Indeed, we were able to resolve the fine crystal field splitting of the roton excitation into three components with difference energies of $\Delta\nu_{12} = 2.00(8)$ cm^{-1} and $\Delta\nu_{02} = 1.98(8)$ cm^{-1}, which correspond to sub-femtosecond differences in the periods of the orientational substates. The splittings are derived from distinct beatings in the roton signal with periods of about 8 ps and 17 ps. This observation also allows us to identify the hcp lattice structure of our crystals without ambiguity. Even more, we determined the lifetime of the observed transversal optical phonon mode with the highest accuracy that was ever reported to be $T_2 = 19(1)$ ps, and are able to present an average lifetime for the three roton substates of $T_2 = 90(30)$ ps. The exceptionally slow dephasing of the rotational excitation made it possible to follow the coherent roton dynamics for more than thousand periods. The well defined transitions and long dephasing times make solid para-hydrogen to an interesting sample for quantum computing.

Analogous long lived phonon dynamics with an only slightly shifted transition energy of $\nu_{TO\,phonon} = 37.5(1)$ cm^{-1} were observed in solid normal-hydrogen, too. The lifetime of the phonon is reduced by a factor of two to $T_2 = 11(3)$ ps, which we attribute to inhomogeneous broadening. Additionally, we observed Raman-active, orientational interactions in solid normal-hydrogen, which are absent in pure para-hydrogen crystals due to the lack of orientational degrees of freedom. However, we were not able to identify rotational excitations in normal-hydrogen without ambiguity, and attribute this to a drastic decrease of the roton lifetime.

Sample preparation and characterisation

The preparation of para-hydrogen and the growth of pure and doped para-hydrogen crystals was introduced to our laboratory. The properties of solid hydrogen are strongly dependent on the ratio of the two nuclear spin states of hydrogen, $I = 0$ para- and $I = 1$ ortho-hydrogen. Thus, the efficient conversion of the 74.9% ortho-hydrogen content of normal-hydrogen to para-hydrogen plays a key role in experiments with solid hydrogen. We reduced the ortho-hydrogen concentration down to 0.03% by catalyst induced spinflips at low temperatures. The residual ortho-hydrogen concentration was determined by spectroscopic means, using the ortho-hydrogen induced infrared absorption of solid para-hydrogen. Para-hydrogen gas was used to grow 3 cm thick crystals in an enclosed cylindrical copper cell with CaF_2 windows. In order to perform polarization sensitive laser spectroscopy, the solid hydrogen samples have to be of exceptional optical quality, which demands controlled growth parameters. Pure para-hydrogen crystals, grown at 13 K within less than an hour, were highly transparent and exhibited single crystal sizes of cubic millimeters to cubic centimeters. Transparent crystals were also grown from the melt in a rapid freezing manner, which was not reported before.

Furthermore, we doped para-hydrogen crystals with small molecules, i.e. methane and carbon monoxide, and analyzed them by Fourier transform infrared spectroscopy. Within this work, we observed and assigned yet unreported forbidden ro-vibrational transitions in the ν_1 stretching-mode of methane in solid para-hydrogen. New transitions were also observed in carbon monoxide doped hydrogen crystals, however, their origin is not yet fully understood. The degree of isolation and the clustering of the dopants with ortho-hydrogen impurities were evaluated in order to perform time resolved experiments on matrix isolated molecules. We were able to prepare weakly clustered, transparent para-hydrogen crystals that were doped with carbon monoxide concentrations of 10 ppm and methane concentrations of 100 ppm. The differences in the clustering behavior may be

attributed to the different electric multipole moments of the dopant molecules, particularly to the presence/absence of a permanent electric dipole moment, and the findings should therefore be transferable to other dopant species. Since we observed the nearly free rotation of isolated molecules at dopant concentrations that correspond to particle densities of up to 4.3×10^{-6} mol/cm^3, time resolved heterodyned 2D OKE spectroscopy of coherent alignment dynamics on dopant molecules becomes possible.

References and notes

[1] H. Cavendish. Three papers, containing experiments on factitious air. *Phil. Trans.*, 56:141–184, 1766.

[2] J. Dewar. Sur la solidification de l'hydrogène. *Annales de Chimie et de Physique*, 18(7):145–150, October 1899.

[3] W. F. J. Hare, Elizabeth J. Allin, and R. E. MacDonald. Infrared absorption of liquid and solid hydrogen. *Phys. Rev.*, 98:554–555, February 1955.

[4] W. N. Hardy and A. J. Berlinsky. Microwave absorption in solid hydrogen. *Phys. Rev. Lett.*, 34(24):1520–1523, June 1975.

[5] R. D. G. Prasad, M. J. Clouter, and S. Paddi Reddy. Observation of U-branch transitions in the infrared fundamental band of solid hydrogen. *Phys. Rev. A*, 17(5):1690–1694, May 1978.

[6] M. Mengel, B.P. Winnewisser, and M. Winnewisser. New infrared transitions in solid parahydrogen in the MIR and NIR/VIS regions. *J. Low Temp. Phys.*, 188(2):221–244, April 1998.

[7] A. P. Mishraa, T. K. Balasubramaniana, R. H. Tipping, and Q. Ma. Absorption spectroscopy in solid hydrogen: challenges to experimentalists and theorists. *J. Mol. Struct.*, 695-696(Winnewisser Special Issue):103–109, June 2004.

[8] T. Oka. High-resolution spectroscopy of solid hydrogen. *Annu. Rev. Phys. Chem.*, 44:299–333, October 1993.

[9] T. Momose and T. Shida. Matrix-isolation spectroscopy using solid parahydrogen as the matrix: Application to high-resolution spectroscopy, photochemistry, and cryochemistry. *Bull. Chem. Soc. Jpn.*, 71(1):1–15, 1998.

[10] T. Momose, H. Hoshina, M. Fushitani, and H. Katsuki. High-resolution spectroscopy and the analysis of ro-vibrational transitions of molecules in solid parahydrogen. *Vib. Spectr.*, 34(1):95–108, June 2004.

[11] L. Kriachtchev. *Physics and Chemistry at Low Temperatures*. Pan Stanford Publishing Pte. Ltd., Singapore, 2011.

[12] M. E. Jacox. Comparison of the electronic energy levels of diatomic molecules in the gas phase and in inert solid matrices. *J. Mol. Struct.*, 157(1-3):43–59, March 1987.

[13] M. E. Jacox. The vibrational energy levels of small transient molecules isolated in neon and argon matrices. *Chem. Phys.*, 189(2):149–170, December 1994.

[14] V.A. Apkarian and V.E. Bondybey. Special issue, photophysics of matrix-isolated molecules. *Chem. Phys.*, 189(2):1–292, 1994.

[15] V. E. Bondybey, A. M. Smith, and J. Agreite. New developments in matrix isolation spectroscopy. *Chem. Rev.*, 96(6):2113–2134, 1996.

[16] V.A. Apkarian and N. Schwentner. Molecular photodynamics in rare gas solids. *Chem. Rev.*, 99(6):1481–1514, June 1999.

[17] T. Momose, M. Fushitani, and H. Hoshina. Chemical reactions in quantum crystals. *Int. Rev. Phys. Chem.*, 24(3-4):533–552, July 2005.

[18] K. Yoshioka, P. L. Raston, and D. T. Anderson. Infrared spectroscopy of chemically doped solid parahydrogen. *Int. Rev. Phys. Chem.*, 25(3):469–496, July 2006.

[19] T. Kiljunen, M. Bargheer, M. Gühr, and N. Schwentner. A potential energy surface and a trajectory study of photodynamics and strong-field alignment of ClF molecule in rare gas (Ar, Kr) solids. *Phys. Chem. Chem. Phys.*, 6(9):2185–2197, 2004.

[20] T. Kiljunen, M. Bargheer, M. Gühr, N. Schwentner, and B. Schmidt. Photodynamics and ground state librational states of ClF molecule in solid Ar. comparison of experiment and theory. *Phys. Chem. Chem. Phys.*, 6(11):2932–2939, 2004.

[21] L. Pauling. The rotational motion of molecules in crystals. *Phys. Rev.*, 36(3):430–443, August 1930.

[22] J. P. Heritage, T. K. Gustafson, and C. H. Lin. Observation of coherent transient birefringence in CS_2 vapor. *Phys. Rev. Lett.*, 34(21):1299–1302, May 1975.

[23] M. Morgen, W. Price, L. Hunziker, P. Ludowise, M. Blackwell, and Y. Chen. Femtosecond Raman-induced polarization spectroscopy studies of rotational coherence in 0_2, N_2 and CO_2. *Chem. Phys. Lett.*, 209(1-2):1–9, June 1993.

[24] V. Renard, M. Renard, S. Guérin, Y. T. Pashayan, B. Lavorel, O. Faucher, and H. R. Jauslin. Postpulse molecular alignment measured by a weak field polarization technique. *Phys. Rev. Lett.*, 90(15):153601 1–4, April 2003.

[25] N. Owschimikow. *Coherence in a thermal ensamble: Creation and decay of laser-induced alignment in nitrogen.* Doctoral Thesis, Department of Physics, Free University of Berlin, 2010.

[26] N. Owschimikow, F. Königsmann, J. Maurer, P. Giese, A. Ott, B. Schmidt, and N. Schwentner. Cross sections for rotational decoherence of perturbed nitrogen measured via decay of laser-induced alignment. *J. Chem. Phys.*, 133(4):044311 1–13, July 2010.

[27] W. T. Lotshaw, D. McMorrow, N. Thantu, J. S. Melinger, and R. Kitchenham. Intermolecular vibrational coherence in molecular liquids. *J. Raman Spectrosc.*, 26(7):571–583, July 1995.

[28] N. A. Smith and S. R. Meech. Optically-heterodyne-detected optical Kerr effect (OHD-OKE): applications in condensed phase dynamics. *Int. Rev. Phys. Chem.*, 21(1):75–100, January 2002.

[29] I. I. Abram, R. M. Hochstrasser, J. E. Kohl, M. G. Semack, and D. White. Decay of vibrational coherence in ortho-para mixtures of solid hydrogen. *Chem. Phys. Lett.*, 71(3):405–408, May 1980.

[30] C. Sierens, A. Bouwen, E. Goovaerts, M. De Mazière, and D. Schoemaker. Roton relaxation in parahydrogen crystals measured by time-resolved stimulated Raman gain. *Phys. Rev. A*, 37(12):4769–4777, June 1988.

[31] L. Bonacina, P. Larrégaray, F. van Mourik, and M. Chergui. Lattice response of quantum solids to an impulsive local perturbation. *Phys. Rev. Lett.*, 95:015301 1–4, 2005.

[32] L. Bonacina, P. Larrégaray, F. van Mourik, and M. Chergui. The ultrafast structural response of solid parahydrogen: A complementary experimental/simulation investigation. *J. Chem. Phys.*, 125:054507 1–11, June 2006.

[33] F. Königsmann, M. Fushitani, N. Owschimikow, D. Anderson, and N. Schwentner. Femtosecond pump-probe 2D optical Kerr effect spectroscopy of molecular hydrogen crystals. *Chem. Phys. Lett.*, 458:303–307, May 2008.

[34] M. Tsubouchi and T. Momose. Pulse shaping and its characterization of mid-infrared femtosecond pulses: Toward coherent control of molecules in the ground electronic states. *Opt. Comm.*, 282(18):3757–3764, September 2009.

[35] I. F. Silvera. The solid molecular hydrogens in the condensed phase: Fundamentals and static properties. *Rev. Mod. Phys.*, 52(2):393–452, April 1980.

[36] J. Van Kranendonk. *Solid hydrogen - Theory of the properties of solid H_2, HD, and D_2.* Plenum Press, New York, 1983.

[37] P. C. Souers. *Hydrogen properties for fusion energy.* University of California Press, Berkeley, California, 1986.

[38] V. G. Manzhelii and Y. A. Freimann. *Physics of cryocrystals.* American Institute of Physics, Woodbury, New York, 1997.

[39] F. Baas and K. D. van den Hout. Measurements of depolarization ratios and polarizability anisotropies of gaseous molecules. *Physica A*, 95(3):597–601, March 1979.

[40] G. W. Collins, W. G. Unites, E. R. Mapoles, and T. P. Bernat. Metastable structures of solid hydrogen. *Phys. Rev. B*, 53(1):102–106, January 1996.

[41] R. W. Hill and B. W. A. Ricketson. A λ-anomaly in the specific heat of solid hydrogen. *Philosophical Magazine Series 7*, 45(362):277–282, 1954.

[42] R. G. Bohn and C. F. Mate. Thermal conductivity of solid hydrogen. *Phys. Rev. B*, 2(6):2121–2126, September 1970.

[43] B. Ya. Gorodilov and V. B. Kokshenev. Analysis of the thermal conductivity of solid hydrogen including configurational relaxation effects. *J. Low Temp. Phys.*, 81(1/2):45–54, May 1990.

[44] J. Van Kranendonk and G. Karl. Theory of the rotational and vibrational excitations in solid parahydrogen, and frequency analysis of the infrared and Raman spectra. *Rev. Mod. Phys.*, 40(3):532–555, July 1968.

[45] M. Nielsen. Phonons in solid hydrogen and deuterium studied by inelastic coherent neutron scattering. *Phys. Rev. B*, 7(4):1626–1635, February 1973.

[46] I. F. Silvera, W. N. Hardy, and J. P. McTague. Raman-active optical phonons in the hexagonal phases of solid H_2, D_2, and HD. *Phys. Rev. B*, 5(4):1578–1586, February 1972.

[47] W. N. Hardy, I. F. Silvera, K. N. Klump, and O. Schnepp. Optical phonons in solid hydrogen and deuterium in the ordered state. *Phys. Rev. Lett.*, 21(5):291–294, July 1968.

[48] M. Leblans, A. Bouwen, C. Sierens, W. Joosen, E. Goovaerts, and D. Schoemaker. Dephasing relaxation of $J = 2$ rotons in parahydrogen crystals doped with hydrogen-deuterium impurities. *Phys. Rev. B*, 40(10):6674–6679, October 1989.

[49] I. F. Silvera, W. N. Hardy, and J. P. McTague. Direct observation of isolated $J = 1$ pairs in solid deuterium and hydrogen by Raman scattering. *Phys. Rev. B*, 4(8):2724–2733, October 1971.

[50] S. Tam and M. E. Fajardo. Ortho/para hydrogen converter for rapid deposition matrix isolation spetroscopy. *Rev. Sci. Instrum.*, 70(4):1926–1932, April 1999.

[51] L. Andrews and X. Wang. Simple ortho-para hydrogen and para-ortho deuterium converter for matrix isolation spectroscopy. *Rev. Sci. Instr.*, 75(9):3039–3044, September 2009.

[52] N. Owschimikow. *private communication.* FU Berlin, 2010.

[53] F. Schmidt. Diffusion and ortho-para conversion in solid hydrogen. *Phys. Rev. B*, 10(10):4480–4484, November 1974.

[54] W. N. Hardy, I. F. Silvera, and J. P. McTague. Raman scattering in oriented crystals of paradeuterium and orthohydrogen. *Phys. Rev. B*, 12(2):753–789, July 1975.

[55] M. Suzuki, M. Katsuragawa, R. S. D. Sihombing, J. Z. Lib, and K. Hakuta. Solid hydrogen for nonlinear optics. *J. Low Temp. Phys.*, 111(3/4):463–468, 1998.

[56] R. J. Van Zee, S. Li, and Jr.' W. Weltner. Carbon molecules in methane and hydrogen matrices: ESR and photolysis. *J. Phys. Chem.*, 97(36):9087–9090, June 1993.

[57] M. E. Fajardo, S. Tam, T. L. Thompson, and M. E. Cordonnier. Spectroscopy and reactive dynamics of atoms trapped in molecular hydrogen matrices. *Chem. Phys.*, 189:351–365, May 1994.

[58] M. E. Fajardo and S. Tam. Rapid vapor deposition of millimeters thick optically transparent parahydrogen solids for matrix isolation spectroscopy. *J. Chem. Phys.*, 108(10):4237–4241, March 1998.

[59] S. Ishimotoa, T. Kobayashib, K. Morimotoa, I. Nomurac, A. Ozawa, S. Suzukia, Y. Takahashie, I. Tanihatad, and T. Tsuru. Windowless solid hydrogen target. *Nucl. Instr. and Meth.*, 480:304–314, March 2002.

[60] A. Frei, E. Gutsmiedl, C. Morkel, A. R. Müller, S. Paul, M. Urban, H. Schober, S. Rols, T. Unruh, and M. Hölzel. Density of states in solid deuterium: Inelastic neutron scattering study. *Phys. Rev. B*, 80(6):064301 1–8, August 2009.

[61] Y. R. Shen. *The Principles of Nonlinear Optics*. John Wiley & Sons, Hoboken, New Jersey, 1984.

[62] H. Bucka, J. Dietrich, J. Geiger, H. Gobrecht, K. Gobrecht, A. Heese, K. Hunger, H. Küsters, M. Lammbeck, G. Lehner, H. Nelkowski, D. Neubert, U. Scherz, R. Seiwert, H. Strunz A. Tausend, L. Thomas, R. Thull, K Ueberreiter, H.-G. Wagemann, and B. Wende. *Bergmann-Schaefer - Lehrbuch der Experimentalphysik - Band 4: Aufbau der Materie*. Walter de Gruyter, Berlin, 1 edition, 1975.

[63] G. Herzberg. *Molecular spectra and molecular structure - Volume I - Spectra of diatomic molecules*. Robert E. Krieger Publishing Company, Malabar, Florida, 1989.

[64] W. Nolting. *Grundkurs theoretische Physik 5/2: Quantenmechanik - Methoden und Anwendungen*. Springer Verlag, Berlin, 4th edition, 2002.

[65] G. Herzberg. *Molecular spectra and molecular structure - Volume III - Electronic spectra and electronic structure of polyatomic molecules*. Robert E. Krieger Publishing Company, Malabar, Florida, 1991.

[66] F. Pawlowski, P. Jørgensen, J. Olsen, F. Hegelund, T. Helgaker, J. Gauss, K. L. Bak, and J. F. Stanton. Molecular equilibrium structures from experimental rotational constants and calculated vibration-rotation interaction constants. *J. Chem. Phys.*, 116(15):6482–6496, April 2002.

[67] D. R. Lide. *CRC Handbook of chemistry and physics, internet version*. Taylor and Francis, Boca Raton, Florida, 2007.

[68] A. Weber. *Raman spectroscopy of gases and liquids*. Springer Verlag, Berlin, Heidelberg, New York, 1979.

[69] P. Agostini and L. F DiMauro. The physics of attosecond light pulses. *Rep. Prog. Phys.*, 67(6):813–855, May 2004.

[70] P. Felker. Rotational coherence spectroscopy: studies of the geometries of large gas-phase species by picosecond time-domain methods. *J. Phys. Chem.*, 96:7844–7857, October 1992.

[71] J. J. Larsen, H. Sakai, C. P. Safvan, I. Wendt-Larsen, and H. Stapelfeldt. Aligning molecules with intense nonresonant laser fields. *J. Chem. Phys.*, 111(17):7774–7781, November 1999.

[72] T. Seideman. Revival structure of aligned rotational wave packets. *Phys. Rev. Lett.*, 83(24):4971–4974, December 1999.

[73] N. Owschimikow, B. Schmidt, and N. Schwentner. State selection in nonresonantly excited wave packets by tuning from nonadiabatic to adiabatic interaction. *Phys. Rev. A*, 80(5):053409 1–10, November 2009.

[74] N. Owschimikow, B. Schmidt, and N. Schwentner. Laser-induced alignment and antialignment of rotationally excited molecules. *Phys. Chem. Chem. Phys.*, February 2011. DOI: 10.1039/C0CP02260H.

[75] J. Ortigoso, M. Rodriguez, M. Gupta, and B. Friedrich. Time evolution of pendular states created by the interaction of molecular polarizability with a pulsed nonresonant laser field. *J. Chem. Phys.*, 110(8):3870–3875, February 1999.

[76] S. Ramakrishna and T. Seideman. Intense laser alignment in dissipative media as a route to solvent dynamics. *Phys. Rev. Lett.*, 95(11):113001 1–4, September 2005.

[77] R. W. Boyd. *Nonlinear Optics*. Academic Press, San Diego, California, 1992.

[78] H. J. Eichler, A. Fleischer, J. Kross, M. Krystek, H. Lang, H. Niedrig, H. Rauch, G. Schmal, H. Schoenebeck, E. Sedlmayr, H. Weber, and K. Weber. *Bergmann-Schaefer - Lehrbuch der Experimentalphysik - Band 3: Optik*. Walter de Gruyter, Berlin, 9 edition, 1993.

[79] P. A. Franken, A. E. Hill, C. W. Peters, and G. Weinreich. Generation of optical harmonics. *Phys. Rev. Lett.*, 7(4):118–119, August 1961.

[80] J. Kerr. On a new relation between electricity and light: Dielectric media birefringent. *Phil. Mag.*, 50(4):337–348, November 1875.

[81] C. V. Raman and K. S. Krishnan. A new type of secondary radiation. *Nature*, 121:501–502, 1928.

[82] H. Haken and H. C. Wolf. *Molekülphysik und Quantenchemie*. Springer Verlag, Berlin, 1998.

[83] G. Eckhardt, R. W. Hellwarth, F. J. McClung, S. E. Schwarz, D. Weiner, and E. J. Woodbury. Stimulated Raman scattering from organic liquids. *Phys. Rev. Lett.*, 9(11):455–457, December 196.

[84] F. T. Arecchi and E. O. Shulz-Dubois. *Laser Handbook - Volume 2*. North-Holland Publishing Company, Amsterdam, 1972.

[85] J. W. Nibler and J. J. Yang. Nonlinear Raman spectroscopy of gases. *Ann. Rev. Phys. Chem.*, 38:349–381, October 1987.

[86] H. W. Schrötter, H. Berger, J. P. Boquillon, B. Lavorel, and G. Millot. High-resolution non-linear Raman spectroscopy in gases. *J. Raman Spectrosc.*, 21:781–789, 2005.

[87] A. Penzkofer, A. Laubereau, and W. Kaiser. High intensity Raman interactions. *Prog. Quant. Electr.*, 6:55–140, 1979.

[88] Q. Zhong and J. T. Fourkas. Optical Kerr effect spectroscopy of simple liquids. *J. Phys. Chem. B*, 112(49):15529–15539, October 2008.

[89] G. Eesley, M. Levenson, and W. Tolles. Optically heterodyned coherent Raman spectroscopy. *IEEE J. Quant. Electron.*, 14(1):45–49, January 1978.

[90] T.-H. Huang, Ch.-Ch. Hsu, T.-H. Wei, and J.-Y. Lin. Momentum conservation in Raman-induced optical Kerr effect. *Chin. J. Phys.*, 40(1):75–85, February 2002.

[91] S. Mukamel. *Principles of nonlinear optical spectroscopy*. Oxford University Press, New York, 1995.

[92] A. Laubereau and W. Kaiser. Vibrational dynamics of liquids and solids investigated by picosecond light pulses. *Rev. Mod. Phys.*, 50(3):607–665, July 1978.

[93] R. Shafer and R. G. Gordon. Quantum scattering theory of rotational relaxation and spectral line shapes in H_2-He gas mixtures. *J. Chem. Phys.*, 58(12):5422–5443, June 1973.

[94] R. A. J. Keijser, J. R. Lombardi, K. D. van den Hout, B. C. Sanctuary, and H. F. P. Knaap. The pressure broadening of the rotational Raman lines of hydrogen isotopes. *Physica*, 76:585–608, 1974.

[95] W. A. Wakeham, A. S. Dickinson, F. R. W. McCourt, and V. Vesovic. *Status and future developments in the study of transport properties*. Kluwer Academic Publishers, Dordrecht, 1992.

[96] S. Constantine, Y. Zhou, J. Morais, and L. D. Ziegler. Dispersed optical heterodyne detected birefringence and dichroism of transparent liquids. *J. Phys. Chem. A*, 101(30):5456–5462, 1997.

[97] Y. Zhou, S. Constantine, S. Harrel, and L. D. Ziegler. The probe frequency dependence of nonresonant femtosecond pump-probe nuclear responses: Undercutting vibrational inhomogeneities. *J. Chem. Phys.*, 110(12):5893–5905, March 1999.

[98] J. A. Gardecki, G. Yu, S. Constantine, J. Peng, Y. Zhou, and L. D. Ziegler. A unified treatment of ultrafast optical heterodyne detected and z-scan spectroscopies. *J. Chem. Phys.*, 114(8):3586–3597, February 2001.

[99] W. Wang, X. Ye, A. A. Demidov, F. Rosca, T. Sjodin, W. Cao, M. Sheeran, and P. M. Champion. Femtosecond multicolor pump-probe spectroscopy of ferrous cytochrome *c*. *J. Phys. Chem. B*, 104(46):10789–10801, June 2000.

[100] F. Rosca, D. Ionascu, A. T. N. Kumar, A. A. Demidov, and P. M. Champion. Femtosecond coherence spectroscopy using spectrally selective differential photodetection. *Chem. Phys. Lett.*, 337:107–116, March 2001.

[101] M. N. Slipchenko, B. D. Prince, S. C. Ducatman, and H. U. Stauffer. Development of a simultaneously frequency- and time-resolved Raman-induced Kerr effect probe. *J. Phys. Chem. A*, 113(1):135–140, January 2009.

[102] D. Heiman, R. W. Hellwarth, M. D. Levenson, and Graham Martin. Raman-induced Kerr effect. *Phys. Rev. Lett.*, 36(4):189–192, January 1976.

[103] J. Maurer. *Temperature and pressure dependence of rotational wavepackets: Polarization dynamics of N_2*. Diploma Thesis, Department of Physics, Free University of Berlin, 2008.

[104] C. Rulliére (Editor). *Femtosecond Laser Pulses, Principles and Experiments*. Springer, New York, 2nd edition, 2005.

[105] R. Trebino, K. W. DeLong, D. N. Fittinghoff, J. N. Sweetser, M. A. Krumbügel, B. A. Richman, and D. J. Kane. Measuring ultrashort laser pulses in the time-frequency domain using frequency-resolved optical gating. *Rev. Sci. Instrum.*, 68(9):3277–3295, September 1997.

[106] F. Träger. *Handbook of lasers and optics*. Springer, New York, 2007.

[107] A. E. Belikov, A. I. Burshtein, S. V. Dolgushev, A. V. Storozhev, M. L. Strekalov, G. I. Sukhinin, and R. G. Sharafutdinov. Rate constans and rotational relaxation times for N_2 in argon: Theory and experiment. *Chem. Phys.*, 139:239–259, 1989.

[108] S. S. Bhatnagar, E. J. Allin, and H. L. Welsh. The Raman spectra of liquid and solid H_2, D_2, and HD at high resolution. *Can. J. Phys.*, 40:9–23, 1962.

[109] R. Sliter and A. F. Vilesov. Temperature dependence of the Raman spectra of liquid parahydrogen. *J. Chem. Phys.*, 131(7):074502 1–11, August 2009.

[110] K. D. van den Hout, P. W. Hermans, E. Mazur, and H. F. P. Knaap. The broadening and shift of the rotational Raman lines for hydrogen isotopes at low temperature. *Physica*, 104 A:509–547, 1980.

[111] D. A. Coombe and W. E. Köhler. The effect of diatom-diatom collisions on depolarized light scattering linewidths: II. application to hydrogen isotopes. *Physica*, 100 A:472–495, 1980.

[112] R. M. Jonkman, G. J. Prangsma, I. Ertas, H. F. P. Knaap, and J. J. M. Beenakker. Rotational relaxation in mixtures of hydrogen and noble gases, Part I.: mixtures with parahydrogen. *Physica*, 38:441–450, 1968.

[113] W. E. Köhler and J. Schaefer. Theoretical studies of H_2-H_2 collisions. V. ab initio calculations of relaxation phenomena in parahydrogen gas. *J. Chem. Phys.*, 78(11):6602–6610, June 1983.

[114] T.-G. Lee, N. Balakrishnan, R. C. Forrey, P. C. Stancil, G. Shaw, D. R. Schultz, and G. J. Ferland. Rotational quenching rate coefficients for H_2 in collisions with H_2 from 2 to 10,000 k. *The Astrophysical Journal*, 689:1105–1110, December 2008.

[115] B. A. Younglove. Thermophysical properties of fluids. I. argon, ethylene, parahydrogen, nitrogen, nitrogen triflouride, and oxygen. *J. Phys. Chem. Ref. Data*, 11:1–347, 1982.

[116] M. Fushitani. *private communication*. FU Berlin, 2006.

[117] G. A. Garrett, T. F. Albrecht, J. F. Whitaker, and R. Merlin. Coherent THz phonons driven by light pulses and the Sb problem: What is the mechanism? *Phys. Rev. Lett.*, 77(17):3661–3664, October 1996.

[118] I. F. Silvera, P. J. Berkhout, and L. M. van Aernsbergen. Frequency dependence of Raman-active phonons in solid hcp hydrogen on ortho-para concentration and temperature. *J. Low Temp. Phys.*, 35(5/6):611–625, 1979.

[119] R. J. Wijngaarden, V. V. Goldman, and I. F. Silvera. Pressure dependence of the optical phonon in solid hydrogen and deuterium up to 230 kbar. *Phys. Rev. B*, 27(8):5084–5087, April 1983.

[120] E. Goovaerts, X. Y. Chen, A. Bouwen, and D. Schoemaker. Relaxation times of $k = 0$ rotons in pure parahydrogen crystals and roton scattering by orthohydrogen impurities. *Phys. Rev. Lett.*, 57(4):479–482, July 1986.

[121] H. Saito, H. Nagao, K. Nishikawa, and K. Kinugawa. Molecular collective dynamics in solid para-hydrogen and ortho-deuterium: The Parrinello-Rahman-type path integral centroid molecular dynamics approach. *J. Chem. Phys.*, 119(2):953–963, July 2003.

[122] D. Colognesi, M. Celli, and M. Zoppi. Density of phonon states in solid parahydrogen from inelastic neutron scattering. *J. Chem. Phys.*, 120(12):5657–5663, March 2004.

[123] M. L. Klein and T. R. Koehler. Self-consistent phonon spectrum of hcp H_2 and D_2. *J. Phys. C: Solid State Phys.*, 3(5):L102–L104, March 1970.

[124] F. G. Mertens and W. Biem. Phonons and librons in solid hydrogen and deuterium. *Z. Phys.*, 250(4):273–292, 1972.

[125] W. B. J. M. Janssen and A. van der Avoird. Dynamics and phase transitions in solid ortho and para hydrogen and deuterium from an ab initio potential. *Phys. Rev. B*, 42(1):838–848, July 1990.

[126] M. Nielsen and H. Bjerrum Møller. Lattice dynamics of solid deuterium by inelastic neutron scattering. *Phys. Rev. B*, 3:4383–4385, June 1971.

[127] M. Vanhimbeeck, H. De Raedt, A. Lagendijk, and D. Schoemaker. Calculation of rotational T_2 relaxation in solid parahydrogen and orthodeuterium. *Phys. Rev. B*, 33(6):4264–4262, March 1986.

[128] M. Fushitani, S. Kuma, Y. Miyamoto, H. Katsuki, T. Wakabayashi, T. Momose, and A. F. Vilesov. Generation of infrared radiation by stimulated Raman scattering in para-hydrogen crystal at 5 k. *Optics Lett.*, 28(1):37–39, January 2003.

[129] Chien-Yu Kuo, R. J. Kerl, N. D. Patel, and C. K. N. Patel. Nonradiative relaxation of excited vibrational states of solid hydrogen. *Phys. Rev. Lett.*, 53(27):2575–2578, December 1984.

[130] W. N. Hardy, I. F. Silvera, and J. P. McTague. Raman scattering in oriented crystals of paradeuterium and orthohydrogen. *Phys. Rev. B*, 12(2):753–789, July 1975.

[131] W. W. Sleator. The absorption of near infra-red radiation by water-vapor. *Astrophysical Journal*, 48:125–143, September 1918.

[132] E. F. Barker P. E. Martin. The infrared absorption spectrum of carbon dioxide. *Phys. Rev.*, 41(3):291–303, June 1932.

[133] M. Fushitani, T. Shida, T. Momose, and M. Räsänen. UV-photolysis of HI-CO_2 complexes in solid parahydrogen: Formation of CO and H_2O. *J. Phys. Chem. A*, 104(16):3635–3641, October 1999.

[134] L. Schriver-Mazzuoli, A. Schriver, and A. Hallou. IR reflection-absorption spectra of thin water ice films between 10 and 160 K at low pressure. *J. Mol. Struct.*, 554:289–300, June 2000.

[135] J. C. McLennan and J. H. McLeod. The Raman effect with liquid oxygen, nitrogen, and hydrogen. *Nature*, 123(3092):160–160, February 1929.

[136] G. Bachet. Collision induced spectra for H_2-He interactions from 79 to 248 K between 200 and 700 cm^{-1}. *J. Quant. Spectrosc. Radiat. Transfer*, 39:327–331, April 1988.

[137] H. L. Welsh, M. F. Crawford, and J. L. Locke. Infra-red absorption of hydrogen and carbon dioxide induced by intermolecular forces. *Phys. Rev.*, 76(4):580–580, July 1949.

[138] W. F. J. Hare, Elizabeth J. Allin, and H. L. Welsh. Infrared absorption of liquid and solid hydrogen with various ortho-para ratios. *Phys. Rev.*, 99:1887–1888, July 1955.

[139] M. Trefler, A. M. Cappel, and H. P. Gush. Absorption by gaseous and solid HD and solid para-H_2 in the far infrared. *Can. J. Phys.*, 47(19):2115–2123, October 1996.

[140] I. Glatt, R. J. Kerl, and C. K. N. Patel. Observation of fourth vibrational overtone of hydrogen. *Phys. Rev. Lett.*, 57(12):1437–1439, September 1986.

[141] M.-C. Chan, M. Okumura, C. M. Gabrys, B. D. Rehfuss L.-W. Xu, and T. Oka. High-resolution infrared spectroscopy of solid hydrogen. *Phys. Rev. Lett.*, 66(16):2060–2063, 1991.

[142] M. Mengel, B.P. Winnewisser, and M. Winnewisser. High-resolution fourier-transform spectroscopy of solid parahydrogen in the first overtone region. *Phys. Rev. B*, 55(16):10420–10433, April 1997.

[143] R. J. Hinde. Absorption intensity of the $Q_1(0)+Q_1(0)$ and $Q_1(0)+Q_2(0)$ double vibrational transitions in solid parahydrogen. *Phys. Rev. B*, 61(17):11451–11453, 2000.

[144] A. P. Mishra and R. W. Field. Absorption intensities of the multipole-field-induced double transitions involving a homonuclear-heteronuclear pair of hydrogen molecules in condensed phase. *Phys. Rev. B*, 68(18):184303 1–8, November 2003.

[145] A. P. Mishra. The crystal-field splitting of rovibrational $W_v(0)$, $Y_v(0)$, and $[\Delta J = 10]_v(0)$ transitions of solid parahydrogen. *J. Chem. Phys.*, 132(16):164514 1–5, April 2010.

[146] Q. Ma, R. H. Tipping, and J. D. Poll. Intensities of multipole-induced zero-phonon transitions in solid parahydrogen. *Phys. Rev. B*, 39(1):132–135, January 1989.

[147] J. Van Kranendonk. Theory of the infrared and Raman spectra of solid para-hydrogen. *Can. J. Phys.*, 38(2):240–261, February 1960.

[148] J. D. Poll and J. Van Kranendonk. Theory of the phonon branches in the infrared spectrum of solid hydrogen. *Can. J. Phys.*, 40(2):163–178, February 1962.

[149] T. K. Balasubramanian, Chen-Hsin Liena, James R. Gainesa, K. Narahari Raoa, E. K. Damonb, and R. J. Nordstrom. Infrared spectrum of hydrogen in the condensed phase with high-sensitivity spectrometers: Experiments with a 0,04 cm^{-1} fourier transform spectrometer in the range 1,5-12 μm. *J. Mol. Spectrosc.*, 92(1):77–84, March 1982.

[150] H. P. Gush, W. F. J. Hare, E. J. Allin, and H. L. Welsh. The infrared fundamental band of liquid and solid hydrogen. *Can. J. Phys.*, 38:176–193, 1960.

[151] M. Okumura, M.-C. Chan, and T. Oka. High-resolution infrared spectroscopy of solid hydrogen: The tetrahexacontapole-induced $\Delta J = 6$ transitions. *Phys. Rev. Lett.*, 62(1):32–35, January 1989.

[152] J. D. Poll and R. H. Tipping. Hexadecapolar induced absorption in solid parahydrogen. *Can. Rev. Phys.*, 56(9):1165–1167, September 1978.

[153] R. A. Steinhoff, B. P. Winnewisser, and M. Winnewisser. Fourier transform spectroscopy with long absorption path length in solid hydrogen: Measurement of $\Delta J = 6$ and $\Delta J = 8$ transitions. *Phys. Rev. Lett.*, 73(21):2833–2836, November 1994.

[154] H.P. Gush. Étude à haute résolution d'une raie de vibration-rotation dans l'hydrogène solide. *J. Phys. Radium*, 22(3):149–153, March 1961.

[155] Y. Zhang, T. J. Byers, M.-C. Chan, T. Momose, K. E. Kerr, D. P. Weliky, and T. Oka. High-resolution infrared spectroscopy of the $J = 1$ H_2 pair in parahydrogen crystals. *Phys. Rev. B*, 58(1):218–233, July 1998.

[156] U. Buontempo, S. Cunsolo, P. Dore, , and L. Nencini. Far infrared absorption spectra in liquid and solid h_2. *Can. J. Phys.*, 60(10):1422–1428, October 1982.

[157] A. F. Devonshire. The rotation of molecules in fields of octahedral symmetry. *Proc. R. Soc. Lond. A*, 153(880):601–621, February 1936.

[158] T. Momose. Rovibrational states of a tetrahedral molecule in a hexagonal close-packed crystal. *J. Chem. Phys.*, 107(19):7695–7706, June 1997.

[159] T. Momose, M. Miki, T. Wakabayashi, T. Shida, M. Chan, S. S. Lee, and T. Oka. Infrared spectroscopic study of rovibrational states of methane trapped in parahydrogen crystal. *J. Chem. Phys.*, 107(19):7707–7716, June 1997.

[160] T. Momose, H. Katsuki, H. Hoshina, N. Sogoshi, T. Wakabayashi, and T. Shida. High-resolution laser spectroscopy of methane clusters trapped in solid parahydrogen. *J. Chem. Phys.*, 107(19):7717–7720, June 1997.

[161] Y. Miyamoto, M. Fushitani, D. Ando, and T. Momose. Nuclear spin conversion of methane in solid parahydrogen. *J. Chem. Phys.*, 128(11):114502 1–10, March 2008.

[162] S. Tam, H. Katsuki, H. Hoshina, T. Wakabayashi, T. Momose, and M. E. Fajardo. High resolution infrared absorption spectra of methane molecules isolated in solid parahydrogen matrices. *J. Chem. Phys.*, 111(9):4191–4198, September 1999.

[163] Y.-J. Wu, X. Yang, and Y.-P. Lee. Infrared matrix-isolation spectroscopy using pulsed deposition of p-H_2. *J. Chem. Phys.*, 120(3):1168–1171, January 2004.

[164] L. H. Jones, S. A. Ekberg, and B. I. Swanson. Hindered rotation and site structure of methane trapped in rare gas solids. *J. Chem. Phys.*, 85(6):3203–3210, September 1986.

[165] J. A. Coxon and P. G. Hajigeorgiou. Direct potential fit analysis of the $X^1\Sigma^+$ ground state of CO. *J. Chem. Phys.*, 121(7):2992–3008, August 2004.

[166] G. E. Leroi, G. E. Ewing, and G. C. Pimentel. Infrared spectra of carbon monoxide in an argon matrix. *J. Chem. Phys.*, 40(8):2298–2303, April 1964.

[167] M. E. Fajardo, C. M. Lindsay, and T. Momose. Crystal field theory analysis of rovibrational spectra of carbon monoxide monomers isolated in solid parahydrogen. *J. Chem. Phys.*, 130(24):244508 1–10, June 2009.

[168] M. Fushitani, T. Shida, T. Momose, and M. Räsänen. UV-photolysis of HI···CO_2 complexes in solid parahydrogen: Formation of CO and H_2O. *J. Phys. Chem. A*, 104(16):3635–3641, March 2000.

[169] S. Tam and M. E. Fajardo. Observation of the high-resolution infrared absorption spectrum of CO_2 molecules. *Low Temp. Phys.*, 26(9-10):653–660, September 2000.

[170] S. Tam and M. E. Fajardo. CO/pH_2: A molecular thermometer. *J. Low Temp. Phys.*, 122(3/4):345–357, February 2001.

[171] G. E. Ewing. Infrared spectra of liquid and solid carbon monoxide. *J. Chem. Phys.*, 37(10):2250–2256, November 1962.

[172] H. Dubost. Infrared absorption spectra of carbon monoxide in rare gas matrices. *Chem. Phys.*, 12(2):139–151, January 1976.

[173] A. G. Maki. Infrared spectra of carbon monoxide as a solid and in solid matrices. *J. Chem. Phys.*, 35(3):931–935, September 1961.

[174] P. J. Fenelon and H. E. Rubalcava. Infrared spectra of carbon monoxide in zeolites. *J. Chem. Phys.*, 51(3):961–967, August 1969.

[175] I. Holleman, G. von Helden, A. van der Avoird, and G. Meijer. An infrared study on CO intercalated in solid C_{60}. *J. Chem. Phys.*, 110(4):2129–2139, January 1999.

[176] S. Moroni, M. Botti, S. De Paolo, and A. R. W. McKeller. Small para-hydrogen clusters doped with carbon monoxide: Quantum monte carlo simulations and observed infrared spectra. *J. Chem. Phys.*, 122(9):094314 1–8, March 2005.

[177] R. J. Hinde, D. T. Anderson, S. Tam, and M. E. Fajardo. Probing quantum solvation with infrared spectroscopy: infrared activity induced in solid parahydrogen by N_2 and Ar dopants. *Chem. Phys. Lett.*, 356(3-4):355–360, April 2002.